HAL
open science

Dynamique quantique ultra-rapide de nanogouttes d'hélium superfluide dopées

François Coppens

▶ **To cite this version:**

François Coppens. Dynamique quantique ultra-rapide de nanogouttes d'hélium superfluide dopées. Mécanique des matériaux [physics.class-ph]. Université Paul Sabatier - Toulouse III, 2018. Français. NNT : 2018TOU30145 . tel-02301575

HAL Id: tel-02301575

https://theses.hal.science/tel-02301575v1

Submitted on 30 Sep 2019

HAL is a multi-disciplinary open access archive for the deposit and dissemination of scientific research documents, whether they are published or not. The documents may come from teaching and research institutions in France or abroad, or from public or private research centers.

L'archive ouverte pluridisciplinaire **HAL**, est destinée au dépôt et à la diffusion de documents scientifiques de niveau recherche, publiés ou non, émanant des établissements d'enseignement et de recherche français ou étrangers, des laboratoires publics ou privés.

Université Fédérale

Toulouse Midi-Pyrénées

THÈSE

En vue de l'obtention du

DOCTORAT DE L'UNIVERSITÉ DE TOULOUSE

Délivré par : *l'Université Toulouse 3 - Paul Sabatier (UT3 Paul Sabatier)*

Présentée et soutenue le *vendredi 15 juin 2018* **par :**

François M.G.J. COPPENS

Ultrafast Quantum Dynamics of Doped Superfluid Helium Nanodroplets

---

JURY

Nadine HALBERSTADT	Directrice de Recherche	Directrice de Thèse
Robert ZILLICH	Professeur d'Université	Rapporteur
Marcel DRABBELS	Directeur de Recherche	Rapporteur
Phuong Mai SEVE DINH	Professeur d'Université	Présidente du Jury
Manuel BARRANCO	Professeur d'Université	Examinateur
Lionel POISSON	Directeur de Recherche	Examinateur

École doctorale et spécialité :
SDM - Sciences de la Matière - Toulouse : Physique
Unité de Recherche :
LCAR-IRSAMC - Laboratoire Collisions Agrégats Réactivité (UMR 5589)
Directrice de Thèse :
Nadine HALBERSTADT
Rapporteurs :
Robert ZILLICH et *Marcel DRABBELS*

Ultrafast Quantum Dynamics of Doped Superfluid Helium Nanodroplets

François M.G.J. Coppens

Submitted: **April 2018**
Defended: **June 2018**

Abstract

In this thesis we investigate two aspects of the dynamics of atomic impurities interacting with superfluid helium (He) nanodroplets, namely the photo-excitation of alkalis on a nanodroplet and the doping process of nanodroplets hosting quantised vortices with noble gas atoms. For the theoretical investigations we use He density functional theory and its time-dependent version.

The first aspect involves a joint experimental and theoretical collaboration that focusses on the photo-excitation of the alkali rubidium (Rb). Alkalis are a very interesting probe of He droplets since they reside in their surface region, where it has been argued that almost 100% Bose-Einstein condensation could be achieved due to a density that is lower than in bulk superfluid He.

In our simulations we find that states excited to the 5p and 6p manifold desorb at very different timescales, separated by 2 orders of magnitude (~100 ps and ~1 ps for 5p and 6p respectively). This is in good agreement with experimental results where the desorption behaviour of photo-excited Rb atoms is determined using a femtosecond pump-probe scheme. However, in our simulations excitation to the $5\mathrm{p}\,^2\Pi_{3/2}$-state results in a surface-bound RbHe exciplex, contrary to the experimental case where the RbHe exciplex desorbs from the droplet's surface. Introducing $^2\Pi_{1/2} \leftarrow {}^2\Pi_{3/2}$ spin-relaxation into the simulations, the RbHe exciplex is able to desorb from the droplet's surface, which resolves this contradiction.

The second aspect concerns a purely theoretical investigation that is inspired by recent work of Gomez and Vilesov *et al.*, where quantised vortices were visualised by doping He nanodroplets with silver atoms, subsequently "soft landing" them on a carbon screen. Electron-microscope images show long filaments of silver atom clusters that accumulated along the vortex cores. Also the formation of quantum-vortex lattices inside nanodroplets is evidenced by using X-ray diffractive imaging to visualise the characteristic Bragg patterns from xenon (Xe) clusters trapped inside the vortex cores.

First, head-on collisions between heliophilic Xe and a He nanodroplet made of 1000 He atoms are studied. The results are then compared with the results of a previous study of an equivalent kinematic case with cesium (Cs), which is heliophobic. Xe acquires a "snowball" of He around itself when it traverses the droplet and much more kinetic energy is required before Xe is able to pierce the droplet completely. When it does, it

takes away some He with it, contrary to the Cs case.

Next, collisions between argon (Ar)/Xe and pristine superfluid He nanodroplets are performed for various initial velocities and impact parameters, to determine the effective cross-section for capture. Finally, the simulations are then repeated for droplets hosting a single quantised vortex line. It is observed that the impact of the impurities induces large bending and twisting excitations of the vortex line, including the generation of helical Kelvin waves propagating along the vortex core. We conclude that Ar/Xe is captured by the quantised vortex line, although not in its core. Also we find that a He droplet, hosting a 6-vortex line array whose cores are filled with Ar atoms, results in added rigidity to the system which stabilises the droplets at low angular velocities.

Our simulations involving droplets hosting quantum vortices open the way to further investigations on droplets hosting an array of vortices, involving multiple impurities.

Résumé

Dans cette thèse, nous étudions deux aspects de la dynamique d'impuretés atomiques interagissant avec des nanogouttes d'hélium superfluide (He) : la photo-excitation d'alcalins sur une nanogoutte et le dopage de nanogouttes contenant des tourbillons (vortex) quantiques avec des atomes de gaz rares. Nous utilisons la théorie de la fonctionnelle de la densité d'hélium ainsi que sa version dépendante du temps pour en faire la description théorique.

Le premier aspect a été effectué dans le cadre d'une collaboration avec des expérimentateurs sur la photo-excitation du rubidium (Rb). Les alcalins sont une sonde très intéressante des gouttelettes d'hélium car ils résident dans leur zone de surface, où il a été prédit qu'un taux de condensation de Bose-Einstein de 100% était possible en raison d'une densité inférieure à celle de l'hélium superfluide.

Nos simulations montrent que les états excités 5p et 6p désorbent à des échelles de temps très différentes, séparées par 2 ordres de grandeur (~100 ps et ~1 ps pour 5p et 6p respectivement). Ces résultats sont en accord avec ceux de l'expérience pompe-sonde à l'échelle femtoseconde qui a étudié la photodesorption d'atomes de Rb. Cependant, dans nos simulations, l'excitation vers $5\mathrm{p}\,^2\Pi_{3/2}$ aboutit à un exciplexe RbHe lié à la surface, contrairement à l'expérience où RbHe est éjecté. L'introduction de la relaxation de spin $^2\Pi_{1/2} \leftarrow {}^2\Pi_{3/2}$ nous a permis de résoudre ce désaccord, l'exciplexe RbHe ayant alors assez d'énergie pour désorber.

Le deuxième aspect concerne une investigation purement théorique inspirée par les travaux récents de Gomez et Vilesov *et al.*, où les tourbillons quantiques étaient visualisés en dopant les nanogouttes d'hélium avec des atomes d'argent, puis en les faisant atterrir en douceur (soft landing) sur un écran de carbone. Les images au microscope électronique montrent de longs filaments d'agrégats d'atomes d'argent qui s'étaient accumulés le long des cœurs des vortex. La formation de réseaux de tourbillons quantiques à l'intérieur de nanogoutelettes dopées par du xénon est également mise en évidence par diffraction de rayons X qui montrent des pics de Bragg caractéristiques d'agrégats de xénon piégés dans les cœurs des vortex.

Nous avons d'abord étudié des collisions frontales entre un atome de xénon, héliophile, et une nanogoutte de 1000 héliums, et comparé les résultats à ceux d'une étude précédente sur le même processus avec le césium (Cs), qui est héliophobe. Dans le cas de Xe

une «boule de neige» se forme autour de lui quand il entre dans la nanogoutte, et il lui faut beaucoup plus d'énergie qu'au Cs pour qu'il puisse en ressortir. Quand il le fait, il emporte des héliums avec lui, contrairement au Cs.

Nous avons ensuite simulé des collisions entre Ar/Xe et des nanogouttes d'hélium superfluides pour différentes vitesses initiales et paramètres d'impact afin de déterminer leur section efficace de capture. Ces simulations ont ensuite été répétées pour des gouttelettes hébergeant un vortex quantique. On observe que l'impact des impuretés induit de grandes déformations de flexion et de torsion de la ligne de vortex, allant jusqu'à la génération d'ondes de Kelvin hélicoïdales qui se propagent le long du cœur du vortex. Ar/Xe est bien finalement capturé par le vortex, mais pas dans son cœur. Nous avons également découvert que l'existence d'un réseau de 6 lignes de vortex dont les noyaux sont remplis d'atomes d'Ar donne une rigidité accrue à la nanogoutte qui permet de stabiliser le système nano-goutte + vortex même à de faibles vitesses angulaires.

Nos simulations impliquant des nanogouttes d'hélium comportant des tourbillons quantiques ouvrent la voie à d'autres investigations sur des nanogouttes hébergeant un ensemble de vortex, en collision avec de multiples impuretés.

Contents

Page

Abstract iii

Résumé v

List of Publications ix

List of Figures xi

List of Tables xvii

1 Introduction 1

1.1 A brief history of superfluidity 1

1.2 Some key concepts 3

1.2.1 Bose-Einstein condensation and long-range order 4

1.2.2 Bogolyubov's approximation 5

1.2.3 Landau's criterion for superfluidity 7

1.2.4 Rotation and vorticity in superfluids 8

1.3 Helium droplets 11

2 The DFT method for heavy impurities 15

2.1 The Kohn-Sham approach 16

2.2 Time-dependent DFT 17

2.3 The Orsay-Trento Density Functional 18

2.4 The Solid-OT Density Functional 20

2.5 Static calculations 21

2.5.1 Droplets with no vorticity 21

2.5.2 Producing vortical states 22

2.5.3 Technical details on how the static equations are solved 23

2.6 Dynamic calculations 24

2.6.1 Diatomics in Molecules 24

2.6.2 Including spin-orbit coupling 26

2.6.3 Absorbing potential at the box boundaries 28

2.6.4 Notes on parallelisation 30

Part I Photo-excitation dynamics of alkalis 31

3 Alkali-doped nanodroplets 33

4 Imaging Excited-State Dynamics 37

5 Desorption dynamics of RbHe exciplexes 45

6 Supervised work: Potassium-doped nanodroplets 61

Part II Capture by quantised vortices 63

7 Quantised vortices in droplets 65
7.1 Introduction 65
7.2 Vortex arrays in ^{4}He droplets doped with Ar atoms 67

8 Head-on collisions of Xe and Cs 73
8.1 Introduction 73
8.2 Results 74

9 Capture by He droplets hosting quantised vortices 81
9.1 Introduction 81
9.2 Xe capture by vortex-free droplets 83
9.3 Helium droplets hosting vortex lines 89
9.4 Dynamics of Xe and Ar capture by vortex lines 97

10 To conclude 103

A Angular velocity and angular momentum 107

Bibliography 111

Résumé étendu en français 123

Acknowledgements 143

Curriculum vitae 145

List of Publications

2017 **Head-on collisions of Xe atoms against superfluid ^{4}He nanodroplets**. François Coppens, Antonio Leal, Manuel Barranco, Nadine Halberstadt and Martí Pi. *J. Low Temp. Phys.* **187**(5), pp. 439-445; DOI: 10.1007/s10909-016-1690-x

2017 **Capture of Xe and Ar atoms by quantized vortices in ^{4}He nanodroplets**. François Coppens, Francesco Ancilotto, Manuel Barranco, Nadine Halberstadt and Martí Pi. *Phys. Chem. Chem. Phys.* **19**(36), pp. 24805-24818; DOI: 10.1039/C7CP03307A

2017 **Imaging Excited-State Dynamics of Doped He Nanodroplets in Real-Time**. Johannes von Vangerow, François Coppens, Antonio Leal, Martí Pi, Manuel Barranco, Nadine Halberstadt, Frank Stienkemeier and Marcel Mudrich. *J. Phys. Chem. Lett.* **8**(1), pp. 307-312; DOI: 10.1021/acs.jpclett.6b02598

2017 **Density functional theory of doped superfluid liquid helium and nanodroplets**. Francesco Ancilotto, Manuel Barranco, François Coppens, Jussi Eloranta, Nadine Halberstadt, Alberto Hernando, David Mateo and Martí Pi. *Int. Rev. Phys. Chem.* **36**(4), pp. 621-707; DOI: 10.1080/0144235X.2017.1351672

2018 **Desorption dynamics of RbHe exciplexes off He nanodroplets induced by spin-relaxation**. François Coppens, Johannes von Vangerow, Manuel Barranco, Nadine Halberstadt, Frank Stienkemeier, Martí Pi and Marcel Mudrich. *Phys. Chem. Chem. Phys.* **20**(14), pp. 9309-9320; DOI: 10.1039/C8CP00482J

List of Figures

1.1 The specific heat of ^{4}He as a function of the temperature. There is a clearly visible singularity around $2.2\,\mathrm{K}$ and the graph itself has the distinct λ-like shape that inspired[9] Willem and Anna Keesom to call the temperature at which the singularity occurs the "λ-point". (Illustration courtesy of R.J. Donnelly[10]) 2

1.2 Left: Lev Landau's 1941 energy dispersion curve[22] for the excitations in liquid helium below T_λ. It exhibits a phonon- and a roton branch. The slope of the linear phonon branch corresponds to the velocity of sound. Right: Lev Landau's 1947 modified dispersion curve. The roton-branch is no longer a separate excitation branch but rather an extension of the phonon-branch. (Illustration courtesy of R.J. Donnelly[10]) 4

1.3 Dispersion relation for elementary excitations in liquid ^{4}He calculated as in[28]. 'Basic' indicates the Orsay-Trento (OT) functional[29] without the non-local kinetic energy correction (KC) nor the back-flow (BF) terms; KC OT-DFT adds to the basic OT-DFT the KC term; BF OT-DFT adds to the basic OT-DFT the BF term. The dots are the experimental data from[30]. The Landau velocity $v_L = E(q)/(\hbar q)|_{min}$ obtained for each functional is 60.3 m/s (OT-DFT); 75.1 m/s (BF OT-DFT); 94.4 m/s (KC OT-DFT); 118 m/s (basic OT-DFT); and 57.5 m/s (experiment). See also Section 2.3. 7

1.4 Cross section of a ^{4}He droplet through a symmetry plane. The droplet is made of 1000 atoms. Superimposed are the streamlines of the velocity field $\mathbf{v}_s$ for $s = 1$. They are concentric circles, centred around the vortex core along the z-axis. The colour scale represents the number density $\rho(r)$ where bluer means a higher value. The radius of the droplet is about 22 Å. 9

1.5 Electron-microscope image of and elongated track-shaped Ag-cluster after it is surface-deposited. 12

2.1 Static response $-\chi$ (see Ref. [29], Eqn. (11)) per atom of liquid ^{4}He at zero pressure. Points: experimental data; dotted line: from the functional of Refs. [51, 52]; dashed line: Orsay-Paris (OP) functional[57]; solid line: OT functional. 19

2.2 Level splitting of the p-orbitals in the presence of helium, that breaks the spherical symmetry. (A) A double degenerate n'$p_{x/y}$-orbital and (B) a single n'p_z-orbital. (Illustration courtesy of M. Martinez[61].) 25

2.3 The set of axis defined in the DIM description. (Illustration courtesy of M. Martinez[61].) 26

3.1 Principle of an alkali-doped helium nanodroplet experiment from Ref. [96] 34

5.1 ^{2}S, 5p ^{2}P, and 6p ^{2}P Rb-He pair potentials used in this work. The splitting introduced by the spin-orbit interaction has been included. The ^{2}S He-Rb pair potential of Ref. [99] is also displayed (bottom dashed line). 47

7.1 Schematic of the experiment. (a) He fluid expands in vacuum and (b) breaks up into rotating droplets. (c) A quantum vortex is formed as a consequence of fast evaporative cooling of the droplet to below T_λ. (d) The droplet is doped with Ag atoms, which are attracted to the vortex core. (e) The droplet then collides with the carbon surface leaving behind the Ag trace, whereas the He evaporates. (Illustration courtesy of Gomez *et al.* 2012, see Ref. [103]) 66

7.2 He droplets doped with Xe atoms. (A and B) X-ray diffraction images of doped droplets, displayed in a logarithmic intensity scale. (C) Droplet and embedded Xe clusters. Images in (A) and (B) correspond to tilted and parallel alignments of the vortex axes with respect to the incident x-ray beam, respectively. (Illustration courtesy of Gomez *et al.* 2014, see Ref. [104]) 67

7.3 Helium droplet configuration hosting six vortices, each doped with a line of regularly spaced Ar atoms (not represented). The top figure shows the density in the $x - y$ symmetry plane (top view), while the bottom figure shows a side view corresponding to the $y - z$ plane. As in some of the previous figures, the bright spots are high density blobs appearing around the impurity atoms. 68

7.4 Calculated equilibrium distance of the 6-vortex ring from the droplet center as a function of the angular momentum per He atom in units of $\hbar$. The dots represent the results for undoped vortices, while the squares are the results for Ar-doped vortices. The lines are drawn as a guide to the eye. 70

8.1 Energy of the Xe@^{4}He$_{1000}$ complex as a function of the distance between the Xe atom and the COM of the droplet. Several two-dimensional helium densities and density profiles are shown for distances between 0 and 40 Å in 5 Å steps. Connected (dots) and disconnected (triangles) helium configurations are shown *(see text)*. Top left inset: Snapshot of the helium density at the first turning point during the dynamic evolution of a Xe atom (green dot) at $v_0 = 600$ m/s attained 78 ps after it has started. (Color figure online.) . 74

8.2 Right panel: Dynamic evolution of a Xe atom (big dot) approaching the ^{4}He$_{1000}$ droplet from below at $v_0 = 200$ m/s. The corresponding time is indicated in each frame. Left panel: Same as the right panel, but for a Cs atom. (Color figure online.) 75

8.3 Top figure: Kinetic and total (kinetic plus potential) energy as a function of time of a Cs atom head-on colliding against a ^{4}He$_{1000}$ droplet at $v_0 = 200$ m/s. Bottom figure: same as top figure for a Xe atom. The vertical arrows indicate the first two turning points at 59 and 145 ps, whose corresponding helium densities are shown in the right Figure 8.2. (Color figure online.) . . 76

8.4 Density profile of the He$_{1000}$ droplet along the incident direction corresponding to the Xe collision at v_0 = 200 m/s after 6 ps. (Color figure online.) . . . 78

8.5 Total energy (left scale) and number of atoms in the droplet (right scale) as a function of time for the Cs@^{4}He$_{1000}$ system at $v_0 = 200$ m/s. (Color figure online.) 79

9.1 Dynamic evolution of a Xe atom (green dot) approaching the ^{4}He$_{1000}$ droplet from below at $v_0 = 600$ m/s. The corresponding time is indicated in each frame. Bright spots correspond to high density regions. (Reproduced from Ref. [139].) 84

9.2 Kinetic energy of the Xe atom in the center of mass (COM) frame of the ^{4}He$_{1000}$ droplet as a function of time for a head-on collision at v_0= 200 and 300 m/s. The kinetic energy increase during the first few picoseconds is due to the acceleration produced by the attractive part of the Xe-He potential. The vertical arrows indicate the first two turning points inside the droplet. 85

9.3 Top: Phase-space trajectory of Xe for a head-on collision at $v_0 = 200$ m/s against a ^{4}He$_{1000}$ droplet with and without a vortex line. The Xe atom is referred to the COM frame of the droplet. Bottom: Same as top panel for Ar at $v_0 = 360$ m/s. The droplet density at $t = 0$ is also represented in arbitrary scale (black profile) 87

9.4 Number of He atoms remaining in the droplet as a function of time for the Xe against ^{4}He$_{1000}$ collision at $v_0 = 200, 300$ and 400 m/s. 88

9.5 Dynamic evolution of a Xe atom (green dot) approaching the $^4He_{1000}$ droplet from below at $v_0 = 200$ m/s with impact parameter $b = 20.3$ Å. The corresponding time is indicated in each frame. The velocity fields are represented in cyan in the panels at 0.5 ps and 226.5 ps. The bright spots are high He density blobs appearing around the Xe atom because of the attractive He-Xe interaction. See the ESI[139] for the movie of the complete evolution. 90

9.6 The same process as in Figure 9.5 but with an impact parameter $b = 22.2$ Å instead of $b = 20.3$ Å. Note that in this case, after about 78 ps (bottom left panel), the Xe atom is ejected with some helium density attached to it. See the ESI[139] for the movie of the complete evolution. 91

9.7 $^4He_{1000}$ droplet at $\omega = 0.0229$ ps^{-1}: Top panels, stationary two-vortex configuration on the $x - z$ plane (left) and $x - y$ plane (right) in the corotating frame. Bottom left panel, trajectory of the vortex cores in the $x - y$ plane of the laboratory frame. The dashed line is the trajectory of one of the vortex cores, and the dotted line that of the other. Both trajectories overlap and show that the vortex cores rotate rigidly and this is also visualised by the velocity field lines shown in the right two panels. Bottom right panel, helium density in the $x - y$ plane at $t = 70$ ps obtained in the laboratory frame starting from the above configuration[139]. 94

9.8 Stationary configuration of the $^4He_{1000}$ droplet at $\omega_c \gtrsim \omega = 0.10\,\mathrm{K}/\hbar = 0.0131\,\mathrm{ps}^{-1}$ in the corotating frame ($x - y$ plane). Superimposed is the irrotational velocity field arising from a velocity potential of the form $\mathcal{S}(\mathbf{r}) = \alpha\, xy$. 96

9.9 Dynamic evolution of a Xe atom (green dot) approaching a $^4He_{1000}$ droplet hosting a vortex line from below at $v_0 = 200$ m/s. The corresponding time is indicated in each frame[139]. 99

9.10 Same as Figure 4 for an Ar atom at $v_0 = 360$ m/s[139]. 100

9.11 Core structure of the vortex line in a $^4He_{1000}$ droplet after colliding with Xe at v_0=200 m/s (right panel, $t = 8$ ps) and Ar at 360 m/s (left panel, t=6.5 ps). The full structure of the droplet is shown in Figure 4 and Figure 9.10. . . . 101

1 Densités 2D (a–d,e–h) et vitesses basées sur TDDFT (i,j) pour un atome de Rb attaché à une goutellette He_{1000} et excité depuis l'équilibre (a) vers des états 6p (colonne de gauche) et 5p (colonne de droite). Les densités sont représentées pour différents temps total de propagation t et différents instants d'ionisation t_+ : (b,e) Rb neutre à $t = \tau_c$ (« fall-back time », temps critique de retour); (c,f) ionisation à $t_+ < \tau_c$, l'ion Rb^+ retombe sur la nanogouttelette; (d,g) $t_+ > \tau_c$, désorption de Rb^+ ; (h) solvatation de Rb^+ ; (i,j) évolution des vitesses Rb* avec le temps t (symboles gris vides), et vitesses finales de Rb^+ (symboles pleins) en fonction de t_+. (Voir Chapitre 4 de la thèse.) 130

2 Instantanés de la densité de l'hélium au cours de l'évolution du complexe $RbHe_{1000}$ excité pour η=15%, Δt=60 ps. Le point vert représente l'atome Rb, excité à l'état $5p\Pi_{3/2}$; le point magenta est l'atome Rb après une relaxation soudaine à l'état $5p\Pi_{1/2}$. (Voir Chapitre 5 de la thèse.) 131
3 Figure supérieure : Énergie cinétique et totale (cinétique et potentielle) en fonction du temps d'un atome de Cs, collision frontale contre une gouttelette de $^4He_{1000}$ à v_0=200 m/s. Figure inférieur : même que le figure supérieur pour un atome de Xe. Les flèches verticales indiquent les deux premiers points de virage à 59 et 145 ps, dont les densités d'hélium correspondantes sont indiquées dans la colonne de droite de la Figure 8.2. (Voir Chapitre 8 de la thèse.) 135
4 Evolution dynamique d'un atome de Xe (point vert) en collision avec une gouttelette de $^4He_{1000}$ hébergeant une ligne de vortex à v_0=200 m/s. Le temps correspondant est indiqué dans chaque image. (Voir Chapitre 9 de la thèse.) 139

List of Tables

2.1 Model parameters for the OT-DFT and solid functionals. 18

9.1 Number of He atoms promptly ejected (N_e) and average energy per ejected atom (E_e) during the first 200 ps. 86

1
Introduction

Superfluids are liquids and gases with remarkable properties. In particular, superfluid helium can flow through a capillary without friction due to its extremely small viscosity (at least 1500 times smaller than normal liquid helium[1]), or creep up the wall of a container, seemingly defying the force of gravity[2] ("Rollin creeping"). Its thermal conductivity is about 3×10^6 times higher than that of liquid helium I or about 200 times higher than that of copper at room temperature[3]. It therefore earned the title of "best heat conducting substance we know" by Willem Keesom and his daughter Anna and dubbed "*supra-heat-conducting*"[3]. Later it was understood why[4-7] and it turns out that heat does not diffuse through the medium as in normal liquids, but rather it travels through the medium in waves (second sound). This makes it an ideal coolant e.g. to stabilise the superconducting magnets in CERN's Large Hadron Collider[8]. Helium is also the only known substance that stays liquid at zero temperature and low pressures and both its angular momentum and vorticity are quantised, making it the first observed macroscopic quantum substance. Helium-4 becomes superfluid below the λ-point, named so by William H. Keesom in 1936 who measured a singularity in the specific heat at $T_\lambda = 2.2\,\mathrm{K}$[3].

1.1 A brief history of superfluidity

Helium was the last gas to be liquefied and was done so by Heike Kamerlingh Onnes in 1908[11,12]. In 1932 John McLennan saw that liquid helium stopped boiling below ~2.2 K[13] and later that year Willem and Anna Keesom observed, while measuring the temperature dependence of the specific heat, a singularity around the same temperature[9]. They called it the "λ-temperature", T_λ, because of the shape of the temperature dependence of the specific heat resembling the Greek letter λ (see Figure 1.1). A few years later in 1935 Burton measured a sharp decrease in the viscosity of liquid helium below T_λ[14]. Around the same time Fritz London was already thinking about macroscopic wave functions and why helium does not freeze at $T = 0\,\mathrm{K}$ under atmospheric

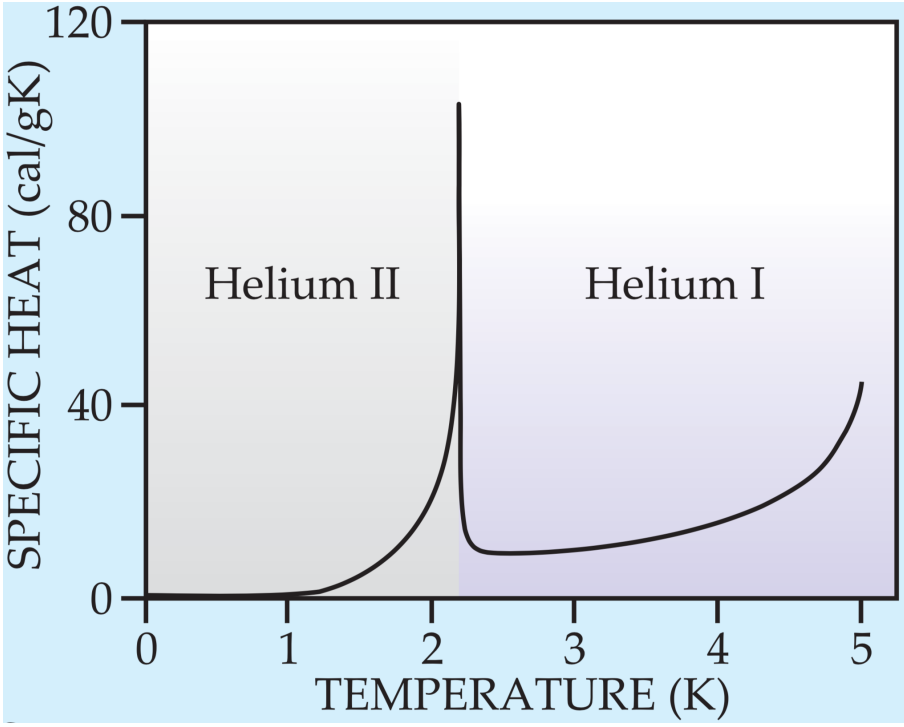

Figure 1.1: The specific heat of ^{4}He as a function of the temperature. There is a clearly visible singularity around $2.2\,\mathrm{K}$ and the graph itself has the distinct λ-like shape that inspired[9] Willem and Anna Keesom to call the temperature at which the singularity occurs the "λ-point". (Illustration courtesy of R.J. Donnelly[10])

pressure[15]. London and Simon concluded that it was caused by the zero point motion of the helium atoms and their associated kinetic energy that is comparable to their Van der Waals energy, effectively preventing liquid helium to solidify[16,17]. The year after, in 1936, Willem and Anna Keesom measured an abnormally high heat conductance below T_λ[3]. This was confirmed roughly one year later by J.F. Allen *et al.*[18] and it was understood that the high thermal conductance was the reason for the helium to stop boiling whenever the temperature drops below T_λ. It was in 1937, when Kapitza tried to determine the viscosity of the laminar flow, that he measured a viscosity that was about 10^4 times smaller than that of hydrogen gas[1]. It was then that Kaptiza, by analogy with superconductors, first coined the word "superfluid"[1] to describe the special state that helium enters below the λ-point where it can flow, seemingly without friction. Allen and Misener realised that superfluid helium is not just a liquid with a very low viscosity, but that its hydrodynamics was completely different from that of ordinary liquids[19] and therefore required a completely new interpretation.

A beginning to this new interpretation was made by London[20] in 1938 when he made a connection between the behaviour of superfluid helium and that of an ideal "Bose-Einstein (BE)" gas. Both his calculated value for $T_c = 3.09\,\mathrm{K}$ and the behaviour of the temperature dependence of the heat capacity for the ideal BE-gas were very similar to the

measured ones for liquid helium below T_λ. He wrote to Nature that "it was difficult not to imagine a connection with "Bose-Einstein condensation (BEC)". Tisza expanded upon London's ideas[21] and considered a Helium II system of total N atoms to consist of two parts; a macroscopic "condensed" part n_0, the superfluid component, in the ground state, and the remaining part $n = N - n_0$, the normal component, where the helium atoms are distributed over the excited states. Assuming this was correct the fraction n_0/N should decrease with increasing temperature according to the equation

$$\frac{n_0}{N} = 1 - \left(\frac{T}{T_0}\right)^s \quad \text{for} \quad T < T_0 \tag{1.1}$$

where $s = 3/2$ for an ideal gas and should be taken larger, e.g. $s = 5$, for a real liquid with stronger interactions between the atoms.

This was the birth of the "two-fluid" model. Within the framework of this model he derived two hydrodynamic equations for liquid helium below T_λ and concluded that within superfluid liquid helium, heat propagates in waves instead of diffusing through the medium, and calculated the velocity of these waves. He also explained why the viscosity is disappearing at low temperatures contrary to classical liquids where the viscosity increases[4-7]. In 1941 Lev Landau reformulated Tisza's theory on a more rigorous footing[22,23]. He assumed, contrary to Tisza, that the normal component of the liquid was made-up of collective excitations instead of excited single atoms. He postulated that the liquid could exhibit two states of motion which he called "potential motion" that is irrotational ($\nabla \times \mathbf{v} = 0$), and "vortex motion" that is rotational ($\nabla \times \mathbf{v} \neq 0$). The corresponding energies of these two motions are separated by an energy gap Δ. In case of potential internal motion the excitations are quanta of longitudinal (sound) waves, i.e., phonons. The excitations of the vortex-spectrum could be called "rotons" (see Figure 1.2).

A theoretical demonstration, explicitly showing that phonons and rotons are collective excitations of the liquid, came in the form of a 1947 paper by Nikolay Bogolyubov[24]. The intimate relationship between superfluidity and BEC was not universally accepted until 1995 when Cornell and Wienman in Colorado and Ketterle at MIT discovered BEC in rubidium quantum gases[25,26].

1.2 Some key concepts

In this section I briefly introduce some key ideas that are used throughout the thesis and that are needed to fully appreciate the discussed material. Most of this introduction is guided by the work of Pitaevskii and Stringari[27] on Bose-Einstein condensation. Also references to more complete and more in-depth treatments are provided for the interested reader.

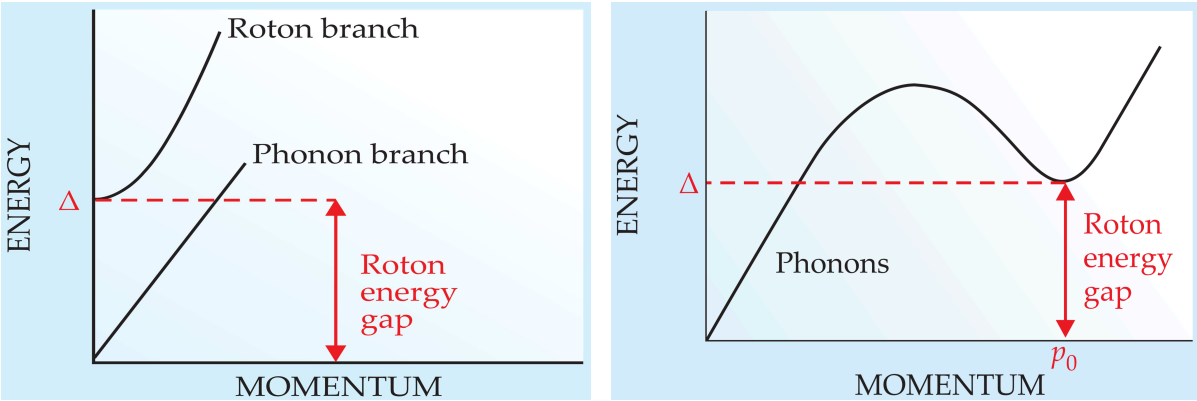

Figure 1.2: Left: Lev Landau's 1941 energy dispersion curve[22] for the excitations in liquid helium below T_λ. It exhibits a phonon- and a roton branch. The slope of the linear phonon branch corresponds to the velocity of sound. Right: Lev Landau's 1947 modified dispersion curve. The roton-branch is no longer a separate excitation branch but rather an extension of the phonon-branch. (Illustration courtesy of R.J. Donnelly[10])

1.2.1 Bose-Einstein condensation and long-range order

The essential concept of Bose-Einstein (BE) condensation is the fact that at low temperatures, multiple bosons, unlike fermions, occupy the same quantum state. In theory there is no upper bound on how many bosons can occupy such a single state. It is then said that, with ever decreasing temperature, a macroscopic part of the total number of bosons will "condense" into the quantum state with the lowest energy.

Another important concept in BEC is the idea of long-range order. Let us start by introducing the one-body density matrix of a system of N bosons in a pure state $\Psi_k(\mathbf{r}_1, \mathbf{r}_2, \ldots, \mathbf{r}_N)$

$$n_k^{(1)}(\mathbf{r}, \mathbf{r}') := N \int \Psi_k^*(\mathbf{r}, \mathbf{r}_2, \ldots, \mathbf{r}_N) \Psi_k(\mathbf{r}', \mathbf{r}_2, \ldots, \mathbf{r}_N)\, \mathrm{d}\mathbf{r}_2\, \mathrm{d}\mathbf{r}_3 \ldots \mathrm{d}\mathbf{r}_N \tag{1.2}$$

where the integral is taken over the $N-1$ coordinates $\mathbf{r}_2, \mathbf{r}_3, \ldots, \mathbf{r}_N$. For a statistical mixture of quantum states one needs to take the weighted average over all the different Ψ_k-states. At thermodynamic equilibrium the states are Boltzmann weighted by their eigenvalues $\{E_k\}$

$$n^{(1)}(\mathbf{r}, \mathbf{r}') = \frac{1}{Q} \sum_k n_k^{(1)}(\mathbf{r}, \mathbf{r}')\, \mathrm{e}^{-E_k/k_B T} \tag{1.3}$$

where Q is the partition function. For more general cases the one-body density matrix is defined

$$n^{(1)}(\mathbf{r}, \mathbf{r}') := \left\langle \hat{\Psi}^\dagger(\mathbf{r}) \hat{\Psi}(\mathbf{r}') \right\rangle \tag{1.4}$$

where $\hat{\Psi}^\dagger(\mathbf{r})/\hat{\Psi}(\mathbf{r})$ are field-operators creating/annihilating a boson at $\mathbf{r}$ and the averaging $\langle \cdots \rangle$ is taken over all states in the mixture. Once it is accepted that a macroscopic part of the total number of bosons can occupy a single quantum state it can be demonstrated

that, while considering a uniform isotropic sytem of N bosons, the one-body density matrix (Equation (1.2)) tends to a constant value when the distance between $\mathbf{r}$ and $\mathbf{r}'$ goes to infinity. In the thermodynamic limit where $N, V \to \infty$ such that $n = N/V$ is kept fixed, the one-body density only depends on the modulus of the relative variable $\mathbf{s} := \mathbf{r} - \mathbf{r}'$ so that we can write it as the Fourier transform of the momentum distribution as

$$n^{(1)}(s) = \frac{1}{V} \int n^{(1)}(\mathbf{p}) \exp(i\mathbf{p} \cdot \mathbf{s}/\hbar)\, \mathrm{d}\mathbf{p} \tag{1.5}$$

For a BEC system, the momentum distribution at small momenta is not smooth but has a sharp peak around $p = 0$ for the bosons that are in the ground state, while the remaining bosons are smoothly distributed over the excited states.

$$n(\mathbf{p}) = N_0 \delta(\mathbf{p}) + \tilde{n}(\mathbf{p}) \tag{1.6}$$

where $\tilde{n}$ is a smoothly varying function of $\mathbf{p}$. When this expression is plugged into Equation (1.5) and taking the limit where s goes to infinity it is obtained that

$$\lim_{s \to \infty} n^{(1)}(s) = \frac{N_0}{V}, \tag{1.7}$$

where $N_0/V := n_0 \leq 1$ is called the condensate fraction. It is called long-range order since it involves the off-diagonal elements of the one-body density matrix; the elements that are usually associated with the coherences.

A set of eigenvalues $\{n_i\}$ of the one-body density matrix can be defined through the following eigenvalue equation

$$\int n^{(1)}(\mathbf{r}, \mathbf{r}') \varphi_i(\mathbf{r}')\, \mathrm{d}\mathbf{r}' = n_i \varphi_i(\mathbf{r}) \tag{1.8}$$

and its solutions $\{\varphi_i\}$ form a natural orthonormal basis set of single boson wave functions $\int \varphi_i^* \varphi_j\, \mathrm{d}\mathbf{r} = \delta_{ij}$, with normalisation condition $\sum_i n_i = N$. This permits writing the one-body density matrix in a useful diagonalised form. Recalling that BEC occurs when a single particle state φ_i is occupied in a macroscopic way, say when $n_{i=0} = N_0$, a number of order N, we separate the condensate part from the rest

$$n^{(1)}(\mathbf{r}, \mathbf{r}') = N_0 \varphi_0^*(\mathbf{r}) \varphi_0(\mathbf{r}') + \sum_{i \neq 0} n_i \varphi_i^*(\mathbf{r}) \varphi_i(\mathbf{r}') \tag{1.9}$$

1.2.2 Bogolyubov's approximation

It is customary, given the importance of the condensate fraction N_0 in a BEC, to write the field operator of a N-body boson system as the sum of the condensate part and the rest, just as the one-body density matrix

$$\hat{\Psi}(\mathbf{r}) = \varphi_0(\mathbf{r}) \hat{a}_0 + \sum_{i \neq 0} \varphi_i(\mathbf{r}) \hat{a}_i \tag{1.10}$$

where $\hat{a}_i$ and $\hat{a}_i^\dagger$ are the annihilation and creation operator of a particle in state φ_i and obey the usual bosonic commutation relations

$$\left[\hat{a}_i, \hat{a}_j^\dagger\right] = \delta_{ij}, \quad \left[\hat{a}_i, \hat{a}_j\right] = 0 = \left[\hat{a}_i^\dagger, \hat{a}_j^\dagger\right] \tag{1.11}$$

Using Equation (1.10) in Equation (1.2) and comparing it to Equation (1.9) one finds the expectation value of $\left\langle \hat{a}_j^\dagger \hat{a}_i \right\rangle = \delta_{ij} n_i$. Now, the Bogolyubov approximation essentially replaces the operators $\hat{a}_0$ and $\hat{a}_0^\dagger$ with the c-number[1] $\sqrt{N_0}$. This is equivalent to ignoring the non-commutative nature of the operators due to the macroscopic occupation of the state φ_0, when $N_0 = \left\langle \hat{a}_0^\dagger \hat{a}_0 \right\rangle \gg 1$. We then rewrite the field operator as the sum of a classical field for the condensed component and a quantum field for the non-condensed component

$$\hat{\Psi}(\mathbf{r}) = \Psi_0(\mathbf{r}) + \delta\hat{\Psi}(\mathbf{r}), \tag{1.12}$$

where $\delta\hat{\Psi}(\mathbf{r}) = \sum_{i\neq 0} \varphi_i(\mathbf{r})\hat{a}_i$ and $\Psi_0(\mathbf{r}) = \sqrt{N_0}\varphi_0(\mathbf{r})$. At $T = 0$ the whole system is condensed and one can ignore $\delta\hat{\Psi}$ altogether; the field operator becomes a normal function of space Ψ_0.

The classical field Ψ_0 is called the *effective*- or *macroscopic* wave function of the condensate. It behaves like an order parameter in the sense that it represents the phase transition between the normal liquid phase and the superfluid phase. It varies continuously between the maximum value $\sqrt{N}$, which is proportional to the total number of bosons in the condensate at $T = 0$, and vanishes at the superfluid/normal liquid phase transition temperature T_λ. It is a complex quantity characterised by a real-valued modulus and phase:

$$\Psi_0(\mathbf{r}) = \left|\sqrt{N_0}\varphi_0(\mathbf{r})\right| \mathrm{e}^{iS(\mathbf{r})} \tag{1.13}$$

The modulus determines the number-density of the condensate, while the phase S plays an important role in the coherence and properties of the superfluid. As we will see in Section 1.2.4, S plays the role of a velocity potential.

Using an order parameter as defined here is equivalent to using the many-body wave function

$$\Phi(\mathbf{r}_1, \mathbf{r}_2, \ldots \mathbf{r}_N) = \prod_{i=1}^{N} \varphi_0(\mathbf{r}_i), \tag{1.14}$$

with a density operator $\hat{\rho}(\mathbf{r}) := \sum_{i=1}^{N} \delta(\mathbf{r} - \mathbf{r}_i)$ (see Section 2.1). One way to see why this wave function plays the role of an order parameter is to look at its time dependence. For normal wave functions the time dependence is determined by the eigenvalues E_i of the Hamiltonian of the system

$$\Psi(\mathbf{r}, t) = \psi(\mathbf{r})\, \mathrm{e}^{-iE_i t/\hbar} \tag{1.15}$$

[1] The term c-number is old nomenclature for a classical number, which can be real or complex, to distinguish them from quantum numbers, or q-numbers, that are represented by operators.

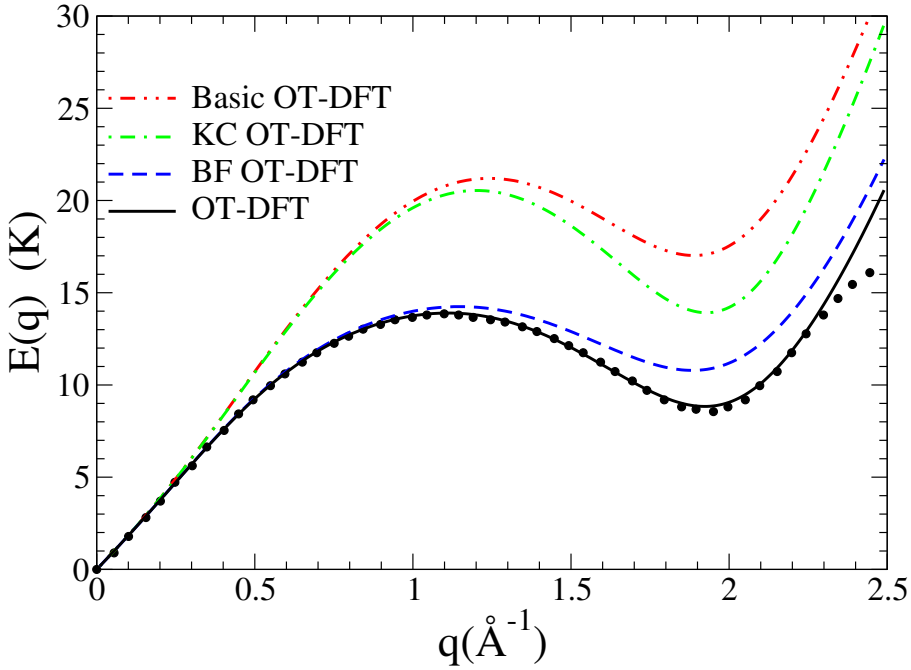

Figure 1.3: Dispersion relation for elementary excitations in liquid ^{4}He calculated as in[28]. 'Basic' indicates the Orsay-Trento (OT) functional[29] without the non-local kinetic energy correction (KC) nor the back-flow (BF) terms; KC OT-DFT adds to the basic OT-DFT the KC term; BF OT-DFT adds to the basic OT-DFT the BF term. The dots are the experimental data from[30]. The Landau velocity $v_L = E(q)/(\hbar q)|_{min}$ obtained for each functional is 60.3 m/s (OT-DFT); 75.1 m/s (BF OT-DFT); 94.4 m/s (KC OT-DFT); 118 m/s (basic OT-DFT); and 57.5 m/s (experiment). See also Section 2.3.

But in this case, the time dependence is determined by the chemical potential $\mu = E(N) - E(N-1) \approx \partial E/\partial N$

$$\Psi_0(\mathbf{r}, t) = \Psi_0(\mathbf{r})\, \mathrm{e}^{-i\mu t/\hbar} \tag{1.16}$$

Another aspect of Ψ_0 being an order parameter and not a true many-body wave function is that two solutions Ψ_a and Ψ_b of the non-linear droplet Hamiltonian corresponding to two different values of the chemical potential μ_a and μ_b are not necessarily orthogonal, i.e. $0 \leq N^{-1} \int \Psi_a^* \Psi_b \, \mathrm{d}\mathbf{r} < 1$.

1.2.3 Landau's criterion for superfluidity

For a gas or liquid to be able to become superfluid Landau postulated that the energy dispersion relation needs to fulfil certain requirements. Specifically for a fluid to flow without dissipation, i.e. a super-flow, the velocity field needs to fulfil the following inequality:

$$v < v_c = \min_{\mathbf{p}} \frac{\epsilon(\mathbf{p})}{p} \tag{1.17}$$

For an ideal Bose gas $\epsilon(\mathbf{p}) = \frac{p^2}{2m}$. In this case

$$\begin{aligned} v_c &= \min_{\mathbf{p}} \frac{\epsilon(\mathbf{p})}{p} \\ &= \min_{\mathbf{p}} \frac{p}{2m} \\ &= 0 \end{aligned} \tag{1.18}$$

Apparently an ideal Bose-gas cannot become superfluid.

But if we allow for some weak interactions between the bosons the energy dispersion relation is given by

$$\epsilon(\mathbf{p}) = \sqrt{\frac{gn}{m}p^2 + \left(\frac{p^2}{2m}\right)^2}, \tag{1.19}$$

Bogolyubov's dispersion law for elementary excitations (1947). And thus

$$\begin{aligned} v_c &= \min_{\mathbf{p}} \sqrt{\frac{gn}{m} + \frac{p^2}{4m^2}} \\ &= \sqrt{\frac{gn}{m}} \\ &= c, \end{aligned} \tag{1.20}$$

the speed of sound. Here $g = \frac{4\pi\hbar^2 a}{m}$, and a the s-wave scattering length. The weakly interacting Bose gases can become superfluid.

Liquid helium below the λ-point has a similar energy dispersion relation (see Figure 1.3) hence reinforcing the notion that superfluidity and Bose-Einstein condensation are two intimately related concepts. The experimental value of the speed of sound in bulk superfluid liquid helium is ~57.5 m/s.

1.2.4 Rotation and vorticity in superfluids

We introduce here the concept of quantised vortices in the DFT approach. It will be shown later in Section 2.2 that within the DFT framework, the order parameter Ψ is a solution of the time-dependent Euler-Lagrange (EL) Equation (2.13). Taking this for granted for now, let us start with Equation (2.13) and the order parameter from Equation (1.13), dropping the ground-state subscript and allowing φ and S to vary in time

$$i\hbar\frac{\partial}{\partial t}\Psi(\mathbf{r},t) = \left[-\frac{\hbar^2}{2m}\nabla^2 + \frac{\delta\mathcal{E}_c}{\delta\rho}\right]\Psi(\mathbf{r},t) \tag{1.21}$$

one left-multiplies it with the complex conjugate of the order parameter Ψ^* and then subtract the complex conjugate of the whole expression on both sides. After some algebra and defining $\rho(\mathbf{r},t) := N\left|\varphi(\mathbf{r},t)\right|^2$, one arrives at the continuity equation

$$\frac{\partial\rho}{\partial t} + \nabla\cdot\mathbf{j} = 0, \tag{1.22}$$

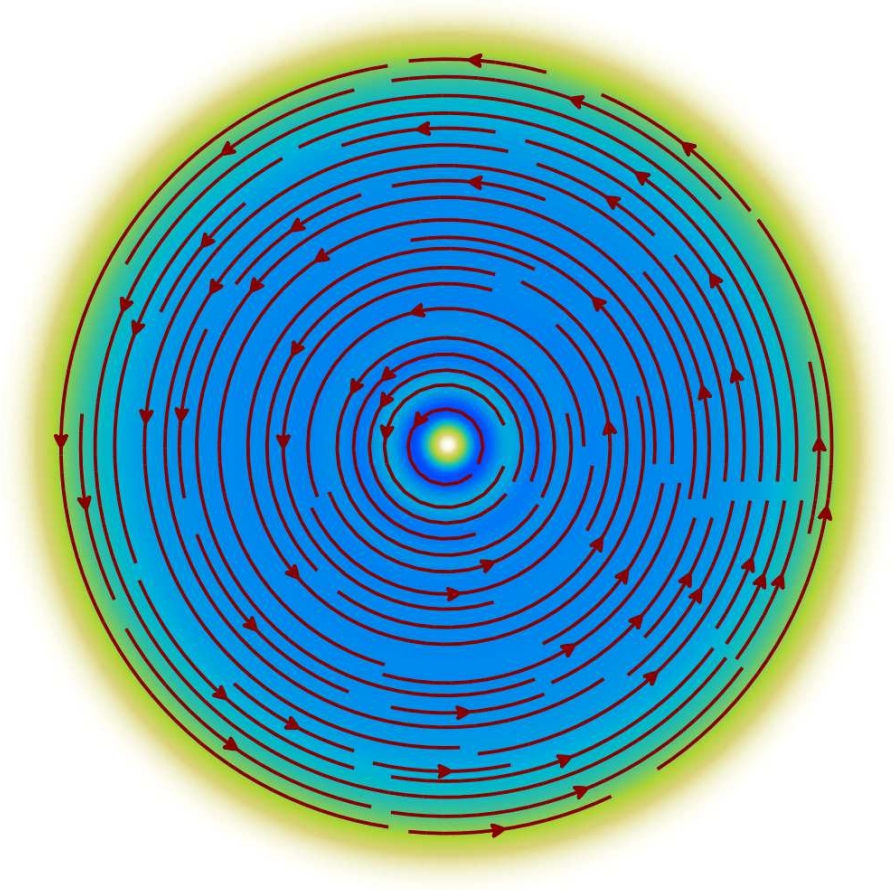

Figure 1.4: Cross section of a ^{4}He droplet through a symmetry plane. The droplet is made of 1000 atoms. Superimposed are the streamlines of the velocity field $\mathbf{v}_s$ for $s = 1$. They are concentric circles, centred around the vortex core along the z-axis. The colour scale represents the number density $\rho(r)$ where bluer means a higher value. The radius of the droplet is about 22 Å.

with

$$\begin{aligned}\mathbf{j}(\mathbf{r},t) &:= -\frac{i\hbar}{2m}\left[\Psi^*(\mathbf{r},t)\nabla\Psi(\mathbf{r},t) - \Psi(\mathbf{r},t)\nabla\Psi^*(\mathbf{r},t)\right] \\ &= \rho(\mathbf{r},t)\frac{\hbar}{m}\nabla S(\mathbf{r},t)\end{aligned} \tag{1.23}$$

From Equation (1.22) it follows that the atomic number density is a conserved quantity.

We can identify the collective velocity $\mathbf{v}_s$ of the superfluid through the relation

$$\mathbf{v}_s(\mathbf{r},t) = \mathbf{j}/\rho = \frac{\hbar}{m}\nabla S(\mathbf{r},t) \tag{1.24}$$

where 's' is the quantised angular momentum that will be defined below. We see that the rotation of the velocity field of the superfluid $\nabla \times \mathbf{v}_s = 0$, i.e. the fluid is said to be *irrotational*; a typical property of superfluids. Conversely, taking the curl $\nabla\times\mathbf{j} = \frac{\hbar}{m}\nabla\rho\times\nabla S$ we see that this is merely a restatement of the fact that one needs a gas or liquid with a

non-uniform density and a non-zero phase for it to be able to support vortices. The fact that a vortex in the gas or liquid exists directly implies $\nabla\rho \neq 0$.

Let us consider the illustrative example of a line vortex through the origin along the z-axis. As will be demonstrated in Section 2.5.2, this is a stationary state of the droplet Hamiltonian and therefore its time dependence is just a multiplicative factor. In cylindrical coordinates (r, φ, z) such a vortex solution has the form

$$\Psi_s(\mathbf{r}) = \sqrt{\rho(r,z)}\,\mathrm{e}^{is\varphi}, \tag{1.25}$$

with s, the angular momentum, an integer. This is an eigenfunction of the angular momentum operator $\hat{L}_z$ with eigenvalue

$$\hat{L}_z\Psi_s(\mathbf{r}) = \frac{\hbar}{i}\frac{\partial}{\partial\varphi}\Psi_s(\mathbf{r}) = \hbar s\Psi_s(\mathbf{r}) \tag{1.26}$$

and with expectation value

$$\begin{aligned}\left\langle\hat{L}_z\right\rangle &= \langle\Psi_s|\hat{L}_z|\Psi_s\rangle \\ &= \hbar s\left\langle\sqrt{N_0}\varphi_0\middle|\sqrt{N_0}\varphi_0\right\rangle \\ &= N_0\hbar s\end{aligned} \tag{1.27}$$

The angular momentum is quantised in units of $\hbar$ and proportional to the number of bosons in the BEC fraction/superfluid. We can calculate the velocity field

$$\mathbf{v}_s = \frac{\hbar}{m}\nabla S = \frac{\hbar}{m}\frac{s}{r}\hat{\boldsymbol{\varphi}} \tag{1.28}$$

The streamlines of $\mathbf{v}_s$ are concentric circles, centred around the z-axis, lying in the xy-plane (see Figure 1.4). Contrary to rigid rotation fields which increase proportional to the distance from the z-axis r, the superfluid rotation field decreases proportional to the inverse of the distance from the z-axis $1/r$ and is singular in the origin. Calculating the circulation of the velocity field $\mathbf{v}_s$ along a closed contour including the z-axis gives

$$\begin{aligned}\oint_{\partial\Sigma}\mathbf{v}_s\cdot\mathrm{d}\mathbf{l} &= \int_0^{2\pi}\frac{\hbar}{m}\frac{s}{r}\hat{\boldsymbol{\varphi}}\cdot r\,\mathrm{d}\varphi\,\hat{\boldsymbol{\varphi}} \\ &= s\frac{h}{m}\end{aligned} \tag{1.29}$$

where $h = 2\pi\hbar$ is Planck's constant. There are two things to note here. Firstly, the circulation around a closed loop that encompasses the z-axis is quantised in units of h/m for $s \in \mathbb{N}_{>0}$. Secondly, the value of the circulation of the velocity field does not depend on the chosen contour as long as it includes the location of the vortex. This means that all the vorticity is contained at the location where the velocity field is singular (the "core" of the vortex), at $r = 0$ along the z-axis.

Because of the pole in the velocity field, Stokes' theorem will lead to the following contradiction

$$s\frac{h}{m} = \oint_{\partial\Sigma}\mathbf{v}_s\cdot\mathrm{d}\mathbf{l} = \iint_{\Sigma}\nabla\times\mathbf{v}_s\cdot\mathrm{d}\boldsymbol{\Sigma} = 0 \tag{1.30}$$

and can therefore not be applied. To emphasise that all the vorticity is concentrated around the vortex core one can write formally

$$\nabla \times \mathbf{v}_s = s\frac{h}{m}\delta^{(2)}(\mathbf{r}_\perp)\,\hat{z} \tag{1.31}$$

where $\delta^{(2)}$ is 2-dimensional Dirac-delta function and $\mathbf{r}_\perp$ a vector in a plane perpendicular to the vortex line.

1.3 Helium droplets

Until the 1980's, most experimental and theoretical work was done on bulk systems, i.e. systems of the order of N_A number of atoms. It was only in the last couple of decades that advancements in technology enabled experimentalists to create nanoscale sized superfluid helium droplets. From the early 1990's onwards, superfluid helium nanodroplets became an active field of study, both experimentally and theoretically.

Helium nanodroplets are considered ideal model systems to explore quantum hydrodynamics in self-contained, isolated superfluids. The main focus has been on the evolution of their properties with the number of atoms in the cluster, until the condensed matter limit is reached. Helium clusters are especially interesting in that quantum effects play a key role in determining their properties. In particular, given that a helium cluster is an ensemble of bosons at about 0.4 K[31,32], manifestations of collective behaviour (such as superfluidity) are expected. On the other hand, it is not yet clear how the finite size of a cluster affects this non-classical (or degenerate) collective behaviour.

Recently, Toennies et al.[33] have measured the electronic spectrum of glyoxal molecules embedded in He clusters and found it consistent with a theoretical simulation computed using the phonon dispersion curve of superfluid bulk He II. The authors themselves, however, point out that at the average cluster size of 5500 He atoms reported in Ref. [33], the clusters are so big that finite size effects in the interior region are negligible (see also Refs. [34, 35]). It is therefore not surprising that they find results consistent with the bulk case, especially for a molecule readily solvated inside the cluster, for which surface effects play a minor role. Therefore the influence of the He clusters size on superfluidity has not been detected so far.

The helium-helium interaction is already weak in bulk liquid helium and in finite self-bound systems such as droplets it is even weaker, e.g. the binding energy per atom is <7.17 K. Because of this helium droplets cool down very rapidly due to fast evaporation and therefore reaching their limiting temperature of about $0.38\,\mathrm{K}$ in microseconds. Pure helium droplets are neutral systems and their properties like their size, binding energy and excitation spectra, are not easy to determine experimentally and are usually obtained by indirect methods. This did not stop the theoreticians describe doped $^4\mathrm{He}_N$

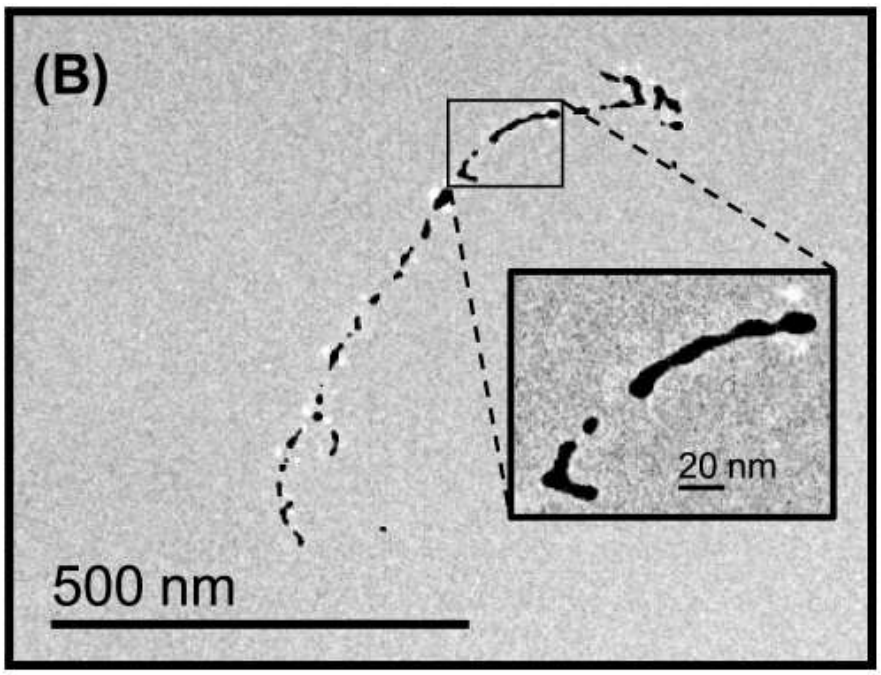

Figure 1.5: Electron-microscope image of and elongated track-shaped Ag-cluster after it is surface-deposited.

droplets using a wide variety of approaches depending on the size and character of the droplets ranging from Quantum Monte Carlo, Hypernetted-Chain/Euler-Lagrange[36], Variational Monte Carlo[37] and many others.

A key property of helium droplets, in contrast to bulk helium, is their ability to pickup any kind of dopants with which they collide. Depending on the strength of the dopant-^{4}He interaction and the surface tension of the droplet, a dimensionless parameter λ can be defined[38] with a critical value $\lambda_0 \sim 1.9$. Below λ_0 impurities are bound to the surface of the droplet (e.g. the alkalis), and above they get solvated into the droplet's interior. Droplets can therefore be doped with almost any kind of atomic- or molecular species.

From the perspective of the droplet it this means that it is possible to use the dopants as gentle probes to determine the superfluid properties of helium droplets that would be inaccessible with other methods. For two examples of this see Refs. [39-41], where a dopant is used to probe the superfluid character of small ^{4}He droplets and Refs. [42, 43] to see their limiting temperatures.

Moreover, from the perspective of the impurities it enables a broad spectrum of possible experimental studies. Due to the fact that helium droplets are ultra cold superfluid liquids, and therefore provide high mobility of any picked-up dopants, one can conduct high resolution spectroscopy studies. Having a fine control over the number of picked-up dopants[29] one can use droplets as a matrix for creating self-organising structures of polar molecules, or very cold metal clusters and study their Coulomb explosion.

One of the most intriguing properties of superfluid helium droplets is the fact that they can host quantised vortices. Because of their ultra low temperature they are true quantum liquids and their vorticity and angular momentum are quantised. The existence of quantised vortices was anticipated because they have been created and observed in BECs made of dilute gases. However, the detection of quantised vortices is still experimentally challenging (see Section 7 in this thesis).

A lot of of work has been done on helium droplets the last few decades, both experimentally and theoretically. From the absorption spectra of alkali metal doped helium droplets, the study of doped mixed ^{3}He-^{4}He droplets, electrons in liquid helium, to the investigation of the critical Landau velocity inside small ^{4}He droplet. For a comprehensive overview of work done in the last two decades, the interested reader is referred to the review papers in Refs. [44-46].

2

The DFT method for heavy impurities

One Functional to rule them all,
One Functional to find them,
One Functional to bring them all
and in a droplet bind them.

F.M.G.J. Coppens

From a theoretical point of view, superfluid helium must be considered as a high dimensional quantum system. Quantum Monte Carlo[47] (QMC) and direct quantum mechanical[48-50] calculations are the most accurate methods, but their computational demand quickly exceeds currently available computer resources when the number of helium atoms increases. Furthermore, QMC cannot describe dynamic evolution of superfluid helium in real time. To address these limitations, semi-empirical methods based on density functional theory (DFT) formalism have been introduced[51-53]. DFT can be applied to much larger systems than QMC and allows for time-dependent formulation. As such, it offers a good compromise between accuracy and computational feasibility. The main drawback of DFT is that the exact energy functional is not known and must therefore be constructed in a semi-empirical manner. Moreover, doped helium droplets are limited to a mean-field description of the dopant-helium interaction. Nevertheless, DFT is the only method to date that can successfully reproduce results from a wide range of time-resolved experiments in superfluid helium, for realistic sizes compared to experimental conditions.

2.1 The Kohn-Sham approach

The starting point for the density functional method is the Hohenberg-Kohn (HK) theorem[54], which states that the ground-state energy E_v of an *interacting inhomogeneous* system in a static potential v can be written in as a unique functional of the one-body density ρ as

$$E_v[\rho] = \int v(\mathbf{r})\rho(\mathbf{r})\,\mathrm{d}\mathbf{r} + F[\rho] \tag{2.1}$$

where $F[\rho]$ is a universal functional—valid for *any* number of particles and *any* external potential v—of the one-body density, defined as

$$\rho(\mathbf{r}) := \langle\Phi|\hat{\rho}(\mathbf{r})|\Phi\rangle = \left\langle\Phi\left|\sum_{i=1}^{N}\delta(\mathbf{r}-\mathbf{r}_i)\right|\Phi\right\rangle \tag{2.2}$$

and $\Phi(\mathbf{r}_1, \mathbf{r}_2, \ldots, \mathbf{r}_N)$ is the many-body wave function of such a system. Furthermore, the functional $F[\rho]$ gives the ground state energy *if and only if* the input density is the true ground state density of the system.

Kohn and Sham (KS) later reformulated[55] the theory by introducing an approximation scheme for the functional $F[\rho]$ that is analogous to Hartree's method, but also contains the major part of the correlation effects inherent in interacting many-body systems. The approximation starts by defining

$$F[\rho] := T[\rho] + E_c[\rho] \tag{2.3}$$

where $T[\rho]$ is now the kinetic energy of a fictitious system of *non-interacting* particles with density ρ and $E_c[\rho]$ is the interaction term of an *interacting* system with the same density, which contains all the other terms of the functional. For the kinetic part this allows us to write the total kinetic energy $T[\rho]$ as the sum of the individual kinetic energies T_i of the non-interacting particles

$$T = \sum_i T_i = -\frac{\hbar^2}{2m_4}\sum_i \langle\varphi_i|\nabla^2|\varphi_i\rangle = -\frac{\hbar^2}{2m}\sum_i \int \varphi_i^*(\mathbf{r})\nabla^2\varphi_i(\mathbf{r})\,\mathrm{d}\mathbf{r}\,, \tag{2.4}$$

where m_4 is the mass of a ^{4}He atom and the $\{\varphi_i\}$ are the Kohn-Sham single-particle orbitals corresponding to the many-body KS wave function $\Phi_{KS}(\mathbf{r}_1, \mathbf{r}_2, \ldots, \mathbf{r}_N) = \prod_i \varphi_i(\mathbf{r}_i)$ and leading to the density (using the definition in Equation (2.2)) $\rho(\mathbf{r}) = \sum_i |\varphi_i(\mathbf{r})|^2$.

There is difference between the true kinetic energy of the interacting system and the fictitious one, due to the neglecting of the correlations. This difference is being corrected and accounted for in the correlation energy $E_c[\rho]$.

Because the functional we used in this work is calibrated to produce the correct behaviour of bulk liquid helium at zero temperature $T = 0$ and zero pressure $P = 0$, we assume complete Bose-Einstein (BE) condensation of the helium. In this case all the

helium atoms occupy the same single-particle KS-orbital φ_0. Therefore the many-body wave function and the density simplifies further to

$$\Phi_{BEC}(\mathbf{r}_1, \mathbf{r}_2, \ldots, \mathbf{r}_N) = \prod_i \varphi_0(\mathbf{r}_i) \tag{2.5}$$

and

$$\rho(\mathbf{r}) = N\left|\varphi_0(\mathbf{r})\right|^2 \tag{2.6}$$

respectively. As explained in Section 1.2.2, it is customary to define an effective wave function

$$\Psi(\mathbf{r}) := \sqrt{\rho(\mathbf{r})} = \sqrt{N}\varphi_0(\mathbf{r}) \tag{2.7}$$

for the condensate (see Equation (1.12)), which is sometimes called a *macroscopic wave function* or *order parameter*. We can now simplify the expression for the kinetic energy (Equation (2.4))

$$T = -\frac{\hbar^2}{2m_4}N\int \varphi_0^*(\mathbf{r})\nabla^2\varphi_0(\mathbf{r})\,\mathrm{d}\mathbf{r} = \frac{\hbar^2}{2m_4}N\int \left|\nabla\varphi_0\right|^2 \mathrm{d}\mathbf{r}\,, \tag{2.8}$$

where we used partial integration to get to the last step and imposed that the orbital φ_0 vanishes at the boundaries. With our definition Equation (2.7) we can now write the kinetic energy as a functional of the density

$$T[\rho] = \frac{\hbar^2}{2m_4}\int \left|\nabla\sqrt{\rho}\right|^2 \mathrm{d}\mathbf{r} \tag{2.9}$$

To summarise, we write the complete energy functional E_v as

$$E_v[\rho] = \int v(\mathbf{r})\rho(\mathbf{r})\,\mathrm{d}\mathbf{r} + \frac{\hbar^2}{2m_4}\int \left|\nabla\sqrt{\rho}\right|^2 \mathrm{d}\mathbf{r} + \int \mathcal{E}_c[\rho]\,\mathrm{d}\mathbf{r} \tag{2.10}$$

where we defined the correlation energy density functional $\mathcal{E}_c$ through

$$E_c[\rho] := \int \mathcal{E}_c[\rho]\,\mathrm{d}\mathbf{r}\,. \tag{2.11}$$

The difficult job is to design a functional $\mathcal{E}_c$ such that the desired physical properties of helium can be recovered. This is far from trivial but several of these density functionals are available now. The one used in this work is discussed in Section 2.3.

2.2 Time-dependent DFT

To describe the time evolution of the system, the Runge-Gross theorem extends DFT to its time-dependent version TDDFT[56]. The functional variation of the associated action (see Equation (2.49) for an example) leads to the following time-dependent Euler-Lagrange (EL) equation

$$i\hbar\frac{\partial}{\partial t}\Psi(\mathbf{r}, t) = \left\{-\frac{\hbar^2}{2m_4}\nabla^2 + \frac{\delta\mathcal{E}_c}{\delta\rho}\right\}\Psi(\mathbf{r}, t) := \mathcal{H}\left[\rho\right]\Psi(\mathbf{r}, t) \tag{2.12}$$

Table 2.1: Model parameters for the OT-DFT and solid functionals.

ϵ_{LJ} (K)	σ (Å)	h (Å)	c_2 (K Å^6)	c_3 (K Å^9)	α_s (Å^3)
10.22	2.556	2.190323	-2.41186×10^4	1.85850×10^6	54.31
ρ_{0s} (Å^{-3})	l (Å)	C (Hartree)	β (Å^3)	ρ_m (Å^{-3})	γ_{11}
0.04	1.	0.1	40.	0.37	−19.7544
γ_{12} (Å^{-2})	α_1 (Å^{-2})	γ_{21}	γ_{22} (Å^{-2})	α_2 (Å^{-2})	
12.5616	1.023	−0.2395	0.0312	0.14912	

As long as we are in the thermodynamic regime the solutions $\Psi(\mathbf{r}, t)$ can be decomposed into the liquid density and associated velocity potential field (see Section 1.2.2 and Section 1.2.4).

Considering only eigenstates $\Psi(\mathbf{r}, t) = \Psi_0(\mathbf{r})\, \mathrm{e}^{-i\mu t/\hbar}$ of the time independent Hamiltonian $\mathcal{H}[\rho]$ the time-dependent EL-equation reduces to a time independent one

$$\left\{-\frac{\hbar^2}{2m_4}\nabla^2 + \frac{\delta \mathcal{E}_c}{\delta \rho}\right\} \Psi_0(\mathbf{r}) = \mu \Psi_0(\mathbf{r}) \tag{2.13}$$

with μ the chemical potential. Solving this equation by iteration will result in the ground state density $|\Psi_0|^2$ of the system. Within the HK-framework and the variation principle that was used to obtain these EL-equations, the nature of the minimisation is such that it gives the lowest energy for a given symmetry. This means that as long as the input state does not break the symmetry of the time-independent EL-equation, it minimises the energy of this state even if it does not lead to the ground state. This can be used to obtain a stationary vortex-line solution. With the inclusion of appropriate constraints in the energy functional the same procedure can be used to obtain helium densities with an array of vortex-lines.

2.3 The Orsay-Trento Density Functional

The functional that is used in the work presented in this thesis is based on the Orsay-Trento (OT) functional[29]. It uses a finite-range, non-local approach and it is, to date the most accurate model in the sense that its parameters were fitted to reproduce the bulk

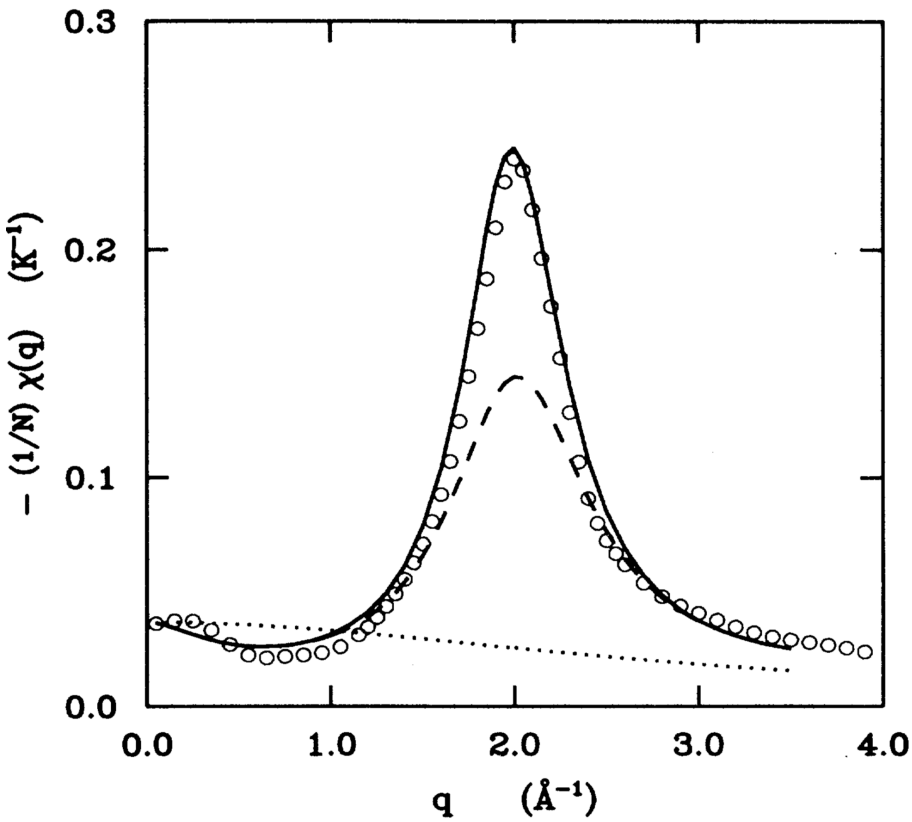

Figure 2.1: Static response $-\chi$ (see Ref. [29], Eqn. (11)) per atom of liquid ^{4}He at zero pressure. Points: experimental data; dotted line: from the functional of Refs. [51, 52]; dashed line: Orsay-Paris (OP) functional[57]; solid line: OT functional.

properties of liquid helium at $T = 0 = P$. It is written as

$$\begin{aligned}\mathcal{E}_c[\rho, \mathbf{v}] = \frac{1}{2}\int\Big\{ & \rho(\mathbf{r})V_{LJ}(|\mathbf{r}-\mathbf{r}'|)\rho(\mathbf{r}') \\ & + \frac{1}{2}c_2\,\rho(\mathbf{r})\left[\bar{\rho}(\mathbf{r})\right]^2 + \frac{1}{3}c_3\,\rho(\mathbf{r})\left[\bar{\rho}(\mathbf{r})\right]^3\Big\}\,\mathrm{d}\mathbf{r}' \\ & - \frac{\hbar^2}{4m_4}\alpha_s\int F(|\mathbf{r}-\mathbf{r}'|)\left[1-\frac{\tilde{\rho}(\mathbf{r})}{\rho_{0s}}\right]\nabla\rho(\mathbf{r})\cdot\nabla\rho(\mathbf{r}')\left[1-\frac{\tilde{\rho}(\mathbf{r}')}{\rho_{0s}}\right]\mathrm{d}\mathbf{r}' \\ & - \frac{m_4}{4}\int V_J(|\mathbf{r}-\mathbf{r}'|)\,\rho(\mathbf{r})\,\rho(\mathbf{r}')\,[\mathbf{v}(\mathbf{r})-\mathbf{v}(\mathbf{r}')]^2\,\mathrm{d}\mathbf{r}'\end{aligned} \tag{2.14}$$

The first term corresponds to a classical Lennard-Jones type two-body interaction between helium atoms. The interaction is screened at short distances where the interaction energy is of the same order as the correlation effects:

$$V_{LJ}(r) = \begin{cases}\epsilon_{LJ}\left[\left(\frac{\sigma}{r}\right)^{12} - \left(\frac{\sigma}{r}\right)^{6}\right] & \text{if} \quad r > h \\ 0 & \text{otherwise}\end{cases} \tag{2.15}$$

In the second line, the terms corresponding to c_2 and c_3, correct for short range correlations when $r < h$. The weighted density $\bar{\rho}$ is the average density ρ over a sphere of radius

h:

$$\bar{\rho}(\mathbf{r}) = \int \Pi_h(|\mathbf{r}-\mathbf{r}'|)\rho(\mathbf{r}')\,\mathrm{d}\mathbf{r}', \tag{2.16}$$

with

$$\Pi_h(r) := \begin{cases} \frac{3}{4\pi h^3} & \text{if} \quad \mathrm{r} \leq \mathrm{h} \\ 0 & \text{otherwise} \end{cases} \tag{2.17}$$

The third line is a non-local correction to the kinetic energy (KC). It partially accounts for the difference $\mathcal{T}[\rho] - T[\rho]$ mentioned in Section 2.1. The gradient-gradient interaction function F is a Gaussian kernel defined as

$$F(r) = \frac{1}{l^3\sqrt{\pi^3}}\,\mathrm{e}^{-r^2/l^2} \tag{2.18}$$

All the parameters are fitted to reproduce the peak of the static response function (see Figure 2.1) in the bulk liquid. The factor $(1-\tilde{\rho}/\rho_{0s})$ is included to match the pressure dependence of the static response function predicted by diffusion Monte Carlo calculations[58]. The quantity $\tilde{\rho}(\mathbf{r})$ is another weighted density, calculated using F as a weight

$$\tilde{\rho}(\mathbf{r}) := \int F(|\mathbf{r}-\mathbf{r}'|)\rho(\mathbf{r}')\,\mathrm{d}\mathbf{r}' \tag{2.19}$$

The density $\tilde{\rho}(\mathbf{r})$ is very close to the normal density $\rho(\mathbf{r})$ except in very inhomogeneous situations. For pure helium droplets and free helium surfaces one can safely use ρ instead of $\tilde{\rho}$. In the presence of significant short-range density oscillations, e.g. in the presence of heavy atomic impurities as presented in this thesis or electrons, the helium density needs to be smoothed by the Gaussian kernel F.

Finally, the last line in Equation (2.14) is called the *back-flow* term and influences the dynamic response of the system. It plays the role of a non-local kinetic energy. Since the back-flow contains the factor $\mathbf{v}-\mathbf{v}'$, with $\mathbf{v}$ defined in Equation (1.24), the contribution will only be non-zero whenever the effective wave function Ψ is complex-valued. Consequently, for time-independent cases it means that this will only affect the vortex states. The phenomenological effective current-current interaction $V_J(r)$ is calibrated so that it reproduces the experimental phonon-roton spectrum (see Figure 1.3):

$$\begin{aligned} V_J(r) = &(\gamma_{11} + \gamma_{12}\,r^2)e^{-\alpha_1 r^2} \\ &+ (\gamma_{21} + \gamma_{22}\,r^2)e^{-\alpha_2 r^2} \end{aligned} \tag{2.20}$$

All the parameters of the functional are given in Table 2.1.

2.4 The Solid-OT Density Functional

In the presence of highly inhomogeneous liquid densities, e.g. atomic impurities with a very strong He-X interaction, the OT-functional Equation (2.14) becomes numerically

unstable. To deal with this problem an additional cut-off can be used

$$\mathcal{E}^{\mathrm{sol}} := C\rho(\mathbf{r})\{1 + \tanh(\beta[\rho(\mathbf{r}) - \rho_{\mathrm{m}}])\} \tag{2.21}$$

where the model parameters $\{C, \beta, \rho_{\mathrm{m}}\}$ are specified in Table 2.1. Including this term in the OT-functional prevents excessive density build-up. $\mathcal{E}^{\mathrm{sol}}$ only starts to deviate from zero whenever the liquid density ρ is comparable to ρ_{m} or larger. Therefore, inclusion of this term in the functional does not alter the density distribution. This penalty term was originally developed to account for the liquid-solid phase transition of ^{4}He[59,60]. The functional that has been used to obtain the result presented in this work is refered to as the "Solid-OT-DFT functional". It consists of the first three terms of the original OT-functional Equation (2.14), plus $\mathcal{E}^{\mathrm{sol}}$

$$\begin{aligned}\mathcal{E}_c^{\mathrm{sol}}[\rho] = \frac{1}{2}\int\Big\{ & \rho(\mathbf{r})V_{LJ}(|\mathbf{r}-\mathbf{r}'|)\rho(\mathbf{r}') \\ & + \frac{1}{2}c_2\,\rho(\mathbf{r})\big[\bar{\rho}(\mathbf{r})\big]^2 + \frac{1}{3}c_3\,\rho(\mathbf{r})\big[\bar{\rho}(\mathbf{r})\big]^3\Big\}\,\mathrm{d}\mathbf{r}' \\ & + C\,\rho(\mathbf{r})\Big\{1 + \tanh\big(\beta\big[\rho(\mathbf{r}) - \rho_{\mathrm{m}}\big]\big)\Big\}\end{aligned} \tag{2.22}$$

2.5 Static calculations

2.5.1 Droplets with no vorticity

In the work presented here all the impurities are heavy compared to the mass of ^{4}He, e.g. the mass of rubidium (Rb) is about 21 times larger than that of helium (He), xenon (Xe) roughly 33 times and argon (Ar) about 10 times. Therefore we are allowed to treat the centre of mass motion of the impurities as classical. It was also checked for potassium (K) which is slightly lighter than Ar[61]. In the functional this will be modelled as an external field V_X, the impurity-He pair interaction

$$E[\rho] \longrightarrow E[\rho] + \int \rho(\mathbf{r})\,V_X(|\mathbf{r}-\mathbf{r}_I|)\,\mathrm{d}\mathbf{r} \tag{2.23}$$

where $\mathbf{r}_I$ is the location of the impurity. Varying the modified functional to minimise the energy one now finds a new EL-equation in which the helium-impurity interaction is included:

$$\left\{-\frac{\hbar^2}{2m_4}\nabla^2 + \frac{\delta\mathcal{E}_c}{\delta\rho} + V_X(|\mathbf{r}-\mathbf{r}_I|)\right\}\Psi(\mathbf{r}) = \mu\Psi(\mathbf{r}) \tag{2.24}$$

This equation is then solved by iteration in a self-consistent way by the imaginary time propagation method (ITM)[62] in cartesian coordinates. The calculations are performed in three dimensions without imposing any symmetries that are present in the external potential. All the quantities are discretised on an evenly spaced Cartesian grid with a step-size that is typically of the order of 0.4 Å. This value is chosen small enough such that

the corresponding maximum momentum in Fourier-space is high enough compared to the helium momenta involved in the dynamics. The differential operators are evaluated using a k-point finite difference method where in most applications $k = 13$ is sufficiently accurate. The integrals in the density-functional can be expressed as convolutions and can therefore be evaluated in momentum-space by exploiting the convolution theorem, using proprietary highly optimised parallel Fast Fourier Transform algorithms.

2.5.2 Producing vortical states

The helium density that minimises the energy of the vortical states Ψ_s

$$\Psi_s(\mathbf{r}) = \sqrt{\rho(r,z)}\,\mathrm{e}^{is\varphi} \tag{2.25}$$

introduced in Section 1.2.4, can be obtained by solving the same EL-equation as for a vortex-free droplet. This becomes clearer when we write Equation (2.13) in cylindrical coordinates:

$$\left\{-\frac{\hbar^2}{2m_4}\left[\frac{1}{r}\frac{\partial}{\partial r}\left(r\frac{\partial}{\partial r}\right) - \frac{s^2}{r^2} + \frac{\partial^2}{\partial z^2}\right] + \frac{\delta\mathcal{E}_c}{\delta\rho}\right\}\Psi_s(\mathbf{r}) = \mu\Psi_s(\mathbf{r}) \tag{2.26}$$

Written like this it is evident that the ground state Ψ_0 is just the special case for $s = 0$. Obtaining the solution using the ITM works as long as the solution has overlap with initial guess for the order parameter. Starting with a trial order parameter similar to Ψ_s will guarantee this. To do this we employ the "imprinting" technique where we use the ground state density of a previously obtained vortex-free droplet and multiply it with a normalised complex factor

$$\Psi(\mathbf{r}) = \sqrt{\rho_0(x,y,z)} \times \frac{x+iy}{\sqrt{x^2+y^2}} \tag{2.27}$$

where ρ_0 is the ground state density of the vortex-droplet. In cylindrical coordinates this factor is equivalent to the one in Equation (1.25) for $s = 1$. After this transformation, the newly obtained trial wave function for the vortical state is relaxed again using ITM to reach the true lowest energy wave function.

This changes for droplets with two or more vortices, where the cylindrical symmetry is broken and the solutions are no longer solutions of Equation (2.26), nor eigenfunctions of the angular momentum operator. In this case the time-independent EL-equation has to be modified to include a rotational constraint solution in the co-rotating frame

$$\mathcal{H} \to \mathcal{H} - \Omega\hat{L}_z \tag{2.28}$$

such that for a suitable choice of Ω the vortex-array solution becomes favourable to the ground state and also to excited states with angular momentum $s \geq 2$. Since these states are no longer eigenstates of the original time-dependent Hamiltonian, these states are no

longer stationary and will start to rotate with frequency Ω. The initial guess for a droplet with n_v vortices can be produced using the same imprinting method as mentioned before

$$\Psi(\mathbf{r}) = \sqrt{\rho_0(x,y,z)} \times \prod_{j=1}^{n_v} \left[\frac{(x-x_j)+i(y-y_j)}{\sqrt{(x-x_j)^2+(y-y_j)^2}} \right] \tag{2.29}$$

where ρ_0 is again the ground state density of the vortex-free droplet and (x_j, y_j) is the initial position of the j-th vortex-line parallel to the z-axis. As before, after imprinting the wave function is again relaxed using ITM to attain the lowest energy configuration for a wave function containing n linear vortices.

2.5.3 Technical details on how the static equations are solved

The static DFT equations are always solved in cartesian coordinates. The calculation is full 3D with no imposed symmetry whatsoever. Densities, wave functions and differential operators are discretised on a 3D cartesian grid (*"calculating box"*).

The minimum and maximum values of x, y, and z for the calculating box are inputs to the programs, as well as the number of points in each direction n_i.

The limits of the calculating box have to be chosen with care, especially if a dynamic calculation follows the (relatively fast) static minimization. One has to make sure that in the course of the dynamics there will be enough room for the droplet and the impurity to wander around without hitting the cell boundaries before obtaining the desired information. The number of points in each direction has to be chosen such that the FFT is efficiently calculated (see below) and that the size step is about the desired value. We typically use a size step $h_x = (x_{\max} - x_{\min})/n_x$, of the order of 0.4 Å.

The differential operators (usually first and second derivatives at most) are represented by k-point formulas. We normally use 13-point formulas, but values up to k=25 are also possible. We have found that increasing the number of points for the derivatives does not improve the numerics -but it increases the CPU time! Decreasing the spatial step can result in a non affordable calculation (too much computing time and too large memory required).

A key tool for the implementation of the method is the use of F ast-Fourier techniques[63] to calculate the convolutions needed to obtain some of the contributions to the total energy of the impurity-droplet complex, as well as the mean field potentials entering the EL equations for the order parameter and the impurity wave function. In order to accelerate the computations, the Fourier transforms of the He-He and He-impurity potentials and of the expressions entering the definition of the coarse-grained helium density in the functional[53,64] are computed once and for all at the beginning of the calculation.

For more technical details about how this method is implemented the interested reader is directed to Ref. [65].

2.6 Dynamic calculations

For the dynamic evolution of atomic impurities excited from ns-states to n's-states, we do not need to keep track of the evolution of the electronic state of the impurity since it keeps its spherically symmetric orbital. In this case we only need to describe the time evolution of the centre of mass coordinate of the impurity. As in the statics, because of the large atomic mass of the impurity compared to helium, the time evolution of the centre of mass coordinate of the impurity is treated classically. To obtain the correct energy for the whole droplet-impurity system the energy functional needs to be extended to include the impurity's centre of mass motion and the impurity-helium interaction

$$E[\rho] \longrightarrow E[\rho] + \frac{1}{2} m_I \dot{\mathbf{r}}_I^2 + \int \rho(\mathbf{r})\, V_{X^*}(|\mathbf{r} - \mathbf{r}_I|)\, \mathrm{d}\mathbf{r} \tag{2.30}$$

where the second term on the right is the classical kinetic energy of the impurity (which was not present in the static case, Equation (2.23)), $\dot{\mathbf{r}}_I$ is the time derivative of the impurity location, m_I is the impurity mass and V_{X^*} is the impurity-He pair interaction potential for an impurity in the ground-, excited n's- or ionised state. The equations of motion for the time evolution of the effective wave function $\Psi(\mathbf{r}, t)$ and the second time derivative of the impurity location $\ddot{\mathbf{r}}_I$ are

$$\begin{aligned} i\hbar \frac{\partial}{\partial t}\Psi &= \left[-\frac{\hbar^2}{2m_4}\nabla^2 + \frac{\delta \mathcal{E}_c}{\delta \rho} + V_{X^*}(|\mathbf{r} - \mathbf{r}_I|) \right] \Psi \\ m_I \ddot{\mathbf{r}}_I &= -\nabla_{\mathbf{r}_I} \left[\int \rho(\mathbf{r}) V_{X^*}(|\mathbf{r} - \mathbf{r}_I|)\, \mathrm{d}\mathbf{r} \right] \\ &= -\int V_{X^*}(|\mathbf{r} - \mathbf{r}_I|)\, \nabla \rho(\mathbf{r})\, \mathrm{d}\mathbf{r} \end{aligned} \tag{2.31}$$

2.6.1 Diatomics in Molecules

The situation becomes more complicated for ns-states excited to n'p-states (effective one-electron excited ^{2}P-states). Since the three p-orbitals are no longer spherically symmetric and start mixing due to the interaction with the He droplet and spin-orbit coupling, we also need to include a description that accounts for the mixing of these orbitals in a dynamic way. To do this we use Diatomics in Molecules[66](DIM). The interaction between a helium atom (^{1}S$_0$-state) and the triply degenerate $L = 1$ electronic state of the impurity partially lifts the degeneracy so that the interaction can be decomposed into a Σ-state and a doubly degenerate Π-state (see Figure 2.2). In the cylindrical symmetry it is customary to use the molecular term symbol $^{2S+1}\Lambda_\Omega$ to label the levels. In the bound region of the potentials S is the electronic spin angular momentum (and $2S + 1$ the spin

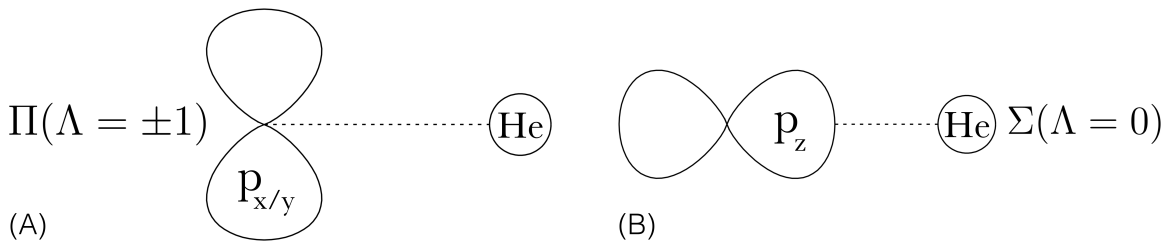

Figure 2.2: Level splitting of the p-orbitals in the presence of helium, that breaks the spherical symmetry. (A) A double degenerate n'$p_{x/y}$-orbital and (B) a single n'p_z-orbital. (Illustration courtesy of M. Martinez[61].)

multiplicity), Λ is the quantum number for the projection of the electronic orbital angular momentum and Ω is the total electronic angular momentum, along the internuclear axis. Or symbolically

$$m_j = m_l + m_s \longrightarrow \Omega = \Lambda + m_s \tag{2.32}$$

Following the spectroscopic notation the orbitals corresponding to $\Lambda = 0, 1, 2, 3, \ldots$ are labeled $\Sigma, \Pi, \Delta, \Phi, \ldots$. The state vector of the impurity interacting with a He atom can be expressed in an uncoupled basis

$$|p_{im}\rangle \in \{|p_{xm}\rangle, |p_{ym}\rangle, |p_{zm}\rangle\} \tag{2.33}$$

of real one-electron p-orbitals oriented along the internuclear axis (see Figure 2.3). The helium-impurity interaction matrix is given by

$$\begin{aligned}\mathcal{V}^{DIM}(r_m) &= V_\Pi(r_m)(|p_{xm}\rangle\langle p_{xm}| + |p_{ym}\rangle\langle p_{ym}|) + V_\Sigma(r_m)\,|p_{zm}\rangle\langle p_{zm}| \\ &= V_\Pi(r_m)(\mathbb{1}_3 - |p_{zm}\rangle\langle p_{zm}|) + V_\Sigma(r_m)\,|p_{zm}\rangle\langle p_{zm}| \\ &= V_\Pi(r_m)\mathbb{1}_3 + \left[V_\Sigma(r_m) - V_\Pi(r_m)\right]|p_{zm}\rangle\langle p_{zm}|\end{aligned} \tag{2.34}$$

where r_m is the modulus of the interatomic separation vector and V_Π and V_Σ are the Π and Σ impurity-He pair potentials in the absence of spin-orbit coupling. For a system consisting of N helium atoms the total interaction energy is calculated by summing over all the contributions of the N individual ^{4}He-X contributions

$$\mathcal{U}^{DIM}(\mathbf{r}_I) = \sum_{m=1}^{N} \mathcal{V}^{DIM}(r_m) \tag{2.35}$$

It is more convenient to express the interaction in a basis common to all impurity-helium pairs, instead of a basis that depends on the particular impurity-helium pair chosen. To do this we apply a rotation $\mathcal{R}_m : \hat{\mathbf{z}}_m \mapsto \hat{\mathbf{z}} \propto \mathbf{r}_I$, so that the matrix corresponding to the mth ^{4}He atom expressed in the common basis is given by

$$|p_{zm}\rangle\langle p_{zm}| = \mathcal{R}_m\,|p_z\rangle\langle p_z|\,\mathcal{R}_m^{-1} \tag{2.36}$$

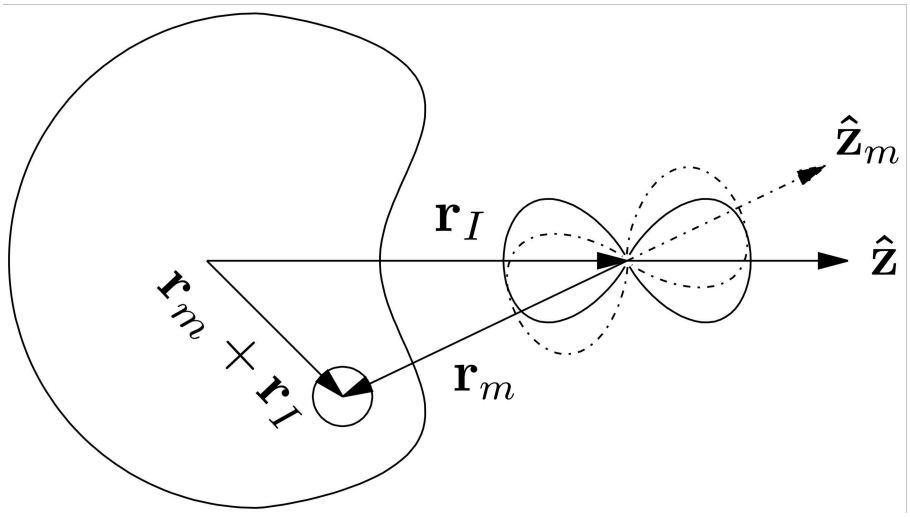

Figure 2.3: The set of axis defined in the DIM description. (Illustration courtesy of M. Martinez[61].)

It can be shown that the elements of this matrix in cartesian coordinates are of the form

$$\langle p_i | \mathcal{R}_m | p_z \rangle \langle p_z | \mathcal{R}_m^{-1} | p_j \rangle = \frac{r_{im}\, r_{jm}}{\|\mathbf{r}_m\|^2} \tag{2.37}$$

where $(i, j) \in \{x, y, z\}$. With these definitions we can write the matrix elements U_{ij}^{DIM} of the interaction energy $\mathcal{U}^{DIM}$

$$U_{ij}^{DIM}(\mathbf{r}_I) = \langle p_i | \mathcal{U}^{DIM} | p_j \rangle = \sum_{m=1}^{N} V_{ij}^{DIM}(r_m) \tag{2.38}$$

where

$$V_{ij}^{DIM}(r_m) := V_\Pi(r_m)\delta_{ij} + \Big[V_\Sigma(r_m) - V_\Pi(r_m) \Big] \frac{r_{im}\, r_{jm}}{\|\mathbf{r}_m\|^2} \tag{2.39}$$

are the matrix elements of $\mathcal{V}^{DIM}$ expressed in the common basis. Since we are working with a continuous helium density $\rho(\mathbf{r})$ and not with discrete atoms, the summation over N helium atoms in the previous expression is replaced by an integral over the density $\sum_m \to \int \rho(\mathbf{r})\, \mathrm{d}\mathbf{r}$. Here we dropped the subscript m, representing the mth helium atom. This finally gives for the matrix element U_{ij}^{DIM}

$$U_{ij}^{DIM}(\mathbf{r}_I) = \int \rho(\mathbf{r} + \mathbf{r}_I)\, V_{ij}^{DIM}(r)\, \mathrm{d}\mathbf{r} \tag{2.40}$$

The eigenvalues $U_k^{\text{np}}(\mathbf{r}_I)$ of this real symmetric matrix define the potential energy curves (PECs) without spin-orbit coupling as a function of the distance between the surrounding helium and the impurity for a given helium density.

2.6.2 Including spin-orbit coupling

For the study of the alkali metal Rb in this work, the spin-orbit (SO) splitting of the energy levels is comparable to the splitting of the orbital angular momentum levels $\Lambda = 0$ and

$\Lambda = \pm 1$ due to the interaction with the helium. Therefore the spin-orbit interaction needs to be included in the total interaction Hamiltonian.

The total electronic Hamiltonian is given by the sum of the DIM-interaction and the SO-interaction

$$\mathcal{H} = \mathcal{U}^{DIM} + \mathcal{V}^{SO}. \tag{2.41}$$

The SO-matrix is approximated by the atomic alkali one, which is approximated by

$$\mathcal{V}^{SO} = g\mathbf{L}\cdot\mathbf{S} = \frac{1}{2}g\left(\mathbf{J}^2 - \mathbf{L}^2 - \mathbf{S}^2\right) \tag{2.42}$$

The coupling constant g is usually approximated by that of the free atom[67]. We can extend the DIM basis Equation (2.33) to include the projection of the electron spin $s = \{\uparrow,\downarrow\}$ corresponding to the quantum numbers $m_s = \left\{\frac{1}{2}, -\frac{1}{2}\right\}$:

$$\left|p_i, s\right\rangle \in \left\{\left|p_x,\uparrow\right\rangle, \left|p_x,\downarrow\right\rangle, \left|p_y,\uparrow\right\rangle, \left|p_y,\downarrow\right\rangle, \left|p_z,\uparrow\right\rangle, \left|p_z,\downarrow\right\rangle\right\}. \tag{2.43}$$

In this basis the matrix $\mathcal{V}^{SO}$ is given by

$$\mathcal{V}^{SO} = \frac{1}{2}g\begin{pmatrix} 0 & 0 & -i & 0 & 0 & 1 \\ 0 & 0 & 0 & i & -1 & 0 \\ i & 0 & 0 & 0 & 0 & -i \\ 0 & -i & 0 & 0 & -i & 0 \\ 0 & -1 & 0 & i & 0 & 0 \\ 1 & 0 & i & 0 & 0 & 0 \end{pmatrix} \tag{2.44}$$

Kramers' theorem states that the two-fold degeneracy of the levels originating from total half-integer spin cannot be broken by electrostatic interactions[68]. Therefore all the electronic eigenstates of $\mathcal{H}$ are doubly degenerate. Diagonalising $\mathcal{H}$ yields three doubly degenerate potential energies between the impurity and surrounding helium.

The dynamic evolution of the electronic excited state of the impurity is described by introducing an additional degree of freedom, a 6-component vector $|\lambda\rangle$, which describes the coefficients of the electronic state in the $\left\{\left|p_i, s\right\rangle\right\}$ basis

$$|\lambda(t)\rangle = \sum_{\substack{i=\{x,y,z\} \\ s=\{\uparrow,\downarrow\}}} \lambda_{is}(t)\left|p_i, s\right\rangle \tag{2.45}$$

such that $\|\langle\lambda|\lambda\rangle\|^2 = 1$. The complete set of variables required to describe the system consists of the complex valued effective wave function for helium $\Psi(\mathbf{r}, t)$ with $\rho(\mathbf{r}, t) = |\Psi(\mathbf{r}, t)|^2$, the impurity position $\mathbf{r}_I(t)$, and the 6-dimensional complex vector to determine its electronic wave function $|\lambda(t)\rangle$. The total energy of the impurity-$^4\mathrm{He}_N$ complex after excitation to the ^{2}P manifold is

$$\begin{aligned} E[\Psi, \mathbf{r}_I, \lambda] = \frac{\hbar^2}{2m_4}\int |\nabla\Psi|^2\,\mathrm{d}\mathbf{r} + \int \mathcal{E}_c[\rho]\,\mathrm{d}\mathbf{r} \\ + \frac{1}{2}m_I\dot{\mathbf{r}}_I^2 + \int \rho(\mathbf{r})\,V_\lambda(\mathbf{r}-\mathbf{r}_I)\,\mathrm{d}\mathbf{r} + \left\langle\lambda\middle|\mathcal{V}^{SO}\middle|\lambda\right\rangle \end{aligned} \tag{2.46}$$

where V_λ is defined as

$$V_\lambda(\mathbf{r}) := \langle\lambda|\mathcal{V}^{DIM}|\lambda\rangle = \sum_{ijss'} \lambda^*_{is} V^{DIM}_{ijss'}(\mathbf{r})\lambda_{js'} \tag{2.47}$$

and the components of the 6×6 matrix $\mathcal{V}^{DIM}$ given by

$$V^{DIM}_{ijss'}(\mathbf{r}) = V^{DIM}_{ij}\delta_{ss'} = \left\{V_\Pi(r)\delta_{ij} + \left[V_\Sigma(r) - V_\Pi(r)\right]\frac{r_i\, r_j}{\|\mathbf{r}_m\|^2}\right\}\delta_{ss'} \tag{2.48}$$

The time evolution of the system is obtained by minimising the following action

$$\begin{aligned}\mathcal{A}[\Psi, \mathbf{r}_I, \lambda] = \int \Bigg\{ & i\hbar \int \Psi^*(\mathbf{r})\frac{\partial}{\partial t}\Psi(\mathbf{r})\,\mathrm{d}\mathbf{r} + m_I\dot{\mathbf{r}}_I^2 \\ & + i\hbar\left\langle\lambda\left|\frac{\partial}{\partial t}\right|\lambda\right\rangle - E[\Psi, \mathbf{r}_I, \lambda]\Bigg\}\,\mathrm{d}t\end{aligned} \tag{2.49}$$

Variation of the action $\mathcal{A}$ with respect to $\{\Psi^*, \langle\lambda|, \mathbf{r}_I\}$ yields the following three coupled EL-equations

$$\begin{aligned} i\hbar\frac{\partial}{\partial t}\Psi &= \left[-\frac{\hbar^2}{2m_4}\nabla^2 + \frac{\delta\mathcal{E}_c}{\delta\rho(\mathbf{r})} + V_\lambda(\mathbf{r}-\mathbf{r}_I)\right]\Psi \\ i\hbar\frac{\partial}{\partial t}|\lambda\rangle &= \mathcal{H}\,|\lambda\rangle \\ m_I\ddot{\mathbf{r}}_I &= -\boldsymbol{\nabla}_{\mathbf{r}_I}\left[\int \rho(\mathbf{r})\,V_\lambda(\mathbf{r}-\mathbf{r}_I)\,\mathrm{d}\mathbf{r}\right] = -\int V_\lambda(\mathbf{r}-\mathbf{r}_I)\,\boldsymbol{\nabla}\rho(\mathbf{r})\,\mathrm{d}\mathbf{r}\end{aligned} \tag{2.50}$$

where the explicit time dependence of the variables is omitted for clarity. The second line of Equation (2.50) is a 6×6 matrix equation with the matrix elements of $\mathcal{H}$ given by

$$H_{ijss'} = U^{DIM}_{ijss'} + V^{SO}_{ijss'} = \int \rho(\mathbf{r})\,V^{DIM}_{ijss'}(\mathbf{r}-\mathbf{r}_I)\,\mathrm{d}\mathbf{r} + V^{SO}_{ijss'} \tag{2.51}$$

In the cases that SO-coupling can be neglected the 6-dimensional electronic state vector $|\lambda\rangle$ reduces to the 3-dimensional vector

$$|\lambda(t)\rangle = \sum_{i=\{x,y,z\}} \lambda_i(t)\,|p_i\rangle \tag{2.52}$$

and the 6×6 matrix $\mathcal{H}$ reduces to the 3×3 matrix of Equation (2.40) with elements

$$H_{ij} = U^{DIM}_{ij} = \int \rho(\mathbf{r})\,V^{DIM}_{ij}(\mathbf{r}-\mathbf{r}_I)\,\mathrm{d}\mathbf{r} \tag{2.53}$$

2.6.3 Absorbing potential at the box boundaries

Equation (2.31) or Equation (2.50) are usually solved within the same box and using the same grid as for the static problem. The time step employed is about 0.5 fs in most applications. We use Hamming's predictor-modifier-corrector method as explained in

Chapter 8 of Ref. [69]. An introductory description of the predictor-corrector and Runge-Kutta methods can be found in Ref. [70]. The presentation of both approaches in Ref. [69] is particularly clear and useful.

During the time evolution of excited impurities in bulk liquid helium, sound waves are released from the surface of the atomic bubble and eventually reach the cell boundary. If no action is taken, they will bounce back and spoil the simulation. In the case of doped droplets, this can also happen when some helium is ejected off the droplet in the course of the dynamics. In this case, particle –and thus energy– leaking appears when some helium density gets near the walls of the calculation box. This leaking is physical, it represents helium atoms leaving the droplet and the energy carried away by them. This material also has to be prevented from bouncing back.

A way to prevent this problem is to include some damping (absorption potential) into the time-dependent equation governing the helium evolution, as *e.g.* Equation (2.31). We make the replacement, $i \longrightarrow i + \Lambda(\mathbf{r})$, into the dynamic equation of the helium[71]. This corresponds to a rotation of the time axis in the complex plane by introducing a damping field $\Lambda(\mathbf{r})$. This is equivalent to adding a purely imaginary potential $i\Lambda(\mathbf{r})$ which has the effect of absorbing helium density in the region where it is non zero. $\Lambda(\mathbf{r})$ is taken as

$$\Lambda(\mathbf{r}) = \Lambda_0 \left[1 + \tanh\left(\frac{s - s_0}{a}\right)\right], \quad s \equiv |\mathbf{r}| \tag{2.54}$$

We have fixed Λ_0= 2 and a= 2 in "internal use" units (see Ref. [65], Appendix B). The evolution is damping-free, $\Lambda(\mathbf{r}) \ll 1$, in a sphere of radius $s < s_0 - 2a$.

The region in which the absorption potential acts has to be large enough to accommodate the part of the system under study, and can be geometry-adapted. This means that absorption can be made to act only on the cell boundaries that are expected to be hit by the "evaporated" helium atoms (top boundary, lateral boundaries, all boundaries, ...). If for instance we just include absorption in the z direction, Equation (2.54) reduces to

$$\Lambda(z) = \Lambda_0 \left[1 + \tanh\left(\frac{|z| - s_0}{a}\right)\right] . \tag{2.55}$$

The value of s_0 is taken to be 2-3 Å less than the maximum $|z|$ value in the calculation box.

The above prescription works extremely well, as it efficiently dampens the excitations of the helium wave function at the cell boundaries in the case of extended systems, or absorbs the helium atoms leaving the simulation box in the case of droplets. Moreover, it does not require a large buffer region. Actually, we use the same box as the one for static calculations.

If the impurity is treated classically, its motion can be followed irrespective of whether it is inside or outside the simulation box. If the impurity dynamics was described by a wave

packet –which we have not done so far– one should also take care of the reflection of the wave packet at the cell boundaries. This could be done by the trick just described, which is commonly used in wave packet propagation where it is called “optical” or “absorbing potential” or “absorbing boundary conditions” method.

Finally, we mention that for the method to work in the bulk liquid, the –known– chemical potential of the helium must be included in the TDDFT evolution equation, see Equation (4) of Ref. [71].

Again, for more details about how this method is implemented the interested reader is directed to Ref. [65]. For the collection of Fortran code that has been used to obtain the results presented here see Ref. [72]. For the manual to use the code, with included example calculations see Ref. [73].

2.6.4 Notes on parallelisation

In the dynamic code, most of the loops and integrals are parallelised using OpenMP, as implemented in Intel Corporation’s Fortran Compiler suite (ifort), which is part of Intel’s Parallel Studio XE development environment. It is optimised to take advantage of Intel’s Xeon processor architecture, which forms the base of the ‘EOS supercomputer’ at CALMIP. The convolution integrals, as mentioned in Section 2.5.3, are computed using the discrete Fourier transform routines from the Intel Math Kernel Library (MKL). The compilation of the code is specifically optimised to run on EOS’s architecture.

Part I

Photo-excitation dynamics of alkalis

3
Alkali-doped nanodroplets

In their 1996 paper[74] Griffin and Stringari have argued that almost 100% Bose-Einstein Condensation could be achieved in the low density surface region of superfluid He at $T = 0$, as opposed to only about 10% in the bulk. It is therefore evident that a minimally perturbing probe capable of investigating the surface of a He cluster is very desirable.

It was argued from a theoretical perspective[75] that the alkali atoms reside on the cluster surface. Experimental evidence for this was found[76-78] later when it was observed that the laser induced fluorescence (LIF) spectrum of sodium was shifted compared to sodium in the gas phase due to the presence of the He cluster. However, not as much as alkali atoms in the bulk of liquid helium.

It comes as no surprise then that alkali atoms are a very natural choice for exactly these type of studies. For example, with a solvation parameter (see Section 1.3) of $\lambda = 0.729$[38], Rb will remain bound to the surface of the droplet. Furthermore, alkalis have a simple, well known, absorption spectrum. Moreover, their simple, one-valence electron structure allows for detailed theoretical modelling. They introduce only weak perturbations (alkali-helium interaction energies are on the order of 1 cm^{-1}[79]). Lastly, theoretical calculations[80,81] and experimental spectra[82-84] of alkali atoms in bulk liquid helium are available for comparison.

Surprisingly, the study of alkali atoms seeded in highly quantum matrices is relevant to the optimisation of solid hydrogen as a rocket propellant, where e.g. doping solid H_2 with lithium results in a gain in the specific impulse[85].

Given that alkalis are ideal objects to probe the boundary region of the nanodroplets, the $n\mathrm{p}\,^2\mathrm{P} \longleftarrow n\mathrm{s}\,^2\mathrm{S}$ transitions of the alkali atoms have attracted much interest from an experimental as well as a theoretical point of view. The spectroscopy of higher excited states has been thoroughly explored[86-95]. The obtained spectra can be successfully reproduced by a pseudo-diatomic model[1], except for the higher excited states, where

[1] Also called the "frozen droplet" model. It is equivalent to the DIM model, explained in Section 2.6.1,

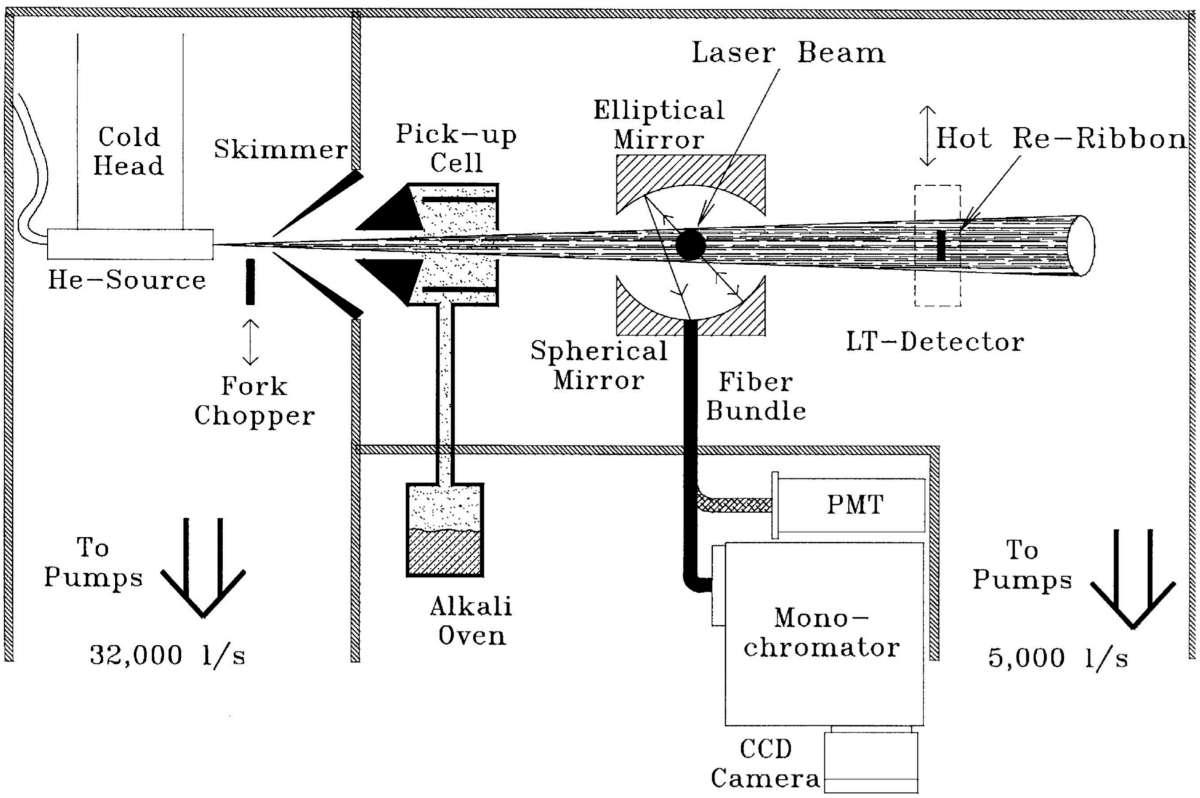

Figure 3.1: Principle of an alkali-doped helium nanodroplet experiment from Ref. [96]

the model progressively fails due to the limitations imposed by its realm of validity[96,97]. While the effect of the excited states on the spectra are now fairly well understood, their influence on the following dynamics is largely unexplored.

In this part of the thesis, the results of the real-time dynamics of a single electronically excited rubidium (Rb) atom residing in the surface dimple of a helium nano-droplet are presented. The atom is excited from its ground state $5s\,^2\Sigma_{1/2}$ to the $5p\,^2\{\Sigma,\Pi\}$ and $6p\,^2\{\Sigma,\Pi\}$ manifold (see Section 2.6.1 for an explanation of the used electronic state labels). Usually they desorb upon excitation either as a bare atom or as a complex with one or more helium atoms, called an "exciplex".

Experimental setup

A beam of large He nanodroplets is produced in a supersonic expansion from a cold nozzle (Figure 3.1). The weak He-He binding energy of 7.7 cm^{-1} [22] requires high stagnation pressures and low nozzle temperatures (T) for large cluster formation. For a set pressure, nozzle aperture and temperature the droplet sizes are log-normal distributed. Doping of the He clusters is realised by sending the beam through a pick-up cell (located a

but where the internal structure of the droplet is neglected, i.e. the whole droplet is considered to be a single huge atom.

short distance after the skimmer) in which a variable pressure of the alkali is maintained by connecting the pick-up cell with the reservoir through a heated tube. For a chosen average droplet size the average number of dopants picked-up by the droplet is governed by Poissonian statistics and can be controlled with the vapour pressure inside the pickup cell. In their path through the cell the larger clusters pick up alkali atoms without being appreciably deflected. Dissipation of the energy of the captured alkali is likely to occur by evaporation of He atoms from the clusters, the terminal temperature of which rapidly returns to its pre pick-up value (~0.4 K) [2].

To probe the picked-up alkali atoms a variety of measurement techniques can be employed, e.g. laser induced fluorescence (LIF) spectroscopy, time-resolved pump-probe spectroscopy, photo-electron spectroscopy and velocity map imaging (VMI). The specific ones used in this work will be introduced generally in the next section.

4
Imaging Excited-State Dynamics

The following article is a combined experimental and theoretical study focussing on imaging and characterising the dynamics following the 5p←5s and 6p←5s excitations of rubidium hosted by a helium nanodroplet. The experiment used femtosecond pump-probe techniques with a first laser exciting the Rb on the droplet surface at time t_{exc} and a second laser ionising it for detection with VMI at time t_{ion}. The results characterised a critical time delay, called the "fall-back time", between two opposite outcomes. If $t_{ion} - t_{exc} \leq \tau$, the departing Rb atom is still rather close to the droplet when the probe laser turns their interaction to attractive. As a result, the Rb^+ turns around and gets solvated. On the other hand, for $t_{ion} - t_{exc} \geq \tau$, ionisation occurs too late for Rb^+ to feel an appreciable attraction from the droplet, and it had already too much kinetic energy, so that it escapes.

The theoretical study focussed on understanding the desorption dynamics and determining the fall-back times to compare with the experiment. It made use of the He-TDDFT presented in Section 2.6, both in the excited and ionised states. The results are presented in the following article which was published in the Journal of Physical Chemistry Letters[98].

THE JOURNAL OF PHYSICAL CHEMISTRY Letters

Letter

pubs.acs.org/JPCL

Imaging Excited-State Dynamics of Doped He Nanodroplets in Real-Time

Johannes von Vangerow,[†] François Coppens,[‡] Antonio Leal,[§] Martí Pi,[§] Manuel Barranco,[§,‡] Nadine Halberstadt,[‡] Frank Stienkemeier,[†] and Marcel Mudrich*,[†]

[†]Physikalisches Institut, Universität Freiburg, Hermann-Herder-Str. 3, 79104 Freiburg, Germany

[‡]Laboratoire des Collisions, Agrégats, Réactivité, IRSAMC, UMR 5589, CNRS et Université Paul Sabatier-Toulouse 3, 118 route de Narbonne, F-31062 Toulouse Cedex 09, France

[§]Departament FQA, Facultat de Física, and IN2UB, Universitat de Barcelona, Diagonal 645, 08028 Barcelona, Spain

Supporting Information

ABSTRACT: The real-time dynamics of excited alkali metal atoms (Rb) attached to quantum fluid He nanodroplets is investigated using femtosecond imaging spectroscopy and time-dependent density functional theory. We disentangle the competing dynamics of desorption of excited Rb atoms off the He droplet surface and solvation inside the droplet interior as the Rb atom is ionized. For Rb excited to the 5p and 6p states, desorption occurs on starkly differing time scales (∼100 versus ∼1 ps, respectively). The comparison between theory and experiment indicates that desorption proceeds either impulsively (6p) or in a transition regime between impulsive dissociation and complex desorption (5p).

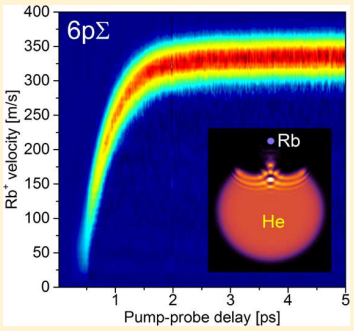

He nanodroplets are intriguing quantum fluid objects of finite size capable of efficiently capturing and cooling atoms, molecules, and clusters for spectroscopy and dynamics studies.[1,2] Upon electronic excitation, embedded atoms and small molecules tend to move toward the droplet surface and may be ejected due to short-range electron He repulsion.[3] In contrast, cations experience attractive forces toward the He droplets mediated by electrostatic polarization, which draw them to the droplet interior, where they may form snowball complexes.[4−7] These two opposing trends lead to a rich dynamics initiated by photoexcitation of embedded species involving desorption, electronic relaxation, complex formation, as well as solvation and desolvation of the ionized impurity.[8−19] Similar dynamics have been observed when exciting pure He droplets with extreme-ultraviolet radiation[20] as well as for other types of clusters.[21]

So far, time-resolved experiments on He droplets doped with alkali (Ak) metal atoms were mostly focused on the formation of AkHe exciplexes induced by laser excitation.[15−18,22,23] The concurrent desorption of these excited species was estimated to proceed on a picosecond time scale.[9,10,13,24−26] This estimate, sufficient for studies employing nanosecond laser pulses, clearly lacks precision for experiments with sub-picosecond time resolution. Thus in the previous measurements as well as in experiments focusing on electronic and vibrational coherences of Ak atoms and molecules[17,19,22,23,27] the exact location of the dopants, attached to the droplets or in the vacuum, has remained somewhat uncertain.

Here we report a combined experimental and theoretical investigation of the excited-state dynamics of doped He nanodroplets in real time. The combination of fs pump−probe spectroscopy with velocity map imaging (VMI)[28] allows us to clearly disentangle complex formation, desorption, and ion solvation. As a model system, we investigate He droplets doped with single rubidium (Rb) atoms. Ground-state Rb atoms and small molecules are weakly bound to the He droplet surface in a dimple structure.[29−31] Therefore, the ejection dynamics of the excited Rb atom (Rb*) is not affected by processes such as the interaction of Rb* with density waves traveling in the bulk of the droplet, as for Ag*.[11]

We excite droplet-bound Rb atoms to states correlating either to the lowest excited state 5p or to the higher lying state 6p. The dynamics is probed by ionizing Rb* at variable delay times between photoexcitation ($t = 0$) and photoionization ($t = t_+$) while monitoring the velocity and signal yield of Rb^+ ions. A simulation based on time-dependent density functional theory (TDDFT) gives us insight into the time evolution both of Rb* and of the Rb^+ ion taking into account the quantum fluid properties of the He environment. Using these techniques, we follow the trajectory of the excited and subsequently ionized Rb atom in detail as it escapes from the droplet surface or submerges into it. Although separated by only ∼1.4 eV in energy, the two states 5p and 6p are found to feature time

Received: November 6, 2016
Accepted: December 20, 2016
Published: December 20, 2016

ACS Publications © 2016 American Chemical Society

DOI: 10.1021/acs.jpclett.6b02598
J. Phys. Chem. Lett. 2017, 8, 307−312

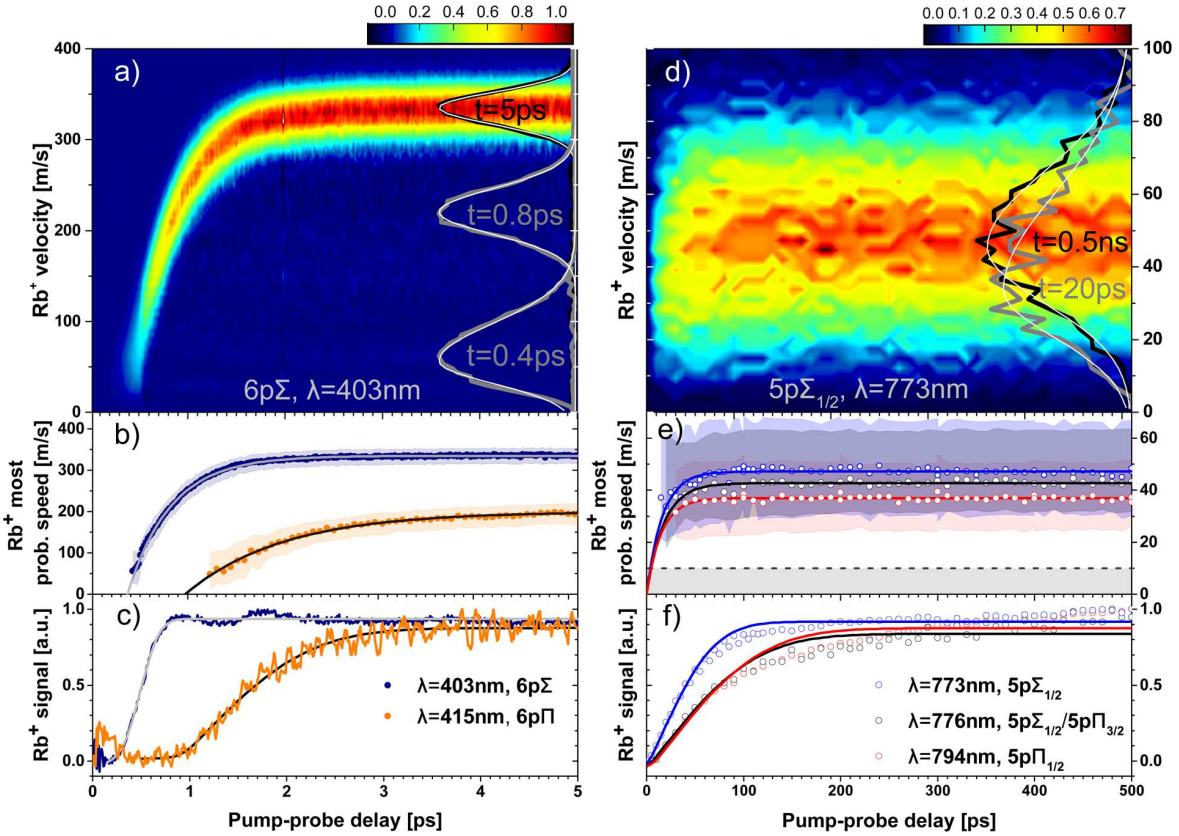

Figure 1. Rb^+ transient speed distributions (a,d), most probable speeds (b,e), and ion yields (c,f) resulting from photoexcitation to He droplet perturbed states correlating to 6p (left column) and 5p states (right column) of Rb (pump) and subsequent ionization (probe). The shaded areas (b,e) indicate the left and right $e^{-1/2}$ widths of the speed distributions. The shaded area at the bottom of panel e depicts the experimental resolution. The smooth lines are fits to the data (see text).

constants of the desorption dynamics differing by about 2 orders of magnitude.

Figure 1a,d shows examples of measured Rb^+ transient speed distributions derived from the VMIs by angular integration. From these distributions we infer the most probable speeds (b,e) by fitting a skewed Gaussian distribution as illustrated by selected speed distributions shown on the right-hand sides of Figure 1a,d.[34] For the droplet perturbed Rb 6p states the most probable speeds (b) as well as the total Rb^+ ion yields (c) show a steep rise within a few picoseconds. In contrast, for the droplet perturbed 5p states we record speed distributions (e) close to our experimental resolution of ~10 m/s (shaded gray area) and ion yields (f) which increase within hundreds of picoseconds.

For the droplet perturbed Rb 6p excitations, the transient ion yield curves (c) have previously been interpreted in terms of the competing effects of repulsion from the He droplet surface and attraction of Rb^+ toward it.[14] Accordingly, the slower dynamics of the 6pΠ state compared with that of the 6pΣ state is due to the weaker repulsion from the droplet. We term "fall-back time", τ_c, the critical delay discriminating between the ion falling back into the droplet and the ion escaping into the vacuum. It is obtained by fitting the 6p and 5p ion yield data with a piecewisely defined asymmetric error function $I(t) = A_0 + A\cdot\{[t \leq \mu]\sigma_-\cdot\mathrm{erf}\,[(t-\mu)/\sigma_-] + [t > \mu]\,\sigma_+\cdot\mathrm{erf}\,[(t-\mu)/\sigma_+]\}$, where $\sigma_\mp$ denote widths on the right and left side of the inflection point μ. τ_c is obtained from computing the 50% rise time of that fit function. The evolution of the most probable speeds $\hat{v}$ is fitted by $\hat{v}(t) = \hat{v}_f\{1-\exp[-\ln 2\cdot(t-t_0)/\tau]\}$, from which we obtain the characteristic 50% rise times $\tau_v = t_0 + \tau$.

Note that for each applied pump−probe delay we measure the final velocity distribution of the ion after it has fully escaped from the droplet. Therefore, the experiment does not give direct access to the desorption dynamics of the neutral Rb* atom. To get a complete picture of the dynamics, simulations based on the TDDFT approach are carried out using the functional of ref 35. Details of this approach have been described before.[9,11,32] In short, we consider droplets consisting of N = 1000 atoms doped with one Rb atom. Because of its large mass compared with that of He we describe the dynamics of the Rb atom classically. The simulations of the full pump−probe sequence consist of two steps: the propagation of Rb* in the excited state starting at t = 0 (step 1) and the propagation of the Rb^+ ion at times $t > t_+$ (step 2). This is achieved by solving the coupled 3D TDDFT and Newton's equations for the He droplet and the Rb impurity, respectively.

In step 1, the Rb*−droplet interaction is obtained from the Rb*−He $n\Sigma$ and $n\Pi$ pair potentials[36] with n = 5 and 6, and includes the spin−orbit interaction in the usual He−Rb* distance-independent way; it also allows for the dynamic evolution of the internal electronic state of the Rb* atom.[11] In step 2, the coupled dynamical equations are now simpler as they do not explicitly take into account the electronic structure of the closed-shell Rb^+ ion. In all simulations, a spatial grid of 0.4 Å and a time step of 0.5 fs are used.

DOI: 10.1021/acs.jpclett.6b02598
J. Phys. Chem. Lett. 2017, 8, 307−312

The Journal of Physical Chemistry Letters Letter

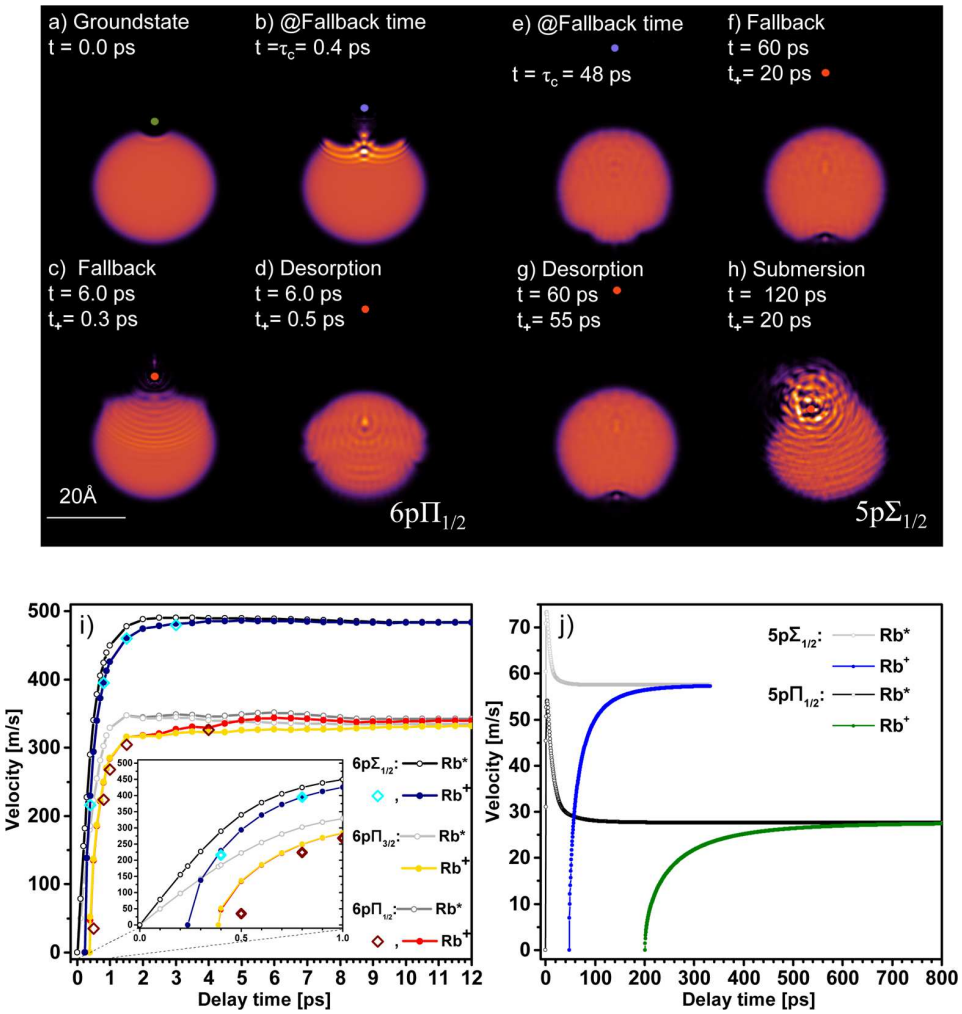

Figure 2. TDDFT-based 2D densities (a–d,e–h) and velocities (i,j) of Rb atoms attached to He_{1000} excited from equilibrium (a) to droplet perturbed 6p (left column) and 5p (right column) states. Configurations are shown for different propagation times t and ionization times t_+: (b,e) neutral Rb at fall-back time $t = \tau_c$; (c,f) $t_+ < \tau_c$, fall-back of Rb^+ ion; (d,g) $t_+ > \tau_c$, desorption of Rb^+; (h) solvation of Rb^+; (i,j) evolution of Rb* velocities with time t (gray open dots), and final velocities of Rb^+ (colored filled dots) as a function of t_+.

For step 1, initial conditions are given by the structure of the neutral Rb–He_{1000} complex in the ground state[32] obtained using the Rb–He potential of ref 37. For step 2 the initial conditions are given by the step 1 simulation at $t = t_+$. Carrying out the full simulations for step 2 is crucial for short and intermediate delays $t_+ \lesssim \tau_c$, as the droplet is still far from being relaxed when Rb* is photoionized. At variance, we have checked that keeping the droplet density frozen as done in ref 14 is a good approximation for long delays $t_+ \gg \tau_c$. In Figure 2i the open diamonds show the difference between carrying out the full simulation and keeping the He density frozen at $t = \tau_c$ for $t_+ \gtrsim \tau_c$ (filled dots). For illustration, these simulations are provided as animations in the Supporting Information.

Figure 2a–d,e–h shows snapshots of the resulting 2D densities for different propagation times t and ionization times t_+ for the $6p\Pi_{1/2}$ (left column) and $5p\Sigma_{1/2}$ (right column) states. The ground-state dimple configuration is depicted in panel a. Figure 2b,e shows the configurations at the fall-back time τ_c. Panels c, d and g, h illustrate the desorption and fall-back processes. When ionization occurs before the fall-back time, $t_+ < \tau_c$, the ion turns around and submerges into the droplet, where it becomes fully solvated (h). For $t_+ > \tau_c$, the ion keeps moving away from the droplet surface and fully desorbs (d, g). Panels i, j show the velocities of Rb* (open symbols) and Rb^+ ions (filled symbols). The inset shows a close-up of the 6p dynamics at short propagation times.

For the 6p states, the Rb* velocity features a steep rise that levels out after ~2 ps propagation time t (gray open dots). The final Rb^+ velocity is reduced compared with the Rb* velocity at short delays $t_+ \lesssim 10$ ps (colored dots) due to the attraction of the Rb^+ ion toward the He droplet. For long delays these values converge as the Rb^+–He droplet attraction drops off at large distances. For the 5p case, the Rb* velocity shows an overshoot at short delays relative to the asymptotic value. This is due to the transient Rb*–He droplet interaction being weakly attractive at intermediate distance, which slows down the ejected Rb* atom. It derives from the Rb*–He potentials featuring an outer attractive region.

A compilation of the time constants for fall-back, τ_c, rise times of the ion speed, τ_v, as well as most probable Rb^+ final velocities, $\hat{v}_f$, inferred from the experimental and theoretical data, is presented in Figure 3. The theory values of τ_v are

DOI: 10.1021/acs.jpclett.6b02598
J. Phys. Chem. Lett. 2017, 8, 307–312

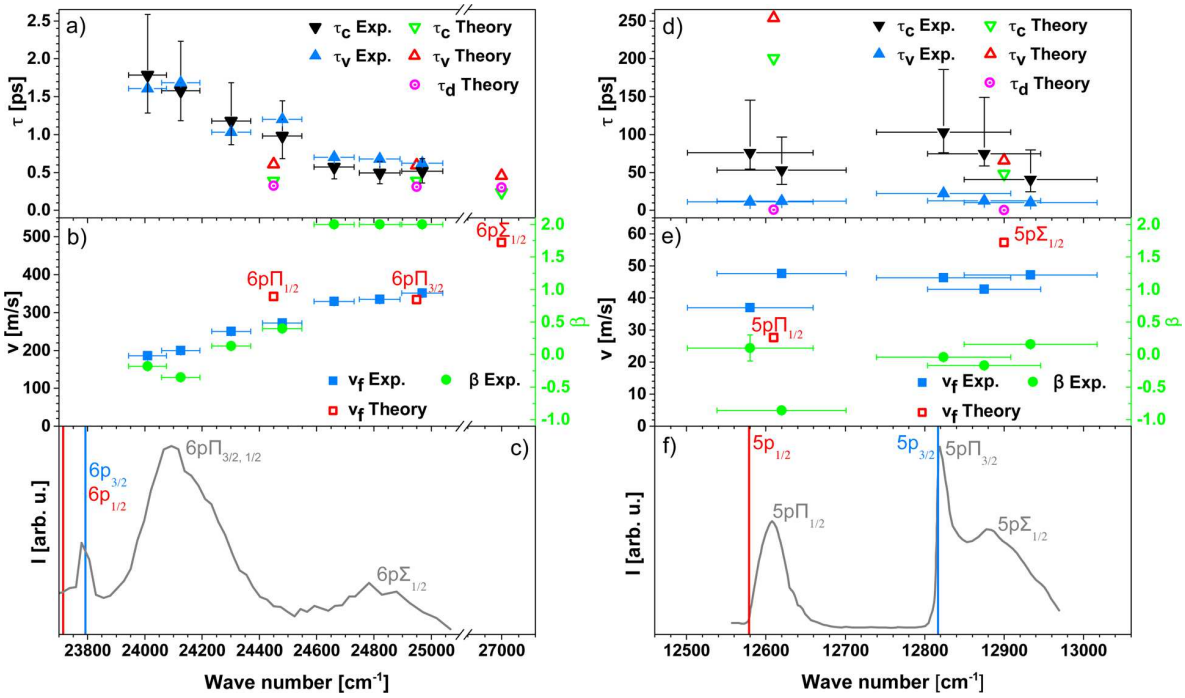

Figure 3. Experimental and theoretical fall-back time constants τ_c (a,d), velocity rise times τ_v (a,d), theoretical Rb* desorption times τ_d (a,d), Rb^+ final most probable speeds $\hat{v}_f$ (b,e), and anisotropy parameters β (b,e) for different excitation wavenumbers corresponding to droplet perturbed Rb states 6p (left column) and 5p (right column). Panels c and f show fluorescence emission spectra as reference.[25,38] Vertical lines indicate free atomic transitions.

determined by fitting the final ion velocities using the same model as for the experimental data. In addition, Figure 3a,d contains desorption times τ_d of the neutral Rb* atoms inferred from the simulation by fitting the same model as for ion velocities. Note that for the $5p\Pi_{1/2}$ and $5p\Sigma_{1/2}$ states we obtain values τ_d = 0.4 and 0.2 ps, respectively, from the rising edges of the speed curves in Figure 2j. Figure 3b,e displays the anisotropy parameter β of the Rb^+ angular distributions measured at long delay times. For reference we include the corresponding fluorescence excitation spectra taken from literature.[25,38] Excitation wavenumbers for the theory values correspond to the peak positions of the simulated absorption spectra (not shown). Vertical error bars are connected to widths of the asymmetric fit function. Horizontal error bars reflect the spectral widths (FWHM) of the fs laser pulses.

The experimentally observed drastic difference between time scales for the 6p and 5p state dynamics is well-reproduced by the calculation. The general trend that fall-back times τ_c decrease and final velocities rise as a function of excitation wavenumber reflects the increasing repulsion acting between Rb* and the He droplet as the excitation energy is tuned up.[9,13,24,26,32] Fall-back times τ_c and speed rise times τ_v exceed the desorption times τ_d of the neutral Rb* atom because the range of Rb^+−He attractive interaction is larger than that of Rb*−He repulsion.[14]

Discrepancies are found for the asymptotic velocities of the 6p states that are smaller in the experiment than in the simulation by a factor of ∼0.7. Accordingly, experimental fall-back and speed rise times exceed the simulated values by a factor of 2 for the $6p\Sigma_{1/2}$ and up to a factor of 4 for the $6p\Pi$ states. We attribute this mainly to the limited accuracy of the $6p\Sigma$ and $6p\Pi$ Rb*-He pair potentials[36] used in the simulation, causing a substantial blue shift of the simulated 6p ← 5s absorption spectrum (not shown) with respect to the measured one.[24,25]

For the 5p states the fall-back times being considerably larger than the speed rise times indicates that the desorption dynamics deviates to some extent from the impulsive model. In the limit of statistical desorption of Rb* atoms by an evaporation-like process, one would expect a continuously rising yield of free atoms and broad thermal distributions. Considering the slightly delayed, slow rise of the Rb^+ yield (Figure 1f) and the peaked but broadened speed distributions that feature only small up-shifts at short delays (Figures 1d,e), we conclude that the dynamics of 5p excited states proceeds in a transition regime from impulsive dissociation to more complex, evaporation-like desorption. This conclusion is supported by the anisotropy parameter β (Figure 3e), whose sign correctly indicates the symmetry of the dissociating complex[9,13,24] but whose absolute value is significantly reduced compared with that expected for impulsively dissociating complexes, in contrast with the 6p case (Figure 3b). Consequently, the quantitative agreement with the simulations, which do describe complex dynamical couplings within the superfluid model (Figure 2j) but do not contain statistical evaporation, is limited.

Aside from this, the experimentally observed higher final ion velocity and smaller fall-back time for the $5p\Pi_{1/2}$ state compared with theory may be due to the measured signals being dominated by excitation of the blue edge of the $5p\Pi_{1/2}$ feature. Considering the observed steep rise of fall-back time and drop of Rb^+ velocity toward the red edge of the $5p\Pi_{1/2}$ feature, our results agree with the previous finding that Rb* remains attached to the droplet surface upon narrow-band excitation at the red edge of the $5p\Pi_{1/2}$ state.[39,40]

DOI: 10.1021/acs.jpclett.6b02598
J. Phys. Chem. Lett. 2017, 8, 307−312

Excitation of the $5p\Pi_{3/2}$ state leads to the formation of RbHe exciplexes because the Rb*He pair interaction is strongly attractive in this state.[15,16,38] While exciplex formation is reproduced by the simulation, the ejection of exciplexes off the He droplet surface is not. However, we find that nonradiative relaxation to the $5p\Pi_{1/2}$ state may supply enough kinetic energy to the Rb* atom to cause ejection. We therefore argue that when tuning the fs laser to the $5p\Pi_{3/2}$ peak, the experimentally observed Rb^+ signal is mainly due to spin relaxation to the $5p\Pi_{1/2}$ state.[38] Possibly the admixture of the nearby repulsive $5p\Sigma_{1/2}$ state also contributes. The relaxation dynamics will be further studied using time-resolved photoelectron spectroscopy. Let us mention that the $RbHe^+$ pump−probe transients (not shown) closely follow the ones of Rb^+ but significantly differ from those previously measured using a one-color NIR scheme.[15,22] This raises some doubts as to the previous interpretation in terms of exciplex formation times and should be further investigated.

In conclusion, the observed dynamics of femtosecond pump−probe photoionization of Rb atoms attached to He nanodroplets is determined by the competition between the repulsive interaction of the droplet with the Rb atom in an excited state and the attractive interaction of the droplet with the Rb^+ cation, causing either desorption of Rb* off the droplet or submersion of the Rb^+ ion into the droplet interior, respectively. The resulting desorption dynamics proceeds impulsively within ∼1 ps for the 6p excited states and in a transition regime between impulsive dissociation and statistical desorption within ∼100 ps for the 5p states. This interplay between opposing trends (Rb* repulsion, Rb^+ attraction) is likely to be present in other types of clusters and condensed phase systems probed by time-resolved photoionization spectroscopy.

■ EXPERIMENTAL METHODS

The experimental setup has been previously described.[14,32] In brief, He droplets with an average diameter of 10 nm are created by continuous supersonic expansion and doped by one Rb atom on average.[14,32] The laser system generates amplified pulses of 100 fs duration at a repetition rate of 5 kHz with a tunable center wavelength in the near-infrared (NIR) region. Light in the visible range (VIS) is generated by frequency doubling. Pulses are split and separated in time in a Mach−Zehnder type interferometer. Droplet perturbed Rb 6p and 5p states are probed by one-color VIS and two-color NIR+VIS pump−probe schemes, respectively. NIR pulses are strongly attenuated to avoid excitations to higher lying states. Photoions are detected by a VMI spectrometer.[24,28,32] For varying pump−probe delay steps, mass-selected ion VMIs are recorded and inverse-Abel transformed.[33] For each pump−probe scheme, a background contribution from ionization of effusive Rb is observed. In the measurement probing the Rb 6p states, additional background arises from single pulse ionization. To extract the pump−probe correlated dynamics, these contributions are subtracted from the signal.

■ ASSOCIATED CONTENT

Supporting Information

The following files are available free of charge. The Supporting Information is available free of charge on the ACS Publications website at DOI: 10.1021/acs.jpclett.6b02598.

Desorption and fall-back dynamics of Rb atoms initially excited to the $5p\Pi_{1/2}$ state and ionized at t_+ = 20 ps. (AVI)

Desorption dynamics for $5p\Pi_{1/2}$ excitation and t_+ = 55 ps. (AVI)

Desorption and fall-back dynamics for $6p\Pi_{1/2}$ excitation t_+ = 0.3 ps. (AVI)

Desorption dynamics for $6p\Pi_{1/2}$ excitation and t_+ = 0.5 ps. (AVI)

■ AUTHOR INFORMATION

Corresponding Author

*E-mail: mudrich@physik.uni-freiburg.de.

ORCID

Marcel Mudrich: 0000-0003-4959-5220

Notes

The authors declare no competing financial interest.

■ ACKNOWLEDGMENTS

Financial support for this work by the Deutsche Forschungsgemeinschaft (grant nos. MU 2347/6-1 and IRTG 2079), DGI, Spain (grant no. FIS2014-52285-C2-1-P), and HPC resources from CALMIP (Grant P1039) is gratefully acknowledged. M.B. thanks the Université Fédérale Toulouse Midi-Pyrénées for financial support through the "Chaires d'Attractivité 2014" program IMDYNHE.

■ REFERENCES

(1) Toennies, J. P.; Vilesov, A. F. *Angew. Chem., Int. Ed.* **2004**, *43*, 2622.

(2) Stienkemeier, F.; Lehmann, K. *J. Phys. B: At., Mol. Opt. Phys.* **2006**, *39*, R127.

(3) Brauer, N. B.; Smolarek, S.; Loginov, E.; Mateo, D.; Hernando, A.; Pi, M.; Barranco, M.; Buma, W. J.; Drabbels, M. *Phys. Rev. Lett.* **2013**, *111*, 153002.

(4) Tiggesbäumker, J.; Stienkemeier, F. *Phys. Chem. Chem. Phys.* **2007**, *9*, 4748−4770.

(5) Müller, S.; Mudrich, M.; Stienkemeier, F. *J. Chem. Phys.* **2009**, *131*, 044319.

(6) Theisen, M.; Lackner, F.; Ernst, W. E. *Phys. Chem. Chem. Phys.* **2010**, *12*, 14861−14863.

(7) Zhang, X.; Drabbels, M. *J. Chem. Phys.* **2012**, *137*, 051102.

(8) Smolarek, S.; Brauer, N. B.; Buma, W. J.; Drabbels, M. *J. Am. Chem. Soc.* **2010**, *132*, 14086−14091.

(9) Hernando, A.; Barranco, M.; Pi, M.; Loginov, E.; Langlet, M.; Drabbels, M. *Phys. Chem. Chem. Phys.* **2012**, *14*, 3996−4010.

(10) Loginov, E.; Drabbels, M. *J. Chem. Phys.* **2012**, *136*, 154302.

(11) Mateo, D.; Hernando, A.; Barranco, M.; Loginov, E.; Drabbels, M.; Pi, M. *Phys. Chem. Chem. Phys.* **2013**, *15*, 18388−18400.

(12) Leal, A.; Mateo, D.; Hernando, A.; Pi, M.; Barranco, M.; Ponti, A.; Cargnoni, F.; Drabbels, M. *Phys. Rev. B: Condens. Matter Mater. Phys.* **2014**, *90*, 224518.

(13) Loginov, E.; Hernando, A.; Beswick, J. A.; Halberstadt, N.; Drabbels, M. *J. Phys. Chem. A* **2015**, *119*, 6033−6044.

(14) von Vangerow, J.; John, O.; Stienkemeier, F.; Mudrich, M. *J. Chem. Phys.* **2015**, *143*, 034302.

(15) Droppelmann, G.; Bünermann, O.; Schulz, C. P.; Stienkemeier, F. *Phys. Rev. Lett.* **2004**, *93*, 0233402.

(16) Reho, J.; Higgins, J.; Lehmann, K. K.; Scoles, G. *J. Chem. Phys.* **2000**, *113*, 9694−9701.

(17) Mudrich, M.; Droppelmann, G.; Claas, P.; Schulz, C.; Stienkemeier, F. *Phys. Rev. Lett.* **2008**, *100*, 023401.

(18) Mudrich, M.; Stienkemeier, F. *Int. Rev. Phys. Chem.* **2014**, *33*, 301−339.

DOI: 10.1021/acs.jpclett.6b02598
J. Phys. Chem. Lett. 2017, 8, 307−312

(19) Bruder, L.; Mudrich, M.; Stienkemeier, F. *Phys. Chem. Chem. Phys.* **2015**, *17*, 23877−23885.
(20) Ziemkiewicz, M. P.; Neumark, D. M.; Gessner, O. *Int. Rev. Phys. Chem.* **2015**, *34*, 239.
(21) Masson, A.; Poisson, L.; Gaveau, M.-A.; Soep, B.; Mestdagh, J.-M.; Mazet, V.; Spiegelman, F. *J. Chem. Phys.* **2010**, *133*, 054307.
(22) Schulz, C. P.; Claas, P.; Stienkemeier, F. *Phys. Rev. Lett.* **2001**, *87*, 153401.
(23) Giese, C.; Mullins, T.; Grüner, B.; Weidemüller, M.; Stienkemeier, F.; Mudrich, M. *J. Chem. Phys.* **2012**, *137*, 244307.
(24) Fechner, L.; Grüner, B.; Sieg, A.; Callegari, C.; Ancilotto, F.; Stienkemeier, F.; Mudrich, M. *Phys. Chem. Chem. Phys.* **2012**, *14*, 3843.
(25) Pifrader, A.; Allard, O.; Auböck, G.; Callegari, C.; Ernst, W.; Huber, R.; Ancilotto, F. *J. Chem. Phys.* **2010**, *133*, 164502.
(26) Loginov, E.; Drabbels, M. *J. Phys. Chem. A* **2014**, *118*, 2738−2748.
(27) Grüner, B.; Schlesinger, M.; Heister, P.; Strunz, W. T.; Stienkemeier, F.; Mudrich, M. *Phys. Chem. Chem. Phys.* **2011**, *13*, 6816−6826.
(28) Eppink, A. T. J. B.; Parker, D. H. *Rev. Sci. Instrum.* **1997**, *68*, 3477.
(29) Ancilotto, F.; DeToffol, G.; Toigo, F. *Phys. Rev. B: Condens. Matter Mater. Phys.* **1995**, *52*, 16125−16129.
(30) Stienkemeier, F.; Higgins, J.; Ernst, W. E.; Scoles, G. *Phys. Rev. Lett.* **1995**, *74*, 3592−3595.
(31) Bünermann, O.; Droppelmann, G.; Hernando, A.; Mayol, R.; Stienkemeier, F. *J. Phys. Chem. A* **2007**, *111*, 12684.
(32) von Vangerow, J.; Sieg, A.; Stienkemeier, F.; Mudrich, M.; Leal, A.; Mateo, D.; Hernando, A.; Barranco, M.; Pi, M. *J. Phys. Chem. A* **2014**, *118*, 6604−6614.
(33) Dick, B. *Phys. Chem. Chem. Phys.* **2014**, *16*, 570−580.
(34) Mudholkar, G. S.; Hutson, A. D. *J. Stat. Plan. Inference* **2000**, *83*, 291−309.
(35) Ancilotto, F.; Barranco, M.; Caupin, F.; Mayol, R.; Pi, M. *Phys. Rev. B: Condens. Matter Mater. Phys.* **2005**, *72*, 214522.
(36) Pascale, J. *Phys. Rev. A: At., Mol., Opt. Phys.* **1983**, *28*, 632−644.
(37) Patil, S. H. *J. Chem. Phys.* **1991**, *94*, 8089−8095.
(38) Brühl, F. R.; Trasca, R. A.; Ernst, W. E. *J. Chem. Phys.* **2001**, *115*, 10220−10224.
(39) Auböck, G.; Nagl, J.; Callegari, C.; Ernst, W. E. *Phys. Rev. Lett.* **2008**, *101*, 035301.
(40) Theisen, M.; Lackner, F.; Ernst, W. E. *J. Phys. Chem. A* **2011**, *115*, 7005−7009.

DOI: 10.1021/acs.jpclett.6b02598
J. Phys. Chem. Lett. 2017, 8, 307−312

5
Desorption dynamics of RbHe exciplexes

How do we resolve the discrepancy between the experimental observation that Rb atoms, excited to the 5p $^2\Pi_{3/2}$ state, detach from the droplet surface, and TD-DFT simulations that show that they result in a surface-bound state? That is the question that led to this work. Upon photo-excitation of Rb to the 5p $^2\Pi_{3/2}$ state, a He atom may be attached to it forming a HeRb exciplex; this cannot happen if Rb is excited to the 5p $^2\Pi_{1/2}$ state because it finds a barrier (see Figure 5.1) preventing exciplex formation.

In the gas phase, a HeRb 5p $^2\Pi_{1/2}$ exciplex can be formed if there is enough kinetic energy for Rb* to overcome the potential barrier; alternatively, the collision of the HeRb 5p $^2\Pi_{3/2}$ exciplex with another atom or complex might relax the Rb* atom from the 5p $^2\Pi_{3/2}$ to the 5p $^2\Pi_{1/2}$ state, overcoming the barrier as the potential wells for both states are at similar Rb-He distances. In the condensed (droplet) phase at 0.4 K temperature, neither of these mechanisms are available to explain the formation of HeRb 5p $^2\Pi_{1/2}$ exciplexes and their potential ejection.

However, another possible way for this to happen is non-radiative de-excitation from the 5p $^2\Pi_{3/2}$ to the 5p $^2\Pi_{1/2}$ that populates the latter state and leaves the Rb* atom with enough kinetic energy so as to be ejected. Notice from Figure 5.1 that the minimum of the 5p $^2\Pi_{3/2}$ potential is 12683 cm^{-1}, and that of the 5p $^2\Pi_{1/2}$ potential is at 12518 cm^{-1}; the value of this potential at the barrier is 12611 cm^{-1}. Thus, non-radiative de-excitation of the Rb* atom may add to its original kinetic energy of up to 165 cm^{-1}. It is worth noting that it will be ejected in the 5p $^2\Pi_{1/2}$ state, and not in the 5p $^2\Pi_{3/2}$ it was previously photo-excited to.

This publication contains a extension of our combined experimental and theoretical investigation presented in the previous section. Here we focus on the formation of

free RbHe-exciplex molecules from laser-excited Rb-doped He nanodroplets through the mechanism of electronic spin relaxation.

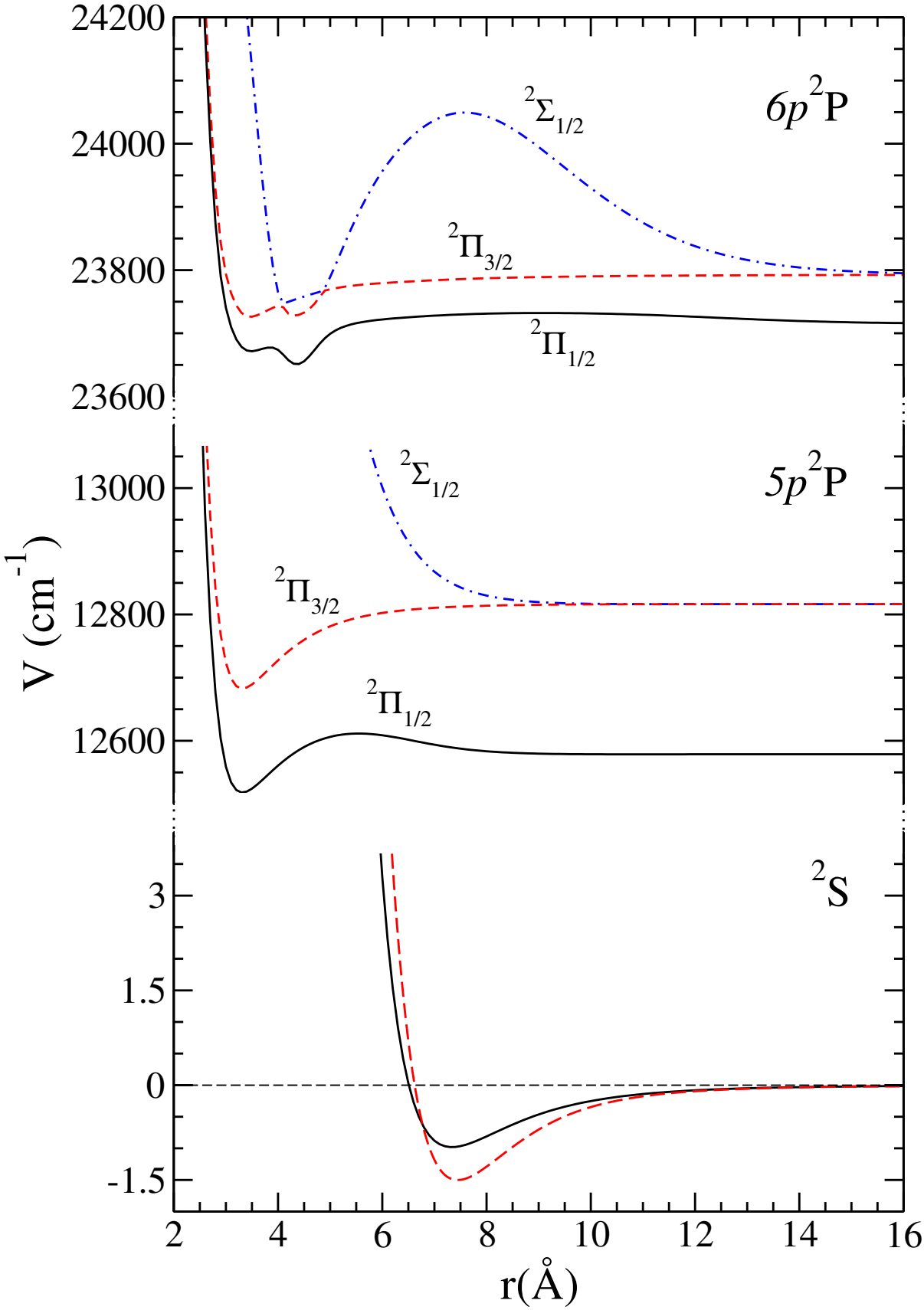

Figure 5.1: ^{2}S, 5p ^{2}P, and 6p ^{2}P Rb-He pair potentials used in this work. The splitting introduced by the spin-orbit interaction has been included. The ^{2}S He-Rb pair potential of Ref. [99] is also displayed (bottom dashed line).

PCCP

PAPER

View Article Online
View Journal | View Issue

Check for updates

Cite this: *Phys. Chem. Chem. Phys.*, 2018, **20**, 9309

Desorption dynamics of RbHe exciplexes off He nanodroplets induced by spin-relaxation†

François Coppens, ‡[a] Johannes von Vangerow,‡[b] Manuel Barranco,[acd] Nadine Halberstadt,[a] Frank Stienkemeier,[b] Martí Pi[cd] and Marcel Mudrich *[e]

Received 22nd January 2018,
Accepted 11th March 2018

DOI: 10.1039/c8cp00482j

rsc.li/pccp

Doped He nanodroplets are ideal model systems to study the dynamics of elementary photophysical processes in heterogeneous nanosystems. Here we present a combined experimental and theoretical investigation of the formation of free RbHe exciplex molecules from laser-excited Rb-doped He nanodroplets. Upon excitation of a droplet-bound Rb atom to the $5p_{3/2}{}^2\Pi_{3/2}$-state, a stable RbHe exciplex forms within about 20 ps. Only due to $^2\Pi_{3/2} \rightarrow {}^2\Pi_{1/2}$ spin-relaxation does the RbHe exciplex detach from the He droplet surface with a half life of about 700 ps, given by the spin-relaxation time and the coupling of spin and translational degrees of freedom.

Published on 12 March 2018. Downloaded by Universite Paul Sabatier on 09/04/2018 10:13:21.

1 Introduction

Understanding the photochemistry of condensed phase systems and surfaces is essential in many research areas, such as atmospheric sciences[1] and photocatalysis.[2] However, complex couplings between electronic and motional degrees of freedom of various subunits of the system often present a major challenge.[3–5] Moreover, the heterogeneity of multi-component solid or liquid systems and experimental difficulties in precisely preparing the sample and reproducing measurements tend to make it hard to unravel specific elementary reactions. In this respect, He nanodroplets doped with single atoms or well-defined complexes are ideal model systems for studying photodynamical processes in the condensed phase, both experimentally and theoretically. Due to their ultralow temperature (0.37 K) and their quantum fluid nature, He nanodroplets have a homogeneous density distribution and dopant particles aggregate into cold clusters mostly inside the droplets.[6,7] Only alkali metal atoms and small clusters are attached to He droplets in loosely bound dimple-like states at the droplet surface.[8–15]

While He nanodroplets are extremely inert and weakly-perturbing matrices for spectroscopy of embedded atoms and molecules in their electronic ground state, a rich photochemical dynamics is initiated upon photoexcitation or photoionization.[16,17] This includes electronic relaxation,[18–21] the ejection of the dopant out of the droplet,[22–29] and chemical reactions within the dopant complex[30–32] and even among the dopant and the surrounding He.[23,33–42]

As a general trend, electronically excited dopant atoms and small molecules tend to be ejected out of He droplets either as bare particles or with a few He atoms attached to them.[18,43–45] In particular, all atomic alkali species promptly desorb off the droplet surface, the only exceptions being Rb and Cs atoms in their lowest excited states.[46,47] The dynamics of the desorption process has recently been studied at an increasing level of detail,[19,24,26,48] including time-resolved experiments and simulations.[27,29] The focus has been on the competing processes of desorption of the dopant induced by laser excitation, and the dopant falling back into the He droplet upon photoionization. The latter occurred at short pump–probe delay times when the distance between the photoion and the droplet was short enough for ion–He attraction to be effective.

The aim of this work is to extend our joint experimental and theoretical study of the photodynamics of Rb-doped He nanodroplets to RbHe exciplexes.[26,29] The simultaneous effect of pair-wise Rb–He attraction and repulsion of Rb from the He droplet as a whole results in an intricate dynamics, and interpretations have remained somewhat ambiguous with respect to the exciplex formation mechanism and characteristic time scale, as well as the origin of free exciplexes detached from the He droplets.[19,29,33,34,36,37] In particular the role of relaxation of internal degrees of freedom of the RbHe exciplex in the desorption process has not been explicitly addressed.[49,50] Here, we discuss

[a] *Laboratoire des Collisions, Agrégats, Réactivité, IRSAMC, Université Toulouse 3- Paul Sabatier, CNRS UMR 5589, 118 route de Narbonne, F-31062 Toulouse Cedex 09, France*
[b] *Physikalisches Institut, Universität Freiburg, Hermann-Herder-Str. 3, 79104 Freiburg, Germany*
[c] *Institute of Nanoscience and Nanotechnology (IN2UB), Universitat de Barcelona, Diagonal 645, 08028 Barcelona, Spain*
[d] *Departament FQA, Facultat de Física, Universitat de Barcelona, Diagonal 645, 08028 Barcelona, Spain*
[e] *Department of Physics and Astronomy, Aarhus University, Ny Munkegade 120, Aarhus 8000 C, Denmark. E-mail: mudrich@phys.au.dk*

† Electronic supplementary information (ESI) available. See DOI: 10.1039/c8cp00482j

‡ F. Coppens and J. von Vangerow contributed equally to this work.

View Article Online
Paper PCCP

Published on 12 March 2018. Downloaded by Universite Paul Sabatier on 09/04/2018 10:13:21.

in detail the interplay of the RbHe formation dynamics, the RbHe desorption off the He droplet surface, and the fall-back of $[RbHe]^+$ created by photoionization in femtosecond pump–probe experiments.[27,29,34] We find that electronic spin-relaxation is the main process driving the desorption of RbHe off the He droplet.

This paper is accompanied by animations showing the real-time dynamics of the Rb–He droplet complex for several excited states and for the scenario of time-delayed spin-relaxation. These animations are presented in the ESI,† S1–S4.

2 Methods

2.1 Theoretical approach

During the last decade, the density functional theory (DFT) approach has emerged as an accurate and flexible tool to describe the statics and dynamics of doped helium droplets. The DFT activity carried out in this field has been summarized in two reviews.[10,17] In the following we give the basic details on how the method has been applied to the present problem, and refer the reader to ref. 17 and 25 for the details.

In this work, we describe the interaction of a Rb atom with a He droplet composed of $N = 1000$ He atoms. Due to its large mass, Rb is treated as an external field in the statics, and as a classical particle in the dynamics. The impurity-droplet interaction is described in a pairwise approximation, and the ground state of the droplet-impurity system is found by solving the Euler–Lagrange equation

$$\left\{-\frac{\hbar^2}{2m}\nabla^2 + \frac{\delta\mathscr{E}_c}{\delta\rho} + V_X(|\mathbf{r}-\mathbf{r}_I|)\right\}\Psi_0(\mathbf{r}) = \mu\Psi_0(\mathbf{r}), \qquad (1)$$

where $\Psi_0(\mathbf{r}) = \sqrt{\rho(\mathbf{r})}$ is the He effective wave function, with $\rho(\mathbf{r})$ being the atom density; μ is the He chemical potential, and V_X is the Rb–He pair potential.[51] The correlation energy density functional $\mathscr{E}_c$ has been taken from ref. 52. The results presented in this work are obtained using the ^{4}He-DFT BCN-TLS computing package.[53] We work in Cartesian coordinates using a space step of 0.4 Å. In the dynamics calculations we use a time step of 0.5 fs.

Once the droplet-equilibrium configuration, shown in Fig. 1(b), is determined, the 5p ← 5s absorption spectrum is obtained using the DF sampling method.[54] To this end, the diatomics-in-molecules (DIM) model is used for the droplet-Rb interaction in the excited $5p^2P$ state.[55,56] The $5p^2\Sigma$ and $5p^2\Pi$ Rb–He pair potentials, shown in Fig. 1(a), are taken from ref. 51 and 52. The resulting simulated absorption dipole spectrum of the $RbHe_{1000}$ complex, shown in Fig. 6 of ref. 17, is in good agreement with the experiment and previous calculations.[34,57]

Fig. 1(c)–(e) show the direction-dependent potentials (spin–orbit term included) which, within the DIM approach, enter the dynamics simulations of Rb in the $5p^2P$-correlated states. In the course of the time evolution of the system, the He atoms have a natural tendency to adapt to these potential surfaces, either going away if the potential is mostly repulsive as in the $^2\Sigma_{1/2}$-state [Fig. 1(d)], or to evolve to a bound RbHe exciplex configuration in the $^2\Pi_{3/2}$-state [(e)] featuring local minima at ($r = 0$, $z = \pm 3.5$ Å).

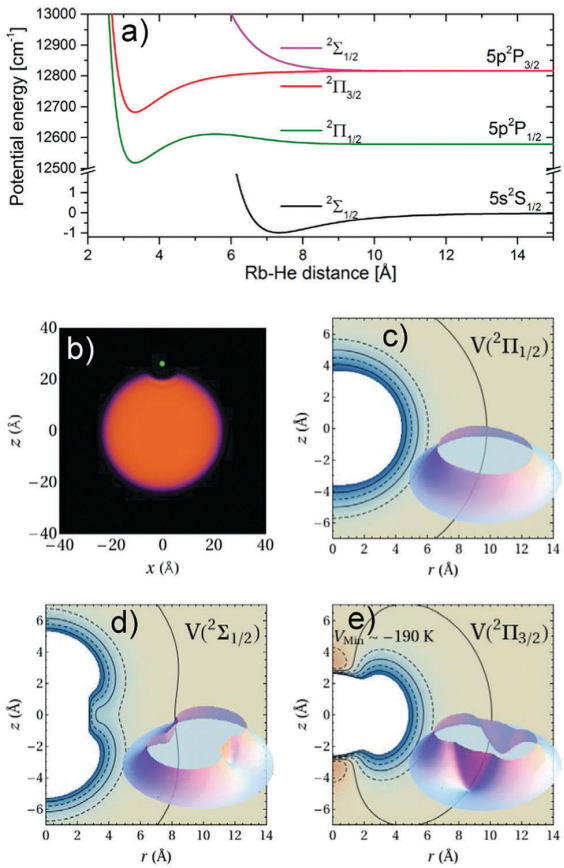

Fig. 1 (a) Rb–He pair potentials used in this work.[51] The potentials correlating to the Rb excited $5p^2P$-state are split due to spin–orbit coupling. (b) Equilibrium dimple configuration of Rb in the ground state in the x–z-plane (represented by a green dot). Panels (c)–(e) display the two-dimensional Rb–He potential surfaces in cylindrical coordinates (r, z) corresponding to this configuration, with the Rb atom located at the origin. Regions where the potentials are attractive (repulsive) are represented in pink (blue). The outermost equidensity line corresponds to zero potential. Notice that in panel (e) the $5p^2\Pi_{3/2}$ potential presents two deep minima of about 190 K on the z-axis. The $5p^2\Pi_{1/2}$ and $5p^2\Sigma_{1/2}$ potentials [(c) and (d)] have shallow attractive minima of about 1 K depth at a distance of ∼10 Å, not represented in the figure. Reprinted from *Int. Rev. Phys. Chem.*, 2017, **36**, 621–707 with permission from Taylor & Francis Ltd, http://www.tandfonline.com.

In the $^2\Pi_{1/2}$-state [(c)], one may also expect the formation of RbHe exciplexes given the potential minimum in the RbHe pair potential around 3.2 Å [(a)]. However, RbHe formation is hampered by a potential barrier which cannot be overcome at the low temperature of the He droplet.[34,58]

2.2 Experimental setup

The setup used for the present experiments has been described previously.[26,27] Briefly, a beam of He droplets with an average diameter of 10 nm is produced by continuously expanding pressurized He (50 bar) out of a cold nozzle (diameter 5 μm, temperature 17 K). The He droplets are doped with one Rb atom

 This journal is © the Owner Societies 2018

Published on 12 March 2018. Downloaded by Universite Paul Sabatier on 09/04/2018 10:13:21.

on average by pickup of Rb atoms inside a heated vapor cell (length 1 cm, temperature 85 °C).

An amplified Ti:Sa laser system generates pulses of 100 fs duration at a repetition rate of 5 kHz. The center wavelength is tunable in the near infrared (NIR) region. The FWHM of the spectral laser profile is 140 cm^{-1}. Light in the visible range (VIS) is generated by frequency doubling. The pulses are split and separated in time in a Mach–Zehnder type interferometer. The droplet-perturbed Rb 5p states are probed by a two-color NIR + VIS pump–probe resonant photoionization scheme. The NIR pulses are strongly attenuated to avoid the excitation of higher lying states by multi-photon processes. The polarizations of the two laser pulses are parallel to one another and parallel to the detector surface.

Photoions and photoelectrons are detected by a velocity-map imaging (VMI) spectrometer operated in single-particle detection mode.[19,26,59,60] Mass-selected ion VMIs are recorded by time-gating the imaging detector at the specific flight times of either Rb^+ or $RbHe^+$ ions. One VMI is recorded for each value of the pump–probe delay time. Both Rb^+ ion images and electron images contain background contributions from resonant ionization of free Rb atoms effusing out of the doping cell. In order to efficiently subtract these contributions, background images are recorded at each pump–probe delay using a chopper that periodically interrupts the He droplet beam at a frequency of 15 Hz. The acquired background and signal + background images are inverse Abel transformed to infer the full three-dimensional velocity distributions.[61,62] The resulting spectra obtained from angular integration are normalized to the number of counts and subtracted from each other, where we exploit the additivity of the inverse Abel transformation.[63]

3 Time-resolved imaging spectroscopy

Typical experimental total electron and $[RbHe]^+$ ion VMIs recorded at a center wavelength of the pump laser pulse λ = 776 nm (12 887 cm^{-1}) and a pump–probe delay of 2 ns are shown in Fig. 2(a) and (c), respectively. The corresponding electron binding energy distribution and ion speed distribution inferred from these images are presented in Fig. 2(b) and (d), respectively. In addition, Fig. 2(b) contains photoelectron spectra measured at λ = 773 (12 937 cm^{-1}) and at λ = 794 nm (12 594 cm^{-1}). Note that the photoelectron spectra in Fig. 2(b) are rescaled in terms of electron binding energies $E_b = h\nu_2 - T_e$, where $h\nu_2 = 2hc/\lambda$ denotes the photon energy of the ionizing laser pulse and T_e is the measured electron kinetic energy. The dashed vertical lines represent E_b for free Rb atoms in their $5p^2P_{1/2}$ and $5p^2P_{3/2}$-states.

3.1 Photoion imaging

The $[RbHe]^+$ ion distribution [Fig. 2(c)] is a round spot with a flat intensity distribution and a slight elongation in x-direction (perpendicular to the laser polarization). The corresponding speed distribution [Fig. 2(d)] is broad and nearly symmetric. The black line depicts a skewed Gaussian distribution fitted to

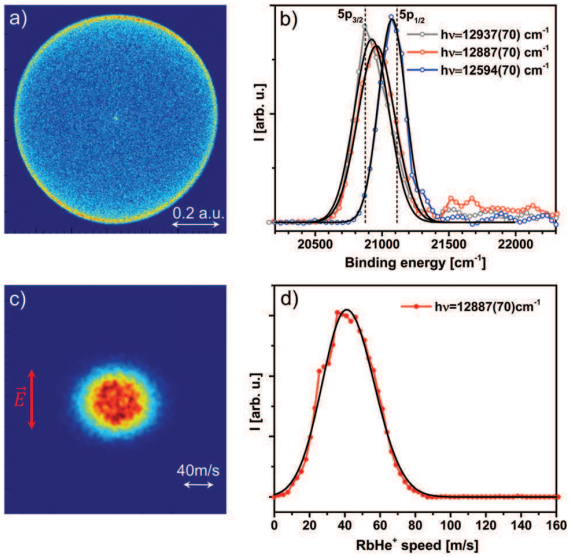

Fig. 2 Raw velocity-map images of photoelectrons (a) and of $[RbHe]^+$ photoions (c) recorded at λ = 776 nm (12 887 cm^{-1}) for a long pump–probe delay time of 2 ns. The red vertical arrow indicates the laser polarization. (b) Electron binding energy spectra inferred from the image shown in (a), from an image recorded at λ = 773 nm (12 937 cm^{-1}), and from an image at λ = 794 nm (12 594 cm^{-1}). (d) $[RbHe]^+$ photoion speed distribution inferred from (c).

the data.[64] This fit is applied repeatedly to each speed distribution measured at various pump–probe delays in order to trace the evolution of the most probable kinetic energy, see Fig. 3(a) and (b). The yields of ions, shown in Fig. 3(c) and (d), are obtained by summing over ion counts contained in each image. Blue and red symbols show the results for Rb^+ and $[RbHe]^+$ ions, respectively. Both kinetic energies and ion yields monotonously increase within 50–500 ps, with a slight overshoot at λ = 773 nm (12 937 cm^{-1}) [Fig. 3(a)]. This increase results from the competing processes of desorption of the excited neutral Rb and RbHe species, and falling back of the Rb^+ and $[RbHe]^+$ photoions into the He droplet due to attractive Rb^+–He interactions, as discussed in ref. 27 and 29. By comparing the experimental data with TD-DFT simulations, we concluded that the 5p-correlated states of Rb and RbHe desorb off He droplets not purely impulsively, but in a more complex evaporation-like process.[29] The overshoot of speeds in Fig. 3(a) is likely due to weak long-range attractive forces acting between the desorbing Rb and RbHe and the He droplet surface, which slightly slow down the relative motion in the later stage of desorption.

The data in Fig. 3(a) are measured at λ = 773 nm (12 937 cm^{-1}), which corresponds to the excitation of the RbHe complex into the $5p^2\Sigma_{1/2}$-state, with some contribution of the $5p^2\Pi_{3/2}$-state due to overlapping absorption bands and due to the broad spectral profile of the laser.[9,34,65] The $5p^2\Sigma_{1/2}$-state is the most repulsive one out of the three states studied here. Accordingly, the asymptotic most probable speed of Rb^+ reached at long delays is comparatively high, $\hat{v}$ = 85 m s^{-1}, corresponding to a kinetic energy of 8 cm^{-1}, whereas for $[RbHe]^+$ we find $\hat{v}$ = 40 m s^{-1} (5.8 cm^{-1}).

View Article Online
Paper PCCP

Published on 12 March 2018. Downloaded by Universite Paul Sabatier on 09/04/2018 10:13:21.

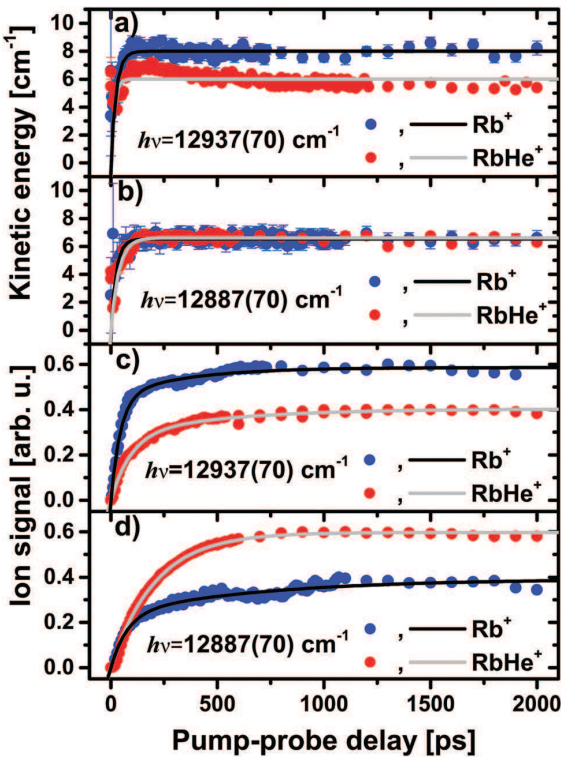

Fig. 3 Rb^+ and $[RbHe]^+$ ion kinetic energies [(a) and (b)] and signal yields [(c) and (d)] recorded at laser wavelengths λ = 773 nm [12 937 cm^{-1}, (a) and (c)] and λ = 776 nm [12 887 cm^{-1}, (b) and (d)]. The smooth gray and black lines are fit curves (see text for details).

Since the diatomic $5p^2\Sigma_{1/2}$ RbHe potential is purely repulsive [Fig. 1(a)], this component of the excited population results in the desorption of neat Rb atoms. Accordingly, the yield of detected Rb^+ ions exceeds that of $[RbHe]^+$ ions by about a factor 1.5.

At λ = 776 nm (12 887 cm^{-1}), a higher contribution of the $5p^2\Pi_{3/2}$-state is excited, which efficiently forms RbHe exciplexes.[34] Thus, the yield of $[RbHe]^+$ ions is higher than that of Rb^+ by a factor 1.5. The Rb^+ and $[RbHe]^+$ asymptotic most probable speed is $\hat{v}$ = 42 m s^{-1} (6.3 cm^{-1}), close to that of $[RbHe]^+$ at λ = 773 nm (12 937 cm^{-1}). At λ = 794 nm (12 594 cm^{-1}), the $5p^2\Pi_{1/2}$-state of the Rb–He droplet complex is excited (not shown), and no $[RbHe]^+$ ions are detected. Therefore we have recorded only Rb^+ ion images at that wavelength.[29] Here, the Rb^+ asymptotic most probable speed is lowest, $\hat{v}$ = 38 m s^{-1} (5.1 cm^{-1}), because dopant-He repulsion is weak.

The transient kinetic energies measured at all laser wavelengths rise within a delay time of about 50 ps. The characteristic energy rise time (to half value), τ_E^i, and the asymptotic ion kinetic energy E_∞^I, are determined by fitting the data with an exponential function

$$E^I(t) = E_\infty^I \cdot (1 - \exp[-\ln 2 \cdot t/\tau_E^i]). \quad (2)$$

The resulting fit parameters are summarized in Table 1.

The ion yields increase with pump–probe delay slightly more slowly than the ion kinetic energies, whereas the Rb^+ ion signal rises faster than the $[RbHe]^+$ ion signal at short delays. The initial fast rise of the Rb^+ ion yield flattens out at delays around 100 ps and continues to rise slightly up to about 2 ns. The $[RbHe]^+$ ion yields show a similar initial fast rise followed by a more pronounced slow increase that levels off somewhat earlier. Therefore, for fitting the Rb^+ and $[RbHe]^+$ ion yield data we use a biexponential function,

$$I(t) = A_1^i \cdot (1 - \exp[-\ln 2 \cdot t/\tau_1^i]) + A_2^i \cdot (1 - \exp[-\ln 2 \cdot t/\tau_2^i]), \quad (3)$$

where (A_1^i, τ_1^i) and (A_2^i, τ_2^i) parametrize the fast and the slow signal rise, respectively.

While neither the Rb^+ and $[RbHe]^+$ asymptotic energies E_∞^I, nor the energy rise times τ_E^i depend much on λ, the rise times of ion yields of $RbHe^+$, τ_1^i, clearly decrease monotonically with decreasing λ (increasing photon energy) by a factor 6, ranging from 186 ps at λ = 780 nm (12 821 cm^{-1}) to 32 ps at λ = 773 nm (12 937 cm^{-1}). The trend that the dynamics proceeds faster with decreasing λ (increasing photon energy) is partly due to the increasingly repulsive dopant-He interaction and agrees with our previous findings.[27,29] However, the observation that the ion yields rise more slowly than the ion kinetic energies cannot be understood with the concept of impulsive desorption and fall-back. In that model, ion kinetic energies should be affected by ion-He attraction up to long delay times exceeding the fall-back time. Note that in previous experiments on the Rb 6p-state, where desorption proceeded impulsively, ion energies indeed increased more slowly than ion yields.[29] Therefore we take our current finding (τ_1^i, $\tau_2^i > \tau_E^i$) as a further indication for a non-impulsive, evaporation-like desorption mechanism.

Furthermore, from our analysis of the VMIs we obtain information about the anisotropy of the ion angular distribution, characterized by the anisotropy parameter β.[66] For $[RbHe]^+$ at

Table 1 Time constants and energies inferred from pump–probe measurements of Rb^+ and $[RbHe]^+$ ion yields at the $5p^2\Sigma_{1/2}$ and $5p^2\Pi_{3/2}$-states of the Rb–He droplet complex, obtained from fits with eqn (2) and (3), see Fig. 3

λ [nm]	State	Ion	E_∞^I [cm^{-1}]	τ_E^i [ps]	A_1^i	τ_1^i [ps]	A_2^i	τ_2^i [ps]	β
773	$^2\Sigma_{1/2}/^2\Pi_{3/2}$	Rb^+	8.0(1)	17(1)	0.45(2)	32(1)	0.14(2)	234(33)	0.17(1)
		$[RbHe]^+$	6.0(1)	10(2)	0.17(2)	41(6)	0.22(2)	178(17)	0.13(1)
776	$^2\Pi_{3/2}/^2\Sigma_{1/2}$	Rb^+	6.5(3)	17(1)	0.24(2)	53(5)	0.16(2)	490(104)	−0.16(1)
		$[RbHe]^+$	6.6(3)	26(1)	0.60(1)	143(2)	0.00(1)	—	−0.39(1)
780	$^2\Pi_{3/2}$	$[RbHe]^+$	6.3(1)	24(2)	0.95(1)	186(1)	0.00(1)	—	0.35(1)

 This journal is © the Owner Societies 2018

Published on 12 March 2018. Downloaded by Universite Paul Sabatier on 09/04/2018 10:13:21.

long delay times we find $\beta = -0.39(1)$ when a higher contribution of the $^2\Pi_{3/2}$-state is excited at $\lambda = 776$ nm (12 887 cm^{-1}). At $\lambda = 773$ nm (mainly $^2\Sigma_{1/2}$-excitation), the anisotropy becomes slightly positive, $\beta = 0.13(1)$. The corresponding values for the Rb^+ ion distributions are $\beta = -0.16(1)$ and $\beta = 0.17(1)$, respectively. While the signs of the β-values are in accordance with the symmetries of the pseudo-diatomic states (ideal perpendicular $^2\Sigma \rightarrow {}^2\Pi$-transition in a diatomic implies $\beta = -1$, parallel $^2\Sigma \rightarrow {}^2\Sigma$-transition implies $\beta = 2$), the absolute values are much smaller. On the one hand, this is due to the mixing of excited $^2\Sigma_{1/2}$ and $^2\Pi_{3/2}$-states. On the other hand, the desorption process is more complex than direct dissociation of a diatomic molecule. We recall that the β-values came much closer to the ideal values in the case of excitation of Rb to the high-lying 6p-correlated states, where desorption proceeded more impulsively.[19,26,29]

We mention that in earlier pump–probe experiments, significantly different Rb^+ and $[RbHe]^+$ ion yield curves were measured.[36] However, in those experiments, NIR light emitted directly from a mode-locked titanium:sapphire laser was used at a pulse repetition rate of 80 MHz. Therefore, a large fraction of the ion signals actually stemmed from Rb and RbHe that had been desorbed off the droplets by preceding pulse pairs. Thus, the observed pump–probe transients may have reflected the internal dynamics of free RbHe instead of the dynamics of the Rb–He droplet interaction. Besides, near-resonant two-photon excitation of higher lying states correlating to the Rb 5d-level were probably involved in the observed dynamics. This raises some doubts as to the conclusions of those previous experiments in terms of exciplex formation times.[29,36] Further studies are needed to clarify this issue.

From the overall resemblance of the $[RbHe]^+$ and Rb^+ kinetic energy curves and ion yields in the present study one is tempted to conclude that RbHe exciplex formation is fast and desorption of RbHe off the He droplet surface proceeds essentially in the same way as for neat Rb atoms. However, the more pronounced biexponential rise of $[RbHe]^+$ ion yields, as well as complementary delay-dependent photoelectron measurements, and numerical simulations presented in the following sections will show that the desorption dynamics of RbHe exciplexes actually is more intricate than that of Rb atoms.

3.2 Photoelectron imaging

The photoelectron spectra recorded at the three characteristic laser wavelengths λ [Fig. 2(b)] exhibit pronounced peaks around the Rb $5p_{1/2}$ and $5p_{3/2}$ atomic binding energies, $E_{5p_{1/2}}$ and $E_{5p_{3/2}}$, respectively. Both the peak position and the peak width significantly vary with λ, as inferred from fits to the data with a Gaussian function, depicted as smooth lines. The resulting peak positions relative to $E_{5p_{1/2}}$ and $E_{5p_{3/2}}$ are plotted in Fig. 4(a) and (b), respectively. Fig. 4(c) shows the Gaussian peak widths σ. For reference, the open symbols represent the peak positions measured for the Rb atomic background. The scatter of data points around the literature value (grey horizontal line) indicates the level of precision of our measurements.

The excess energies for the $5p^2\Sigma_{1/2}$ and $5p^2\Pi_{3/2}$-states, $E_b - E_{5p_{1/2},5p_{3/2}}$ shown in Fig. 4(b), exhibit a fast decay (E_1^e, τ_1^e)

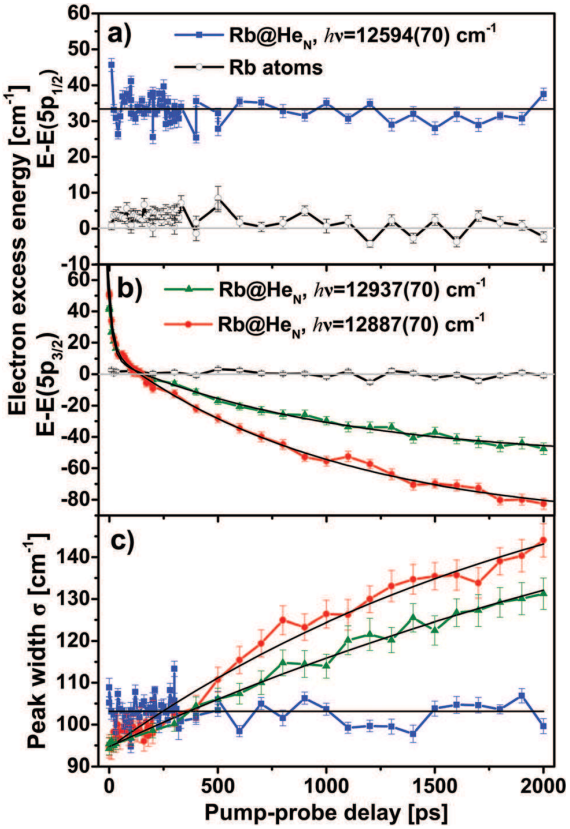

Fig. 4 Photoelectron energies as a function of pump–probe delay (filled circles) recorded at laser wavelengths $\lambda = 794$ nm (12 594 cm^{-1}, $5p^2\Pi_{1/2}$) (a), $\lambda = 773$ nm (12 937 cm^{-1}, $5p^2\Sigma_{1/2}$), and $\lambda = 776$ nm (12 887 cm^{-1}, $5p^2\Pi_{3/2}$) (b). Open circles indicate the electron energies measured for atomic Rb background signal. The widths of electron distributions are depicted in (c).

above and a slow decay (E_2^e, τ_2^e) below $E_{5p_{3/2}}$ (horizontal line at $y = 0$). Therefore, these data are fitted with a biexponential decay function

$$E^e(t) = E_1^e \cdot \exp(-\ln 2 \cdot t/\tau_1^e) + E_2^e \cdot \exp(-\ln 2 \cdot t/\tau_2^e) + E_\infty^e. \quad (4)$$

Here, E_∞^e denotes the asymptotic energy value at long delay times. When exciting the $5p^2\Pi_{1/2}$-state at $\lambda = 794$ nm (12 594 cm^{-1}), the transient droplet correlated peak position remains constant within the experimental scatter. Therefore, merely the mean value E_1^e is determined. The resulting energies and time constants are summarized in Table 2. The increasing peak widths in the cases of $\lambda = 773$ (12 937 cm^{-1}) and 776 nm (12 887 cm^{-1}) are fitted by the simple exponential function given by eqn (2).

The fact that the droplet-related photoelectron energy E_1^e for the $^2\Pi_{1/2}$-state is constant but shifted with respect to the atomic value indicates that most of the Rb atoms remain attached to the droplet surface upon electronic excitation, in accordance with previous studies.[46,67] Thus, the slowly rising Rb^+-ion signal measured at that wavelength, indicative for excited Rb desorption, reflects only a small fraction of Rb atoms, most of which actually remain bound to the droplets. The measured up-shift of

View Article Online
Paper PCCP

Published on 12 March 2018. Downloaded by Universite Paul Sabatier on 09/04/2018 10:13:21.

Table 2 Time constants and energies inferred from fits of eqn (4) to the transient photoelectron energies (Fig. 4)

λ [nm]	State	E_1^e [cm^{-1}]	τ_1^e [ps]	E_2^e [cm^{-1}]	τ_2^e [ps]	E_∞^e [cm^{-1}]
773	$^2\Sigma_{1/2}/^2\Pi_{3/2}$	32(2)	15(2)	63(4)	683(130)	−53(5)
776	$^2\Pi_{3/2}/^2\Sigma_{1/2}$	36(2)	13(2)	110(4)	709(70)	−96(5)
794	$^2\Pi_{1/2}$	33(2)	—	—	—	—

electron energy of E_1^e = 33(2) cm^{-1} is attributed to a lowering of the ionization threshold induced by the He environment. This value is in reasonable agreement with previous measurements, where the ionization threshold was found to be lowered by 50(10) cm^{-1} at comparable conditions.[67]

The similar dynamics of electron energies and ion yields for the $^2\Sigma_{1/2}$ and $^2\Pi_{3/2}$-states, a biexponential evolution with a fast component (tens of ps) and a slow component (hundreds of ps), are taken as a confirmation that two distinct relaxation processes occur simultaneously. The fast process – prompt desorption of excited Rb off the He droplet – is associated mainly with the $^2\Sigma_{1/2}$-component of the excited state, whereas the $^2\Pi_{3/2}$-component undergoes slow relaxation. The latter will be discussed in the following sections. Deviations of the time constants τ_1^i *vs.* τ_1^e, and τ_2^i *vs.* τ_2^e, are mainly due to the different nature of the observables. Both ion yields and speeds are affected by the dynamics occurring after the probe-ionization, whereas electron spectra probe the electronic state (affected by the He configuration around the Rb) at the moment of ionization. In particular, ion signals provide information only about that fraction of ions that eventually detach from the He droplets, whereas electron signals are measured for all photoionization events, including those where the ion falls back into the droplet; in this respect the electron spectra are the better probes of the full dynamics, with the restriction that we cannot distinguish between the final products (Rb, RbHe, and Rb attached to a He droplet).

We mention that at λ = 776 nm (12 887 cm^{-1}, $^2\Pi_{3/2}$-state), an extended low intensity distribution is present in the spectrum of Fig. 2(b) at higher electron binding energies $\geq$21 500 cm^{-1} (lower electron kinetic energies). We attribute this component to elastic scattering of photoelectrons with He atoms as they propagate through the He droplet. Low-energy features in photoelectron spectra due to electron-He scattering have been observed before, in particular when using one-photon ionization.[68–71] The fact that this feature is most pronounced for the $^2\Pi_{3/2}$-excitation may be related to the more abundant formation of RbHe exciplexes which enhances the electron-He scattering probability.

4 TD-DFT dynamics simulation

Time-dependent density functional theory (TD-DFT) simulations are carried out as thoroughly described in ref. 17 and 25. Starting with the Rb-droplet equilibrium configuration, the dynamics is initiated by a "vertical DFT transition" into the excited state. This is realized by suddenly switching from the potential energy surface of the Rb–He droplet ground state to that of the Rb–He excited state. The subsequent evolution of the system can be followed in real-time, as illustrated by the series of snapshots of the He density distribution (red area) and the position of the Rb atom (green and magenta dots) in Fig. 5. The animated version of this evolution is shown in the Video S4 in the ESI.† Here, excitation of the 5p$^2\Pi_{3/2}$-state at t = 0 is followed by relaxation to the 5p$^2\Pi_{1/2}$-state at t = 60 ps. This time has been chosen rather arbitrarily; the only constraint is that it should be long enough to allow the exciplex around the 5p$^2\Pi_{3/2}$-state to fully develop, see Fig. 7 below.

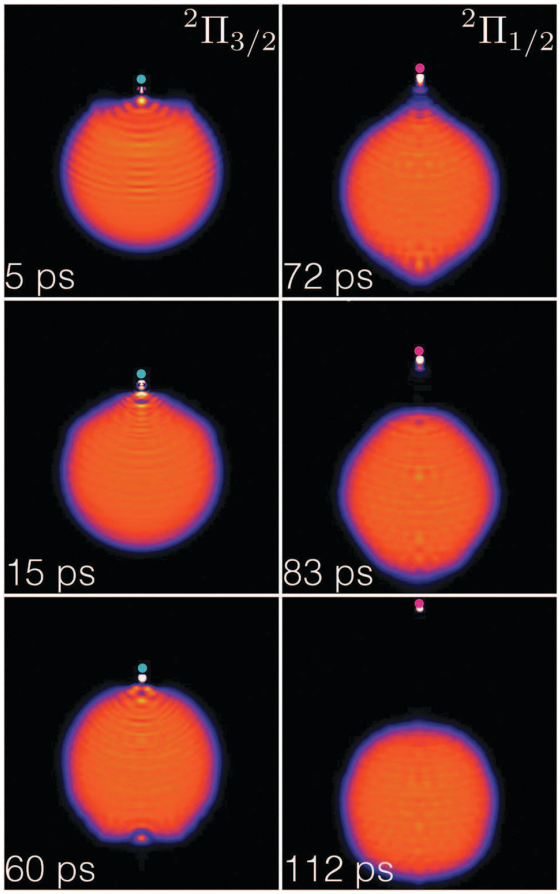

Fig. 5 Snapshots of the He density during the evolution of the excited $RbHe_{1000}$ complex for η = 15%, Δt = 60 ps. The green dot represents the Rb atom excited into the 5p$^2\Pi_{3/2}$-state; the magenta dot is the Rb atom after suddenly relaxing to the 5p$^2\Pi_{1/2}$-state. The white spot accompanying the green or magenta dot representing the Rb atom depicts the He density carried away with it.

4.1 Direct ejection of bare Rb atoms from the $^2\Sigma_{1/2}$ and $^2\Pi_{1/2}$-states

From the results of the simulation we now derive the relevant quantities to compare with the experimental data, such as the kinetic energy of the Rb atom relative to the droplet, the occurrence of He density attached to Rb which we identify with the formation of an exciplex, and the transient interaction energy of the neutral and ionized Rb atom with the surrounding He. The latter is related to the

 This journal is © the Owner Societies 2018

Published on 12 March 2018. Downloaded by Universite Paul Sabatier on 09/04/2018 10:13:21.

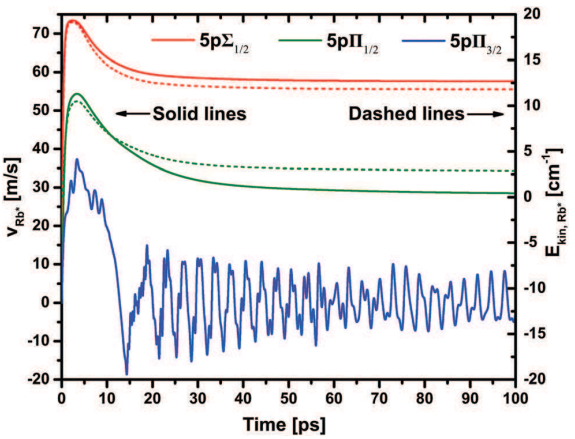

Fig. 6 Velocity (solid lines, left scale) and kinetic energy (dashed lines, right scale) of the Rb atom excited to the 5p-state as a function of time. The kinetic energy of the $5p^2\Pi_{3/2}$-state is not given as this state remains bound to the droplet.

kinetic energy of a photoelectron created in a time-delayed photoionization process.

Fig. 6 collects our results for the dynamics of the Rb atom excited to the droplet-perturbed states correlating to the atomic 5p-state. For the $^2\Sigma_{1/2}$ and $^2\Pi_{1/2}$-states, the velocities (dashed lines) and kinetic energies (solid lines) feature a rapid increase to reach a maximum at time t = 2–5 ps after excitation, followed by a drop due to droplet-impurity long-range attractive forces acting on the desorbing Rb atom. The asymptotic values are reached for $t > 50$ ps. When exciting the $^2\Pi_{3/2}$-state, the Rb-velocity features a damped oscillation around zero indicating that the Rb atom remains bound to the He droplet surface. The following conclusions can be drawn from these results:

(i) Rb excited to the $5p^2\Sigma_{1/2}$-state detaches from the droplet reaching an asymptotic kinetic energy of 13 cm^{-1}. This value deviates from the experimental one (8.0 cm^{-1}) due to contributions of $^2\Pi_{3/2}$-excitation to the experimental signal. Despite the shallow local minima in the corresponding Rb–He droplet potential surface [Fig. 1(c)], no binding of He density to the departing Rb atom occurs. This finding is in accordance with experiments,[19,34,36] where mostly free Rb atoms were detected following excitation at wavelengths $\lambda < 774$ nm ($>$12 920 cm^{-1}). The full evolution of the excited Rb–He nanodroplet complex is shown in the Video S1 in the ESI.†

(ii) Rb excited to the $5p^2\Pi_{1/2}$-state also detaches from the He droplet, but the asymptotic kinetic energy is much lower, 2.8 cm^{-1}. For this case, the evolution is shown in the Video S2 in the ESI.† This value of the Rb kinetic energy again deviates from the experimental one (5.1 cm^{-1}), but the trend that desorption of the less repulsive $^2\Pi_{1/2}$-state yields a lower energy than for the $^2\Sigma_{1/2}$-state is well reproduced. The potential well at short distance $\sim$3.2 Å would in principle support a stable RbHe exciplex (Fig. 1). However, at the low temperature of the He droplet, exciplex formation is hindered by a potential barrier located at $\sim$5 Å, between the well and the range where the $5p^2\Pi_{1/2}$-state is populated by excitation from the $5s^2\Sigma_{1/2}$-ground state (7 Å).[33,34,58]

We recall that in previous experiments using narrow-band excitation of the low energy edge of the $^2\Pi_{1/2}$-resonance, it was observed that Rb and Cs dopants remained attached to the He droplet surface.[46] However, our simulations correspond to the excitation at the peak of the resonance, where free Rb atoms are also observed in the experiment. Thus, our simulations are not in conflict with the experimental findings. Note that Quantum Monte Carlo (QMC) calculations carried out for this state[72] yielded a weakly bound Rb in a shallow dimple. Had we carried out a static DFT relaxation, we would also have found a bound structure, due to the shallow minimum on the Rb–He droplet potential surface. However, in the dynamical TD-DFT simulation this minimum is too shallow to retain the departing Rb atom.

(iii) In our simulation we find that Rb excited to the $5p^2\Pi_{3/2}$-state remains bound to the He droplet surface where it forms a RbHe exciplex (see Video S3 in the ESI†). Fig. 1e shows two deep barrierless potential wells at a Rb–He distance of about 3.5 Å. In the course of the dynamics, the Rb atom is drawn to the well close to the droplet surface, develops a RbHe exciplex that remains bound to it, and oscillates around an equilibrium position of $\sim$3 Å above the static equilibrium position at the dimple as shown in Fig. 6. This result is in full agreement with static QMC calculations by Leino *et al.*[49] Note that our simulations do not provide any indication that the vibrational motion of the RbHe exciplex structure leads to its desorption from the He droplet.

The dynamics of the exciplex formation process can be quantitatively represented by integrating over the He density within a spherical inclusion volume with radius r_{incl} around Rb. The result is shown in Fig. 7. Thus, for r_{incl} = 5.7 Å, which contains the entire localized He density at the Rb atom without including He density of the remaining droplet, we find a rise to 75% of the final value at t = 20 ps. For $t > 60$ ps the He number

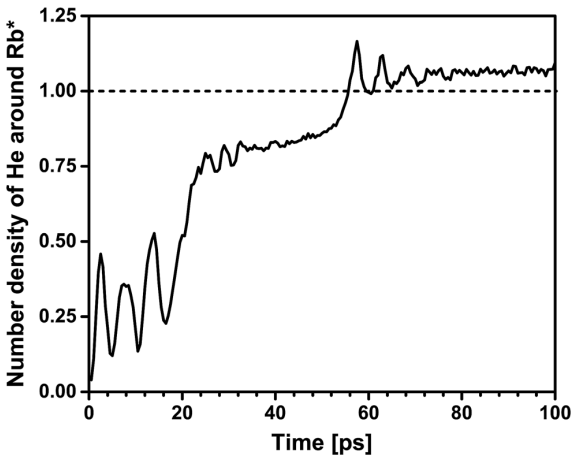

Fig. 7 Simulated time evolution of the integrated He density within an inclusion volume of radius r_{incl} = 5.7 Å around the Rb atom excited to the $5p^2\Pi_{3/2}$-state.

Published on 12 March 2018. Downloaded by Universite Paul Sabatier on 09/04/2018 10:13:21.

density stabilizes close to 1, indicating the full evolution of a RbHe exciplex containing 1 He atom. This result is in good agreement with the formation time estimated using the tunneling model by Reho *et al.*[33] using model parameters inferred from the previous fs–ps pump–probe measurements (42 ps).[50]

The finding that the RbHe exciplex remains attached to the He droplet is in apparent contradiction to experiments where the ejection of free Rb and RbHe was clearly observed.[19,34,36] Therefore, an additional mechanism must be active that induces the desorption of the RbHe molecule off the He droplet surface.

4.2 RbHe exciplex formation around the $5p^2\Pi_{1/2}$-state: non-radiative relaxation from the $5p^2\Pi_{3/2}$-state

In the gas phase, a RbHe exciplex can form in the $5p^2\Pi_{1/2}$-state if enough kinetic energy is provided by collisions such that the Rb can overcome the potential barrier.[58] Alternatively, collisions of a RbHe formed in the $5p^2\Pi_{3/2}$-state with another atom or complex might induce relaxation into a RbHe electronic state correlating to the Rb $5p^2P_{1/2}$-state. In this case the barrier is circumvented by the relaxation process, as the potential wells for the two states $^2\Pi_{3/2}$ and $^2\Pi_{1/2}$ are at similar Rb–He distances. In the condensed (droplet) phase at 0.4 K temperature, none of these mechanisms are active to explain the formation of RbHe $5p^2\Pi_{1/2}$ exciplexes and their potential ejection.

However, Fig. 1(a) indicates another possible mechanism: non-radiative de-excitation from the $5p^2\Pi_{3/2}$ to the $5p^2\Pi_{1/2}$-state accompanied by transfer of energy into the relative motion of the Rb atom with respect to the He droplet. Notice from the figure that the minimum of the $5p^2\Pi_{3/2}$-potential is at $\sim$12 683 cm^{-1}, and that of the $5p^2\Pi_{1/2}$-potential is at $\sim$12 518 cm^{-1}; the value of this potential at the barrier is 12 611 cm^{-1}. Thus, non-radiative de-excitation of the Rb atom may add to its original kinetic energy a fraction of this 165 cm^{-1} energy difference. Consequently, the RbHe exciplex will be ejected in the $5p^2\Pi_{1/2}$-state, and not in the $5p^2\Pi_{3/2}$-state that was originally photo-excited. Non-radiative electronic relaxation induced by the He droplet has been observed for a number of metal atoms.[18–21,41,44,73] In particular, previous measurements of the dispersed fluorescence emitted upon excitation of Rb into the $5p^2\Pi_{3/2}$-state of the Rb–He droplet complex have evidenced large populations of free Rb atoms in the $5p^2\Pi_{1/2}$-state.[34] Efficient spin-relaxation of $5p^2\Pi_{3/2}$-excited Rb atoms can be rationalized by the large cross section for mixing of fine structure states in collisions of alkali metal atoms with He.[74] For low-temperature Rb–He collisions, the fine structure relaxation rate was found to be enhanced by the transient formation of a RbHe exciplex by orders of magnitude compared to binary Rb–He collisions.[58]

Here, we explore this scenario within TD-DFT. Starting from Rb in the $5p^2\Pi_{3/2}$-state, we induce a "vertical DFT transition" by suddenly switching potential energy surfaces from $5p^2\Pi_{3/2}$ to $5p^2\Pi_{1/2}$, imparting to the Rb a kinetic energy corresponding to a fraction η of the available non-radiative de-excitation energy. The time Δt elapsing between the vertical excitation and de-excitation has to be chosen as well; this time influences the degree of RbHe $5p^2\Pi_{3/2}$ exciplex formation which, as we have seen, may require some tens of ps. The actual value of these inputs cannot be determined by the model itself.

In the following, we present results obtained from simulations using as input parameters the delay before relaxation Δt = 60 ps, and several values of η. As shown in Fig. 6 (see also the bottom left panel of Fig. 5), this — arbitrary — time is sufficient to allow for a full development of the $5p^2\Pi_{3/2}$ RbHe exciplex and to bring it to a rather stationary configuration.

The snapshots in Fig. 5 and the corresponding animation (Video S4 in the ESI†) illustrate the evolution following the $5s^2\Sigma_{1/2} \rightarrow 5p^2\Pi_{3/2} \rightarrow 5p^2\Pi_{1/2}$ process for η = 15%, Δt = 60 ps. Thus, upon sudden relaxation to the $5p^2\Pi_{1/2}$-state, the RbHe structure promptly detaches from the remaining He droplet. The velocity of the Rb atom as a function of time is depicted in Fig. 8 for this and other values of η. Clearly, as the fraction of relaxation energy converted to Rb kinetic energy is increased from 10% to 15%, the initial speed, and even more so, the asymptotic value for long evolution times rises significantly. Table 3 collects the results obtained for various values of η. It can be seen that a fairly small $\eta \geq 10\%$ is enough to induce the ejection of the RbHe complex. For a value η = 12.5%, the asymptotic value of the RbHe velocity matches best the experimental one measured for maximum $5p^2\Pi_{3/2}$-excitation at λ = 776 nm (12 887 cm^{-1}).

When assuming that the relaxation-induced RbHe desorption proceeds as an impulsive dissociation reaction, the conversion factor η can be related to an effective mass, m_{eff}, of the He droplet. This effective mass quantifies those He atoms in the droplet that, due to the short range character of the He-impurity interaction, interact most effectively with the impurity.[24] From η = 12.5% we obtain m_{eff} = 12.7 amu, which corresponds to about 3 He atoms effectively interacting with the excited RbHe. This value is significantly less than what was found for the prompt desorption of Rb and RbHe upon excitation of the Rb

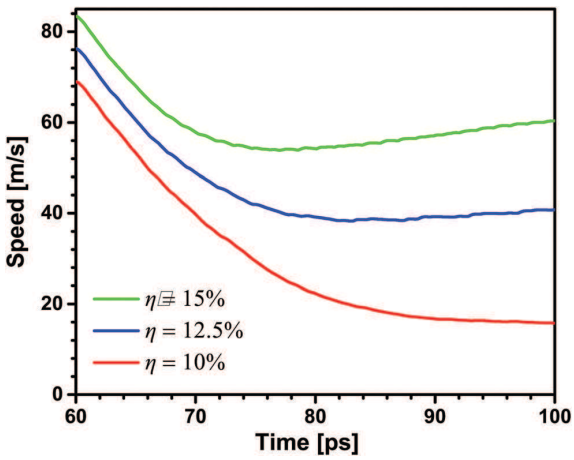

Fig. 8 Velocity of the excited Rb atom with attached He density as a function of time after $5p^2\Pi_{3/2} \rightarrow 5p^2\Pi_{1/2}$ relaxation at Δt = 60 ps for various values of the energy conversion factor η.

 This journal is © the Owner Societies 2018

Published on 12 March 2018. Downloaded by Universite Paul Sabatier on 09/04/2018 10:13:21.

Table 3 Asymptotic velocity and kinetic energy of the ejected RbHe exciplex for various values of the fraction η of the $5p^2\Pi_{3/2,1/2}$-energy spacing of 165 cm^{-1}, which is converted into kinetic energy of Rb by relaxation from the $5p^2\Pi_{3/2}$ into the $5p^2\Pi_{1/2}$-state. The calculations are carried out at a delay time Δt = 60 ps between photo-excitation and non-radiative de-excitation of the Rb atom

η (%)	v_∞ (m s^{-1})	Kin. energy (cm^{-1})
5	Bound	—
10	13.4	0.64
12.5	43.0	6.6
15	62.4	13.9
20	80.4	23.0

6s and 6p-correlated states.[19,26] This is no surprise, though, since the orbital overlap between the excited RbHe and the He droplet is smaller than for the higher excited and more extended 6s and 6p-states. Besides, the effective mass model is not strictly valid in the present situation, since it neglects the internal degrees of freedom of the RbHe exciplex.

Now that we have established the RbHe formation and desorption mechanisms, we can take our comparative study one step further and compute from the simulation results the electron binding energies to compare with the experimental photoelectron spectra. For this, we evaluate the interaction energy of the excited Rb* atom and of the Rb^+ ion with the droplet by calculating, respectively,

$$U^*(t) = \int d\mathbf{r}\, \mathscr{V}_{He-Rb^*}(|\mathbf{r} - \mathbf{r}_{Rb^*}|)\rho(\mathbf{r}, t) \quad (5)$$

and

$$U^+(t) = \int d\mathbf{r}\, \mathscr{V}_{He-Rb^+}(|\mathbf{r} - \mathbf{r}_{Rb^+}|)\rho(\mathbf{r}, t). \quad (6)$$

Here the He–Rb^+ pair potential $\mathscr{V}_{He-Rb^+}$ is taken from ref. 40. The He–Rb* potential in eqn (5) is a direction-dependent combination of Π and Σ pair potentials.[25]

The interaction energies $U^*(t)$ and $U^+(t)$ are shown in Fig. 9 for Rb in the $^2\Sigma_{1/2}$-state in (a), for the $^2\Pi_{1/2}$-state in (b), and for the $^2\Pi_{3/2}$-state in (c). Fig. 9(d) shows the evolution following the sudden relaxation of Rb to the $^2\Pi_{1/2}$-state at t = 60 ps. The prompt desorption of Rb in the $^2\Sigma_{1/2}$ and $^2\Pi_{1/2}$-states is seen as a sudden drop of $U^*(t)$ near t = 0 followed by a slow rise towards zero due to long-range van der Waals attraction as Rb departs from the He droplet. Due to the purely attractive interaction of the Rb^+ ion with the He droplet, $U^+(t)$ monotonically rises to zero. The exciplex formation dynamics in the $^2\Pi_{3/2}$-state is reflected by the irregular behavior of $U^*(t)$ and $U^+(t)$, eventually stabilizing at $t > 60$ ps at negative values, *i.e.* in a configuration where Rb is bound to the He droplet. Only when allowing for a sudden relaxation into the $^2\Pi_{1/2}$-state at t = 60 ps, the RbHe exciplex receives a momentum "kick" and subsequently detaches from the He droplet, in spite of a rising $U^*(t)$. The asymptotic values of U^* and U^+ are then given by the binding energy of the free RbHe exciplex configuration. The fast oscillations at $t > 65$ ps indicate that RbHe keeps vibrating as it is ejected.

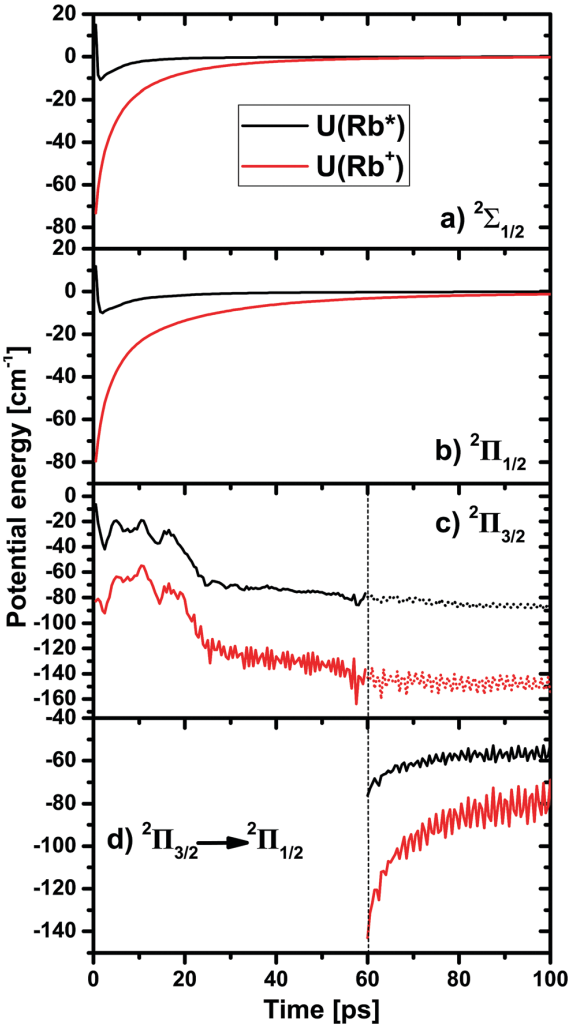

Fig. 9 (a)–(c) Simulated interaction energies of the Rb-atom excited into various states interacting with the surrounding He distribution (black lines), and of the Rb^+ ion for the same instantaneous geometry (red lines). In (d), the excited state of Rb is suddenly switched from $^2\Pi_{3/2}$ to $^2\Pi_{1/2}$ to simulate the dynamics initiated by spin-relaxation.

5 Discussion

Knowledge of the interaction energies $U^*(t)$ and $U^+(t)$ allows us to determine the electron binding energy $E_b(t) = U^+(t) - U^*(t)$ and to compare it with the experimental photoelectron spectra. Here, $U^*(t)$ and $U^+(t)$ are referenced to their asymptotic values, *i.e.* the binding energies of free Rb and Rb^+, respectively. The resulting values of E_b are depicted as thick colored lines in Fig. 10 in the range of delay times 0–100 ps. Compared to the experimental values, we note both matches and deviations. The TD-DFT values of E_b for the $^2\Pi_{1/2}$-state (red line) converge within 100 ps to the value of the free Rb($5p^2P_{1/2}$)-atom, as in the simulation Rb in that state detaches from the droplet. In contrast, the experimental values (blue symbols) are

Published on 12 March 2018. Downloaded by Universite Paul Sabatier on 09/04/2018 10:13:21.

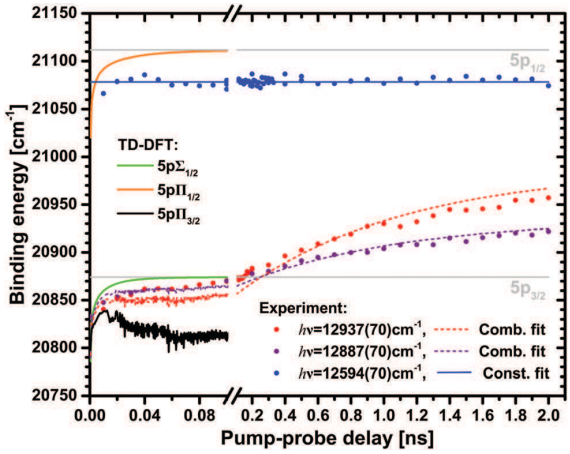

Fig. 10 Comparison of experimental and simulated electron binding energies. Thick solid lines: TD-DFT results. Dashed lines: combined TD-DFT and analytical model. Thin solid lines: biexponential fits of the experimental data.

constant and below the atomic value because most of the atoms actually remain bound to the He droplet, see Section 3.2.

The TD-DFT values for the $^2\Sigma_{1/2}$-state (green line) quickly rise to $E_{5p_{3/2}}$ within a few tens of ps, again due to prompt desorption, yielding free Rb $5p^2P_{3/2}$ atoms. The experimental values for excitation at 12 937 and 12 887 cm^{-1} (red and grey symbols) show a very similar increase in that time range. This supports our conclusion that the fast dynamics observed both in the photoelectron peak position and in the yield of photo-ions mainly results from prompt desorption of the $^2\Sigma_{1/2}$-component of the excited state. In the experiment we found that the [RbHe]$^+$ ion signal associated with $^2\Pi_{3/2}$-component of the excitation features a weak fast rising component as well [Fig. 3(c)]. This we attribute to a finite rate of prompt desorption of Rb and RbHe in the $^2\Pi_{3/2}$-state.

The TD-DFT curve for the $^2\Pi_{3/2}$-state without relaxation (black line) drops in binding energy, at odds with the experiment. However, when $^2\Pi_{3/2} \rightarrow {}^2\Pi_{1/2}$-relaxation is included, the simulated curve also rises, staying only slightly below the experimental values in the time range 20–100 ps. Thus, we achieve good agreement of our extended TD-DFT simulations with the experiment for the fast (tens of ps) desorption of the $^2\Sigma_{1/2}$-state, and qualitative agreement with regard to the desorption of the $^2\Pi_{3/2}$-state when allowing for spin-relaxation.

The lacking quantitative agreement is not surprising given the instantaneous spin-relaxation approximation made in the calculations. Naturally, this relaxation process has its own time dependence. If we identify the latter with the observed slow variation of photoelectron spectra and ion yields, we can set up a more realistic, combined model. Hereby, we account for the populations $p_{\Sigma_{1/2}}$ in the $^2\Sigma_{1/2}$-state and $p_{\Pi_{3/2}}$ in the $^2\Pi_{3/2}$ state, which are determined by the spectral profile of the laser $I_\ell(h\nu)$. The coefficients $p_{\Sigma_{1/2},\Pi_{3/2}}$ are calculated from the state-selective absorption profiles $I_\Sigma(h\nu)$ and $I_\Pi(h\nu)$ using LeRoy's LEVEL program[75] based on the spin–orbit corrected pseudodiatomic potentials by Callegari and Ancilotto.[65] In a second step, the absorption profiles are weighted with $I_\ell(h\nu)$ and integrated over $h\nu$, yielding $p_{\Pi_{3/2}} = 0.28$ for the center frequency $h\nu$ = 12 937 cm^{-1} and $p_{\Pi_{3/2}} = 0.52$ for $h\nu$ = 12 887 cm^{-1}.

The transient energy of the $^2\Pi_{3/2}$-state, $E_{\Pi_{3/2}}(t)$, consists of a contribution of the binding energy $\left[U^+_{\Pi_{3/2}\rightarrow\Pi_{1/2}} - U^*_{\Pi_{3/2}\rightarrow\Pi_{1/2}}\right]$ for the dynamics including relaxation to $^2\Pi_{1/2}$, and a contribution $\left[U^+_{\Pi_{3/2}} - U^*_{\Pi_{3/2}}\right]$ for the $^2\Pi_{3/2}$-state without relaxation. When assuming an exponential time dependence of the relaxation with a time constant τ, we get

$$E(t) = p_{\Sigma_{1/2}} \cdot \left[U^+_{\Sigma_{1/2}} - U^*_{\Sigma_{1/2}}\right] + p_{\Pi_{3/2}} \cdot \mathrm{e}^{-\ln 2\cdot/\tau} \cdot \left[U^+_{\Pi_{3/2}} - U^*_{\Pi_{3/2}}\right] + p_{\Pi_{3/2}} \cdot \left(1 - \mathrm{e}^{-\ln 2\cdot t/\tau}\right) \cdot \left[U^+_{\Pi_{3/2}\rightarrow\Pi_{1/2}} - U^*_{\Pi_{3/2}\rightarrow\Pi_{1/2}}\right].$$

Here, $U^*(t)$ and $U^+(t)$ are extrapolated for long times $t > 200$ ps by constants for the $^2\Sigma_{1/2}$ and $^2\Pi_{3/2}$-states and by an exponential function for the $^2\Pi_{3/2} \rightarrow {}^2\Pi_{1/2}$ case. For simplicity, we neglect the 60 ps time delay between excitation and relaxation which is short compared to the full relaxation dynamics.

If we assign to τ the experimental value of the slow time constant of the fit of photoelectron energies, $\tau = \tau^e_2$, we obtain the dashed lines in Fig. 10, which nicely match the experimental data. Thus, we identify the slow variations of ion and electron signals spanning hundreds of ps to He-induced spin-relaxation, which proceeds on that time scale and causes the desorption of RbHe exciplexes. The fact that the Rb$^+$ signal associated mainly with $^2\Sigma_{1/2}$-excitation features a weak slowly rising component as well [Fig. 3(c) and (d)], we take as an indication that spin-relaxation also causes the desorption of neat Rb($5p^2P_{1/2}$)-atoms to some extent.

6 Conclusion

In summary, we have presented a detailed study of the formation and desorption dynamics of RbHe exciplexes initiated by laser excitation of Rb atoms attached to He nanodroplets. Experimentally, the two-color femtosecond pump–probe photoionization scheme allows us to selectively probe the dynamics of the lowest three excited states of the Rb–He droplet complex. Both photoion and photoelectron signals feature pump–probe dynamics proceeding on two distinct time scales (~30 and 700 ps). By comparing with time-dependent DFT simulations, complemented by a spin-relaxation mechanism, we conclude that the fast dynamics is due to prompt desorption of Rb atoms when exciting the $^2\Sigma_{1/2}$-state. The slow desorption of RbHe exciplexes is induced by $^2\Pi_{3/2} \rightarrow {}^2\Pi_{1/2}$ spin-relaxation. By analyzing the rearrangement of the He surrounding the Rb atom in the $^2\Pi_{3/2}$-state, we infer a formation time of the RbHe exciplex ranging between 20 and 50 ps. When exciting the lowest state of the Rb–He droplet complex, $^2\Pi_{1/2}$, we find that a small fraction of Rb atoms desorbs as free atoms, as predicted by the DFT simulation, whereas the larger fraction of Rb atoms remains bound to the He droplets.

 This journal is © the Owner Societies 2018

Published on 12 March 2018. Downloaded by Universite Paul Sabatier on 09/04/2018 10:13:21.

While this work represents in our opinion the most complete investigation of the real-time dynamics of an alkali metal–He exciplex, still some uncertainties remain. In the experiment, a better reconcilability of electron and ion signals may be achieved by detecting electrons and ions in coincidence.[71,76] Furthermore, extending such studies to other types of dopant species which are solvated more deeply inside He droplets (*e.g.* alkaline earth metals, transition metals) would give further insight into the mechanisms of desolvation and ejection of excited impurity atoms out of He nanodroplets.[18,20,21,77]

On the theory side, a more complete description of the couplings between electronic states and the configurational degrees of freedom in such excited complexes induced by the He droplet environment would be highly desirable.[3,4] In a recent advance, electronic relaxation of Ba^+ ions in He nanodroplets, based on a diabatization of the He–Ba^+ ground and excited electronic states interaction potentials,[5] has been proposed as a mechanism for ejecting Ba^+ and Ba^+He_n off He droplets. These mechanisms for spin-relaxation and inter-electronic state relaxation have to be confirmed by real-time dynamics studies.

Conflicts of interest

There are no conflicts to declare.

Acknowledgements

The authors would like to thank Marcel Drabbels for useful exchanges. Financial support by the Deutsche Forschungsgemeinschaft (MU 2347/6-1 and IRTG 2079) is greatfully acknowledged. This work has been performed under Grant No. FIS2017-87801-P from DGI, Spain. M. B. thanks the Université Fédérale Toulouse Midi-Pyrénées for financial support throughout the "Chaires d'Attractivité 2014" Programme IMDYNHE. The dynamics simulations presented in this work have been carried out thanks to the HPC resources of CALMIP supercomputing center (Grant P1039).

References

1 C. George, M. Ammann, B. D'Anna, D. J. Donaldson and S. A. Nizkorodov, *Chem. Rev.*, 2015, **115**, 4218–4258.
2 J. Schneider, D. Bahnemann, J. Ye, G. L. Puma and D. D. Dionysiou, *Photocatalysis: Fundamentals and Perspectives*, The Royal Society of Chemistry, Cambridge CB4 0WF, UK, 2016.
3 K. D. Closser, O. Gessner and M. Head-Gordon, *J. Chem. Phys.*, 2014, **140**, 134306.
4 A. Masson, M.-C. Heitz, J.-M. Mestdagh, M.-A. Gaveau, L. Poisson and F. Spiegelman, *Phys. Rev. Lett.*, 2014, **113**, 123005.
5 P. Vindel-Zandbergen, M. Barranco, F. Cargnoni, M. Drabbels, M. Pi and N. Halberstadt, Helium-induced electronic transitions in photo-excited Ba^+–He_n exciplexes, *J. Chem. Phys.*, 2018, in print.
6 J. P. Toennies and A. F. Vilesov, *Angew. Chem., Int. Ed.*, 2004, **43**, 2622.
7 F. Stienkemeier and K. Lehmann, *J. Phys. B: At., Mol. Opt. Phys.*, 2006, **39**, R127.
8 F. Ancilotto, G. DeToffol and F. Toigo, *Phys. Rev. B: Condens. Matter Mater. Phys.*, 1995, **52**, 16125–16129.
9 F. Stienkemeier, J. Higgins, C. Callegari, S. I. Kanorsky, W. E. Ernst and G. Scoles, *Z. Phys. D: At., Mol. Clusters*, 1996, **38**, 253–263.
10 M. Barranco, R. Guardiola, S. Hernández, R. Mayol, J. Navarro and M. Pi, *J. Low Temp. Phys.*, 2006, **142**, 1–81.
11 C. Stark and V. V. Kresin, *Phys. Rev. B: Condens. Matter Mater. Phys.*, 2010, **81**, 085401.
12 L. An der Lan, P. Bartl, C. Leidlmair, H. Schöbel, R. Jochum, S. Denifl, T. D. Märk, A. M. Ellis and P. Scheier, *J. Chem. Phys.*, 2011, **135**, 044309.
13 L. An der Lan, P. Bartl, C. Leidlmair, H. Schöbel, S. Denifl, T. D. Märk, A. M. Ellis and P. Scheier, *Phys. Rev. B: Condens. Matter Mater. Phys.*, 2012, **85**, 115414.
14 J. Höller, E. Krotscheck and R. E. Zillich, *Eur. Phys. J. D*, 2015, **69**, 198.
15 F. Calvo, *Phys. Rev. B*, 2017, **95**, 035429.
16 M. Mudrich and F. Stienkemeier, *Int. Rev. Phys. Chem.*, 2014, **33**, 301–339.
17 F. Ancilotto, M. Barranco, F. Coppens, J. Eloranta, N. Halberstadt, A. Hernando, D. Mateo and M. Pi, *Int. Rev. Phys. Chem.*, 2017, **36**, 621–707.
18 E. Loginov and M. Drabbels, *J. Phys. Chem. A*, 2007, **111**, 7504–7515.
19 L. Fechner, B. Grüner, A. Sieg, C. Callegari, F. Ancilotto, F. Stienkemeier and M. Mudrich, *Phys. Chem. Chem. Phys.*, 2012, **14**, 3843.
20 A. Kautsch, M. Koch and W. E. Ernst, *J. Phys. Chem. A*, 2013, **117**, 9621–9625.
21 F. Lindebner, A. Kautsch, M. Koch and W. E. Ernst, *Int. J. Mass Spectrom.*, 2014, **365–366**, 255–259.
22 M. Koch, G. Auböck, C. Callegari and W. E. Ernst, *Phys. Rev. Lett.*, 2009, **103**, 035302.
23 S. Smolarek, N. B. Brauer, W. J. Buma and M. Drabbels, *J. Am. Chem. Soc.*, 2010, **132**, 14086–14091.
24 A. Hernando, M. Barranco, M. Pi, E. Loginov, M. Langlet and M. Drabbels, *Phys. Chem. Chem. Phys.*, 2012, **14**, 3996–4010.
25 D. Mateo, A. Hernando, M. Barranco, E. Loginov, M. Drabbels and M. Pi, *Phys. Chem. Chem. Phys.*, 2013, **15**, 18388–18400.
26 J. von Vangerow, A. Sieg, F. Stienkemeier, M. Mudrich, A. Leal, D. Mateo, A. Hernando, M. Barranco and M. Pi, *J. Phys. Chem. A*, 2014, **118**, 6604–6614.
27 J. von Vangerow, O. John, F. Stienkemeier and M. Mudrich, *J. Chem. Phys.*, 2015, **143**, 034302.
28 A. Sieg, J. von Vangerow, F. Stienkemeier, O. Dulieu and M. Mudrich, *J. Phys. Chem. A*, 2016, **120**, 7641–7649.
29 J. von Vangerow, F. Coppens, A. Leal, M. Pi, M. Barranco, N. Halberstadt, F. Stienkemeier and M. Mudrich, *J. Phys. Chem. Lett.*, 2017, **8**, 307–312.
30 A. Przystawik, S. Göde, T. Döppner, J. Tiggesbäumker and K.-H. Meiwes-Broer, *Phys. Rev. A: At., Mol., Opt. Phys.*, 2008, **78**, 021202.

Published on 12 March 2018. Downloaded by Universite Paul Sabatier on 09/04/2018 10:13:21.

31 S. Müller, S. Krapf, T. Koslowski, M. Mudrich and F. Stienkemeier, *Phys. Rev. Lett.*, 2009, **102**, 183401.
32 A. Kautsch, M. Koch and W. E. Ernst, *Phys. Chem. Chem. Phys.*, 2015, **17**, 12310–12316.
33 J. Reho, J. Higgins, C. Callegari, K. K. Lehmann and G. Scoles, *J. Chem. Phys.*, 2000, **113**, 9694–9701.
34 F. R. Brühl, R. A. Trasca and W. E. Ernst, *J. Chem. Phys.*, 2001, **115**, 10220–10224.
35 C. P. Schulz, P. Claas and F. Stienkemeier, *Phys. Rev. Lett.*, 2001, **87**, 153401.
36 G. Droppelmann, O. Bünermann, C. P. Schulz and F. Stienkemeier, *Phys. Rev. Lett.*, 2004, **93**, 0233402.
37 M. Mudrich, G. Droppelmann, P. Claas, C. Schulz and F. Stienkemeier, *Phys. Rev. Lett.*, 2008, **100**, 023401.
38 S. Müller, M. Mudrich and F. Stienkemeier, *J. Chem. Phys.*, 2009, **131**, 044319.
39 M. Theisen, F. Lackner and W. E. Ernst, *Phys. Chem. Chem. Phys.*, 2010, **12**, 14861–14863.
40 A. Leal, D. Mateo, A. Hernando, M. Pi, M. Barranco, A. Ponti, F. Cargnoni and M. Drabbels, *Phys. Rev. B: Condens. Matter Mater. Phys.*, 2014, **90**, 224518.
41 E. Loginov, A. Hernando, J. A. Beswick, N. Halberstadt and M. Drabbels, *J. Phys. Chem. A*, 2015, **119**, 6033–6044.
42 M. Kuhn, M. Renzler, J. Postler, S. Ralser, S. Spieler, M. Simpson, H. Linnartz, A. G. G. M. Tielens, J. Cami, A. Mauracher, Y. Wang, M. Alcamí, F. Martín, M. K. Beyer, R. Wester, A. Lindinger and P. Scheier, *Nat. Commun.*, 2016, **7**, 13550.
43 N. B. Brauer, S. Smolarek, E. Loginov, D. Mateo, A. Hernando, M. Pi, M. Barranco, W. J. Buma and M. Drabbels, *Phys. Rev. Lett.*, 2013, **111**, 153002.
44 M. Koch, A. Kautsch, F. Lackner and W. E. Ernst, *J. Phys. Chem. A*, 2014, **118**, 8373–8379.
45 Y. Seki, T. Takayanagi and M. Shiga, *Phys. Chem. Chem. Phys.*, 2017, **19**, 13798–13806.
46 G. Auböck, J. Nagl, C. Callegari and W. E. Ernst, *Phys. Rev. Lett.*, 2008, **101**, 035301.
47 M. Theisen, F. Lackner and W. E. Ernst, *J. Phys. Chem. A*, 2011, **115**, 7005–7009.
48 T. Takayanagi and M. Shiga, *Phys. Chem. Chem. Phys.*, 2004, **6**, 3241.
49 M. Leino, A. Viel and R. E. Zillich, *J. Chem. Phys.*, 2011, **134**, 024316.
50 C. Giese, T. Mullins, B. Grüner, M. Weidemüller, F. Stienkemeier and M. Mudrich, *J. Chem. Phys.*, 2012, **137**, 244307.
51 S. H. Patil, *J. Chem. Phys.*, 1991, **94**, 8089–8095.
52 F. Ancilotto, M. Barranco, F. Caupin, R. Mayol and M. Pi, *Phys. Rev. B: Condens. Matter Mater. Phys.*, 2005, **72**, 214522.
53 M. Pi, F. Ancilotto, F. Coppens, N. Halberstadt, A. Hernando, A. Leal, D. Mateo, R. Mayol and M. Barranco, ^{4}He-DFT BCN-TLS: A Computer Package for Simulating Structural Properties and Dynamics of Doped Liquid Helium-4 Systems. https://github.com/bcntls2016/.
54 D. Mateo, A. Hernando, M. Barranco, R. Mayol and M. Pi, *Phys. Rev. B: Condens. Matter Mater. Phys.*, 2011, **83**, 174505.
55 A. Hernando, M. Barranco, R. Mayol, M. Pi and M. Krośnicki, *Phys. Rev. B: Condens. Matter Mater. Phys.*, 2008, **77**, 024513.
56 J. Pascale, *Phys. Rev. A: At., Mol., Opt. Phys.*, 1983, **28**, 632–644.
57 O. Bünermann, G. Droppelmann, A. Hernando, R. Mayol and F. Stienkemeier, *J. Phys. Chem. A*, 2007, **111**, 12684.
58 K. Hirano, K. Enomoto, M. Kumakura, Y. Takahashi and T. Yabuzaki, *Phys. Rev. A: At., Mol., Opt. Phys.*, 2003, **68**, 012722.
59 A. T. J. B. Eppink and D. H. Parker, *Rev. Sci. Instrum.*, 1997, **68**, 3477.
60 A. Wituschek, J. von Vangerow, J. Grzesiak, F. Stienkemeier and M. Mudrich, *Rev. Sci. Instrum.*, 2016, **87**, 083105.
61 G. A. Garcia, L. Nahon and I. Powis, *Rev. Sci. Instrum.*, 2004, **75**, 4989–4996.
62 B. Dick, *Phys. Chem. Chem. Phys.*, 2014, **16**, 570–580.
63 A. Braun and M. Drabbels, *J. Chem. Phys.*, 2007, **127**, 114303.
64 G. S. Mudholkar and A. D. Hutson, *J. Stat. Plann. Inference*, 2000, **83**, 291–309.
65 C. Callegari and F. Ancilotto, *J. Phys. Chem. A*, 2011, **115**, 6789–6796.
66 R. N. Zare, *Mol. Photochem.*, 1972, **44**, 1.
67 M. Theisen, F. Lackner, G. Krois and W. E. Ernst, *J. Phys. Chem. Lett.*, 2011, **2**, 2778–2782.
68 E. Loginov, D. Rossi and M. Drabbels, *Phys. Rev. Lett.*, 2005, **95**, 163401.
69 D. S. Peterka, J. H. Kim, C. C. Wang and D. M. Neumark, *J. Phys. Chem. B*, 2006, **110**, 19945–19955.
70 C. C. Wang, O. Kornilov, O. Gessner, J. H. Kim, D. S. Peterka and D. M. Neumark, *J. Phys. Chem. A*, 2008, **112**, 9356.
71 D. Buchta, S. R. Krishnan, N. B. Brauer, M. Drabbels, P. O'Keeffe, M. Devetta, M. Di Fraia, C. Callegari, R. Richter, M. Coreno, K. C. Prince, F. Stienkemeier, R. Moshammer and M. Mudrich, *J. Phys. Chem. A*, 2013, **117**, 4394–4403.
72 M. Leino, A. Viel and R. E. Zillich, *J. Chem. Phys.*, 2008, **129**, 184308.
73 E. Loginov and M. Drabbels, *J. Phys. Chem. A*, 2014, **118**, 2738–2748.
74 L. Krause, in *Adv. Chem. Phys.*, ed. J. W. McGowan, Wiley, New York, 1975.
75 R. LeRoy, *Chemical Physics Research Report*, University of Waterloo, CP-555, 1995.
76 A. C. LaForge, V. Stumpf, K. Gokhberg, J. von Vangerow, F. Stienkemeier, N. V. Kryzhevoi, P. O'Keeffe, A. Ciavardini, S. R. Krishnan, M. Coreno, K. C. Prince, R. Richter, R. Moshammer, T. Pfeifer, L. S. Cederbaum and M. Mudrich, *Phys. Rev. Lett.*, 2016, **116**, 203001.
77 E. Loginov and M. Drabbels, *J. Chem. Phys.*, 2012, **136**, 154302.

 This journal is © the Owner Societies 2018

6

Supervised work: Potassium-doped nanodroplets

Under the supervision of Nadine Halberstadt and me, a master research internship – *M2 Physique Fondamentale* – titled "***Dynamics of a superfluid helium nanodroplet doped with a single potassium atom***" has been performed by Maxime Martinez.

The project investigates the static and dynamic behaviour of a single potassium (K) atom excited from the K-$^4He_{1000}$ equilibrium configuration to the K*(4p)-$^4He_{1000}$ and K*(5s)-$^4He_{1000}$ states. The choice of potassium was motivated by a discrepancy in the time-resolved experimental studies[100-102]. Moreover, the mass of potassium sits between those of the heavier alkalis like rubidium and cesium, and the lighter ones, like lithium and sodium. Therefore, potassium presents an interesting case, being on the borderline between the classical regime for heavy alkalis and a quantum-mechanical regime for the lighter ones. Both treatments of the equilibrium properties and the 5s←4s excitation are studied. This work is not included in the thesis but can be found in Ref. [61].

It is concluded that quantum effects of K do exist but are not essential to the understanding and description of the dynamics. Therefore the K*(4p)-$^4He_{1000}$ excitation is studied with a classical description of K.

Part II

Capture by quantised vortices

7
Quantised vortices in droplets

One of the most unambiguous signatures of the quantum mechanical nature of a substance —and indeed of superfluidity— is the appearance of quantised vortices. The work in this part of the thesis is mostly inspired and motivated by experiments performed by Gomez, Loginov and Vilesov[103,104].

7.1 Introduction

Normal fluids rotate rigidly when their containers are spinning at low angular velocities, with an angular velocity $v_\perp$ proportional to the distance r from the axis of rotation $v_\perp \propto r$. This behaviour changes completely when the normal fluid is replaced by a superfluid like liquid helium below T_λ; below a critical angular velocity, the fluid remains at rest. When the angular velocity of the container is increased above this critical velocity, one or more quantised vortices are nucleated. In contrast to a normal fluid, the angular velocity v_s of a superfluid directly outside the vortex core is inversely proportional to the distance from the vortex core $v_s \propto 1/r$. These vortices can be described by an effective wave function and a quantised circulation Γ of the velocity field

$$\Gamma = s\frac{h}{m} \tag{7.1}$$

where s is the angular momentum quantum number, h is Planck's constant and m is the mass of the ^{4}He atom (see Equation (1.29) for a derivation and Refs. [105, 106]). An important aspect in the study of vorticity in finite systems is the energy and momentum transfer between vortices and surface excitations, because they determine nucleation dynamics, shape and the stability of vortices. But the study of quantum vortices is no longer confined to superfluids like liquid helium. Recently[106,107] it has been extended to BECs confined in magnetic traps. Contrary to confined BECs, superfluid helium droplets are self-contained systems that do not require an external trap to keep them from falling apart. Moreover, they provide an opportunity to study the regime of a strongly interacting quantum system. The width of vortex cores, about 0.2 nm[105] in

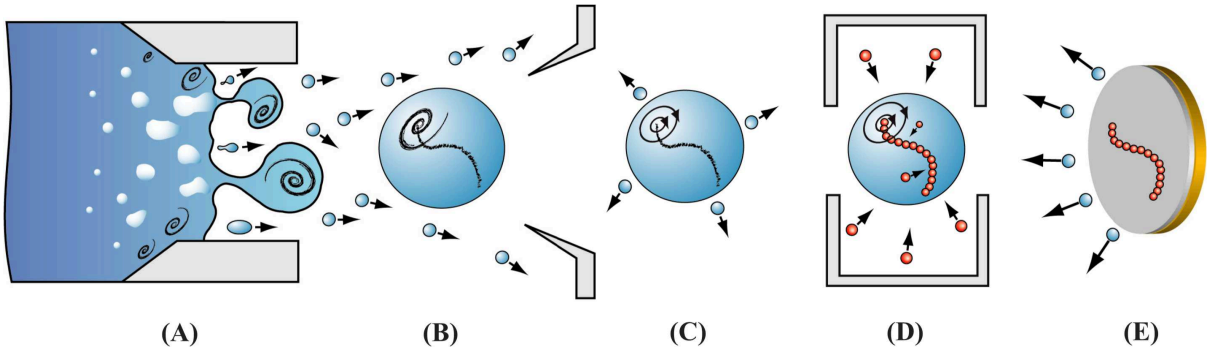

Figure 7.1: Schematic of the experiment. (a) He fluid expands in vacuum and (b) breaks up into rotating droplets. (c) A quantum vortex is formed as a consequence of fast evaporative cooling of the droplet to below T_λ. (d) The droplet is doped with Ag atoms, which are attracted to the vortex core. (e) The droplet then collides with the carbon surface leaving behind the Ag trace, whereas the He evaporates. (Illustration courtesy of Gomez *et al.* 2012, see Ref. [103])

superfluid helium-4, is small compared to the size of the droplets (typically a diameter of ~4.4-10.9 nm), suggesting a rich variety of three-dimensional phenomena. Quantum vortices in superfluid droplets are therefore a very active field of interest[108-111].

Recently, Gomez *et al.* performed experiments[103] where vortices inside superfluid ^{4}He nanodroplets, produced by the expansion of liquid helium, were doped with Ag atoms which then clustered along the vortex lines in the droplets. The helium droplets needed by these kind of experiments need to be larger than the ones used before for single atom spectroscopy and dynamics studies, because they need to be big enough to be able to host an array of vortices, doped with many Ag clusters.

A schematic of the experimental principle is shown in Figure 7.1. Helium droplets are produced by expansion of He, at 20 bars and a temperature T_0=5.4-7 K, into a vacuum through a nozzle. The droplets cool down rapidly by evaporation and reach a temperature of 0.37 K[32]. This temperature is well below the superfluid transition temperature T_λ=2.17 K[105,106]. Further along the apparatus, the droplets capture about 10^3-10^6 Ag atoms in an oven[112]. The droplets are then collided against a thin carbon film substrate at room temperature[112]. When the droplets hit the carbon film they evaporate while leaving behind on the surface the Ag filaments, which are subsequently imaged via a transmission electron microscope (TEM).

The ubiquity of elongated filament-shaped deposits (see Figure 1.5) shows that vortices are present in droplets larger than about 300 nm (about 10^9 atoms) and that their lifetime exceeds a few milliseconds.

Two years later Gomez *et al.* reported[104] on the formation of quantum vortex lattices inside droplets. They used single-shot femtosecond X-ray coherent diffractive imaging to

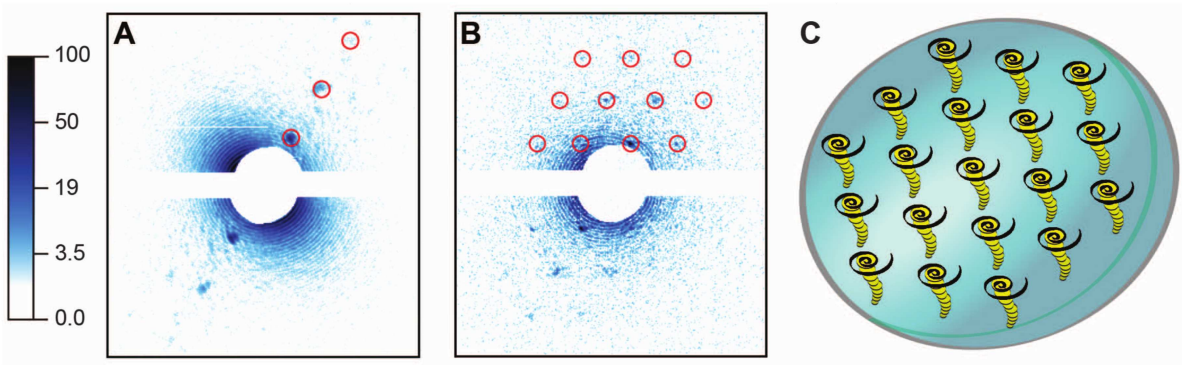

Figure 7.2: He droplets doped with Xe atoms. (A and B) X-ray diffraction images of doped droplets, displayed in a logarithmic intensity scale. (C) Droplet and embedded Xe clusters. Images in (A) and (B) correspond to tilted and parallel alignments of the vortex axes with respect to the incident x-ray beam, respectively. (Illustration courtesy of Gomez *et al.* 2014, see Ref. [104])

investigate the rotation of single, isolated superfluid helium-4 droplets containing about 10^8-10^{11} atoms, corresponding to radii of ≃100-1000 nm. The formation of quantum vortex lattices inside the droplets was confirmed by observing the characteristic Bragg patterns from xenon clusters trapped in the vortex cores (see Figure 7.2).

7.2 Vortex arrays in ^{4}He droplets doped with Ar atoms

The existence of ordered vortex lattices inside ^{4}He droplets has been established by the appearance of Bragg patterns from Xe clusters trapped inside the vortex cores in droplets made of $N = 10^8 - 10^{11}$ atoms (corresponding to radii from 100 to 1000 nm)[104,113]. We have recently studied the stability of vortex arrays made of up to $n_v = 9$ vortices inside a ^{4}He nanodroplet using the DFT approach[114]. It was found that the energetically favored structure for $n_v > 6$ is a ring of vortices encircling a vortex at the center of the droplet. Fot $n_v = 6$, the configuration with a six-vortex ring is found to have almost the same energy as the five-fold ring plus a vortex at the center. The former structure has been experimentally observed[104,113,115], although classical vortex theory predicts for it a much higher free energy cost than for the latter[116]. Similar equilibrium structures have been obtained within DFT for helium nanocylinders hosting vortex arrays[117].

In the experiments of Ref. [113] the diffraction images show that rotating ^{4}He nanodroplets of about 200 nm in diameter contain a small number of symmetrically arranged quantum vortices whose cores are filled with regularly spaced Xe clusters. Unexpected large distances of the vortices from the droplet center (~0.7-0.8 droplet radii) are observed and explained as a result of the balance between the contribution of the Xe atoms to the total angular momentum of the droplets and the solvation potential of

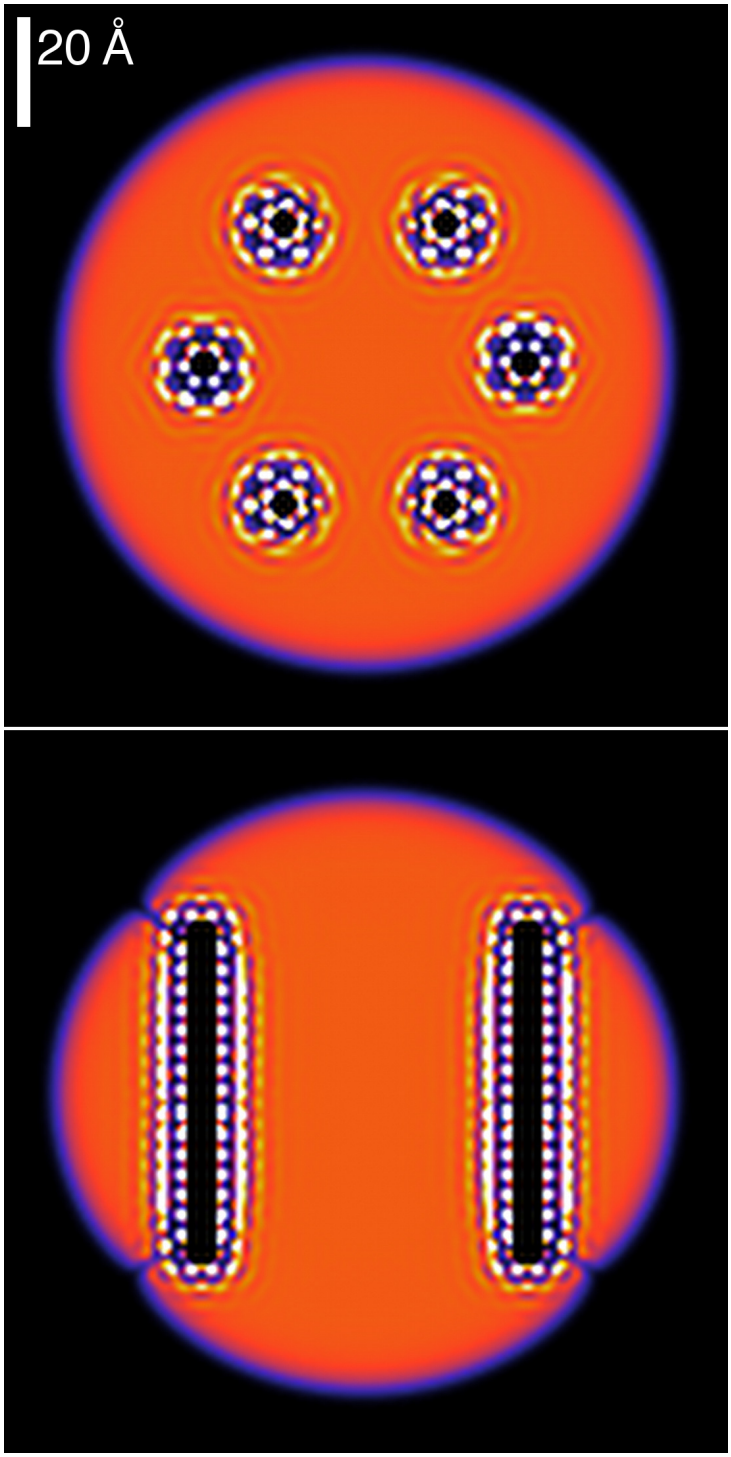

Figure 7.3: Helium droplet configuration hosting six vortices, each doped with a line of regularly spaced Ar atoms (not represented). The top figure shows the density in the $x-y$ symmetry plane (top view), while the bottom figure shows a side view corresponding to the $y-z$ plane. As in some of the previous figures, the bright spots are high density blobs appearing around the impurity atoms.

the embedded Xe atoms, which opposes the migration of vortices towards the droplet surface and their annihilation there, as it would happen instead in the case of undoped vortices for low values of the droplet rotational frequency.

In practice, as more and more Xe atoms become attached to a vortex, they adopt the angular velocity of its revolution about the droplet center. If the Xe capture is isotropic, the total angular momentum of the droplet is conserved, and thus the angular momentum accompanying the Xe rotational motion must be transferred from the vortices to the impurities. This reduction in the angular momentum of the vortices causes them to move outwards, resulting in the larger equilibrium distances of the vortices observed in the experiments. The actual equilibrium radial positions result from a balance between this tendency to move towards the droplet surface and the solvation potential, which tends instead to draw impurities towards the droplet center.

We have looked for stationary configurations of a 6-vortex ring in a rotating He_{15000} droplet by solving the EL equations in the corotating frame with a fixed angular velocity. Each vortex core is filled with Ar atoms, and the system is allowed to fully relax. In the end, the column of atoms inside each vortex core reaches an equilibrium structure where the Ar atoms are separated by a distance which is roughly that of the Ar dimer. One such configuration is shown in Figure 7.3. Note that the vortex cores are almost straight lines, whereas in an undoped droplet rotating with the same velocity the vortex lines would be bent, as shown e.g. in Figure 9.7. The Ar atoms are not shown in the Figure. The localized structures appearing in the vortex cores are regions of highly inhomogeneous, high ^{4}He density resulting from the Ar-He attractive potential.

The presence of impurities thus confers rigidity to the vortex lines, preventing them from bending. Yet, the small segment of the vortex line free from impurities bends so as to hit the droplet surface perpendicularly, see the bottom Figure 7.3. Note that in the absence of vortices, Ar atoms initially placed in a linear chain structure would relax towards the lower energy, compact configuration of an Ar cluster in the bulk of the droplet. However, once trapped by a vortex core, their collapse into such a cluster structure does not occur, i.e. an energy barrier appears and prevents the formation of Ar clusters. Our simplified description of the more complex experimental conditions (where each vortex line hosts chains of regularly spaced atomic clusters, instead of chains of single atoms) is due to computational limitations.

Our choice of Ar instead of Xe as a dopant is motivated by the weaker He-Ar and Ar-Ar interactions, which facilitates the imaginary-time relaxation. The interaction of the helium environment with several close-by impurities increases the strength of dopant-droplet interaction, producing helium localization around the impurities (snowball structures), see Figure 4. Stabilizing these structures is extremely time consuming, especially when the He-impurity interaction is strong. Experiments were also carried out with Ar atoms as

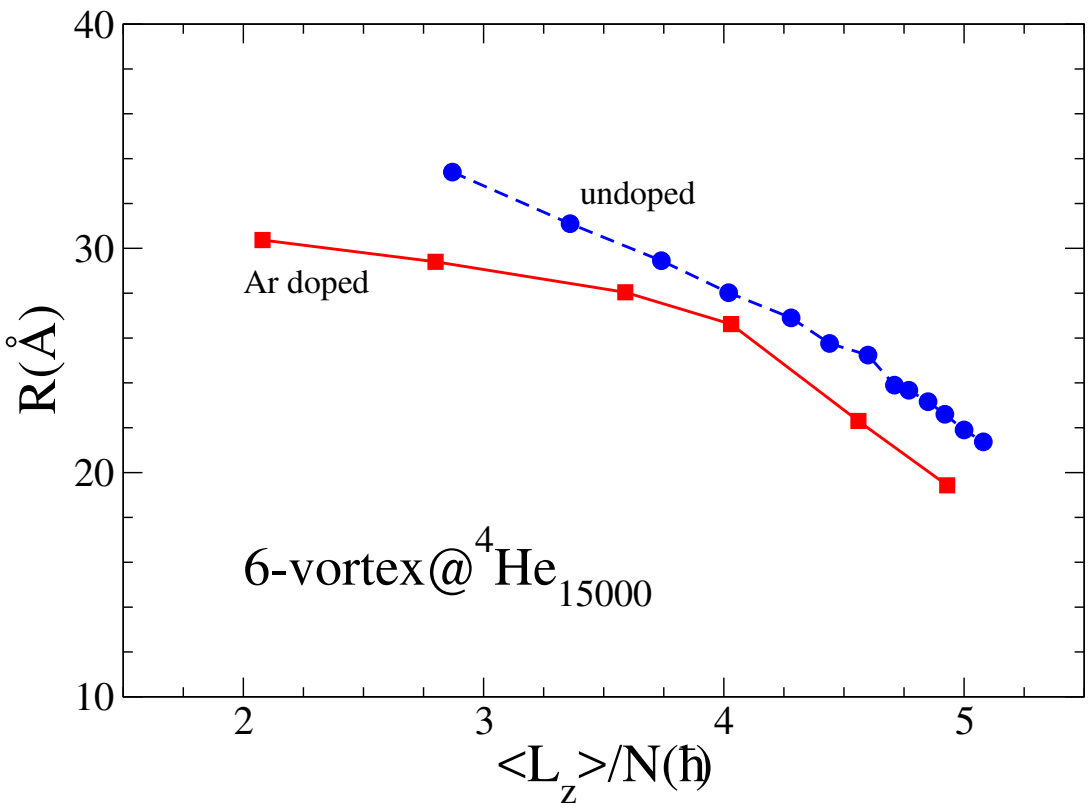

Figure 7.4: Calculated equilibrium distance of the 6-vortex ring from the droplet center as a function of the angular momentum per He atom in units of $\hbar$. The dots represent the results for undoped vortices, while the squares are the results for Ar-doped vortices. The lines are drawn as a guide to the eye.

dopants, but have not been analyzed yet. However, no significant difference is expected between argon and xenon, neither from the experimental nor from the theoretical viewpoint.

There are obvious differences in scales between our simulations and the actual experiments, due to computational cost. In experiments heavier impurities are used (Xe), the droplets are much larger and the doping is known to occur by filling the vortex cores with a chain of equally spaced Xe clusters, each made of hundreds of atoms, instead of atom chains as done in our simulations. In spite of these differences, we find results which qualitatively explain the unusual behavior of vortex lines experimentally observed in doped rotating helium droplets.

We have looked for the equilibrium structure of the Ar@6-vortex ^{4}He$_{15000}$ droplet for different imposed values of the angular velocity of rotation. The results show that the doping inside each vortex core adds a substantial stability to the system, such that doped vortices are still stable in a droplet rotating at rather low values of the angular velocities, whereas undoped vortices for such values would be pushed towards the surface of the droplet and eventually expelled. The solvation potential effect becomes apparent below

some critical value of the angular velocity, where the vortices cease to move towards the surface and the system reaches an equilibrium maximum distance of the vortices from the droplet center. This is shown in the Figure 7.4, where we plot the radial distance of the vortices from the center as a function of the angular momentum of the system. Note how doped vortices are stable for values of the angular momentum well below the stability limit of an undoped droplet. A similar behavior has been observed in the experiment (see for instance Figure 2 in the Supplemental Material of Ref. [113], see DOI: 10.1103/PhysRevB.93.180510).

8

Head-on collisions of Xe and Cs[1]

8.1 Introduction

It is well established that helium droplets can readily capture in their interior almost any atom or molecule interacting with them, as first shown for the case of Ne atoms[118], with the notable exception of alkali[96] and some alkaline-earth[119] atoms. This property, together with the very low temperature (T) achieved in helium droplets – of the order of 0.4 K – makes them the perfect ultracold and inert environment for hosting and studying isolated atoms and molecules, which is at the basis of current applications of helium droplets for spectroscopic studies of atoms and molecules. Besides, the superfluid nature of helium facilitates binary encounters of atoms/molecules in the bulk of the droplet while absorbing the energy released upon recombination, making possible chemical reactions which would not otherwise occur in the gas phase. These unique properties of helium droplets have had a huge impact on their study[111,120-123].

The pickup of Ar, Kr and Xe atoms in the gas phase by ^4He_N droplets with $N > 10^3$ atoms produced by nozzle beam expansions was studied about twenty years ago by Toennies and coworkers[124]. In these experiments the droplets in the helium beam were deflected by impacting with a secondary beam made of rare gas atoms in order to detect the pick-up.

Very recently, time-dependent density functional theory (TDDFT) has been used to address the capture of Cs or Ne atoms by ^{4}He nanodroplets[125,126]. The Cs capture was treated fully three dimensionally with the Cs atom described as a classical particle, whereas for the Ne capture study the Ne atom was described quantum-mechanically but the description was strictly one-dimensional.

[1] Published work, see: F. Coppens, A. Leal, M. Barranco *et al*, J Low Temp Phys **187**, 439 (2017).

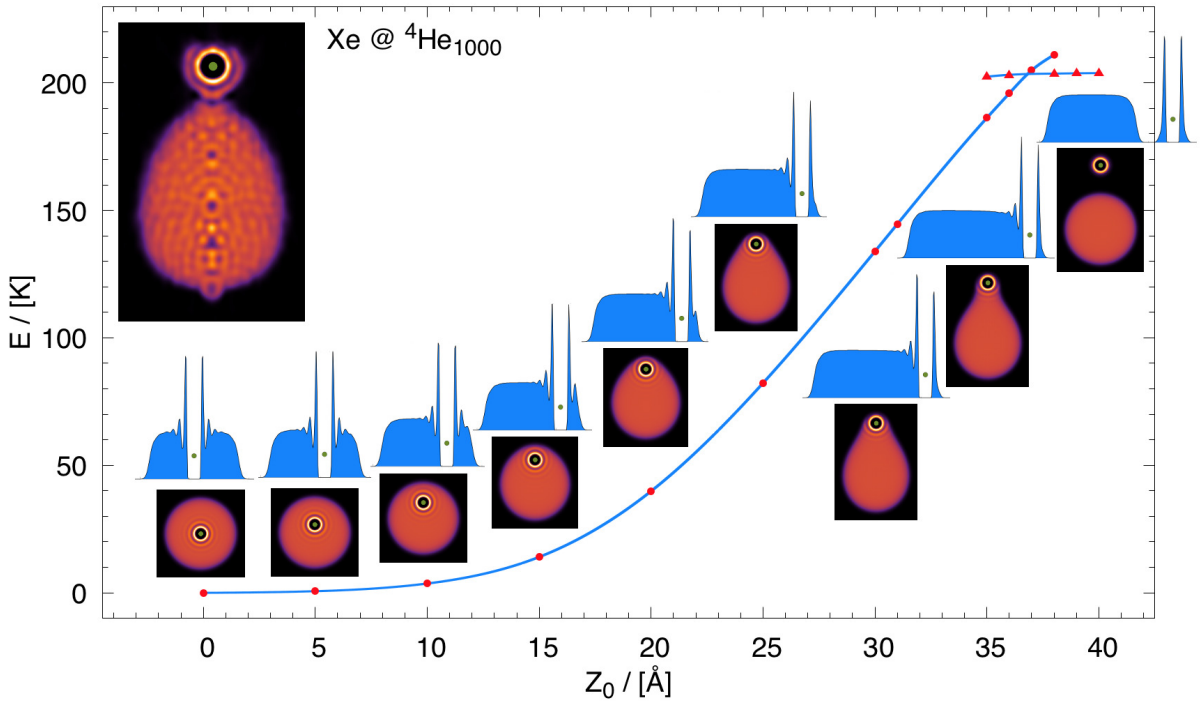

Figure 8.1: Energy of the Xe@^{4}He$_{1000}$ complex as a function of the distance between the Xe atom and the COM of the droplet. Several two-dimensional helium densities and density profiles are shown for distances between 0 and 40 Å in 5 Å steps. Connected (dots) and disconnected (triangles) helium configurations are shown *(see text)*. Top left inset: Snapshot of the helium density at the first turning point during the dynamic evolution of a Xe atom (green dot) at $v_0 = 600$ m/s attained 78 ps after it has started. (Color figure online.)

Motivated by recent experiments that use Xe atoms to visualise vortex arrays in very large helium droplets[104,127], we present here a first step towards the description of the capture of Xe atoms by helium droplets, namely head-on collisions of Xe atoms against a ^{4}He$_{1000}$ droplet. A discussion on the dynamic capture of Xe atoms by droplets hosting vortex lines and vortex arrays will be provided by a forthcoming study combining DFT simulation of vortex arrays as in Refs. [114, 117] for helium nanocylinders and nanodroplets and collision with Xe atoms as in this work. Whenever possible, the results for Xe, a heliophilic atom, are contrasted with results for Cs, a heliophobic atom with similar mass. We use TD-DFT as described in Section 2.6.

8.2 Results

Due to computational constraints we consider a droplet made of $N = 1000$ helium atoms. Its ground state structure is obtained using DFT and gives a sharp-density radius of about

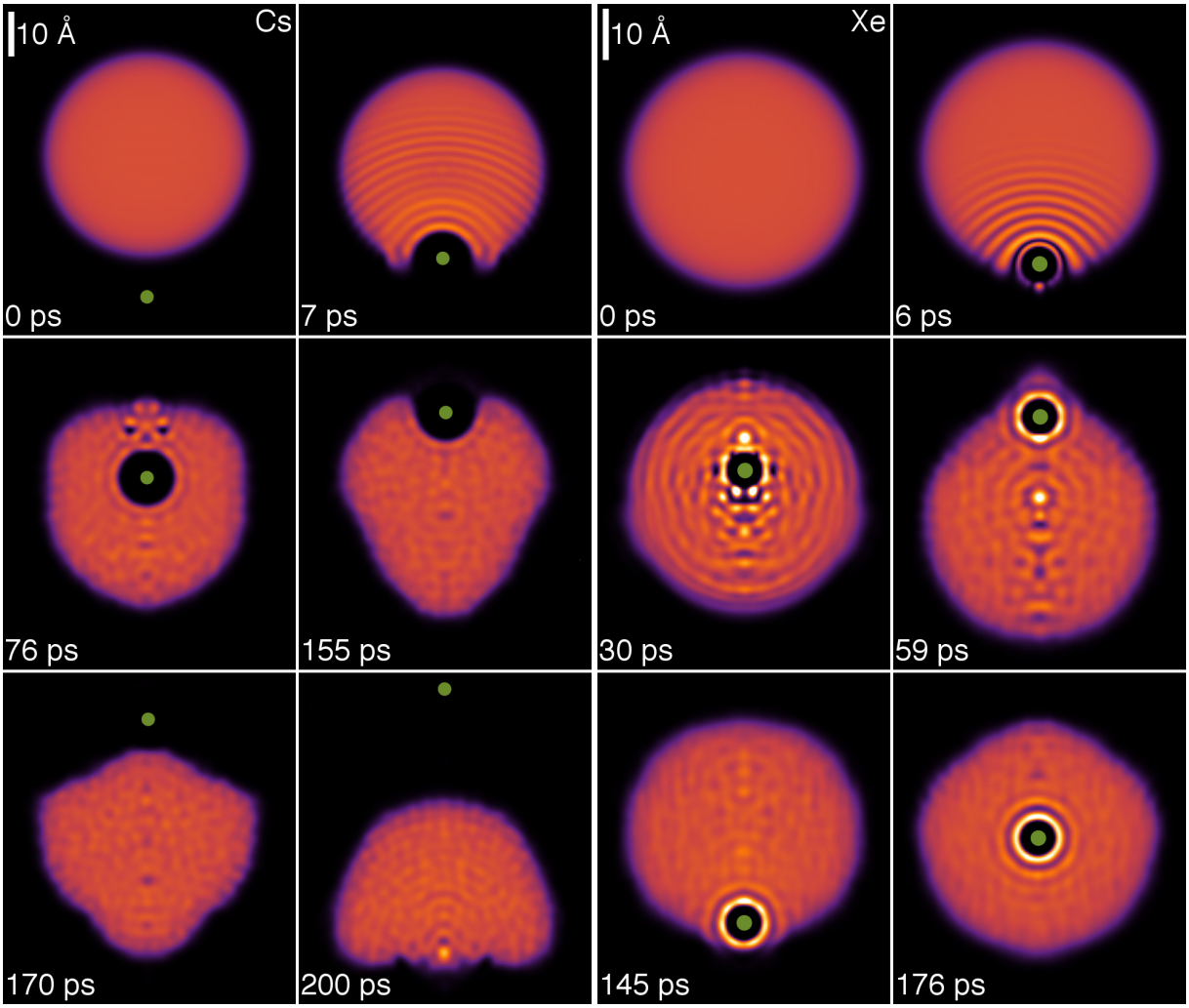

Figure 8.2: Right panel: Dynamic evolution of a Xe atom (big dot) approaching the $^4He_{1000}$ droplet from below at $v_0 = 200$ m/s. The corresponding time is indicated in each frame. Left panel: Same as the right panel, but for a Cs atom. (Color figure online.)

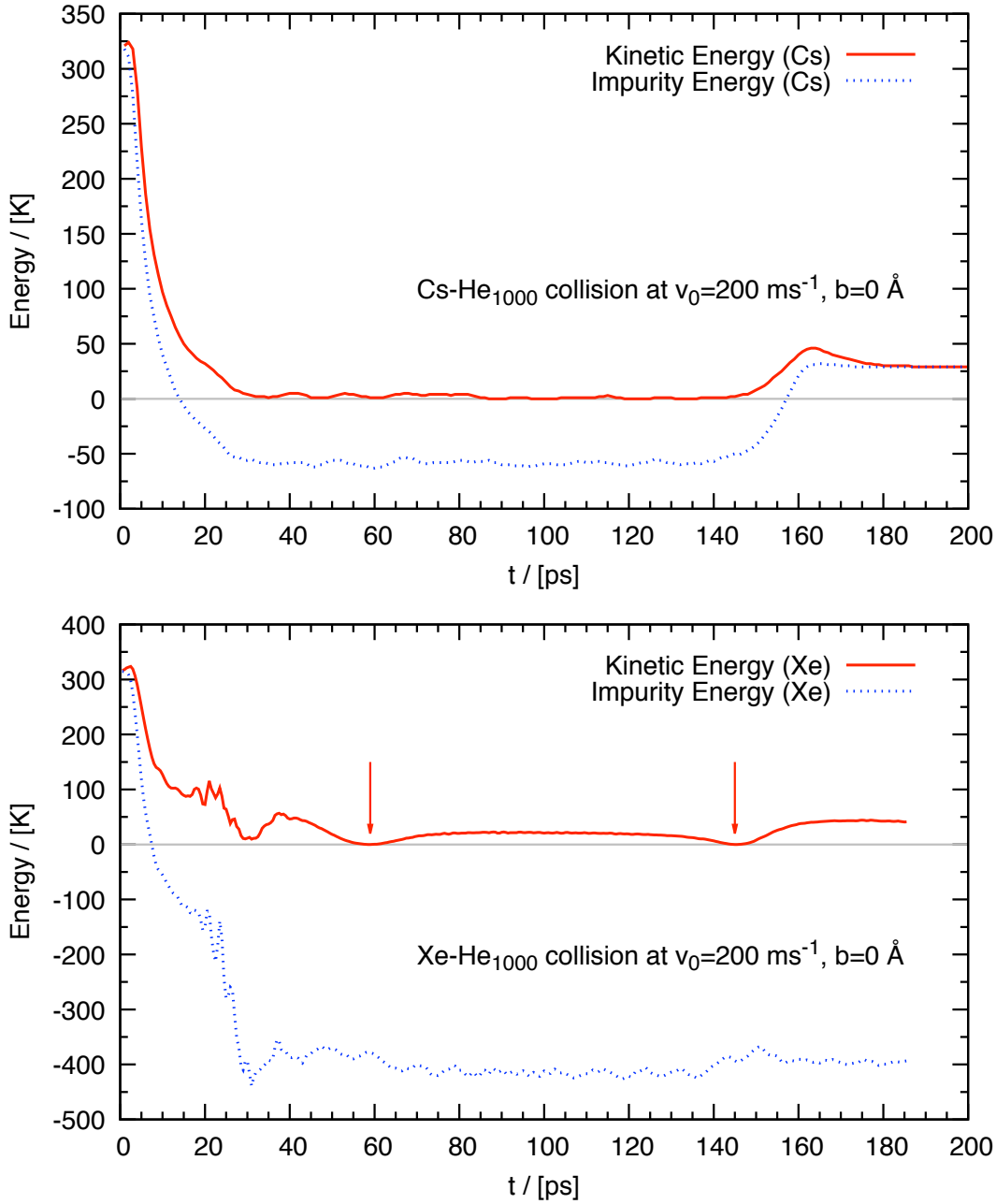

Figure 8.3: Top figure: Kinetic and total (kinetic plus potential) energy as a function of time of a Cs atom head-on colliding against a $^4He_{1000}$ droplet at $v_0 = 200$ m/s. Bottom figure: same as top figure for a Xe atom. The vertical arrows indicate the first two turning points at 59 and 145 ps, whose corresponding helium densities are shown in the right Figure 8.2. (Color figure online.)

22.2 Å. Then the dynamics is initiated by placing the Xe atom 32 Å away from the center of mass (COM) of the droplet with an impact parameter equal to zero (head-on collision). The simulations are carried out for initial Xe velocities v_0 ranging from 200 to 600 m/s in the system of reference of the droplet, corresponding to kinetic energies between 315.8 K and 2842 K. These energies can be compared to the solvation energy of a Xe atom at the center of a $^4\mathrm{He}_{1000}$ droplet, $S_{\mathrm{Xe}} = E(\mathrm{Xe@}^4\mathrm{He}_{1000}) - E(^4\mathrm{He}_{1000}) = -316.3$ K. For the sake of comparison, the solvation energy of Cs is -5.2 K and its equilibrium position is in a dimple at the outer droplet surface, about 26.6 Å from its centre.

Thermal Xe atoms ($v_0 \sim 240$ m/s) are used in the experiments[104,127], and the average droplet velocity is about 170 m/s[128].

Figure 8.1 shows the energy of the Xe@$^4\mathrm{He}_{1000}$ complex referred to that of the equilibrium configuration (Xe at the center of the droplet, -5716.4 K) as a function of the distance between the Xe atom and the COM of the droplet. It is obtained by a constrained calculation similar to that presented in Ref. [129] for Ba^+. With increasing distance, the stretched droplet-Xe configuration eventually breaks into a minicluster around the Xe atom containing about 22 helium atoms disconnected from the rest of the droplet. The appearance of this minicluster is at variance with the situation for a heliophobic impurity such as Cs[125]. The stretched (connected) configuration energies are represented by dots, the disconnected ones by triangles. The two corresponding curves cross at 37 Å. At shorter distances the connected configuration is stable and the disconnected one metastable, and at larger distances the roles are inverted. In an actual dynamics the number of He atoms in the minicluster depends on the velocity of the Xe projectile.

Figure 8.2 displays two-dimensional plots of the helium density for Xe head-on colliding against the $^4\mathrm{He}_{1000}$ droplet at $v_0 = 200$ m/s, and Figure 3 the energy of the impinging atom as a function of time, with the corresponding plots for Cs collisions for the sake of comparison. It can be seen that for both species most of the initial kinetic energy is spent in piercing the droplet surface, after which the impurity moves inside the droplet at a velocity well below the critical Landau velocity v_L.

Figure 8.2 also shows that the collision launches a series of density waves in the droplet that are reflected at the droplet free surface producing complex interference patterns in its bulk. As an illustrative example, Figure 8.4 shows the density profile along the incident direction (z axis) corresponding to the Xe collision at $v_0 = 200$ m/s, 6 ps after the process starts. The wave number associated to this wave can be estimated from the wavelength λ of the oscillations, $q = 2\pi/\lambda \sim 2.7$ Å^{-1}.

In the case of Xe, Figure 8.2 and Figure 3 reveal the appearance of turning points at which the velocity of the impurity is zero. Note that these points are not fixed during the dynamics since the droplet deforms due to the swift motion of Xe inside it; the droplet is not a rigid object and reacts to the motion of the impurity, with energy being transferred

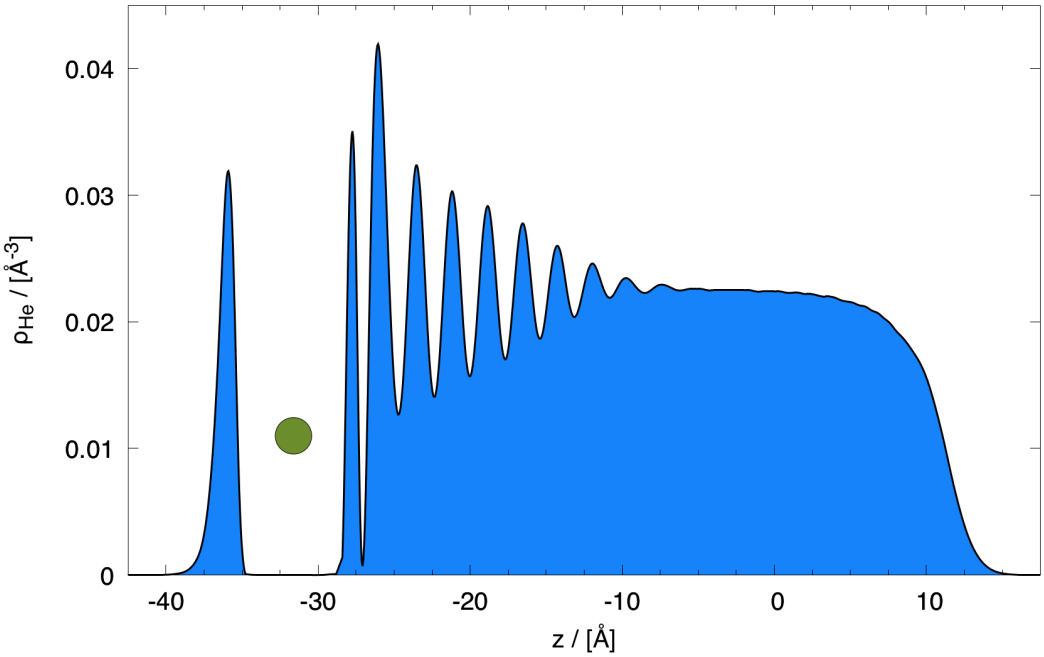

Figure 8.4: Density profile of the He_{1000} droplet along the incident direction corresponding to the Xe collision at v_0 = 200 m/s after 6 ps. (Color figure online.)

not only from the impurity to the droplet but also the other way around[130].

The top left inset in Figure 8.1 shows a snapshot obtained at the first turning point for v_0 = 600 m/s, with 57 He atoms around the Xe dopant. We have found that the Xe atom has to hit the droplet at a velocity above 600 m/s in order to go across the helium droplet, otherwise it remains attached to the droplet. The kinetic energy lost by the Xe atom is partially deposited in the droplet and partially carried away by prompt-emitted helium atoms, *i.e.* atoms expelled early on in the collision and with a significant kinetic energy. The number of He atoms emitted during the first 78 ps is about 47. For comparison, about 19 atoms are emitted after 185 ps for v_0 = 200 m/s. Eventually, the energy deposited into the droplet should be lost by atom evaporation; however, the time scale for this to happen is beyond the reach of any realistic simulation.

The piercing of the droplet by the Cs atom produces a density wave that travels on its surface and collapses at the surface region opposite to the hitting point. This collapse nucleates a vortex ring (the two dark spots in the 76 ps plot of the left panel of Figure 8.2)[125].

It is worth pointing out that the falloff of the Xe velocity in the $t = 20 - 30$ ps interval observed in Figure 3 is due to the increase of its inertia as a result of the appearance of a dynamic "snowball" -a crust of helium atoms surrounding the Xe bubble indicated by the bright spots in Figure 8.2- that is eventually washed out at larger times. At variance with our findings for Ba^+[130], vortex rings have not been nucleated in the case of Xe; in

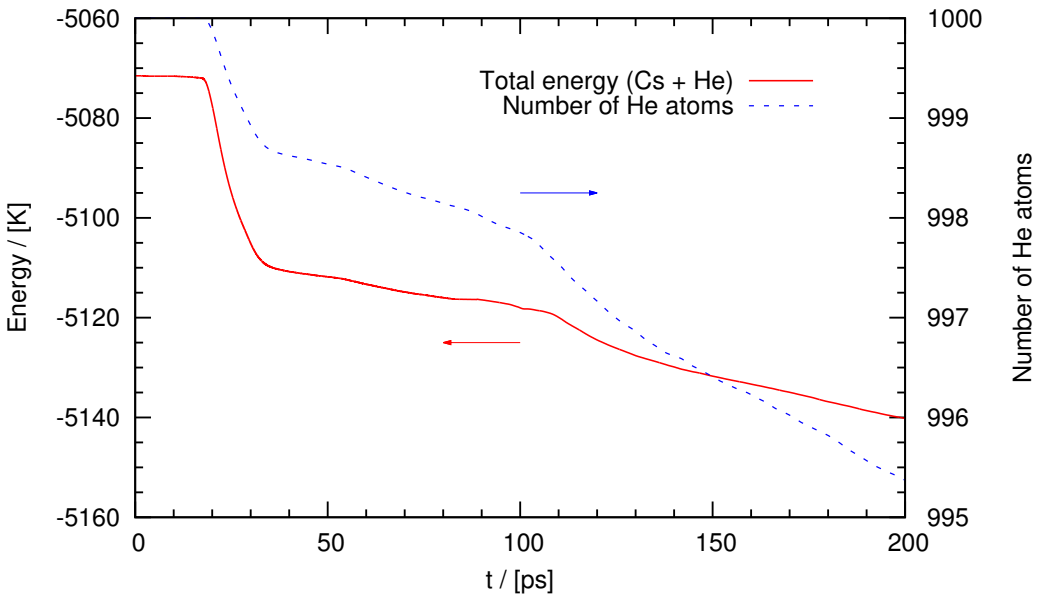

Figure 8.5: Total energy (left scale) and number of atoms in the droplet (right scale) as a function of time for the Cs@^{4}He$_{1000}$ system at $v_0 = 200$ m/s. (Color figure online.)

particular, we have checked that the two dark spots in the 30 ps plot of the right panel of Figure 8.2 for Xe do not correspond to a vortex ring.

The collapse of the Cs bubble at the surface of the droplet some 150 ps after the process gives back to the impurity part of the kinetic energy it has lost in the piercing of the droplet. The Cs atom is expelled at 64.5 m/s (corresponding to 33.6 K kinetic energy). The number of prompt-emitted helium atoms is 5, which is smaller than for Xe at the same collision energy (19 atoms). As revealed by Figure 8.5, they are preferentially emitted as a forward burst (first sharp drop around 20 ps in the number of atoms) and as a backward burst (second sharp drop slightly after 100 ps).

9
Capture by He droplets hosting quantised vortices[1]

9.1 Introduction

As presented in Section 8.1, it is well established that helium droplets can readily capture in their interior almost any atom or molecule interacting with them. Recently, a technique has been introduced to determine the size of large He droplets ($N > 10^5$). It is based on the attenuation of a continuous droplet beam through collisions with Ar atoms at room temperature[128]. The pickup chamber of the droplet beam apparatus is filled with argon gas and the helium droplets experience multiple, isotropic collisions with the Ar atoms on their way towards the detection chamber.

Large helium droplets could also be doped in this way. This method, using Xe atoms, has been instrumental for detecting and imaging quantized vortex arrays in helium droplets[104,113]. Xe atoms were used in these experiments because of their large sensitivity to the x-ray coherent diffractive imaging employed to detect them within the helium droplets. Experiments with large superfluid helium droplets are reviewed in a recent publication[131].

The impurity-droplet interaction in the presence of vortices is also relevant as the first stage of a more complex process leading to the formation of nanowires, see e.g. Refs. [132-135]. Long filaments made of micrometer-sized solid hydrogen particles trapped on quantized vortex cores were used to directly image the vortex reconnection between quantized vortices in superfluid helium[136].

The impact and capture of impurities interacting with pure helium droplets has been addressed recently within time-dependent density functional theory (TDDFT). Real time simulations have been carried out for heliophobic[125] (Cs) and heliophilic[126] (Ne) atoms.

[1] Published work, see: F. Coppens, F. Ancilotto, M. Barranco *et al*, Phys. Chem. Chem. Phys. **19**, 24805-2481 (2017).

In addition to the TDDFT equation for ^{4}He, heavy impurities are treated as classical particles using Newton's equation of motion, whereas a time-dependent Schrödinger equation has been used in the case of light impurities within the mean field model[126,137]. A comparison between the results for head-on collisions of Cs and Xe atoms –heliophobic and heliophilic atoms of similar mass– has been presented in Chapter 8 (see Ref. [138] for the published version).

Here we present results obtained within TDDFT for the collision and capture of Xe and Ar atoms by a ^{4}He$_{1000}$ droplet at different kinetic energies and impact parameters. Special attention is paid to the time-dependent interaction of Xe and Ar atoms with helium nanodroplets hosting vortex lines, and to the effect of multiply-doped vortex arrays in large helium droplets.

Due to the heavy computational cost of the TDDFT simulations presented here, we address only a few facets of the capture process that we consider of experimental relevance rather than carrying out a systematic study of the process. In particular:

• We study the capture of Xe atoms by a ^{4}He nanodroplet, both for head-on collisions and for different impact parameters, with velocities ranging from thermal values up to several hundred m/s. The results of peripheral collisions with different values of the impact parameter are used to estimate the cross section for the Xe capture.

• We study how a Xe atom dynamically interacts with a droplet hosting a vortex line, under different initial conditions resulting in different velocity regimes of the impurity as it collides with the vortex core: i) a Xe atom initially at rest on the droplet surface and sinking under the effect of solvation forces; (ii) a head-on collision of a moving Xe or Ar atom against the ^{4}He nanodroplet.

• We study the stationary state of a large ^{4}He$_{15000}$ droplet hosting a ring of six vortex lines, doped with Ar atoms completely filling all six vortex cores. This is the simplest system that mimics those experimentally described in Ref. [104], where doped vortex arrays embedded in rotating ^{4}He microdroplets have been imaged.

Multimedia materials accompany this work, showing the real time dynamics of several impact/capture processes described here. These materials are presented in the Electronic Supplementary Information (ESI) of Ref. [139] (see DOI: 10.1039/C7CP03307A). They constitute an important part of this work, since often it is only by viewing how a complex microscopic process unfolds in real time that one can catch important physical details which would otherwise escape in a written account.

9.2 Xe capture by vortex-free droplets

We have simulated head-on collisions of a Xe atom with a $^4He_{1000}$ droplet at relative velocities v_0 ranging from 200 to 600 m/s. Figure 9.1 displays two-dimensional plots of the helium density for the highest value, $v_0 = 600$ m/s. This velocity is well above the range of velocities typically encountered in experiments[104,113,128]. In spite of the appearance of disconnected helium density shown in the $t = 87$ ps frame, we have found that the Xe atom eventually turns around and is captured again inside the droplet even at that relatively high impact velocity. Note that the Xe impurity, even when it temporarily emerges from the bulk of the droplet, appears to be coated with a few ^{4}He atoms, see the configuration at 87 ps.

Figure 9.1 also shows the development of bow waves in the density profile, moving ahead of the impurity at supersonic velocity, and an incipient conic density wave front with its vertex at the Xe bubble. Similar conic shapes, characteristic of supersonic flows, are found when an impurity moves in bulk liquid helium. In the present case the limited size of the droplet and the loss of kinetic energy during the first stages of the collision smooth out this front, making it just barely visible in the figure.

For low initial velocities of the impurity, we find that Xe moves back and forth inside the droplet. The turning points are not fixed, because the droplet deforms due to the displacement of the Xe atom and to the waves that are continuously emitted by the moving impurity (mainly in the direction of its motion), hit the droplet surface, and are reflected back inside it[138]. This is shown in Figure 9.2 for $v_0 = 200$ and 300 m/s.

Thermal Xe atoms ($v_0 \sim 240$ m/s) are used in the vortex imaging experiments[104,113], and the average droplet velocity as it travels through the pick-up chamber is about 170 m/s[128], corresponding to relative collision velocities which are within the range investigated here. The kinetic energy gained by the Xe atom after the turning point at 140 -150 ps is precisely due to the fact that the droplet is not a rigid object and reacts to the motion of the impurity. As a consequence, energy is transferred not only from the impurity to the droplet but also the other way around. We want to emphasize that the droplet experiences large deformations rather than large displacements; the velocity of the center of mass (COM) of the droplet is rather small (below 6 m/s for $v_0 = 200$ and 300 m/s as well) due to the large mass difference between the impurity and the droplet.

We have found that most of the energy is transferred from the Xe to the droplet in the first stages of the collision. This is why, for collisions in this kinetic energy range leading to Xe capture, the motion of the impurity inside the droplet is independent on the initial kinetic energy to a large extent. This is shown in Figure 9.3, which displays the trajectory of Xe (Ar) in phase space for $v_0 = 200$ (360) m/s. The figure also shows similar trajectories in the case where a vortex is present in the droplet; these cases will be discussed later in

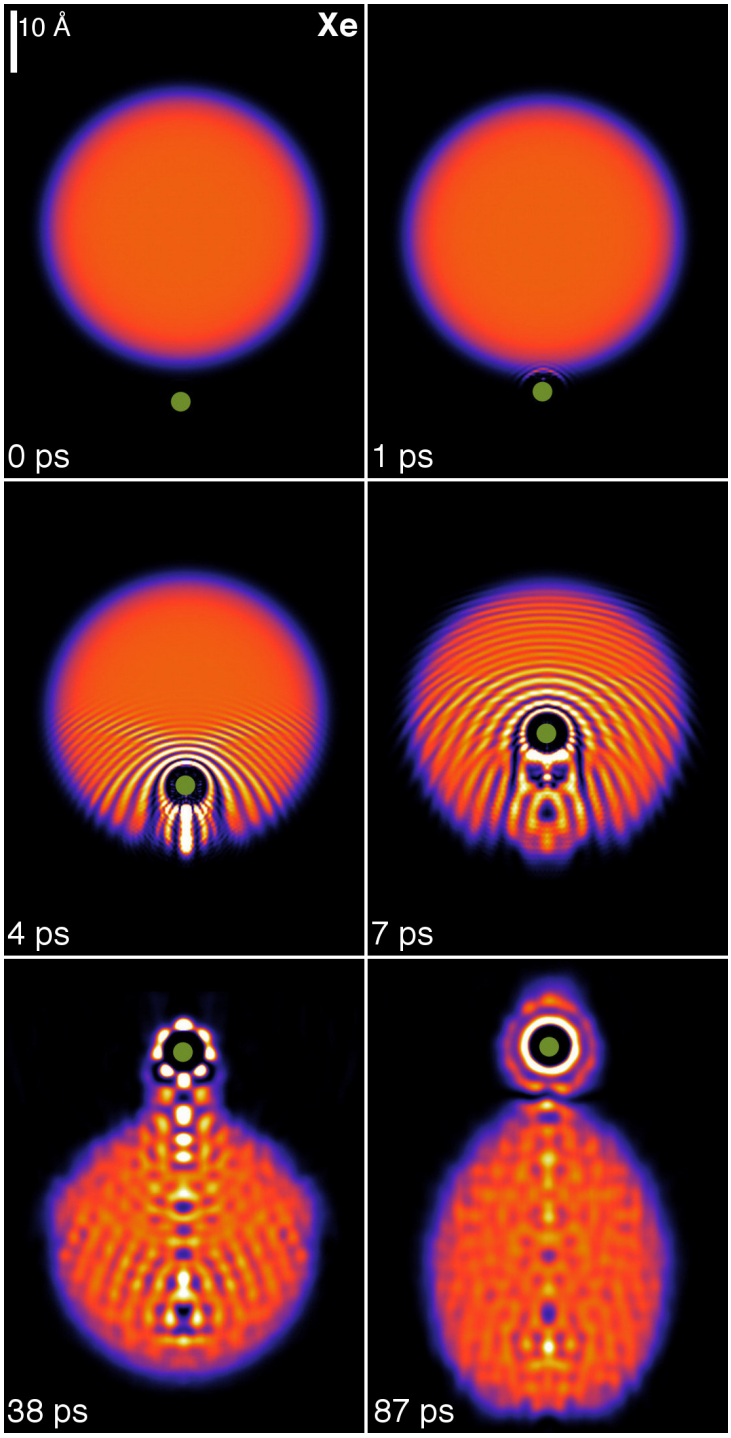

Figure 9.1: Dynamic evolution of a Xe atom (green dot) approaching the $^4He_{1000}$ droplet from below at $v_0 = 600$ m/s. The corresponding time is indicated in each frame. Bright spots correspond to high density regions. (Reproduced from Ref. [139].)

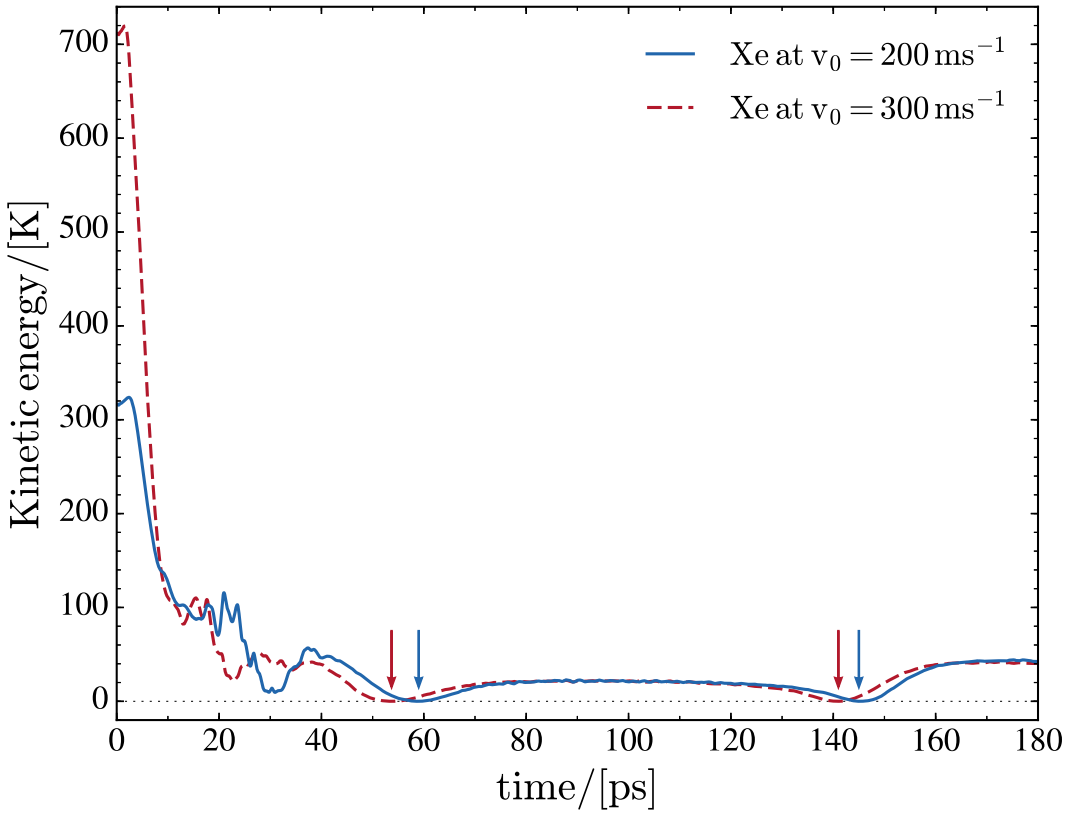

Figure 9.2: Kinetic energy of the Xe atom in the center of mass (COM) frame of the $^4He_{1000}$ droplet as a function of time for a head-on collision at v_0= 200 and 300 m/s. The kinetic energy increase during the first few picoseconds is due to the acceleration produced by the attractive part of the Xe-He potential. The vertical arrows indicate the first two turning points inside the droplet.

Table 9.1: Number of He atoms promptly ejected (N_e) and average energy per ejected atom (E_e) during the first 200 ps.

Species	v_0 (m/s)	N_e	E_e (K)
Xe	200	18	19
	300	28	23
	400	37	30
Ar	360	16	22

this chapter.

The kinetic energy lost by the impurity atom is partly deposited in the droplet, where it produces large deformations and sound waves, and partly carried away by prompt-emitted helium atoms. These are atoms with a significant kinetic energy which are expelled from the droplet early on in the collision process.

Figure 9.4 shows the number of atoms remaining in the simulation cell as a function of time for collisions with Xe at $v_0 = 200, 300$ and 400 m/s.

Eventually, the energy deposited into the droplet should be lost by atom evaporation. The energy carried away by the ejected He atoms during the first 200 ps is collected in Table 9.1 for the head-on collisions described in this paper. For comparison, the calculated binding energy of a helium atom in the $^4He_{1000}$ droplet is 6.0 K. Note that helium atom ejection continues after 200 ps, the droplet still being far from "thermalized" (equilibrated).

In the case of heavy dopants it is possible to obtain a simple expression for their capture cross section $\sigma(E)$. Defining

$$\kappa = \sqrt{\frac{2\mu E}{\hbar^2}} \ , \tag{9.1}$$

where μ is the reduced mass of the system and E is the available energy in the center-of-mass frame, and provided that the reduced de Broglie wave length of the impurity $\lambda/(2\pi) = 1/\kappa$ is much smaller than the dimensions of the droplet (which is the case for all v_0 in this study), the system behaves classically and[125]

$$\sigma(E) = \frac{\pi}{\kappa^2}\sum_{\ell=0}^{\ell_{cr}}(2\ell+1) = \frac{\pi}{\kappa^2}(\ell_{cr}+1)^2 \tag{9.2}$$

where ℓ_{cr} is the largest relative angular momentum leading to the impurity capture. For a given energy, ℓ_{cr} is determined by carrying out simulations with different impact parameters b using $\ell = \mu v_0 b/\hbar$. We have done it for Xe at $v_0 = 200$ m/s. Figure 9.5 shows the simulation corresponding to the largest impact parameter among the ones we have calculated which led to Xe capture, $b = 20.3$ Å, and Figure 9.6 shows the simulation

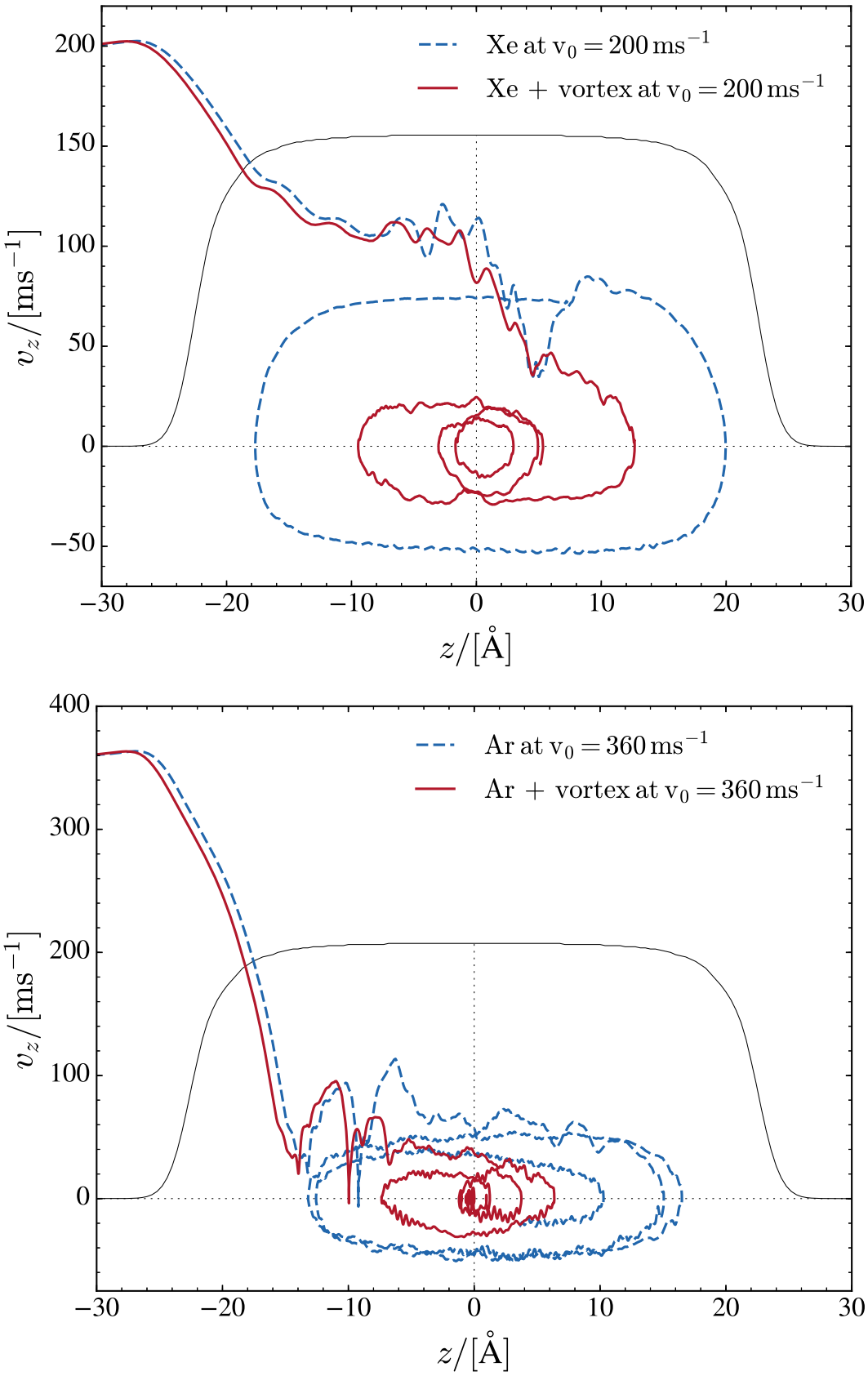

Figure 9.3: Top: Phase-space trajectory of Xe for a head-on collision at $v_0 = 200$ m/s against a $^4\mathrm{He}_{1000}$ droplet with and without a vortex line. The Xe atom is referred to the COM frame of the droplet. Bottom: Same as top panel for Ar at $v_0 = 360$ m/s. The droplet density at $t = 0$ is also represented in arbitrary scale (black profile)

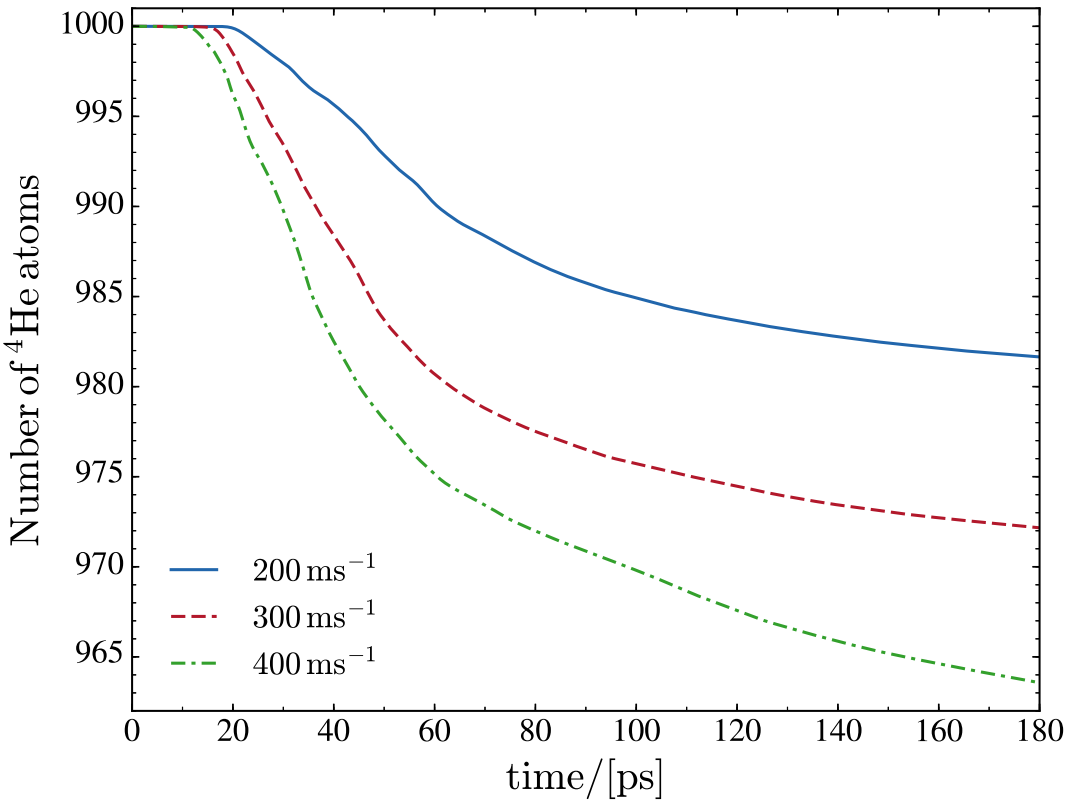

Figure 9.4: Number of He atoms remaining in the droplet as a function of time for the Xe against ^{4}He$_{1000}$ collision at $v_0 = 200, 300$ and 400 m/s.

corresponding to the smallest one which led to Xe deflection, $b = 22.2$ Å. The radius of the droplet, which is defined as $R = r_0 N^{1/3}$ with $r_0 = 2.22$ Å, is 22.2 Å for $N = 1000$. Hence, at this energy -well within the thermal conditions of the experiment- the cross section for Xe capture is very similar to the geometric droplet cross section.

The circulation lines of the superflow are displayed in two selected panels in Figure 9.5 and Figure 9.6. They show the flow pointing towards the approaching Xe atom at the beginning of the collision and the appearance of vortex loops in the droplet (only visible in Figure 9.5) at the latest stages of the simulation. Vortex loops appear from local distortions of the droplet surface[140]. The circulation lines displayed in the figures of this work have been drawn inside the region where the density is above 0.5 ρ_0 (with ρ_0= 0.0218 Å^{-3}) that defines the dividing surface of the droplet.

In peripheral collisions not only energy but also angular momentum is deposited into the droplet, which allows to visualize the irrotational flow of the superfluid helium. In particular, for Xe at v_0 =200 m/s and b=22.2 Å the initial angular momentum is 917 $\hbar$. This collision was followed for some 220 ps and produced the ejection of 15 He atoms, 5 of them attached to the Xe atom, see Figure 9.6. After the collision, the Xe+^{4}He$_5$ complex carries away 522 angular momentum units, while some 95 units are deposited in the droplet as vortex loops and capillary waves[141], see bottom right panel of Figure 9.5 and Figure 9.6. The remaining angular momentum is taken away by the ejected helium atoms.

9.3 Helium droplets hosting vortex lines

To determine the structure of a droplet hosting a singly-quantized linear vortex we have started the imaginary time iteration from a helium density in which the vortex is "imprinted". As described in Section 2.5.2, a vortex line along the z can be described by the effective wave function

$$\Psi_0(\mathbf{r}) = \rho_0^{1/2}(r)\, e^{i\,\mathcal{S}(\mathbf{r})} = \rho_0^{1/2}(\mathbf{r})\, \frac{(x+iy)}{\sqrt{x^2+y^2}} \tag{9.3}$$

where $\rho_0(\mathbf{r})$ is the density of either the pure or the impurity-doped droplet without vortex. Vortex lines along other directions passing through a chosen point can be imprinted as well[142].

In the case represented by Equation (9.3), if the impurity is within the vortex core along a symmetry axis of the impurity-droplet complex, the effective wave function $\Psi_0(\mathbf{r})$ – before and after relaxation– is an eigenvector of the angular momentum operator $\hat{L}_z$. The angular momentum of the droplet is then

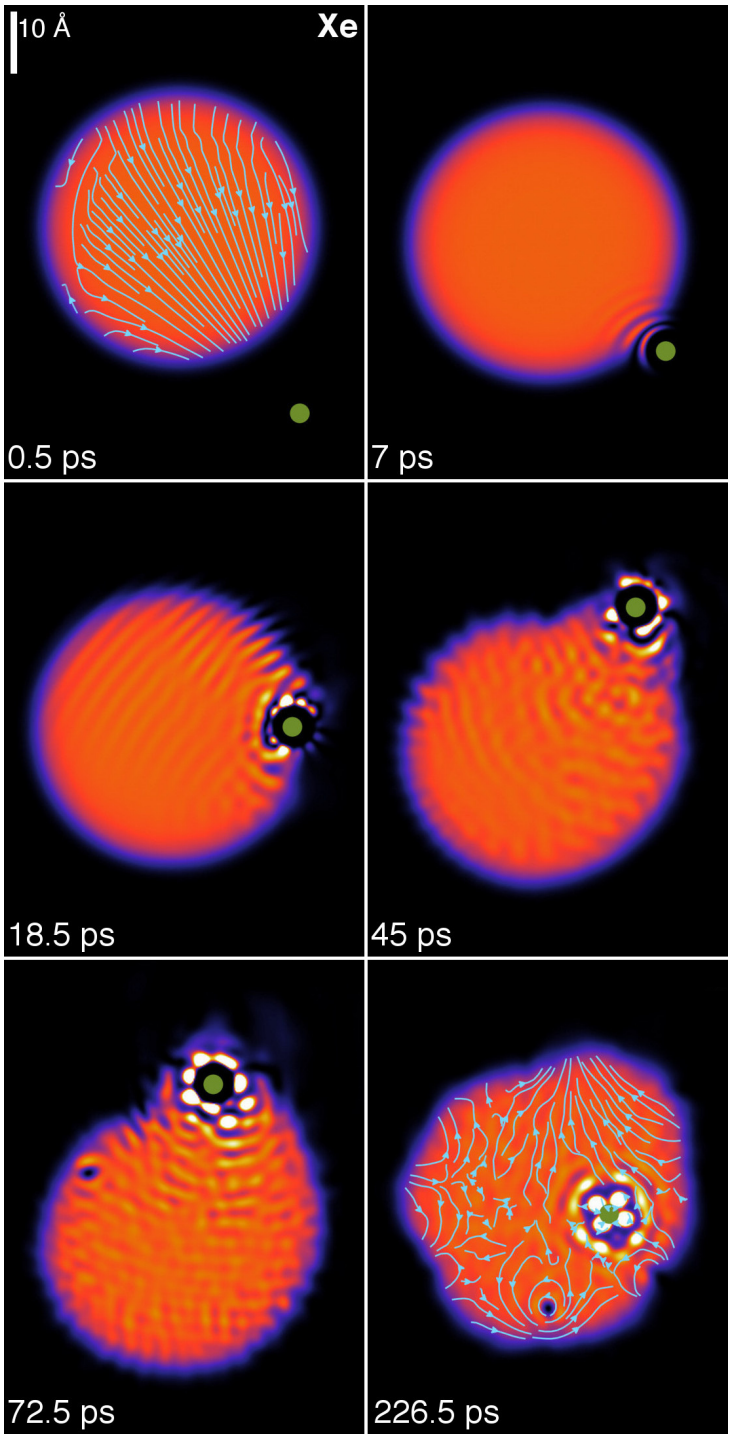

Figure 9.5: Dynamic evolution of a Xe atom (green dot) approaching the $^4He_{1000}$ droplet from below at $v_0 = 200$ m/s with impact parameter $b = 20.3$ Å. The corresponding time is indicated in each frame. The velocity fields are represented in cyan in the panels at 0.5 ps and 226.5 ps. The bright spots are high He density blobs appearing around the Xe atom because of the attractive He-Xe interaction. See the ESI[139] for the movie of the complete evolution.

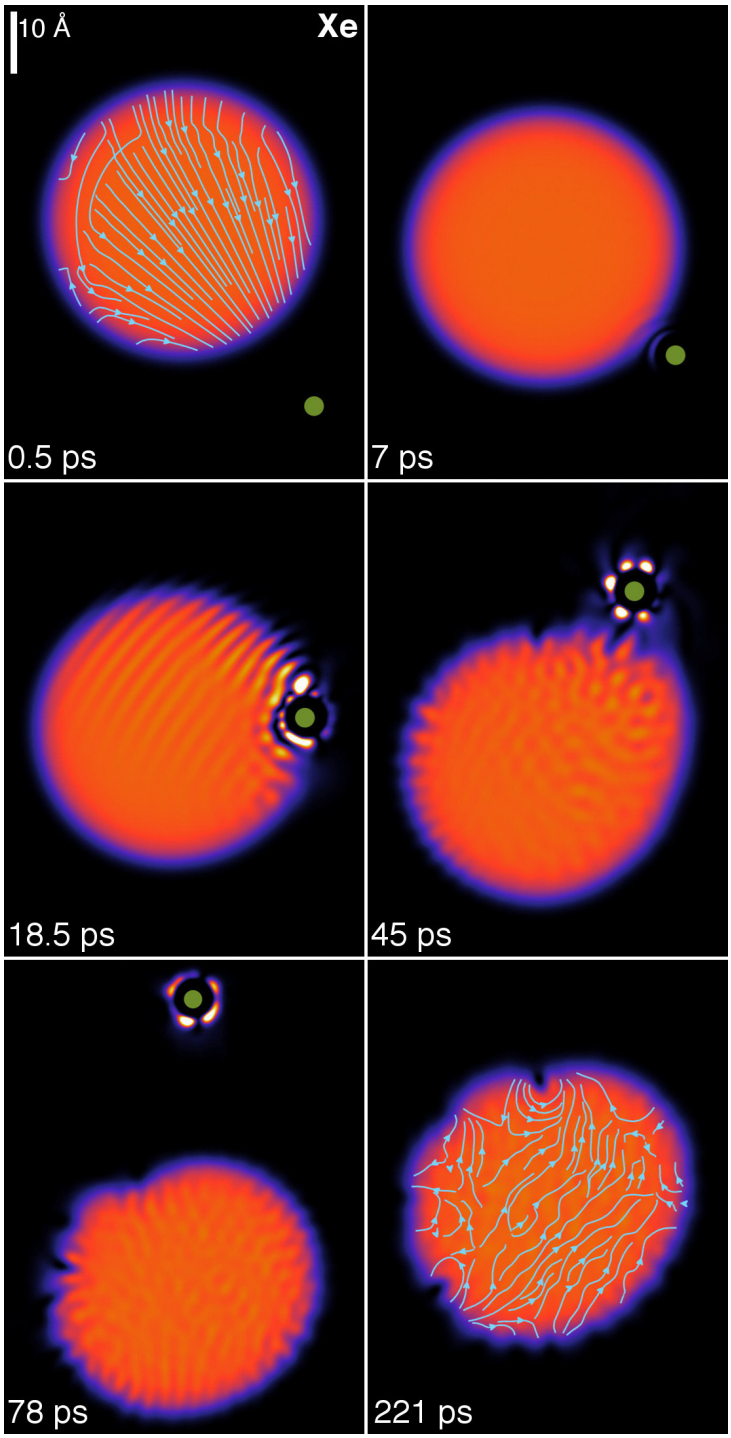

Figure 9.6: The same process as in Figure 9.5 but with an impact parameter $b = 22.2$ Å instead of $b = 20.3$ Å. Note that in this case, after about 78 ps (bottom left panel), the Xe atom is ejected with some helium density attached to it. See the ESI[139] for the movie of the complete evolution.

$$\langle \hat{L}_z \rangle = \langle \Psi_0(\mathbf{r}) | \hat{L}_z | \Psi_0(\mathbf{r}) \rangle = N\,\hbar \tag{9.4}$$

(see Section 1.2.4). Different energy balances involving pure and doped droplets hosting vortices are defined[114,142,143]:

- Solvation energy of the impurity:

  $S_X = E(X@^4\mathrm{He}_N) - E(^4\mathrm{He}_N)$

- Vortex energy:

  $E_V = E(V@^4\mathrm{He}_N) - E(^4\mathrm{He}_N)$

- Binding energy of the impurity to the vortex:

  $B_X = S_X - \{E[(X+V)@^4\mathrm{He}_N] - E(V@^4\mathrm{He}_N)\}$

Using the functional of Ref. [59] and the He-rare gas pair potentials of Ref. [144], solvation energies of -316.3 K and -215.7 K have been found for Xe and Ar atoms, respectively. Thus, for the same incident kinetic energy, about 100 K of additional energy have to be dissipated in the case of Xe in order to get the same kinematic conditions than for Ar.

The binding energy of the impurity to the vortex is the result of a delicate balance between terms which are individually much larger than their difference. It can thus be affected by relatively large inaccuracies. Within DFT, it has been found that the Xe atom is barely bound to the vortex line, with $B_{\mathrm{Xe}} \sim 3-5$ K[117,143].

A critical angular velocity ω_c exists above which nucleation of vortices with quantized velocity circulation in units of h/m_4 occurs. The critical angular velocity for nucleating a vortex line along a diameter in a droplet made of N helium atoms is

$$\omega_c = \frac{1}{\hbar}\frac{E_V}{N} \tag{9.5}$$

This expression is obtained by computing the energy that minimizes $\langle H - \omega L_z \rangle$ (*i.e.* corresponding to the equilibrium configuration in the corotating frame) with and without a vortex line[145].

Using the values appropriate for a $^4\mathrm{He}_{1000}$ droplet we obtain $\omega_c = 0.127$ K/$\hbar$ = 0.0167 ps^{-1}.

When the angular velocity is increased above ω_c, larger amounts of angular momentum may be stored into the superfluid by increasing the number of nucleated vortices. The higher the angular velocity, the more packed the vortex array is around the rotation axis. These vortices arrange themselves into ordered structures whose existence in bulk superfluid ^{4}He was established long ago[146,147].

To generate vortex arrays we have worked in the fixed-droplet frame of reference (corotating frame at angular velocity ω), *i.e.* we look for solutions of the following EL equation:

$$\{\mathcal{H}[\rho] - \omega\,\hat{L}_z\}\,\Psi(\mathbf{r}) = \mu_4\,\Psi(\mathbf{r})\,, \tag{9.6}$$

In this case, $\Psi(\mathbf{r})$ no longer is an eigenvector of the angular momentum. To determine $\Psi(\mathbf{r})$ describing a configuration where n_v vortex lines are present we have followed again the imprinting strategy, starting the imaginary-time evolution of Equation (9.6) with the helium effective wave function

$$\Psi_0(\mathbf{r}) = \rho_0^{1/2}(\mathbf{r}) \prod_{j=1}^{n_v} \left[\frac{(x - x_j) + i(y - y_j)}{\sqrt{(x - x_j)^2 + (y - y_j)^2}} \right] \tag{9.7}$$

where $\rho_0(\mathbf{r})$ is the density of the vortex-free droplet and (x_j, y_j) is the initial position of the j-vortex linear core with respect to the z-axis of the droplet (note that in Refs. [114, 117] $\Psi_0(\mathbf{r})$ was incorrectly written). We underline the fact that during the functional minimization of the total energy, the vortex positions and shapes will change to provide at convergence the lowest energy vortex configuration for the given value of the angular velocity ω.

Figure 9.7 shows the two-vortex stationary configuration of a $^4\mathrm{He}_{1000}$ droplet in the corotating frame at angular frequency ω= 0.175 K/ $\hbar$ = 0.0229 ps^{-1}. The angular momentum of this configuration is $\langle \hat{L}_z \rangle = 1836\ \hbar$. Notice the bending of the vortex line so that they meet the droplet surface perpendicularly at both ends, and also the flattening of the droplet in the z direction due to centrifugal forces.

At variance with the single vortex line along the symmetry axis of the droplet, the two-vortex configuration is not stationary in the laboratory frame, where the density and velocity field change with time. To show this, $\Psi(\mathbf{r})$ has been evolved in the laboratory for about 150 ps taking as initial condition the stationary configuration in the corotating frame. As expected, the vortex cores appear to rotate in the laboratory frame. Within the numerical accuracy, they do so rigidly. This can be seen in Figure 9.7. Besides, they rotate precisely at ω= 0.0229 ps^{-1}. This is a stringent test on the accuracy of the dynamics and the consistency of the method. It can be seen in the ESI material how the two vortex lines turn around each other.

Figure 9.7 shows how a superfluid droplet hosting a vortex array "rotates". The fact that the vortex cores rotate rigidly is not in contradiction with the irrotational character of the superfluid flow, since they are empty. The cores carry along with them the superfluid whose velocity field is irrotational, whereas for a rigid solid or a classical liquid in steady flow one has $\mathbf{v} = \omega \times \mathbf{r}$, hence $\nabla \times \mathbf{v} = 2\,\omega$. The circulation lines in Figure 9.7 do not correspond to a rigid rotation, but to an irrotational flow in the presence of two vortices.

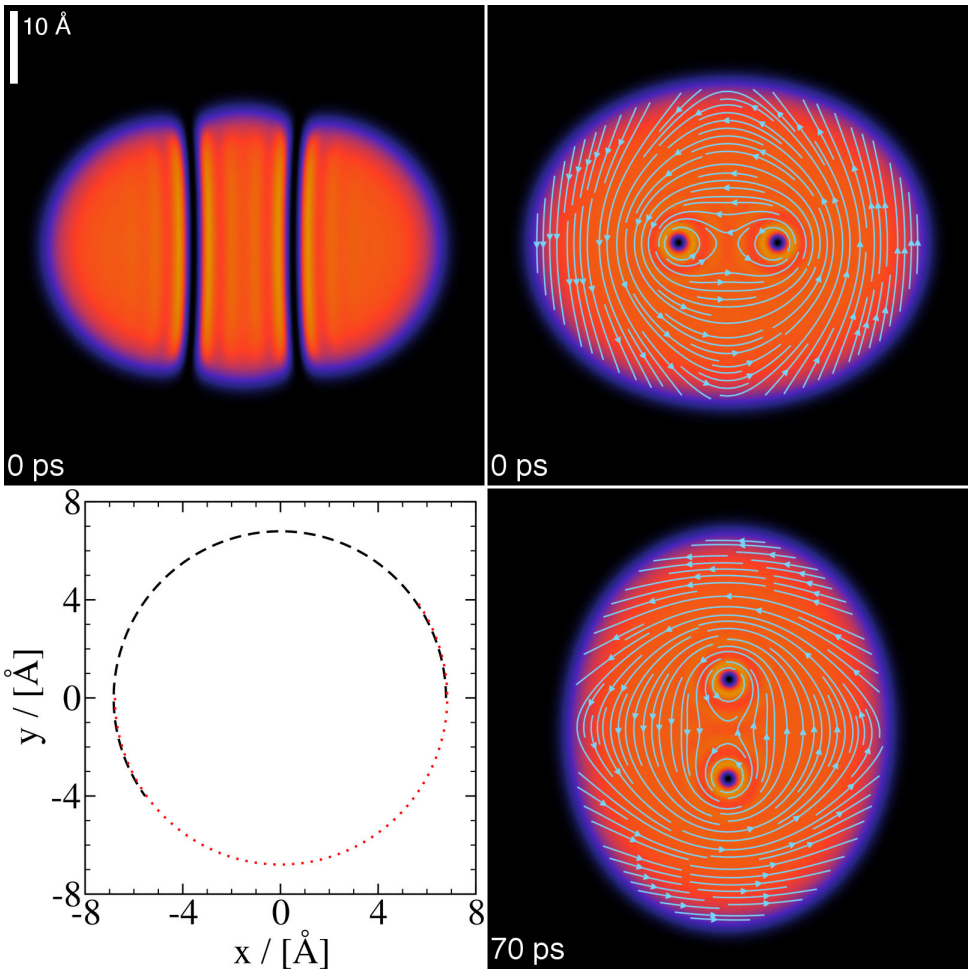

Figure 9.7: $^4He_{1000}$ droplet at $\omega = 0.0229$ ps^{-1}: Top panels, stationary two-vortex configuration on the $x - z$ plane (left) and $x - y$ plane (right) in the corotating frame. Bottom left panel, trajectory of the vortex cores in the $x - y$ plane of the laboratory frame. The dashed line is the trajectory of one of the vortex cores, and the dotted line that of the other. Both trajectories overlap and show that the vortex cores rotate rigidly and this is also visualised by the velocity field lines shown in the right two panels. Bottom right panel, helium density in the $x - y$ plane at $t = 70$ ps obtained in the laboratory frame starting from the above configuration[139].

The helium density adapts to the vortex cores as they rotate and this gives the appearance of a solid rotation in the laboratory frame, but it is not.

It is worth discussing the different configurations that may appear when $\omega < \omega_c$. The lowest energy corresponds to the current-free (CF) $\langle L_z \rangle = 0$ configuration. Metastable one-vortex ($1V$) configurations with $\langle L_z \rangle = N\hbar$ also exist in this angular frequency range[114,117]. Other irrotational (IR) configurations with $\langle L_z \rangle < N\hbar$ do exist, arising from velocity potentials such as e.g. $\mathcal{S}(\mathbf{r}) = \alpha\, xy$. For an ellipsoidal droplet with a sharp surface, the parameter α is related to the angular velocity around the z-axis and the deformation of the ellipsoid, see the Appendix and Refs. [148-150].

These IR configurations may be generated by using the phase $\mathcal{S}(\mathbf{r}) = \alpha\, xy$ in Equation (9.3) and minimizing $\langle H - \omega \hat{L}_z \rangle$. At a given value of $\omega < \omega_c$, the energies in the corotating frame are ordered as $E_{CF} < E_{IR} < E_{1V}$. Figure 9.8 shows the stationary configuration in the corotating frame corresponding to $\omega = 0.10$ K/$\hbar$= 0.0131 ps^{-1}. Although this angular frequency is close to ω_c, this configuration is hardly distorted and hosts a negligible amount of angular momentum: less than $5 \times 10^{-2}\,\hbar$, compared to the value of $10^3\,\hbar$ at ω_c). The circulation lines can be analytically calculated if the density profile is approximated by that of an ellipsoid with constant density, see the Appendix.

Figures similar to Figure 9.8 are shown in Refs. [148, 149] for a rotating elliptic vessel filled with a fluid whose flow is irrotational. Whereas in the case of a rigid solid or viscous liquid in steady flow the entire system rotates as a whole, an irrotationally flowing fluid in a rotating vessel is just pushed by the walls of the container; the same happens for a Bose-Einstein condensed gas in a rotating trap[150]. For an isolated self-bound ^{4}He droplet, the apparent "rotation" of the system in the laboratory arises from deformations of the fluid elements constituting the droplet, but not from their local rotation which is forbidden by the irrotational condition. The vorticity Ω (defined in hydrodynamics as[151] $\Omega = \nabla \times \mathbf{v}(\mathbf{r})$), initially distributed in the helium droplet when it is in the normal phase, concentrates in the vortex lines when the droplet becomes superfluid and its velocity field becomes irrotational.

The above discussion shows how difficult is to set a superfluid droplet in rotation. Experimentally[104,113,115] the situation is different, since the helium droplet is initially in a normal phase state at a temperature above the normal-to-superfluid transition temperature T_λ (about 2.17 K in bulk liquid at 1 bar). As a consequence, it may store large amounts of angular momentum and experience large deformations. Copious evaporation drives the droplet into a superfluid state at a temperature below T_λ and the angular momentum remaining in the droplet is then stored in vortex arrays that are being nucleated.

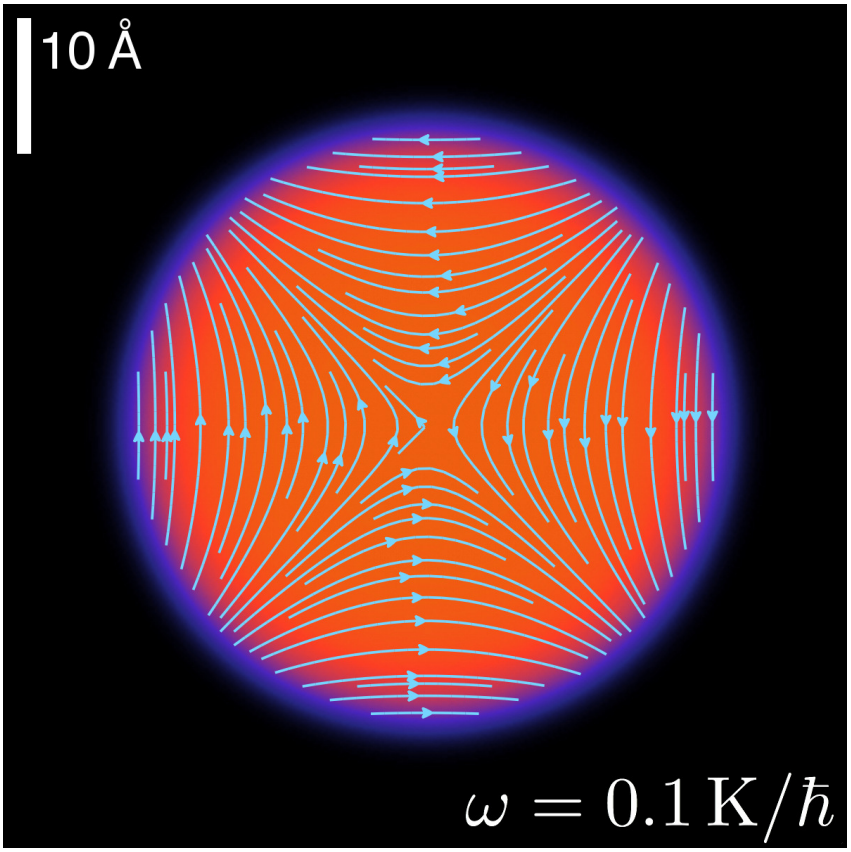

Figure 9.8: Stationary configuration of the $^4\mathrm{He}_{1000}$ droplet at $\omega_c \gtrsim \omega = 0.10\,\mathrm{K}/\hbar = 0.0131\,\mathrm{ps}^{-1}$ in the corotating frame ($x-y$ plane). Superimposed is the irrotational velocity field arising from a velocity potential of the form $\mathcal{S}(\mathbf{r}) = \alpha\, x y$.

9.4 Dynamics of Xe and Ar capture by vortex lines

To study the interaction of an atomic impurity with vortices, we have imprinted a vortex line in the $^4He_{1000}$ droplet and prepared the Xe atom in different kinematic conditions.

The inelastic scattering of xenon atoms by quantized vortices in superfluid bulk helium has been addressed in Ref. [152]. It was found that a head-on collision leads to the capture of Xe by the vortex line for v_0 = 15.4 m/s, but not for v_0=23.7 m/s. We have carried out an equivalent simulation by initially placing the Xe atom inside the droplet 10 Å away from the vortex line and sending it head-on towards the vortex at a velocity of 10 m/s. This velocity is of the order of the thermal velocity of a Xe atom in a droplet under experimental conditions, once the droplet has thermalized after capturing the Xe atom (T ~0.4 K)[120]. Since the equilibrium position of the Xe atom is at the center of the droplet, it moves to this region and remains there during the rest of the simulation. In this region of the droplet, the Xe atom is also attracted by the vortex, but it is deflected by the superfluid flow around the vortex line and ends up orbiting around it. Hence it is captured by the vortex without getting into its core.

A detailed analysis of the Xe capture as a function of the impact parameter has also been carried out in Ref. [152], with the conclusion that when the impact parameter of the Xe atom approaching the vortex line is larger than about 5 Å, Xe is deflected but not captured. In the case of droplets, the final result is very different. Upon capture, the Xe atom wanders erratically inside the droplet, as we have seen in the case of vortex-free droplets. The surface of the droplet deforms dynamically and acts as a "pinball machine", which eventually brings the Xe atom close enough to the vortex line if it missed it in the first attempt or was not previously ejected off the droplet.

The smoothest capture process one might think of corresponds to the Xe atom being initially placed at rest on the droplet surface, as no kinetic energy is given to the impurity. The Xe atom is accelerated towards the center of the droplet due to the attractive He-Xe interaction. We show that, under these kinematic conditions, some He atoms are first drawn towards the impurity because they are lighter, see also Figure 4, Figure 9.10 and the Electronic Supplementary Information available at doi: 10.1039/C7CP03307A for the continuous movie corresponding to the simulation.

Eventually, the impurity with its "solvation structure" sinks, acquires some velocity, and is also deflected by the velocity field of the vortex line.

We have tried two different initial locations of the Xe atom on the droplet surface. One is a point on the equator of the droplet, in a plane perpendicular to the vortex line; the other location is one of the open vortex core ends. Our aim was to see if a sensible difference in the transit time of Xe across the droplet could be detected. The simulations do not show important differences between the time taken by the impurity to reach the center

of the droplet. It is about 20 % larger when Xe starts from the equator than from the core end[139]. It is worth noting that in the latter case the sliding of the impurity along the core proceeds rather smoothly, and that the impurity oscillates back and forth much as in the vortex-free case.

The simulation of Xe (v_0=200 m/s) and Ar (v_0=360 m/s) atoms head-on colliding with a $^4He_{1000}$ droplet perpendicularly to the vortex line has been analyzed and compared with the result corresponding to a vortex-free droplet. The trajectory of the Xe and Ar atoms in phase space is shown Figure 9.3. In both cases the trajectory of the impurity is limited to the region of the droplet around the vortex line. The impurity orbits around the vortex line because the superfluid flow does so. Since in the DFT approach no dissipation is included, the signature of the capture of an impurity by a vortex is its close orbiting around the vortex line, as shown in the figure and especially in Ref. [139]. The ESI material shows that whereas Ar is captured during its first transit across the droplet, the Xe atom is only captured in its second transit. We attribute this difference to the larger solvation energy of Xe (see Section 9.3), which requires more time to be dissipated. It can be seen[139] that when Xe detaches from the vortex in the first transit, the vortex line is reconnected near the atomic solvation structure because no open ends can remain in the bulk of the droplet.

Figure 4 and Figure 9.10 show that when the impurity hits the droplet surface a series of surface and volume density waves are launched. These waves travel much faster than the impurity itself, which has lost a large amount of kinetic energy when it pierced the surface.

The displacement of the atom in the droplet produces sound waves in the liquid and distortions along the vortex line (Kelvin modes). It is worth seeing that before the bending by the collision with the impurity, the vortex line is twisted (helical Kelvin mode). This is due to the interference between the spherical wave front flow produced by the hitting of the droplet surface, that travels from bottom to top, and the flow around the vortex core. The spherical wave front hits first the central portion of the vortex line, whose ends are anchored on the droplet surface. This yields the appearance of the helical distortion along the vortex line shown in Figure 9.11. The twisting can no longer be followed after the impurity solvation structure reaches the vortex line, bending and dragging it along in the course of its orbiting around it. But it is clearly visible before as shown in Figure 9.11, that displays the density of the droplet around the vortex line at the indicated collision time.

We have thus shown that Xe and Ar atoms are readily captured by vortex lines in helium droplets under conditions prevailing in the experiments[104,113]. Simulating the capture of a huge number of impurities or clusters by vortex arrays in very large droplets is beyond reach at present. However, the results presented in this subsection are the proof

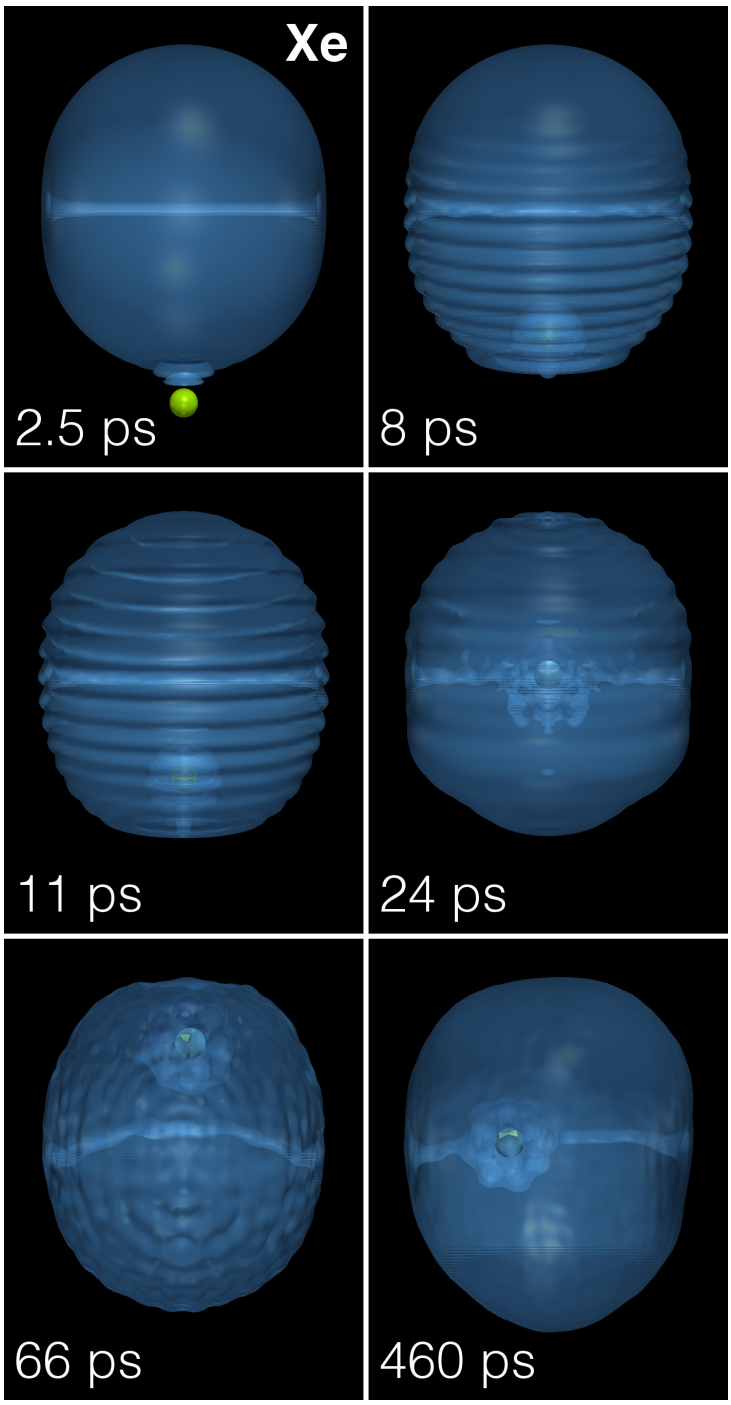

Figure 9.9: Dynamic evolution of a Xe atom (green dot) approaching a $^4He_{1000}$ droplet hosting a vortex line from below at $v_0 = 200$ m/s. The corresponding time is indicated in each frame[139].

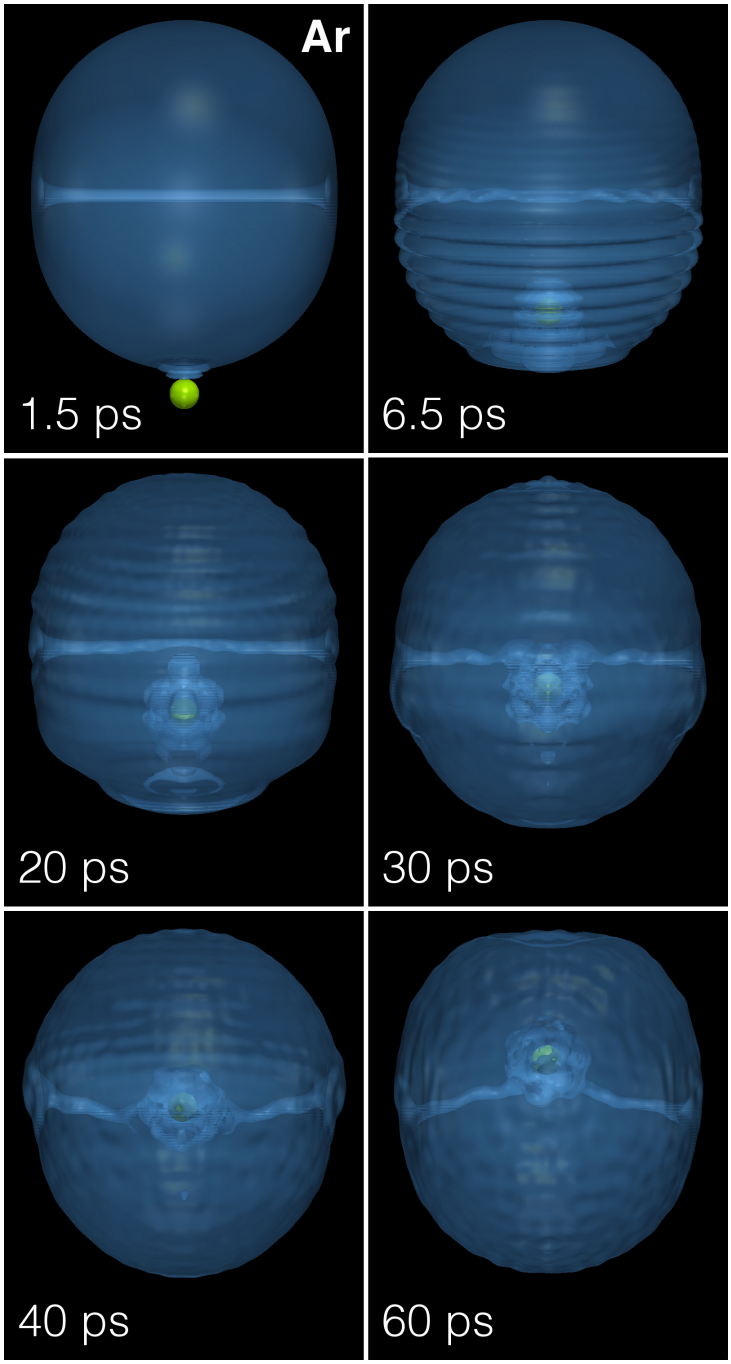

Figure 9.10: Same as Figure 4 for an Ar atom at $v_0 = 360$ m/s[139].

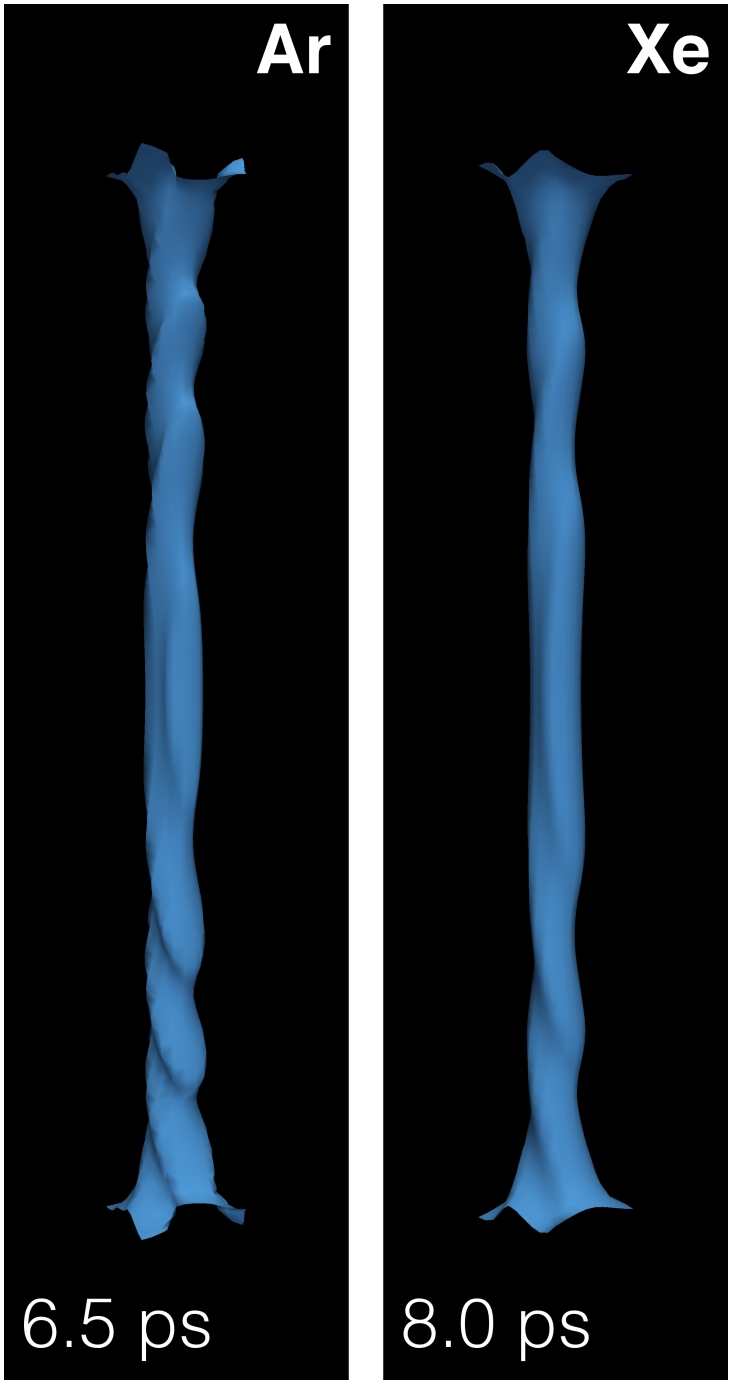

Figure 9.11: Core structure of the vortex line in a $^4He_{1000}$ droplet after colliding with Xe at v_0=200 m/s (right panel, $t = 8$ ps) and Ar at 360 m/s (left panel, t=6.5 ps). The full structure of the droplet is shown in Figure 4 and Figure 9.10.

of concept that the limitation is technical and not conceptual.

10
To conclude

In this thesis we have explored two complementary aspects of the dynamics of atomic dopants interacting with helium nanodroplets: the fate of a photo-excited alkali on the droplet surface, and the doping process itself. Photo-excited alkalis have been studied in a joint theoretical and experimental effort, whereas the atom-helium droplet collisions leading to doping have been studied only theoretically, but with the view of proposing some fundamental explanations for basic steps in the remarkable experiments leading to the formation of filament shaped nanostructures of atomic cluster.

As a theoretical tool we have made extensive use of the ^{4}He-DFT approach, in its static version to obtain equilibrium properties and in its time-dependent version (^{4}He-TDDFT) to simulate excited state dynamics and collisions, as explained in Chapter 2. We have applied it to study helium nanodroplets of several thousand atoms (routinely 1000) interacting with atomic dopants. As shown in the following results chapters, this approach has provided deep insight about all the processes studied, as well as quantitative agreement in most of the simulations when comparison with experimental data was possible. This agreement is so reliable that in the few cases where it was not the case, it lead to the identification of a process that had not been taken into account thus far.

The first part of the results was dedicated to excited-state dynamics of an alkali atom bound to the helium droplet surface. In Chapter 4 we have studied the dynamics of femtosecond pump-probe photoionisation of Rb atoms attached to He nanodroplets in a combined theory-experiment investigation. We have concluded that it was governed by the competition between the repulsive interaction of the droplet with the Rb atom in an excited state and the attractive interaction of the droplet with the Rb^+ cation. Depending on the time delay between the pump and the probe laser pulse, this caused either desorption of Rb* off the droplet or submersion of the Rb^+ cation into the droplet interior. We have been able to determine the critical time delay separating these two behaviours and obtained an excellent agreement with experiments, except in the case of the 5p $^2\Pi_{3/2}$ excitation of Rb where theory found a surface bound Rb*(5p $^2\Pi_{3/2}$)-He

exciplex whereas experiment observed its dissociation from the droplet. This agreement allowed us to characterise the desorption dynamics as impulsive with a time scale of ~1 ps for the 6p-excited states and as intermediate between impulsive dissociation and statistical desorption with a time scale of ~100 ps for the 5p-excited states. This interplay between opposing trends (He-Rb* repulsion, He-Rb$^+$ attraction) will be present in other types of clusters and condensed phase systems probed by time-resolved photoionisation spectroscopy. Hence ^{4}He-TDDFT simulations will be helpful in interpreting the experimental results in many cases.

In Chapter 5 we have gone back to understanding the disagreement observed between theory and experiment for Rb*(5p $^2\Pi_{3/2}$) excitation. The dynamics of the lowest three excited states (5p) of the Rb-He droplet complex have been selectively probed experimentally using a two-colour femtosecond pump-probe photoionisation scheme. Both photo-ion and photo-electron signals have revealed a dissociation dynamics proceeding on two distinct time scales (~30 ps and 700 ps). By comparing with time-dependent DFT simulations, we concluded that the fast dynamics was due to prompt desorption of Rb atoms when exciting the $^2\Sigma_{1/2}$-state. The formation time of the surface bound excimer observed in these simulations upon excitation to the $^2\Pi_{3/2}$ state was between 20 ps and 50 ps. By introducing a $^2\Pi_{3/2} \longrightarrow {}^2\Pi_{1/2}$ spin-orbit relaxation process in the time-dependent DFT simulations we were able to reproduce dissociation of this exciplex from the droplet surface. Fitting the experimental results gave a lifetime of ~700 ps for spin-orbit relaxation.

The second part of the results was devoted to helium droplet doping, and the influence of the existence of vortex lines on this process. In Chapter 8 we have shown that head-on collisions of helium nanodroplets with xenon, a heliophilic atom, involve a kinetic energy exchange of the same order of magnitude as cesium, a heliophobic atom with similar mass. In both cases, this energy is largely dissipated by producing energetic waves in the droplet or it is carried away by promptly emitted helium atoms. The difference between the two atoms is due to the different nature of their interaction with helium. Density build up is observed around the heliophilic xenon during the dynamics, whereas a bubble is created around the heliophobic cesium. Thus it takes a much higher velocity for xenon to go through the droplet and escape than for cesium, as could be expected.

And finally in Chapter 9 we have demonstrated that Xe and Ar atoms at thermal velocities are readily captured by helium droplets, with a capture cross section similar to the geometric cross section of the droplet. Crucially for the subsequent capture of impurities by vortex lines, we have also shown that most of the kinetic energy of the impinging impurity is lost in the capture process during the first tens of picoseconds. This happens either by the ejection of prompt-emitted He atoms, or by the production of sound waves and large deformations in the droplet.

In addition, we have also shown that if the droplet hosts a vortex, slowly moving impurities are readily captured by the vortex line. Rather than being trapped inside the vortex core, the impurity is bound to move at a close distance around it. Besides the crucial energy loss when the impurity hits the droplet, the capture by the vortex is favoured by a further energy transfer from the impurity to the droplet: large amplitude displacements of the vortex line —as shown in the ESI[153]— take place, constituting another source of the kinetic energy loss in the final stages of the capture. A related issue is the appearance of Kelvin modes in the vortex line, that is not only bent, but also twisted in the course of the collision.

We can conclude that if the kinematic conditions of the collision (kinetic energy and impact parameter) lead to the capture of the impurity by the droplet, the pinball effect caused by the droplet surface can facilitate the meeting of the Xe/Ar atom and the vortex line —and the possible capture of the atom by the vortex— since both have a tendency to remain in the inner region of the droplet. We have shown this in the case of Xe at v_0=200 m/s: Xe is captured during its second transit across the droplet, whereas this could not have happened in bulk liquid helium[152]. This effect could explain the capture of impurities by vortex lines even in the very large droplets used in the observation of filament-shaped nanostructures.

Future prospects

Our work on the real-time dynamics of the photo-excitation of an alkali metal atom on the surface of a helium nanodroplet was quite extensive. Conducting the same type of studies on other types of dopant species which are solvated more deeply inside He droplets (e.g. alkaline earth metals, transition metals) would give further insight into the mechanisms of desolvation and ejection of excited impurity atoms out of He nanodroplets[154-157].

Moreover, a more complete description of the couplings between electronic states and the configurational degrees of freedom in such excited complexes induced by the He droplet environment would be highly desirable[158,159]. In a recent advance, electronic relaxation of Ba^+ cations in He nanodroplets, based on a diabatisation of the He-Ba^+ ground and excited electronic states interaction potentials[160], has been proposed as a mechanism for ejecting Ba^+ and Ba^+He_n off He droplets. These mechanisms for spin-relaxation and inter-electronic state relaxation have to be confirmed by real-time dynamics studies.

Finally, the capabilities of the He-DFT approach might help elucidate processes of experimental interest, such as the capture of one or several impurities by large droplets hosting a vortex array and how several atomic impurities, impinging upon a rotating droplet

hosting vortices, react to form small clusters, eventually being trapped within the vortex cores as shown by the appearance of filament-shaped nanostructures in experiments.

In all these future lines of investigation, ^{4}He-DFT and TDDFT will be essential tools, given their ability to accurately describe the equilibrium and dynamics properties of realistic size helium nanodroplets, possibly hosting vortices, in interaction with dopants. In this context it will be extremely interesting to couple ^{4}He-TDDFT with quantum molecular dynamics in order to go beyond the mean field approximation of the dopant dynamics in the helium environment. A promising alternative in the correlated basis function (CBF) approach and its multi-component approach recently developed by Rader *et al.* [161]

A

Angular velocity and angular momentum

In this Appendix we discuss the relationship between angular velocity and angular momentum of a deformed droplet below the critical angular frequency for vortex nucleation.

Let us consider an ellipsoidal vessel filled with liquid ^{4}He uniformly rotating around the z axis, $\omega = \omega\,\hat{\mathbf{k}}$. The ellipsoid has the equation

$$F(x,y,z) = \frac{x^2}{R_1^2} + \frac{y^2}{R_2^2} + \frac{z^2}{R_3^2} - 1 = 0$$

If $\mathbf{v}$ is the irrotational velocity of a point in the laboratory, $\mathbf{v}'$ the velocity of the same point in the vessel (corotating frame), and $\mathbf{V} = \omega \times \mathbf{r}$, one has

$$\mathbf{v}' = \mathbf{v} - \mathbf{V} = \frac{\hbar}{m_4}\nabla\mathcal{S} - \omega \times \mathbf{r}$$

where $\mathcal{S}$ is the velocity potential defined here so as that

$$\mathbf{v} = \frac{\hbar}{m_4}\nabla\mathcal{S}(x,y,z)$$

Its existence is granted by irrotationality; we also have $\mathbf{V} = \omega \times \mathbf{r} = \omega(-y,\, x,\, 0)$. A vector perpendicular to the ellipsoid surface is $\mathbf{n} = \nabla F(x,y,z)$. From the stationarity condition $(\mathbf{v}' \cdot \mathbf{n})|_{surf} = 0$ one obtains

$$\mathbf{v}' \cdot \mathbf{n} = 0 = \left(\frac{\hbar}{m_4}\frac{\partial\mathcal{S}}{\partial x} + \omega y\right)\frac{x}{R_1^2} + \left(\frac{\hbar}{m_4}\frac{\partial\mathcal{S}}{\partial y} - \omega x\right)\frac{y}{R_2^2} + \left(\frac{\hbar}{m_4}\frac{\partial\mathcal{S}}{\partial z}\right)\frac{z}{R_3^2}\Bigg|_{surf}$$

It can be checked that $\mathcal{S} = \alpha x y$ is a solution to this equation provided that

$$\frac{\hbar}{m_4}\left(\frac{1}{R_1^2} + \frac{1}{R_2^2}\right)\alpha = \left(\frac{1}{R_2^2} - \frac{1}{R_1^2}\right)\omega$$

Hence,

$$\alpha = \frac{m_4}{\hbar}\left(\frac{R_2^2 - R_1^2}{R_1^2 + R_2^2}\right)\omega$$

and

$$\mathcal{S} = \frac{m_4}{\hbar}\left(\frac{R_2^2 - R_1^2}{R_1^2 + R_2^2}\right)\omega\, x y$$

The velocity in the laboratory is $\mathbf{v} = (\hbar/m_4)\nabla\mathcal{S} = (\hbar/m_4)\alpha(y, x, 0)$, and in the vessel (corotating frame) is $\mathbf{v}' = \beta(R_1^2 y, -R_2^2 x, 0)$, where $\beta \equiv 2\,\omega/(R_1^2 + R_2^2)$. Once they have been determined, their circulation lines are straightforwardly obtained. In the laboratory frame they are

$$x^2 - y^2 = c \quad ,$$

which is the appearance of the circulation lines displayed in Figure 9.8. In the vessel frame, they are

$$\frac{x^2}{(\xi R_1)^2} + \frac{y^2}{(\xi R_2)^2} = 1 \quad .$$

These lines are "parallel" to the ellipsoidal surface.

We define the deformation parameter ϵ

$$\epsilon = \frac{\langle x^2\rangle - \langle y^2\rangle}{\langle x^2\rangle + \langle y^2\rangle}$$

where e.g.,

$$\langle x^2\rangle = \frac{1}{N}\int d\mathbf{r}\, x^2\, |\Psi(\mathbf{r})|^2$$

For the sharp surface ellipsoid above,

$$\alpha = \frac{m_4}{\hbar}\,\epsilon\,\omega \tag{A.1}$$

This relationship is not general but can be used as a guide for our more general approach. Let us now discuss the angular momentum and moment of inertia of the irrotational fluid droplet. Recalling that

$$L_z = -\imath\,\hbar\left(x\frac{\partial}{\partial y} - y\frac{\partial}{\partial x}\right)$$

if we write

$$\Psi(\mathbf{r}) = \Phi(\mathbf{r})e^{\imath\alpha x y}$$

with $\Phi(\mathbf{r})$ a real function,

$$\langle L_z\rangle = \hbar\,\alpha\int d\mathbf{r}\,(x^2 - y^2)\,\Phi^2(\mathbf{r})$$

If Equation (A.1) holds,

$$\begin{aligned}\langle L_z\rangle &= \epsilon\, m_4 N[\langle x^2\rangle - \langle y^2\rangle]\,\omega \\ &= m_4 N\left(\frac{[\langle x^2\rangle - \langle y^2\rangle]^2}{\langle x^2\rangle + \langle y^2\rangle}\right)\omega \equiv \mathcal{I}_{irr}\,\omega\end{aligned} \tag{A.2}$$

where

$$\mathcal{I}_{irr} = m_4 N \left(\frac{[\langle x^2 \rangle - \langle y^2 \rangle]^2}{\langle x^2 \rangle + \langle y^2 \rangle} \right)$$

is the irrotational moment of inertia. For a rigid solid,

$$\mathcal{I}_{rig} = m_4 \int d\mathbf{r}\, (x^2 + y^2)\, \Phi^2(\mathbf{r}) = m_4 N [\langle x^2 \rangle + \langle y^2 \rangle]$$

Hence,

$$\frac{\mathcal{I}_{irr}}{\mathcal{I}_{rig}} = \left[\frac{\langle x^2 \rangle - \langle y^2 \rangle}{\langle x^2 \rangle + \langle y^2 \rangle} \right]^2 \to 0 \quad \text{if} \quad \epsilon \to 0$$

Finally, we discuss the kinetic energy of the droplet

$$E_{kin} = \frac{\hbar^2}{2m_4} \int d\mathbf{r}\, |\nabla \Psi(\mathbf{r})|^2$$

From the above $\Psi(\mathbf{r})$,

$$E_{kin} = \frac{\hbar^2}{2m_4} \int d\mathbf{r}\, |\nabla \Phi(\mathbf{r})|^2$$
$$+ \quad \frac{\hbar^2}{2m_4} \alpha^2 \int d\mathbf{r}\, (x^2 + y^2) \Phi^2(\mathbf{r}) = E_{intr} + E_{coll}$$

where the first term is the "intrinsic" kinetic energy and the second term arises from the irrotational velocity field

$$E_{coll} = \frac{\hbar^2}{2m_4} \alpha^2 \int d\mathbf{r}\, (x^2 + y^2) \Phi^2(\mathbf{r}) =$$
$$\frac{1}{2} \left\{ m_4\, \epsilon^2 \int d\mathbf{r}\, (x^2 + y^2) \Phi^2(\mathbf{r}) \right\} \omega^2 = \frac{1}{2}\, \mathcal{I}_{irr}\, \omega^2$$

These expressions may be used to obtain some estimates from the actual DFT calculations. For a $^4He_{1000}$ droplet and ω=0.10 K/$\hbar$ we have obtained $\langle x^2 \rangle$= 100.82 Å^2 and $\langle y^2 \rangle$= 101.82 Å^2; hence, $\epsilon \sim -1/200$. Since $\hbar^2/m_4$= 12.12 K Å^2, from Equation (A.1) one has $\alpha \sim -4.2 \times 10^{-5}$ Å^{-2}. From Equation (A.2) we obtain $\langle L_z \rangle \sim 4 \times 10^{-2}\, \hbar$.

In a Bose-Einstein condensate the deformation ϵ is a control parameter that can be set to a very large value (close to unity). For a self-bound ^{4}He droplet deformation comes from "rotation" itself and it turns out to be minute even for angular frequencies close to the critical frequency for one-vortex nucleation; the conclusion is that the droplet "does not rotate"; in other words, it is unable to store an appreciable amount of angular momentum before vortex nucleation.

Bibliography

[1] P. Kapitza, Nature **141**, 74 (1938), URL http://dx.doi.org/10.1038/141074a0.

[2] B. Rollin and F. Simon, Physica **6**, 219 (1939), ISSN 0031-8914, URL http://www.sciencedirect.com/science/article/pii/S0031891439800131.

[3] W. Keesom and M. A. Keesom, Physica **3**, 359 (1936), ISSN 0031-8914, URL http://www.sciencedirect.com/science/article/pii/S0031891436803127.

[4] L. Tisza, Comptes rendus hebdomadaires des séances de l'Académie des sciences **207**, 1035 (1938), URL http://gallica.bnf.fr/ark:/12148/bpt6k31590/f1035.item.

[5] L. Tisza, Comptes rendus hebdomadaires des séances de l'Académie des sciences **207**, 1186 (1938), URL http://gallica.bnf.fr/ark:/12148/bpt6k31590/f1186.item.

[6] L. Tisza, J. Phys. Radium **1**, 164 (1940), URL https://doi.org/10.1051/jphysrad:0194000105016400.

[7] L. Tisza, J. Phys. Radium **1**, 350 (1940), URL https://doi.org/10.1051/jphysrad:0194000108035000.

[8] P. Lebrun, Cryogenics **34**, 1 (1994), ISSN 0011-2275, fifteenth International Cryogenic Engineering Conference, URL http://www.sciencedirect.com/science/article/pii/S0011227505800037.

[9] W. Keesom and M. A. Keesom, KNAW, Proceedings **35**, 736 (1932), URL http://www.dwc.knaw.nl/DL/publications/PU00016277.pdf.

[10] R. J. Donnelly, Physics Today **62**, 34 (2009), https://doi.org/10.1063/1.3248499, URL https://doi.org/10.1063/1.3248499.

[11] H. Kamerlingh Onnes, KNAW, Proceedings **10**, 744 (1908), URL http://www.dwc.knaw.nl/toegangen/digital-library-knaw/?pagetype=publDetail&pId=PU00013699.

[12] H. Kamerlingh Onnes, KNAW, Proceedings **11**, 168 (1909), URL http://www.dwc.knaw.nl/toegangen/digital-library-knaw/?pagetype=publDetail&pId=PU00013525.

[13] P. J. McLennan, H. Smith, and J. Wilhelm, The London, Edinburgh, and Dublin Philosophical Magazine and Journal of Science **14**, 161 (1932), https://doi.org/10.1080/14786443209462044, URL https://doi.org/10.1080/14786443209462044.

[14] E. F. Burton, Nature **135**, 265 (1935), URL http://dx.doi.org/10.1038/135265a0.

[15] M. v. Laue, F. London, and H. London, Zeitschrift für Physik **96**, 359 (1935), ISSN 0044-3328, URL https://doi.org/10.1007/BF01343868.

[16] F. Simon, Nature **133**, 529 (1934), URL http://dx.doi.org/10.1038/133529a0.

[17] F. London, Proceedings of the Royal Society of London A: Mathematical, Physical and Engineering Sciences **153**, 576 (1936), ISSN 0080-4630, http://rspa.royalsocietypublishing.org/content/153/880/576.full.pdf, URL http://rspa.royalsocietypublishing.org/content/153/880/576.

[18] J. F. Allen, R. Peierls, and M. Zaki Uddin, Nature **140**, 62 (1937), URL http://dx.doi.org/10.1038/140062a0.

[19] J. F. Allen and A. D. Misener, Nature **141**, 75 (1938), URL http://dx.doi.org/10.1038/141075a0.

[20] F. London, Nature **141**, 643 (1938), URL http://dx.doi.org/10.1038/141643a0.

[21] L. Tisza, Nature **141**, 913 (1938), URL http://dx.doi.org/10.1038/141913a0.

[22] L. Landau, Phys. Rev. **60**, 356 (1941), URL https://link.aps.org/doi/10.1103/PhysRev.60.356.

[23] L. Landau, Phys. Rev. **75**, 884 (1949), URL https://link.aps.org/doi/10.1103/PhysRev.75.884.

[24] N. N. Bogolyubov, J. Phys. (USSR) **11**, 23 (1947), [Izv. Akad. Nauk Ser. Fiz.11,77(1947)], URL https://ufn.ru/ru/articles/1967/11/o/.

[25] E. A. Cornell and C. E. Wieman, Rev. Mod. Phys. **74**, 875 (2002), URL https://link.aps.org/doi/10.1103/RevModPhys.74.875.

[26] W. Ketterle, Rev. Mod. Phys. **74**, 1131 (2002), URL https://link.aps.org/doi/10.1103/RevModPhys.74.1131.

[27] L. Pitaevskii and S. Stringari, *Bose-Einstein Condensation and Superfluidity*, vol. 164 of *International Series of Monographs on Physics* (Oxford University Press, Great Clarendon Street, Oxford, OX2 6DP, United Kingdom, 2016), first edition ed., ISBN 978-0-19-875888-4, URL http://dx.doi.org/10.1093/acprof:oso/9780198758884.001.0001.

[28] D. Mateo, M. Barranco, and J. Navarro, Phys. Rev. B **82**, 134529 (2010).

[29] F. Dalfovo, A. Lastri, L. Pricaupenko, S. Stringari, and J. Treiner, Phys. Rev. B **52**, 1193 (1995), URL https://link.aps.org/doi/10.1103/PhysRevB.52.1193.

[30] R. J. Donnelly, J. A. Donnelly, and R. N. Hills, J. Low Temp. Phys. **44**, 471 (1981).

[31] D. M. Brink and S. Stringari, Zeitschrift für Physik D Atoms, Molecules and Clusters **15**, 257 (1990), ISSN 1431-5866, URL https://doi.org/10.1007/BF01437187.

[32] M. Hartmann, R. E. Miller, J. P. Toennies, and A. Vilesov, Phys. Rev. Lett. **75**, 1566 (1995), URL https://link.aps.org/doi/10.1103/PhysRevLett.75.1566.

[33] M. Hartmann, F. Mielke, J. P. Toennies, A. F. Vilesov, and G. Benedek, Phys. Rev. Lett. **76**, 4560 (1996), URL https://link.aps.org/doi/10.1103/PhysRevLett.76.4560.

[34] M. V. R. Krishna and K. B. Whaley, The Journal of Chemical Physics **93**, 746 (1990), https://doi.org/10.1063/1.459525, URL https://doi.org/10.1063/1.459525.

[35] S. A. Chin and E. Krotscheck, Phys. Rev. B **45**, 852 (1992), URL https://link.aps.org/doi/10.1103/PhysRevB.45.852.

[36] E. Krotscheck and R. Zillich, The Journal of Chemical Physics **115**, 10161 (2001), https://aip.scitation.org/doi/pdf/10.1063/1.1400780, URL https://aip.scitation.org/doi/abs/10.1063/1.1400780.

[37] M. Gartner, Master's thesis, Johannes Kepler University, Linz, Austria (2018).

[38] F. Ancilotto, P. B. Lerner, and M. W. Cole, J. Low Temp. Phys. **101**, 1123 (1995).

[39] S. Grebenev, J. P. Toennies, and A. F. Vilesov, Science **279**, 2083 (1998).

[40] P. Sindzingre, M. L. Klein, and D. M. Ceperley, Phys. Rev. Lett. **63**, 1601 (1989).

[41] M. V. Rama Krishna and K. B. Whaley, Phys. Rev. Lett. **64**, 1126 (1990), URL https://link.aps.org/doi/10.1103/PhysRevLett.64.1126.

[42] M. Hartmann, N. Pörtner, B. Sartakov, J. P. Toennies, and A. F. Vilesov, The Journal of Chemical Physics **110**, 5109 (1999), https://doi.org/10.1063/1.479111, URL https://doi.org/10.1063/1.479111.

[43] J. Harms, M. Hartmann, B. Sartakov, J. P. Toennies, and A. F. Vilesov, The Journal of Chemical Physics **110**, 5124 (1999), https://doi.org/10.1063/1.479110, URL https://doi.org/10.1063/1.479110.

[44] M. Barranco, R. Guardiola, S. Hernández, R. Mayol, J. Navarro, and M. Pi, Journal of Low Temperature Physics **142**, 1 (2006), ISSN 1573-7357, URL https://doi.org/10.1007/s10909-005-9267-0.

[45] F. Ancilotto, M. Barranco, F. Coppens, J. Eloranta, N. Halberstadt, A. Hernando, D. Mateo, and M. Pi, International Reviews in Physical Chemistry **36**, 621 (2017), http://dx.doi.org/10.1080/0144235X.2017.1351672, URL http://dx.doi.org/10.1080/0144235X.2017.1351672.

[46] M. Mudrich and F. Stienkemeier, International Reviews in Physical Chemistry **33**, 301 (2014), https://doi.org/10.1080/0144235X.2014.937188, URL https://doi.org/10.1080/0144235X.2014.937188.

[47] E. Krotscheck and J. Navarro, eds., *Microscopic approaches to quantum liquids in confined geometries*, vol. 4 of *Series on Advances in Quantum Many-Body Theory* (World Scientific, Singapore, 2002).

[48] M. P. de Lara-Castells, G. Delgado-Barrio, P. Villarreal, and A. O. Mitrushchenkov, J. Chem. Phys. **125**, 221101 (2006).

[49] M. P. de Lara-Castells, N. F. Aguirre, P. Villarreal, G. Delgado-Barrio, and A. O. Mitrushchenkov, J. Chem. Phys. **132**, 194313 (2010).

[50] N. F. Aguirre, P. Villarreal, G. Delgado-Barrio, A. O. Mitrushchenkov, and M. P. de Lara-Castells, Phys. Chem. Chem. Phys. **15**, 10126 (2013).

[51] S. Stringari and J. Treiner, Phys. Rev. B **36**, 8369 (1987).

[52] S. Stringari and J. Treiner, J. Chem. Phys. **87**, 5021 (1987).

[53] F. Dalfovo, A. Lastri, L. Pricaupenko, S. Stringari, and J. Treiner, Phys. Rev. B **52**, 1193 (1995).

[54] P. Hohenberg and W. Kohn, Phys. Rev. **136**, B864 (1964), URL https://link.aps.org/doi/10.1103/PhysRev.136.B864.

[55] W. Kohn and L. J. Sham, Phys. Rev. **140**, A1133 (1965), URL https://link.aps.org/doi/10.1103/PhysRev.140.A1133.

[56] E. Runge and E. K. U. Gross, Phys. Rev. Lett. **52**, 997 (1984).

[57] J. Dupont-Roc, M. Himbert, N. Pavloff, and J. Treiner, Journal of Low Temperature Physics **81**, 31 (1990), ISSN 1573-7357, URL https://doi.org/10.1007/BF00683150.

[58] S. Moroni, D. M. Ceperley, and G. Senatore, Phys. Rev. Lett. **69**, 1837 (1992), URL https://link.aps.org/doi/10.1103/PhysRevLett.69.1837.

[59] F. Ancilotto, M. Barranco, F. Caupin, R. Mayol, and M. Pi, Phys. Rev. B **72**, 214522 (2005).

[60] F. Caupin, F. Ancilotto, M. Barranco, R. Mayol, and M. Pi, J. Low Temp. Phys. **148**, 731 (2007).

[61] M. Martinez, Master's thesis, Université Toulouse III Paul Sabatier (2017), URL https://github.com/bcntls2016/M2Report-M_Martinez/blob/master/report/report.pdf.

[62] L. Lehtovaara, J. Toivanen, and J. Eloranta, Journal of Computational Physics **221**, 148 (2007), ISSN 0021-9991, URL http://www.sciencedirect.com/science/article/pii/S0021999106002798.

[63] M. Frigo and S. G. Johnson, Proc. IEEE **93**, 216 (2005).

[64] F. Ancilotto, F. Dalfovo, L. P. Pitaevskii, and F. Toigo, Phys. Rev. B **71**, 104530 (2005).

[65] M. Barranco, F. Coppens, N. Halberstadt, A. Hernando, A. Leal, D. Mateo, R. Mayol, and M. Pi (2017), URL https://github.com/bcntls2016/DFT-Guide/blob/master/dft-guide.pdf.

[66] F. O. Ellison, Journal of the American Chemical Society **85**, 3540 (1963), https://doi.org/10.1021/ja00905a002, URL https://doi.org/10.1021/ja00905a002.

[67] Z. J. Jakubek, Q. Hui, and M. Takami, Phys. Rev. Lett. **79**, 629 (1997).

[68] A. Nakayama and K. Yamashita, J. Chem. Phys. **114**, 780 (2001).

[69] A. Ralston and H. S. Wilf, *Mathematical methods for digital computers* (John Wiley and Sons, New York, 1960).

[70] W. H. Press, S. A. Teukolsky, W. T. Vetterling, and B. P. Flannery, *Numerical Recipes* (Cambridge University Press, Cambridge, 1992).

[71] D. Mateo, D. Jin, M. Barranco, and M. Pi, J. Chem. Phys. **134**, 044507 (2011).

[72] M. Pi, F. Ancilotto, F. Coppens, N. Halberstadt, A. Hernando, A. Leal, D. Mateo, R. Mayol, and M. Barranco, *4HeDFT BCN-TLS* (2017), URL https://github.com/bcntls2016/.

[73] F. Coppens, *4HeDFT BCN-TLS | User Manual* (2017), URL https://github.com/bcntls2016/4hedft-bcntls-manual.

[74] A. Griffin and S. Stringari, Phys. Rev. Lett. **76**, 259 (1996), URL https://link.aps.org/doi/10.1103/PhysRevLett.76.259.

[75] F. Dalfovo, Zeitschrift für Physik D Atoms, Molecules and Clusters **29**, 61 (1994), ISSN 1431-5866, URL https://doi.org/10.1007/BF01437166.

[76] F. Stienkemeier, J. Higgins, W. E. Ernst, and G. Scoles, Zeitschrift für Physik B Condensed Matter **98**, 413 (1995), ISSN 1431-584X, URL https://doi.org/10.1007/BF01338416.

[77] F. Stienkemeier, J. Higgins, W. E. Ernst, and G. Scoles, Phys. Rev. Lett. **74**, 3592 (1995), URL https://link.aps.org/doi/10.1103/PhysRevLett.74.3592.

[78] F. Ancilotto, E. Cheng, M. W. Cole, and F. Toigo, Zeitschrift für Physik B Condensed Matter **98**, 323 (1995), ISSN 1431-584X, URL https://doi.org/10.1007/BF01338398.

[79] S. H. Patil, J. Chem. Phys. **94**, 8089 (1991).

[80] F. Ancilotto, G. DeToffol, and F. Toigo, Phys. Rev. B **52**, 16125 (1995), URL https://link.aps.org/doi/10.1103/PhysRevB.52.16125.

[81] S. I. Kanorsky, M. Arndt, R. Dziewior, A. Weis, and T. W. Hänsch, Phys. Rev. B **50**, 6296 (1994), URL https://link.aps.org/doi/10.1103/PhysRevB.50.6296.

[82] B. Tabbert, M. Beau, M. Foerste, H. Günther, C. Hönninger, H. Hust, K. Layer, G. zu Putlitz, and T. Schumacher, Zeitschrift für Physik B Condensed Matter **98**, 399 (1995), ISSN 1431-584X, URL https://doi.org/10.1007/BF01338414.

[83] Y. Takahashi, K. Sano, T. Kinoshita, and T. Yabuzaki, Phys. Rev. Lett. **71**, 1035 (1993), URL https://link.aps.org/doi/10.1103/PhysRevLett.71.1035.

[84] J. H. Beijersbergen, Q. Hui, and M. Takami, Physics Letters A **181**, 393 (1993), ISSN 0375-9601, URL http://www.sciencedirect.com/science/article/pii/037596019390394F.

[85] P. Carrick, ed., *Theoretical Performance of Atomic and Molecular HEDM Additives to Solid H_2*, p. 412 (Proceedings of the High Energy Density Matter (HEDM) Contractor's Conference, Woods Hole, MA.; Edwards Air Force Base, CA, 1993), URL http://www.dtic.mil/docs/citations/ADA274452.

[86] E. Loginov and M. Drabbels, Phys. Rev. Lett. **106**, 083401 (2011).

[87] E. Loginov, C. Callegari, F. Ancilotto, and M. Drabbels, J. Phys. Chem. A **115**, 6779 (2011).

[88] F. Lackner, G. Krois, M. Koch, and W. E. Ernst, The Journal of Physical Chemistry Letters **3**, 1404 (2012), pMID: 26286790, https://doi.org/10.1021/jz300381y, URL https://doi.org/10.1021/jz300381y.

[89] F. Lackner, G. Krois, and W. E. Ernst, Molecular Physics **111**, 2118 (2013), https://doi.org/10.1080/00268976.2013.788792, URL https://doi.org/10.1080/00268976.2013.788792.

[90] M. Theisen, F. Lackner, and W. E. Ernst, J. Chem. Phys. **135**, 074306 (2011).

[91] L. Fechner, B. Grüner, A. Sieg, C. Callegari, F. Ancilotto, F. Stienkemeier, and M. Mudrich, Phys. Chem. Chem. Phys. **14**, 3843 (2012).

[92] A. Pifrader, O. Allard, G. Auböck, C. Callegari, W. E. Ernst, R. Hubert, and F. Ancilotto, J. Chem. Phys. **133**, 164502 (2010).

[93] F. Lackner, G. Krois, M. Theisen, M. Koch, and W. E. Ernst, Phys. Chem. Chem. Phys. **13**, 18781 (2011).

[94] M. Theisen, F. Lackner, F. Ancilotto, C. Callegari, and W. E. Ernst, The European Physical Journal D **61**, 403 (2011), ISSN 1434-6079, URL https://doi.org/10.1140/epjd/e2010-10504-5.

[95] F. Lackner, J. Poms, G. Krois, J. V. Pototschnig, and W. E. Ernst, J. Phys. Chem. A **117**, 11866 (2013).

[96] F. Stienkemeier, J. Higgins, C. Callegari, S. I. Kanorsky, W. E. Ernst, and G. Scoles, Z. Phys. D **38**, 253 (1996).

[97] O. Bünermann, G. Droppelmann, A. Hernando, R. Mayol, and F. Stienkemeier, The Journal of Physical Chemistry A **111**, 12684 (2007), pMID: 17997536, https://doi.org/10.1021/jp0760760, URL https://doi.org/10.1021/jp0760760.

[98] J. von Vangerow, F. Coppens, A. Leal, M. Pi, M. Barranco, N. Halberstadt, F. Stienkemeier, and M. Mudrich, The Journal of Physical Chemistry Letters **8**, 307 (2017), pMID: 27996261, http://dx.doi.org/10.1021/acs.jpclett.6b02598, URL http://dx.doi.org/10.1021/acs.jpclett.6b02598.

[99] J. Pascale, Phys. Rev. A **28**, 632 (1983).

[100] C. P. Schulz, P. Claas, and F. Stienkemeier, Phys. Rev. Lett. **87**, 153401 (2001), URL https://link.aps.org/doi/10.1103/PhysRevLett.87.153401.

[101] J. Reho, J. Higgins, K. K. Lehmann, and G. Scoles, The Journal of Chemical Physics **113**, 9694 (2000), https://doi.org/10.1063/1.1321034, URL https://doi.org/10.1063/1.1321034.

[102] J. Reho, J. Higgins, C. Callegari, K. K. Lehmann, and G. Scoles, The Journal of Chemical Physics **113**, 9686 (2000), https://doi.org/10.1063/1.1321033, URL https://doi.org/10.1063/1.1321033.

[103] L. F. Gomez, E. Loginov, and A. F. Vilesov, Phys. Rev. Lett. **108**, 155302 (2012), URL http://link.aps.org/doi/10.1103/PhysRevLett.108.155302.

[104] L. F. Gomez, K. R. Ferguson, J. P. Cryan, C. Bacellar, R. M. P. Tanyag, C. Jones, S. Schorb, D. Anielski, A. Belkacem, C. Bernando, et al., Science **345**, 906 (2014).

[105] R. J. Donnelly, *Quantized vortices in helium II*, vol. 3 of *Cambridge Studies in Low Temperature Physics* (Cambridge University Press, Cambridge, U.K., 1991).

[106] L. Pitaevskii and S. Stringari, *Bose-Einstein Condensation*, vol. 116 (International Series of Monographs on Physics 116 (Clarendon), Oxford, U.K, 2003).

[107] A. L. Fetter, Rev. Mod. Phys. **81**, 647 (2009), URL https://link.aps.org/doi/10.1103/RevModPhys.81.647.

[108] J. D. Close, F. Federman, K. Hoffmann, and N. Quass, J. Low Temp. Phys. **111**, 661 (1998).

[109] K. K. Lehmann and R. Schmied, Phys. Rev. B **68**, 224520 (2003), URL https://link.aps.org/doi/10.1103/PhysRevB.68.224520.

[110] M. Barranco, R. Guardiola, S. Hernández, R. Mayol, J. Navarro, and M. Pi, J. Low Temp. Phys. **142**, 1 (2006).

[111] F. Stienkemeier and K. K. Lehmann, J. Phys. B **39**, R127 (2006).

[112] E. Loginov, L. F. Gomez, and A. F. Vilesov, J. Phys. Chem. A **115**, 7199 (2011).

[113] C. F. Jones, C. Bernando, R. M. P. Tanyag, C. Bacellar, K. R. Ferguson, L. F. Gomez, D. Anielski, A. Belkacem, R. Boll, J. Bozek, et al., Phys. Rev. B **93**, 180510 (2016), URL https://link.aps.org/doi/10.1103/PhysRevB.93.180510.

[114] F. Ancilotto, M. Pi, and M. Barranco, Phys. Rev. B **91**, 100503(R) (2015).

[115] C. Bernando, R. Mayro, P. Tanyag, C. Jones, C. Bacellar, M. Bucher, K. R. Ferguson, D. Rupp, M. P. Ziemkiewicz, L. F. Gomez, et al., Phys. Rev. B **95**, 064510 (2017).

[116] L. J. Campbell and R. M. Ziff, Phys. Rev. B **20**, 1886 (1979), URL https://link.aps.org/doi/10.1103/PhysRevB.20.1886.

[117] F. Ancilotto, M. Pi, and M. Barranco, Phys. Rev. B **90**, 174512 (2014).

[118] A. Scheidemann, J. P. Toennies, and J. A. Northby, Phys. Rev. Lett. **64**, 1899 (1990).

[119] A. Hernando, R. Mayol, M. Pi, M. Barranco, F. Ancilotto, O. Bünermann, and F. Stienkemeier, J. Phys. Chem. A **111**, 7303 (2007).

[120] J. P. Toennies and A. F. Vilesov, Angew. Chem. Phys. **43**, 2622 (2004).

[121] J. Tiggesbäumker and F. Stienkemeier, Phys. Chem. Chem. Phys. **9**, 4748 (2007).

[122] C. Callegari and W. E. Ernst, in *Handbook of High Resolution Spectroscopy* (Whiley, New York, 2011), vol. 3, p. 1551.

[123] M. Mudrich and F. Stienkemeier, Int. Rev. Phys. Chem. **33**, 301 (2014).

[124] M. Lewerenz, B. Schilling, and J. P. Toennies, J. Chem. Phys. **102**, 8191 (1995).

[125] A. Leal, D. Mateo, A. Hernando, M. Pi, and M. Barranco, Phys. Chem. Chem. Phys. **16**, 23206 (2014).

[126] A. Vilà, M. González, and R. Mayol, Phys. Chem. Chem. Phys. **18**, 2006 (2016).

[127] C. F. Jones, C. Bernando, R. M. P. Tanyag, C. Bacellar, K. R. Ferguson, L. F. Gomez, D. Anielski, A. Belkacem, R. Boll, J. Bozek, et al., Phys. Rev. B **93**, 180510(R) (2016).

[128] L. F. Gomez, E. Loginov, R. Sliter, and A. F. Vilesov, J. Chem. Phys. **135**, 154201 (2011).

[129] A. Leal, X. Zhang, M. Barranco, F. Cargnoni, A. Hernando, D. Mateo, M. Mella, M. Drabbels, and M. Pi, J. Chem. Phys. **144**, 094302 (2016).

[130] D. Mateo, A. Leal, A. Hernando, M. Barranco, M. Pi, F. Cargnoni, M. Mella, X. Zhang, and M. Drabbels, J. Chem. Phys. **140**, 131101 (2014).

[131] R. M. P. Tanyag, C. F. Jones, C. Bernando, S. M. O. O'Connell, D. Verma, and A. F. Vilesov, *Experiments with large superfluid helium nanodroplets* (Royal Society of Chemistry, Cambridge, UK, 2017), chap. 8, (to be published).

[132] V. Lebedev, P. Moroshkin, B. Grobety, E. Gordon, and A. Weis, Journal of Low Temperature Physics **165**, 166 (2011), ISSN 1573-7357, URL https://doi.org/10.1007/s10909-011-0384-7.

[133] L. F. Gomez, E. Loginov, and A. F. Vilesov, Phys. Rev. Lett. **108**, 155302 (2012).

[134] E. Latimer, D. Spence, C. Feng, A. Boatwright, A. M. Ellis, and S. Yang, Nano Lett. **14**, 2902 (2014).

[135] P. Thaler, A. Volk, F. Lackner, J. Steurer, D. Knez, W. Grogger, F. Hofer, and W. E. Ernst, Phys. Rev. B **90**, 155442 (2014).

[136] G. P. Bewley, M. S. Paoletti, K. R. Sreenivasan, and D. P. Lathrop, Proceedings of the National Academy of Sciences **105**, 13707 (2008), ISSN 0027-8424, http://www.pnas.org/content/105/37/13707.full.pdf, URL http://www.pnas.org/content/105/37/13707.

[137] A. Hernando, M. Barranco, M. Pi, E. Loginov, M. Langlet, and M. Drabbels, Phys. Chem. Chem. Phys. **14**, 3996 (2012).

[138] F. Coppens, A. Leal, M. Barranco, N. Halberstadt, and M. Pi, Journal of Low Temperature Physics **187**, 439 (2017), ISSN 1573-7357, https://doi.org/10.1007/s10909-016-1690-x, URL https://doi.org/10.1007/s10909-016-1690-x.

[139] F. Coppens, F. Ancilotto, M. Barranco, N. Halberstadt, and M. Pi, Phys. Chem. Chem. Phys. **19**, 24805 (2017), URL http://dx.doi.org/10.1039/C7CP03307A.

[140] A. Leal, D. Mateo, A. Hernando, M. Pi, M. Barranco, A. Ponti, F. Cargnoni, and M. Drabbels, Phys. Rev. B **90**, 224518 (2014).

[141] D. L. Whitaker, M. A. Weilert, C. L. Vicente, H. J. Maris, and G. M. Seidel, Journal of Low Temperature Physics **110**, 173 (1998), ISSN 1573-7357, URL https://doi.org/10.1023/A:1022539406733.

[142] M. Pi, R. Mayol, A. Hernando, M. Barranco, and F. Ancilotto, J. Chem. Phys. **126**, 244502 (2007).

[143] F. Dalfovo, R. Mayol, M. Pi, and M. Barranco, Phys. Rev. Lett **85**, 1028 (2000).

[144] K. T. Tang and J. P. Toennies, Zeitschrift für Physik D Atoms, Molecules and Clusters **1**, 91 (1986), ISSN 1431-5866, URL https://doi.org/10.1007/BF01384663.

[145] F. Dalfovo and S. Stringari, Phys. Rev. A **53**, 2477 (1996).

[146] Proceedings of the Royal Society of London A: Mathematical, Physical and Engineering Sciences **260**, 218 (1961), ISSN 0080-4630, http://rspa.royalsocietypublishing.org/content/260/1301/218.full.pdf, URL http://rspa.royalsocietypublishing.org/content/260/1301/218.

[147] G. A. Williams and R. E. Packard, Phys. Rev. Lett. **33**, 280 (1974).

[148] G. M. Seidel and H. J. Maris, Physica B: Condensed Matter **194-196**, 577 (1994), ISSN 0921-4526, URL http://www.sciencedirect.com/science/article/pii/0921452694906181.

[149] A. Bohr and B. Mottelson, *Nuclear Structure*, vol. 2 (1975).

[150] A. Recati, F. Zambelli, and S. Stringari, Phys. Rev. Lett. **86**, 377 (2001), URL https://link.aps.org/doi/10.1103/PhysRevLett.86.377.

[151] E. Guyon, J.-P. Hulin, L. Petit, and C. Mitescu, *Physical Hydrodynamics* (Oxford University Press, Oxford, U.K., 2015), 2nd ed.

[152] I. A. Pshenichnyuk and N. G. Berloff, Phys. Rev. B **94**, 184505 (2016).

[153] *Electronic Supplementary Information* (ESI), URL http://dx.doi.org/10.1039/C7CP03307A.

[154] E. Loginov and M. Drabbels, J. Phys. Chem. A **111**, 7504 (2007), pMID: 17569515, http://pubs.acs.org/doi/pdf/10.1021/jp0716278, URL http://pubs.acs.org/doi/abs/10.1021/jp0716278.

[155] E. Loginov and M. Drabbels, J. Chem. Phys. **136**, 154302 (2012), URL http://scitation.aip.org/content/aip/journal/jcp/136/15/10.1063/1.3701565.

[156] A. Kautsch, M. Koch, and W. E. Ernst, J. Phys. Chem. A **117**, 9621 (2013), http://pubs.acs.org/doi/pdf/10.1021/jp312336m, URL http://pubs.acs.org/doi/abs/10.1021/jp312336m.

[157] F. Lindebner, A. Kautsch, M. Koch, and W. E. Ernst, Int. J. Mass Spectrom. **365-366**, 255 (2014), ISSN 1387-3806, URL http://www.sciencedirect.com/science/article/pii/S1387380613004582.

[158] K. D. Closser, O. Gessner, and M. Head-Gordon, J. Chem. Phys. **140**, 134306 (2014), URL http://scitation.aip.org/content/aip/journal/jcp/140/13/10.1063/1.4869193.

[159] A. Masson, M.-C. Heitz, J.-M. Mestdagh, M.-A. Gaveau, L. Poisson, and F. Spiegelman, Phys. Rev. Lett. **113**, 123005 (2014), URL https://link.aps.org/doi/10.1103/PhysRevLett.113.123005.

[160] P. V. Zandbergen, M. Barranco, F. Cargnoni, M. Drabbels, M. Pi, and N. Halberstadt, The Journal of Chemical Physics **148**, 144302 (2018), https://doi.org/10.1063/1.5022863, URL https://doi.org/10.1063/1.5022863.

[161] M. Rader, M. Hebenstreit, and R. E. Zillich, Phys. Rev. A **95**, 033625 (2017), URL https://link.aps.org/doi/10.1103/PhysRevA.95.033625.

Résumé étendu en français

Dans cette thèse, j'ai étudié deux aspects de la dynamique des impuretés atomiques interagissant avec des nanogouttelettes d'hélium superfluide (He), à savoir la photo-excitation d'atomes d'alcalins sur une nanogouttelette et le dopage de nanogouttelettes contenant des tourbillons quantiques avec des atomes de gaz rares. Pour les investigations théoriques, nous utilisons la théorie de la fonctionnelle de la densité d'hélium (He-DFT), similaire à la DFT électronique mais avec la densité d'hélium à la place de la densité électronique, et sa version dépendant du temps (He-TDDFT).

Le premier aspect de cette étude s'est effectué dans le cadre d'une collaboration avec l'équipe expérimentale de Mudrich et Stienkemeier à Heidelberg. Il concerne la photo-excitation du rubidium (Rb). Les atomes d'alcalins constituent une sonde très intéressante des gouttelettes d'He car ils résident dans leur région de surface. Dans cette région il a été suggéré qu'un taux de près de 100% de condensation de Bose-Einstein pouvait être obtenu en raison d'une densité inférieure à celle de l'hélium superfluide dans le volume.

Le deuxième aspect concerne une investigation purement théorique inspirée par des travaux récents de Gomez et Vilesov *et al.*, où les tourbillons quantiques ont été visualisés en dopant des nanoparticules d'He avec des atomes d'argent, puis en les faisant atterrir en douceur (« soft landing ») sur un écran de carbone. Les images au microscope électronique montrent de longs filaments d'agrégats d'atomes d'argent qui s'accumulent le long des noyaux des vortex. La formation de réseaux de tourbillons quantiques à l'intérieur de nanogouttelettes est également mise en évidence en utilisant l'imagerie par diffraction des rayons X pour visualiser les motifs de Bragg caractéristiques des agrégats de xénon (Xe) piégés à l'intérieur des noyaux des vortex.

Nos simulations impliquant des gouttelettes hébergeant des tourbillons quantiques ouvrent la voie à d'autres investigations sur des gouttelettes hébergeant une série de vortex, impliquant de multiples impuretés.

Introduction (Chapitre 1)

Jusqu'aux années 1980, la plupart des travaux expérimentaux et théoriques ont été effectués sur des systèmes macroscopiques, c'est-à-dire des systèmes pour lesquels le nombre d'atomes est de l'ordre de grandeur du nombre d'Avogadro N_A. Ce n'est qu'au cours des deux dernières décennies que les progrès technologiques ont permis aux expérimentateurs d'obtenir des gouttelettes d'hélium superfluides de taille nanométrique. Dès le début des années 1990, les nanogouttelettes d'hélium superfluides sont devenues un champ d'étude actif, tant sur le plan expérimental que théorique.

Les nanogouttelettes d'hélium sont considérées comme des systèmes modèles idéaux pour explorer l'hydrodynamique quantique dans des superfluides autonomes et isolés. L'objectif principal a été l'évolution de leurs propriétés en fonction du nombre d'atomes, depuis l'agrégat de petite taille jusqu'à la limite de la matière condensée. Les agrégats d'hélium sont particulièrement intéressants dans la mesure où les effets quantiques jouent un rôle clé dans la détermination de leurs propriétés. En particulier, étant donné qu'une nanogouttelette d'hélium constitue un ensemble de bosons à environ 0.4 K[31,32], des manifestations de comportement collectif (comme la superfluidité) sont attendues. D'autre part, il n'est pas encore clair comment la taille finie de cet ensemble affecte ce comportement collectif non-classique.

Récemment, Toennies *et al.* ont mesuré le spectre électronique de molécules de glyoxal solvatées dans des nanogouttelettes d'hélium,[33] et l'ont trouvé compatible avec une simulation théorique utilisant la courbe de dispersion de phonons d'He II superfluide macroscopique. Les auteurs eux-mêmes soulignent cependant que pour la taille moyenne des nanogouttelettes dans lesquelles ont été effectuées les expériences, qui était de 5500 atomes d'He, Ref. [33], les effets de taille finie dans la région intérieure devraient être négligeables (voir aussi Refs. [34, 35]). Il n'est donc pas surprenant qu'ils trouvent des résultats cohérents avec le cas du superfluide macroscopique, en particulier pour une molécule comme le glyoxal qui est solvatée à l'intérieur de la nanogouttelette, et pour laquelle les effets de surface jouent donc un rôle mineur. Par conséquent, l'influence de la taille des clusters d'He sur la superfluidité n'a pas été déterminée de façon concluante jusqu'à présent.

L'interaction hélium-hélium est déjà faible dans l'hélium liquide macroscopique. Dans les systèmes auto-liés finis tels que les gouttelettes elle est encore plus faible: l'énergie de liaison par atome est <7.17 K. De ce fait, les gouttelettes d'hélium se refroidissent très rapidement par évaporation, qui est très rapide, et atteignent ainsi leur température limite d'environ 0.38 K en quelques microsecondes. Les gouttelettes d'hélium pur sont des systèmes neutres et leurs propriétés comme leur taille, leur énergie de liaison et leur spectre d'excitation ne sont pas faciles à déterminer expérimentalement. Ces pro-

priétés sont généralement obtenues par des méthodes indirectes. Cela n'a pas empêché les théoriciens de décrire des gouttelettes dopées ^4He_N en utilisant une grande variété d'approches en fonction de la taille et du caractère des gouttelettes. Ces méthodes incluent Monte Carlo quantique (de diffusion, ou variationnel[37], Hypernetted-Chain/Euler-Lagrange[36]) et beaucoup d'autres.

Une propriété remarquable des gouttelettes d'hélium, contrairement à l'hélium liquide macroscopique, est leur capacité à capturer n'importe quel type de dopants avec lesquels ils entrent en collision. En fonction de la force de l'interaction dopant-^{4}He et de la tension superficielle de la gouttelette, on peut définir un paramètre sans dimension λ[38] avec une valeur critique λ_0 ~1.9. Au-dessous de λ_0, les impuretés sont liées à la surface de la gouttelette (c'est le cas des atomes d'alcalins par exemple) qu'elles déforment pour une meilleure interaction. Au-dessus e λ_0, elles sont solvatées à l'intérieur de la gouttelette. Les gouttelettes peuvent donc être dopées avec presque toutes sortes d'espèces atomiques ou moléculaires.

Du point de vue de la gouttelette, cela signifie qu'il est possible d'utiliser les dopants comme des sondes peu perturbantes pour déterminer les propriétés superfluides des gouttelettes d'hélium qui seraient inaccessibles avec d'autres méthodes. Pour deux exemples de ceci, voir Refs. [39-41], où un dopant est utilisé pour sonder le caractère superfluide de petites gouttelettes d'hélium ^{4}He et Refs. [42, 43] pour déterminer leur température limite.

De plus, du point de vue des impuretés, la solvatation en nanogouttes d'hélium permet un vaste spectre d'études expérimentales. Du fait que les gouttelettes d'hélium constituent un environnement liquide superfluide ultra-froid, avec très peu d'interaction avec le dopant, on peut réaliser des études de spectroscopie à haute résolution. De plus, en contrôlant finement le nombre de dopants [29], on peut utiliser des gouttelettes comme matrices pour créer des structures auto-organisées de molécules polaires, ou des agrégats de métaux très froids et étudier leur explosion de Coulomb.

L'une des propriétés les plus intrigantes des gouttelettes d'hélium superfluides est le fait qu'elles peuvent héberger des vortex quantifiés. En raison de leur température ultra basse, ce sont de véritables liquides quantiques et leur moment cinétique est quantifié. L'existence de tourbillons quantiques a été anticipée car ceux-ci ont été créés et observés dans des condensats de Bose-Einstein (BEC) constitués de gaz dilués. Cependant, la détection de tourbillons quantiques est encore expérimentalement difficile (voir Section 7 de cette thèse).

Parmi les nombreux travaux menés sur les gouttelettes d'hélium au cours des dernières décennies, à la fois expérimentalement et théoriquement, on peut citer les spectres d'absorption de gouttelettes d'hélium dopées par des métaux alcalins, l'étude de gouttelettes dopées mixtes ^{3}He-^{4}He, celle des électrons dans de l'hélium liquide, l'étude de

la vitesse critique de Landau à l'intérieur de petites ^{4}He gouttelettes... Pour un aperçu plus complet et plus exhaustif, je renvoie aux articles de revue Refs. [44-46].

Méthodes utilisées (Chapitre 2)

D'un point de vue théorique, l'hélium superfluide doit être considéré comme un système quantique de grande dimension. Les calculs quantiques Monte Carlo[47] (QMC) et quantique direct[48-50] sont les méthodes les plus précises, mais ils demandent des ressources informatiques qui dépassent rapidement les capacités actuellement disponibles lorsque le nombre d'atomes d'hélium augmente. De plus, QMC ne peut pas décrire l'évolution dynamique de l'hélium superfluide en temps réel. Pour pallier ces limitations, des méthodes semi-empiriques basées sur le formalisme de la DFT ont été introduites:[51-53]. La DFT peut être appliquée à des systèmes beaucoup plus grands que QMC et permet une formulation dépendante du temps. Elle offre le meilleur compromis entre précision, faisabilité computationnelle, et taille réaliste des systèmes traités par rapport aux tailles des systèmes expérimentaux. Le principal inconvénient de la DFT est que la fonction énergétique exacte n'est pas connue et doit donc être construite de manière semi-empirique. De plus, la description de l'interaction dopant-hélium dans les gouttelettes d'hélium dopées est limitée à une approche de champ moyen. Néanmoins, la DFT est la seule méthode à ce jour capable de reproduire avec succès les résultats d'une vaste gamme d'expériences résolues en temps dans l'hélium superfluide, pour des tailles réalistes par rapport aux conditions expérimentales.

Le point de départ de la méthode fonctionnelle de densité est le théorème de Hohenberg-Kohn[54] (HK), qui indique que l'énergie de l'état fondamental E_v d'un système *interagir inhomogène* dans un potentiel statique v peut être écrit comme une fonctionnelle unique de la densité à un corps ρ, dénotée $F[\rho]$, une fonctionnelle universelle —valable pour *n'importe quel* nombre de particules et *n'importe quel* potentiel externe v— de la densité.

Kohn et Sham ont ensuite reformulé[55] la théorie en introduisant un schéma d'approximation pour la fonctionnelle $F[\rho]$ qui est analogue à la méthode de Hartree, mais qui contient également la majeure partie des effets de corrélation inhérents à l'interaction des systèmes à plusieurs corps. L'approximation commence par scinder la fonctionnelle en une énergie cinétique et une partie d'énergie de corrélation. L'énergie cinétique est celle d'un système fictif de particules *sans interaction* de densité ρ. La partie de corrélation correspond à un système de particules *en interaction* avec la même densité. Pour la partie cinétique, cela nous permet d'écrire l'énergie cinétique totale comme la somme des énergies cinétiques individuelles des particules sans interaction. La différence entre la véritable énergie cinétique du système en interaction et celle du système fictif est prise en compte dans la partie énergie de corrélation. C'est seulement la somme de ces deux

termes qui donne l'énergie d'état fondamental correcte pour un système de particules en interaction.

Parce que la fonction que nous avons utilisée dans ce travail est calibrée pour reproduire le bon comportement de l'hélium liquide à température nulle et sans pression, nous supposons une condensation complète de l'hélium entre Bose-Einstein (BE). Dans ce cas, tous les atomes d'hélium occupent le même état fondamental, pris comme orbitale Kohn-Sham. Les expressions de la fonction d'onde à N-corps et de la densité se simplifient alors davantage et permettent de décrire l'ensemble du système en définissant une fonction d'onde efficace qui ne dépend que d'une coordonnée dans un espace cartésien à trois dimensions.

La difficulté consiste à concevoir une fonction telle que les propriétés physiques souhaitées de l'hélium puissent être bien décrites. C'est loin d'être trivial mais plusieurs de ces fonctionnelles de la densité sont disponibles à l'heure actuelle. La fonctionnelle de la densité utilisée dans ce travail est basée sur la fonctionnelle d'*Orsay-Trento* qui est discutée dans la Section 2.3 de la thèse. Elle utilise une approche non locale à échelle finie et constitue, à ce jour, le modèle le plus précis dans la mesure où ses paramètres ont été ajustés pour reproduire les propriétés globales de l'hélium liquide à température nulle.

Dans le cas de densités de liquide hautement inhomogènes, par ex. en présence d'impuretés atomiques avec une interaction He-X très forte, la fonctionnelle OT devient numériquement instable. Pour résoudre ce problème, un terme de pénalité énergétique est ajouté. L'inclusion de ce terme dans la fonctionnelle OT empêche l'accumulation excessive de densité. La suppression des termes non locaux de la fonction OT d'origine et l'ajout de ce terme de pénalité donnent une fonctionnelle de densité modifiée qui est appelée fonctionnelle du solide *(Solid Functional)*. Voir Section 2.4 pour plus de détails et pour les valeurs de ses paramètres.

Pour décrire l'évolution temporelle du système, le théorème de Runge-Gross étend la DFT à sa version dépendante du temps TDDFT[56]. La variation fonctionnelle de l'action associée (voir Equation (2.49) pour un exemple) conduit à une équation d'Euler-Lagrange (EL) dépendante du temps. En considérant seulement les états stationnaires du Hamiltonien, on obtient une équation EL indépendante du temps qui, lors de la résolution, donne l'énergie de l'état fondamental du système.

Pour plus de détails sur la façon dont les calculs statiques et dynamiques sont résolus pour les différentes impuretés dans des potentiels d'interactions isotropes et anisotropes, veuillez vous reporter aux Sections 2.3 et 2.4.

Dynamique d'état excité des nanogouttelettes dopées aux alcalis (Chapitre 3)

Dans un article de 1996[74], Griffin et Stringari ont fait valoir que près de 100% de condensation de Bose-Einstein pouvait être obtenue dans la région superficielle à faible densité d'He superfluide à $T = 0$, contre seulement 10% dans le volume du liquide. Il est donc évident qu'une sonde à perturbation minimale capable d'étudier la surface d'un cluster He est très souhaitable.

Il a été proposé d'un point de vue théorique[75] que les atomes d'alcalins résident sur la surface de la nanogoutte. Des preuves expérimentales ont été trouvées[76-78] plus tard quand il a été observé que le spectre de fluorescence induite par laser (LIF) du sodium était déplacé par rapport à celui du sodium dans la phase gazeuse en raison de la présence de l'environnement d'hélium, mais seulement d'environ la moitié par rapport à celui du même alcalin à l'intérieur de l'hélium liquide.

Les atomes d'alcalins sont donc un choix très naturel pour ce type d'études. Par exemple, avec un paramètre de solvatation (voir Section 1.3) λ de 0.729[38], Rb reste lié à la surface de la gouttelette. De plus, les atomes d'alcalin ont un spectre d'absorption simple et bien connu. Par ailleurs, leur structure électronique simple à un électron de valence permet une modélisation théorique détaillée. Ces atomes n'introduisent que des perturbations faibles (les énergies d'interaction alcalin-hélium sont de l'ordre de 1 cm^{-1}[79]). Enfin, des calculs théoriques[80,81] et des spectres expérimentaux[82-84] d'atomes d'alcalins à l'intérieur de l'hélium liquide sont disponibles à titre de comparaison.

Les transitions $n\mathrm{p}\,^2\mathrm{P} \leftarrow n\mathrm{s}\,^2\mathrm{S}$ des atomes d'alcalins ont suscité beaucoup d'intérêt d'un point de vue expérimental aussi bien que théorique. La spectroscopie des états excités supérieurs a été largement explorée[86-95]. Les spectres obtenus peuvent être reproduits avec succès par un modèle pseudo-diatomique dans lequel la nanogouttelette est représentée par un pseudo-atome. Pour les états excités supérieurs, ce modèle échoue progressivement en raison des limitations de son domaine de validité[96,97]. Alors que l'effet de l'environnement d'une nanogoutte d'hélium sur le spectre des états excités d'un alcalin en sa surface est maintenant assez bien compris, la dynamique induite par l'excitation d'un de ces états est peu explorée.

Dans cette partie de la thèse, les résultats de la dynamique en temps réel d'un seul atome de rubidium (Rb) électroniquement excité résidant initialement dans une cuvette en surface d'une nano-gouttelette d'hélium sont présentés. L'atome est excité depuis son état fondamental $5\mathrm{s}\,^2\Sigma_{1/2}$ vers les états $5\mathrm{p}\,^2\{\Sigma,\Pi\}$ et $6\mathrm{p}\,^2\{\Sigma,\Pi\}$ (voir Section 2.6.1 pour une explication des étiquettes d'état électroniques utilisées). Habituellement, cette excitation provoque la désorption soit de l'atome nu, soit d'un complexe de l'alcalin avec

un ou plusieurs atomes d'hélium, appelé un « exciplexe ».

Imager la dynamique des états excités (Chapitre 4)

Le Chapitre 4 correspond à une étude combinée expérimentale et théorique centrée sur l'imagerie et la caractérisation de la dynamique induite par les excitations 5p←5s et 6p←5s du rubidium hébergé par une nanogouttelette d'hélium. L'expérience a utilisé des techniques pompe-sonde à l'échelle femtoseconde, avec un premier laser excitant le Rb sur la surface des gouttelettes au temps t_{exc} et un second laser l'ionisant pour la détection par imagerie des vecteurs vitesse (VMI) au temps t_{ion}. Les résultats ont permis de caractériser un délai critique τ_c, appelé « fall-back time »(temps de retour), entre deux processus opposés. Si $t_{ion} - t_{exc} \leq \tau_c$, l'atome Rb sortant est encore assez proche de la gouttelette pour que l'énergie d'attraction dans l'état ionique atteint par le laser sonde soit supérieure à son énergie cinétique. Par conséquent, le Rb^+ fait demi-tour et il finit solvaté. A l'opposé, pour $t_{ion} - t_{exc} \geq \tau_c$, l'ionisation se produit trop tard pour que Rb^+ ressente une attraction appréciable de la part de la gouttelette, et il avait déjà trop d'énergie cinétique, il s'échappe.

L'étude théorique a porté sur la compréhension de la dynamique de désorption et sur la détermination des temps de retour, pour comparer avec l'expérience. Elle a fait usage de l'He-TDDFT présentée dans Section 2.6, à la fois dans les états excités et les états ionisés. Les résultats sont présentés dans l'article incorporé à la suite dans ce chapitre, article qui a été publié dans le Journal of Physical Chemistry Letters[98].

Dans nos simulations, nous trouvons que les états excités 5p et 6p désorbent à des échelles de temps très différentes, séparées par deux ordres de grandeur (~100 ps et ~1 ps pour respectivement 5p et 6p). Ceci est en bon accord avec les résultats expérimentaux, et permet de conclure à un processus impulsif de désorption par excitation dans le cas de l'excitation 6p, alors que le mécanisme de désorption pour l'excitation 5p est plus complexe.

Dynamique de désorption des exciplexes RbHe (Chapitre 5)

Les résultats du Chapitre 4 montre un bon accord théorie-expérience pour les états 6p et $^2\Sigma_{1/2}$ et $^2\Pi_{1/2}$ de l'excitation 5p. Par contre, dans nos simulations, l'excitation à l'état 5p $^2\Pi_{3/2}$ aboutit à un exciplexe de RbHe lié à la surface, contrairement au cas expérimental où un exciplexe RbHe est bien formé, mais il désorbe de la surface des gouttelettes. Comment résoudre cette apparent désaccord? C'est la question qui a conduit à ce travail. Nous avons montré qu'en introduisant la relaxation de spin $^2\Pi_{1/2} \leftarrow {}^2\Pi_{3/2}$ dans les simulations, l'exciplexe RbHe est capable de désorber à partir de la surface de la

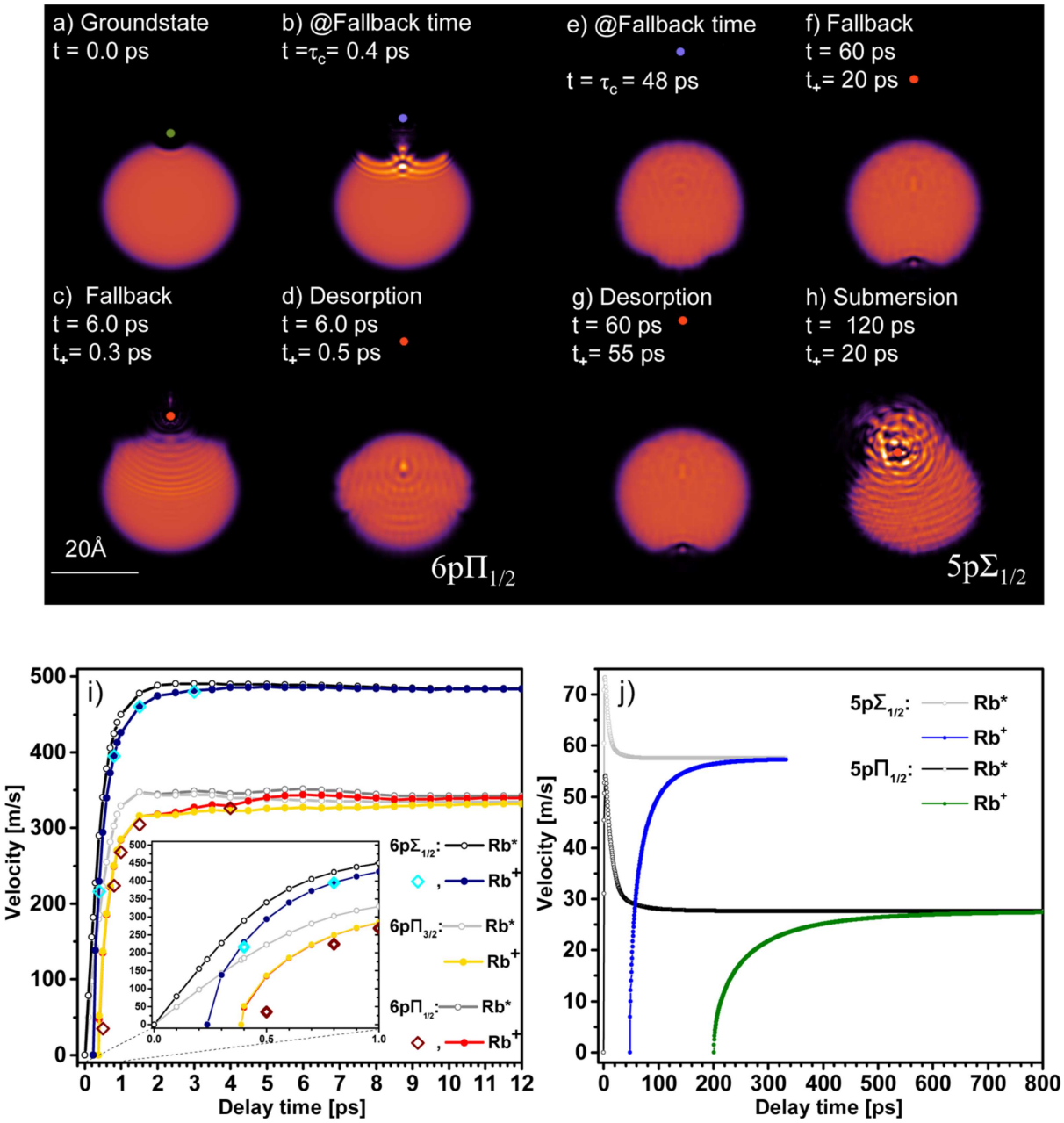

Figure 1: Densités 2D (a–d,e–h) et vitesses basées sur TDDFT (i,j) pour un atome de Rb attaché à une goutellette He_{1000} et excité depuis l'équilibre (a) vers des états 6p (colonne de gauche) et 5p (colonne de droite). Les densités sont représentées pour différents temps total de propagation t et différents instants d'ionisation t_+ : (b,e) Rb neutre à $t = \tau_c$ (« fall-back time », temps critique de retour); (c,f) ionisation à $t_+ < \tau_c$, l'ion Rb^+ retombe sur la nanogouttelette; (d,g) $t_+ > \tau_c$, désorption de Rb^+ ; (h) solvatation de Rb^+ ; (i,j) évolution des vitesses Rb* avec le temps t (symboles gris vides), et vitesses finales de Rb^+ (symboles pleins) en fonction de t_+. (Voir Chapitre 4 de la thèse.)

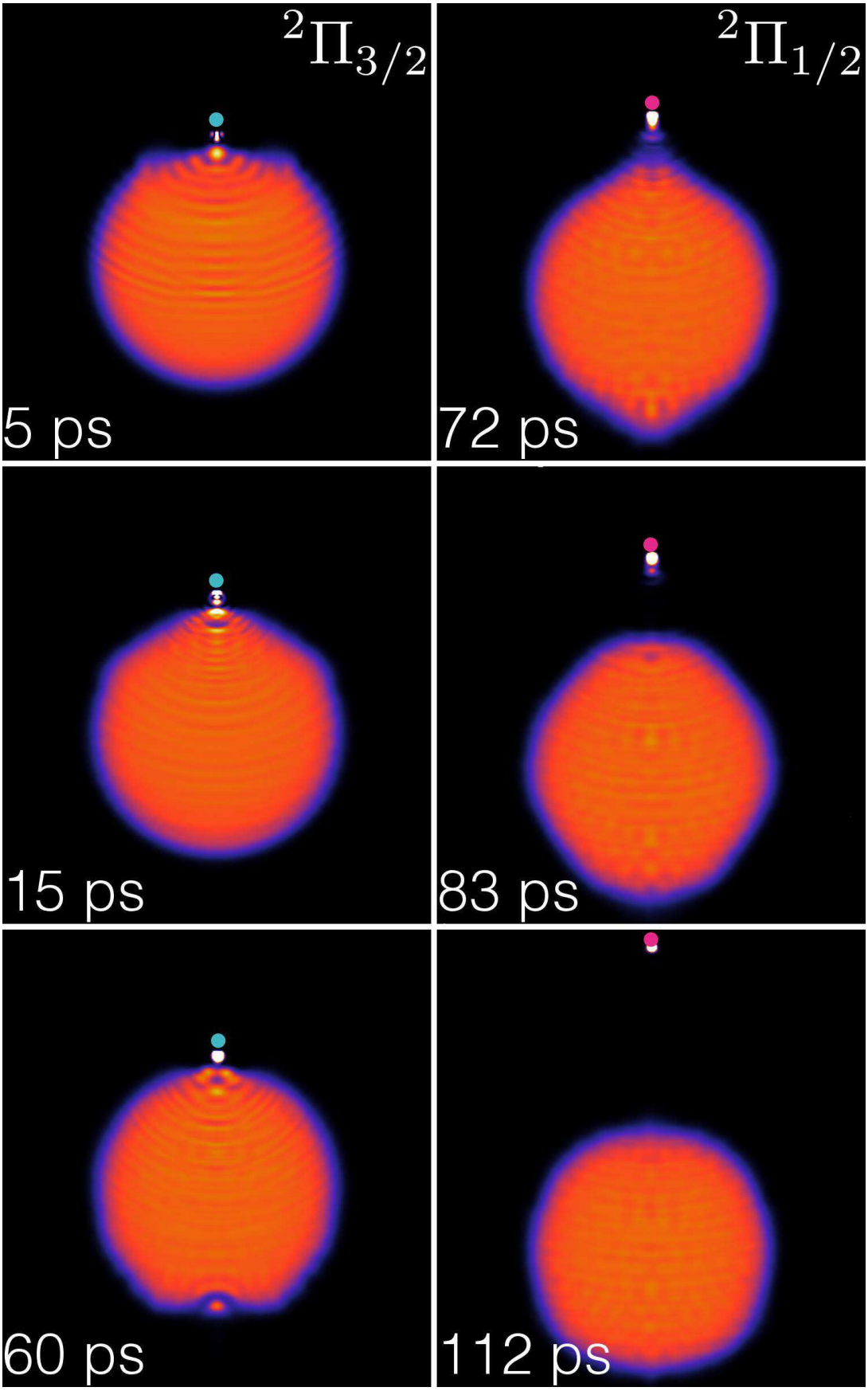

Figure 2: Instantanés de la densité de l'hélium au cours de l'évolution du complexe $RbHe_{1000}$ excité pour η=15%, Δt=60 ps. Le point vert représente l'atome Rb, excité à l'état $5p\Pi_{3/2}$; le point magenta est l'atome Rb après une relaxation soudaine à l'état $5p\Pi_{1/2}$. (Voir Chapitre 5 de la thèse.)

gouttelette, ce qui résout cette contradiction.

Lors de la photo-excitation de Rb à l'état 5p $^2\Pi_{3/2}$, un atome d'He peut s'y attacher, formant ainsi un exciplexe HeRb. Ce processus ne peut pas se produire si Rb est excité à l'état 5p $^2\Pi_{1/2}$ à cause de l'existence d'une barrière (voir Figure 5.1) qui empêche la formation d'exciplexe.

Dans la phase gazeuse, un exciplexe HeRb 5p $^2\Pi_{1/2}$ peut être formé s'il y a assez d'énergie cinétique pour que Rb* surmonte la barrière de potentiel. Alternativement, la collision de l'exciplexe HeRb 5p $^2\Pi_{3/2}$ avec un autre atome ou complexe pourrait faire relaxer l'atome Rb* de l'état 5p $^2\Pi_{3/2}$ vers l'état 5p $^2\Pi_{1/2}$, surmontant alors la barrière car les puits de potentiel pour les deux états sont à des distances Rb-He similaires. En surface des nanogouttelettes à la température de 0.4 K, aucun de ces mécanismes n'est disponible pour expliquer la formation des exciplexes HeRb 5p $^2\Pi_{1/2}$ et leur éjection potentielle.

Cependant, la désexcitation non radiative de l'atome Rb* depuis l'état 5p $^2\Pi_{3/2}$ vers l'état 5p $^2\Pi_{1/2}$ fournit assez d'énergie pour que l'atome ou l'exciplexe puisse être éjecté. Notez dans la Figure 5.1 que le minimum du potentiel 5p $^2\Pi_{3/2}$ est à 12683 cm^{-1}, et celui du 5p $^2\Pi_{1/2}$ potentiel est à 12518 cm^{-1}; la valeur de ce potentiel à la barrière est de 12611 cm^{-1}. Ainsi, une désexcitation non radiative de l'atome Rb* peut ajouter à son énergie cinétique d'origine jusqu'à 165 cm^{-1}. Il est à noter qu'il sera éjecté dans l'état 5p $^2\Pi_{1/2}$, et non dans le 5p $^2\Pi_{3/2}$ où il était précédemment photo-excité, mais les mesures expérimentales ne permettaient pas de déterminer l'état électronique final de l'atome ou de l'exciplexe.

Les simulations ont consisté à induire de façon soudaine la relaxation vers l'état 5p $^2\Pi_{1/2}$ (après une phase de stabilisation dans l'état 5p $^2\Pi_{3/2}$), et à attribuer au Rb* une proportion η des 165 cm^{-1} d'énergie disponible. Nous avons conclu qu'une proportion $\eta = 15$ % permettait de reproduire l'expulsion, et d'obtenir un bon accord avec les résultats expérimentaux. Cette étude a fait l'objet d'une publication.

Nanogouttelettes de potassium dopées (Chapitre 6)

Sous la supervision de Nadine Halberstadt et moi-même, un projet de recherche M2 –*M2 Physique Fondamentale*– intitulé ***« Dynamique d'une nanogouttelette d'hélium superfluide dopée avec un seul atome de potassium »*** a été mené par Maxime Martinez.

Ce projet étudiait le comportement statique et dynamique d'un atome de potassium (K) excité de la configuration d'équilibre K-^{4}He$_{1000}$ aux états K*(4p)-^{4}He$_{1000}$ et K*(5s)-^{4}He$_{1000}$. Le choix du potassium a été motivé par un désaccord dans les études expérimentales résolues en temps[100-102] sur les constantes de temps pour la désorption. De plus, la masse de potassium se situe entre celles des alcalins plus lourds comme le rubidium

et le césium, et les plus légers, comme le lithium et le sodium. Par conséquent, le potassium présente un cas intéressant, étant à la limite entre le régime classique pour les alcalins lourds et un régime quantique pour les plus légers. Les deux approches pour la description du potassium, classique et quantique, sont testées pour la description des propriétés d'équilibre et de l'excitation 5s ← 4s. Ce travail n'est pas inclus dans cette thèse mais peut être trouvé à la Ref. [61].

On conclut que les effets quantiques de K existent mais ne sont pas essentiels à la compréhension et à la description de la dynamique. Donc l'excitation K*(4p)-^{4}He$_{1000}$ est étudiée avec une description classique de K.

Tourbillons quantifiés en gouttelettes (Chapitre 7)

Le deuxième aspect de la dynamique d'impuretés atomiques en interaction avec des nanogouttelettes d'hélium étudié dans cette thèse concerne une investigation purement théorique inspirée par des travaux récents de Gomez et Vilesov *et al.* Dans ces expériences, les tourbillons quantifiés ont été visualisés en dopant des nanoparticules d'He avec des atomes d'argent, puis en les faisant atterrir en douceur (« soft landing ») sur un écran de carbone. Les images au microscope électronique montrent de longs filaments d'agrégats d'atomes d'argent qui s'accumulent le long des noyaux des vortex. La formation de réseaux de tourbillons quantiques à l'intérieur de nanogouttelettes est également mise en évidence en utilisant l'imagerie par diffraction des rayons X pour visualiser les motifs de Bragg caractéristiques des agrégats de xénon (Xe) piégés à l'intérieur des noyaux de vortex.

L'une des signatures les plus claires de la nature quantique d'une substance - et en fait de la superfluidité - est l'apparition de vortex quantiques. Contrairement à un fluide normal, qui tourne comme un corps solide lorsque son récipient se déplace à une faible vitesse angulaire, un superfluide reste au repos. Cependant, au-dessus d'une certaine vitesse angulaire critique, l'état thermodynamiquement stable d'un superfluide comprend un ou plusieurs vortex quantiques. Un tel vortex peut être caractérisé par une fonction d'onde macroscopique et une circulation de vitesse quantifiée en unités de $\kappa = \frac{h}{m}$, où h est la constante de Planck et m est la masse d'un atome ^{4}He[105,106]. Récemment, l'étude de la vorticité a été étendue à des systèmes finis tels que les condensats de Bose-Einstein (BEC) confinés dans des pièges[106,107]. Le transfert d'énergie et de moment cinétique dans les systèmes finis entre les tourbillons quantiques et les excitations de surface est particulièrement intéressant car il définit la dynamique de nucléation, la forme et la stabilité des vortex impliqués[106,107]. En comparaison avec les BEC confinés, les gouttelettes ^{4}He sont autonomes et présentent un cas de superfluide à interaction forte. De plus, le diamètre d'un noyau de vortex est d'environ 0,2 nm dans le superfluide ^{4}He[105],

ce qui est petit par rapport à la taille des gouttelettes, et suggère une tridimensionnalité des vortex dans les gouttelettes. Les tourbillons quantiques dans des gouttelettes d'^{4}He a donc attiré un intérêt considérable[108-111].

Dans les expériences de Gomez *et al.* citées plus haut,[133] les tourbillons à l'intérieur des gouttelettes superfluides ^{4}He, produites par l'expansion d'hélium liquide, ont été détectés en introduisant des atomes d'argent qui se groupaient le long des lignes de vortex dans les gouttelettes. Les gouttelettes d'hélium nécessaires à ce type d'expériences doivent être plus grandes que celles pour la spectroscopie atomique simple et les études de dynamique car elles doivent être suffisamment grandes pour pouvoir héberger une série de vortex dopés avec de nombreux agrégats d'Ag. Un schéma du principe expérimental est montré dans la Figure 7.1. Les gouttelettes d'hélium sont produites par détente d'hélium, à 20 bars et à une température T_0=5.4-7 K, dans le vide à travers une buse. Les gouttelettes refroidissent rapidement par évaporation et atteignent une température de 0.37 K[32], ce qui est bien en dessous de la température de transition superfluide $T_\lambda = 2.17\,\mathrm{K}$[105,106]. Plus loin en aval, les gouttelettes capturent 10 atomes de dopant en passant au travers d'un four[112]. Les gouttelettes sont ensuite déposées sur un substrat de film de carbone mince à température ambiante[112]. Lors de l'impact, les gouttelettes s'évaporent, laissant sur la surface des traces d'Ag, qui sont ensuite visualisées par un microscope électronique à transmission (TEM). La prévalence de dépôts allongés en forme de piste (voir Figure 1.5) montre que les tourbillons sont présents dans des gouttelettes de plus de 300 nm et que leur durée de vie dépasse quelques millisecondes.

Deux ans plus tard Gomez *et al.* ont publié un article[104] sur la formation de réseaux de vortex quantiques à l'intérieur des gouttelettes d'hélium. Ils ont utilisé l'imagerie par diffraction de rayons X femtoseconde à une seule prise pour étudier la rotation de gouttelettes d'hélium-4 superfluides seules, isolées, contenant environ 10^8-10^{11} atomes. La formation de réseaux de vortex quantique à l'intérieur des gouttelettes a été confirmée en observant les spectres de Bragg caractéristiques des agrégats de xénons piégés dans les noyaux des vortex (voir la Figure 7.2).

Collisions frontales (Chapitre 8)

Motivés par des expériences récentes utilisant des atomes Xe pour visualiser des réseaux de vortex dans de très grandes gouttelettes d'hélium[104,127], j'ai abordé dans un premier temps la description de la capture d'atomes de Xe par des gouttelettes d'hélium lors de collisions d'atomes de xénon contre une gouttelette $^4\mathrm{He}_{1000}$. Cette première étape prépare une étude future sur la capture dynamique des atomes de Xe par des gouttelettes hébergeant plusieurs lignes de vortex, combinant la simulation DFT des réseaux de vortex comme dans les Refs. [114, 117] pour les nanocylindres et nanogouttelettes

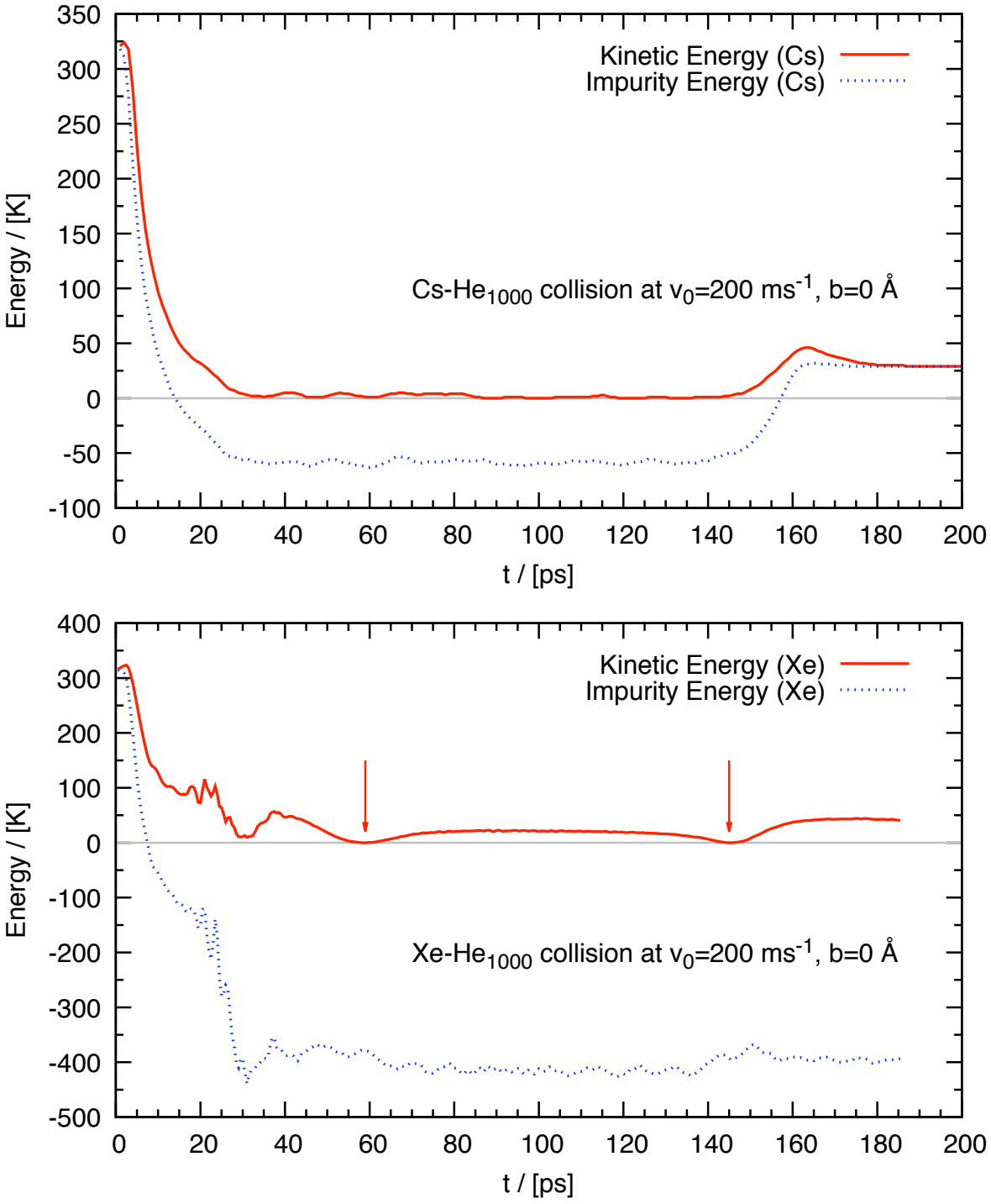

Figure 3: Figure supérieure : Énergie cinétique et totale (cinétique et potentielle) en fonction du temps d'un atome de Cs, collision frontale contre une gouttelette de $^4He_{1000}$ à v_0=200 m/s. Figure inférieur : même que le figure supérieur pour un atome de Xe. Les flèches verticales indiquent les deux premiers points de virage à 59 et 145 ps, dont les densités d'hélium correspondantes sont indiquées dans la colonne de droite de la Figure 8.2. (Voir Chapitre 8 de la thèse.)

d'hélium et la collision avec les atomes de Xe de ce travail. Dans la mesure du possible, les résultats pour Xe, qui est héliophile, sont mis en contraste avec les résultats pour Cs, un atome héliophobe de masse similaire.

Les simulations sont effectuées pour une gouttelette de $N = 1000$ atomes d'hélium. Sa structure d'état fondamental est obtenue en utilisant la He-DFT, qui donne un rayon d'environ 22.2 Å. Ensuite, la dynamique est initiée en plaçant l'atome Xe à 32 Å du centre de masse (COM) de la gouttelette avec un paramètre d'impact égal à zéro (collision frontale). Différentes vitesses initiales v_0 sont testées pour le xénon, de 200 à 600 m/s dans le système de référence de la gouttelette, ce qui correspond à des énergies cinétiques comprises entre 315.8 K et 2842 K. Ces énergies peuvent être comparées à l'énergie de solvatation d'un atome de Xe au centre d'une gouttelette $^4\mathrm{He}_{1000}$, $S_{\mathrm{Xe}} = E(\mathrm{Xe}@^4\mathrm{He}_{1000}) - E(^4\mathrm{He}_{1000}) = -316.3$ K. Par comparaison, l'énergie de solvatation de Cs est de -5.2 K et sa position d'équilibre est dans une cuvette à la surface extérieure des gouttelettes, à environ 26.6 Å de son centre.

Dans les expériences[104,127], les atomes Xe sont à des vitesses thermiques (v_0~240 m/s), et la vitesse moyenne des gouttelettes est d'environ 170 m/s[128].

Les résutats montrent que les collisions frontales de nanogouttelettes d'hélium avec du xénon, un atome héliophile, impliquent un échange d'énergie cinétique du même ordre de grandeur que le césium, un atome héliophobe de masse similaire. Dans les deux cas, cette énergie est largement dissipée par la production d'ondes énergétiques dans la gouttelette, ou bien elle est emportée par des atomes d'hélium rapidement émis. La différence entre les deux atomes (Xe ou Cs) est due à la nature différente de leur interaction avec l'hélium. Une accumulation de densité est observée autour du xénon héliophile lors de la dynamique, alors qu'une bulle est créée autour du césium héliophobe. Il faut donc une vitesse initiale beaucoup plus grande pour le xénon pour qu'il traverse la gouttelette et s'échappe que pour le césium, comme on pouvait s'y attendre.

Capture par He gouttelettes (Chapitre 9)

Récemment, une technique a été introduite pour déterminer la taille des grosses gouttelettes d'He ($N > 10^5$). Elle est basée sur l'atténuation d'un faisceau continu de gouttelettes par des collisions avec des atomes d'Ar à température ambiante[128]. La chambre de dopage de l'appareil à faisceau de gouttelettes est remplie d'argon gazeux et les gouttelettes d'hélium subissent de multiples collisions isotropes avec les atomes Ar sur leur chemin vers la chambre de détection.

De grosses gouttelettes d'hélium peuvent également être dopées de cette manière. Cette méthode, utilisant des atomes Xe, a été instrumentale pour la détection et l'imagerie des réseaux de vortex quantifiés dans les gouttelettes d'hélium[104,113]. Des atomes Xe

ont été utilisés dans ces expériences en raison de leur grande sensibilité à l'imagerie par diffraction cohérente aux rayons X utilisée pour les détecter dans les gouttelettes d'hélium. Des expériences avec de grandes gouttelettes d'hélium superfluides sont passées en revue dans une publication récente[131].

L'interaction impureté-gouttelette en présence de vortex est également pertinente en tant que première étape d'un processus plus complexe conduisant à la formation de nanofils, voir par exemple Refs. [132-135]. Des filaments longs constitués de particules d'hydrogène solides de taille micrométrique piégées sur des noyaux vortex quantifiés ont été utilisés pour imager directement la reconnection entre les vortex quantifiés dans l'hélium superfluide[136].

Dans cette thèse nous présentons les résultats obtenus par la TDDFT pour la collision et la capture des atomes Xe et Ar par une gouttelette $^4He_{1000}$ à différentes énergies cinétiques et paramètres d'impact. Une attention particulière est accordée à l'interaction dépendante du temps des atomes de Xe et d'Ar avec des nanogouttelettes d'hélium contenant des lignes de vortex, et à l'effet de réseaux de tourbillons dopés dans de grosses gouttelettes d'hélium.

En raison du coût de calcul élevé des simulations TDDFT pour ces systèmes, j'ai abordé seulement quelques facettes du processus de capture qui sont pertinentes pour les comparaisons avec les expériences plutôt que d'effectuer une étude systématique du processus. En particulier:

- J'ai étudié la capture d'atomes de Xe par une nanogoutte de ^{4}He, à la fois pour des collisions frontales et pour différents paramètres d'impact, avec des vitesses de valeurs thermiques allant jusqu'à plusieurs centaines de m / s. Les résultats des collisions périphériques avec différentes valeurs du paramètre d'impact sont utilisés pour estimer la section efficace pour la capture du Xe.

- J'ai étudié comment un atome de Xe interagit dynamiquement avec une gouttelette hébergeant une ligne de vortex, avec différentes conditions initiales correspondant à différents régimes de vitesse de l'impureté lorsqu'elle entre en collision avec le noyau du vortex:

  i) un atome Xe initialement au repos sur la surface des gouttelettes et s'enfonçant sous l'effet des forces de solvatation;

  ii) une collision frontale d'un atome Xe ou Ar en mouvement contre la nanogouttelette de ^{4}He.

- J'ai étudié l'état stationnaire d'une grosse gouttelette de $^4He_{15000}$ contenant un anneau de six lignes de vortex dopées avec des atomes d'Ar remplissant complètement les six noyaux des vortex. C'est le système le plus simple qui imite ceux décrits

expérimentalement dans la Ref. [104], où des réseaux de vortex dopés incorporés dans des microgouttes de ^{4}He en rotation ont été imagés.

Capture par des gouttelettes sans vortex

J'ai simulé des collisions frontales d'un atome Xe avec une gouttelette $^4\mathrm{He}_{1000}$ à des vitesses relatives v_0 allant de 200 à 600 m/s. La Figure 9.1 montre les diagrammes en deux dimensions de la densité d'hélium pour la valeur la plus élevée, v_0 =600 m/s. Cette vitesse est bien au-dessus de la plage typiquement rencontrée dans les expériences[104,113,128]. Malgré l'apparition d'une densité d'hélium déconnectée dans le cadre t=87 ps, la simulation montre que l'atome Xe fait finalement demi-tour et est à nouveau capturé à l'intérieur de la gouttelette même à cette vitesse d'impact relativement élevée. Notez que l'impureté Xe, même lorsqu'elle émerge temporairement de la gouttelette, apparaît recouverte de quelques atomes de ^{4}He, voir la configuration à 87 ps.

Tourbillons de ligne

Pour déterminer la structure d'une gouttelette hébergeant un tourbillon linéaire quantique, la propagation en temps imaginaire est lancée à partir d'une densité d'hélium dans laquelle le tourbillon est « imprimé ». A cet effet, une ligne de vortex le long de z peut être décrite par la fonction d'onde effective

$$\Psi_0(\mathbf{r}) = \rho_0^{1/2}(r)\,\mathrm{e}^{i\,\mathcal{S}(\mathbf{r})} = \rho_0^{1/2}(\mathbf{r})\,\frac{(x+iy)}{\sqrt{x^2+y^2}} \tag{1}$$

où $\rho_0(\mathbf{r})$ est la densité de la gouttelette pure ou dopée par une impureté dopée mais sans vortex. Les lignes de vortex le long d'autres directions passant par un point choisi peuvent également être imprimées de cette façon[142].

Dans le cas représenté par l'Equation (1), si l'impureté est dans le vortex le long d'un axe de symétrie du complexe impureté-gouttelette, la fonction d'onde effective $\Psi_0(\mathbf{r})$ – avant et après relaxation– est un vecteur propre de l'opérateur de moment angulaire $\hat{L}_z = -i\,\hbar\partial/\partial\theta$. Le moment angulaire de la gouttelette est alors

$$\langle\hat{L}_z\rangle = \langle\Psi_0(\mathbf{r})|\hat{L}_z|\Psi_0(\mathbf{r})\rangle = N\,\hbar \tag{2}$$

Dynamique de capture par les tourbillons quantiques

Pour étudier l'interaction d'une impureté atomique avec des vortex, j'ai imprimé une ligne de vortex dans la gouttelette $^4\mathrm{He}_{1000}$ et préparé l'atome Xe dans différentes conditions cinématiques.

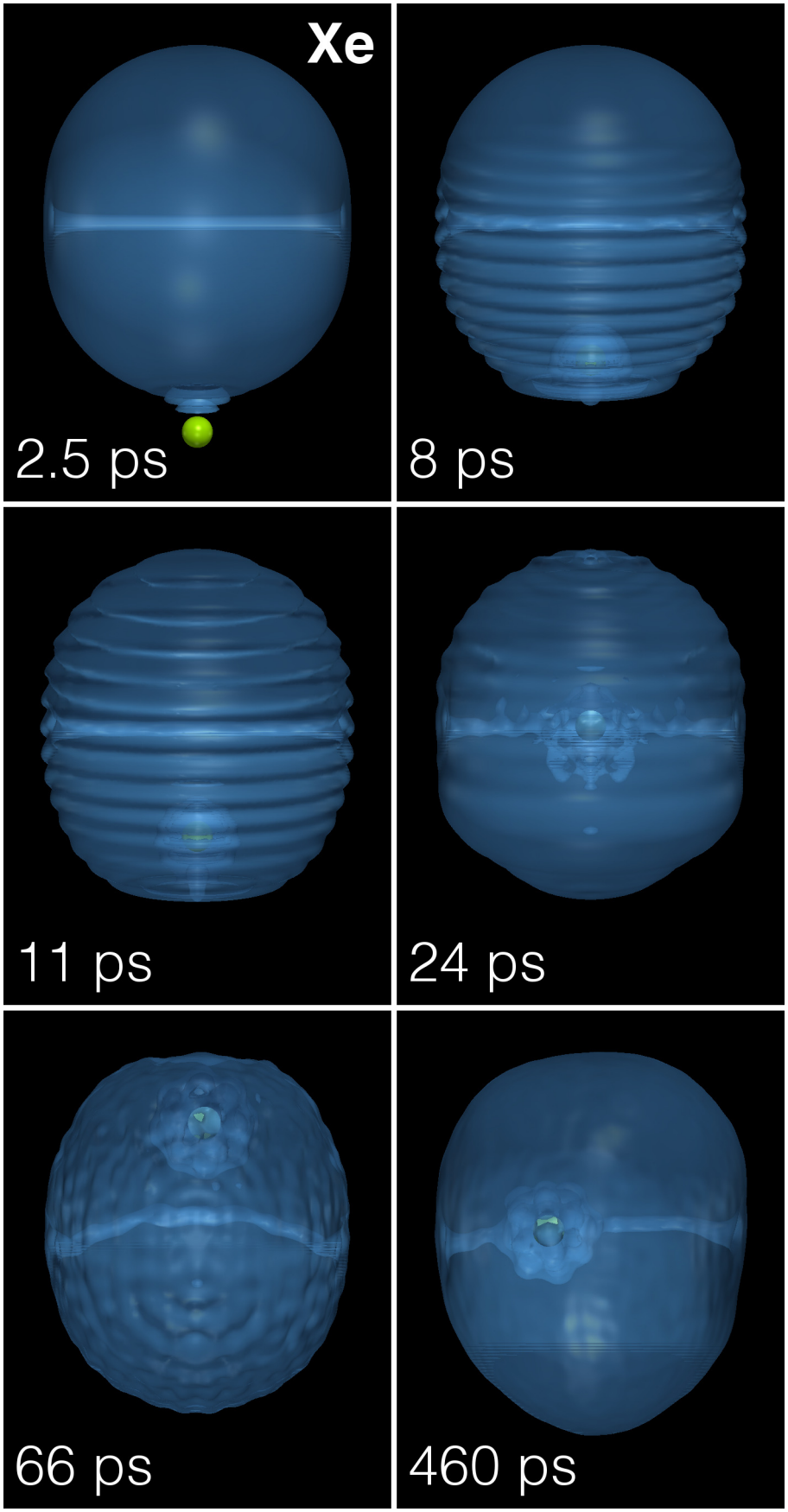

Figure 4: Evolution dynamique d'un atome de Xe (point vert) en collision avec une gouttelette de $^4He_{1000}$ hébergeant une ligne de vortex à v_0=200 m/s. Le temps correspondant est indiqué dans chaque image. (Voir Chapitre 9 de la thèse.)

La diffusion inélastique d'atomes de xénon par des vortex quantiques dans de l'hélium superfluide a été traitée dans Ref. [152]. Il s'est avéré qu'une collision frontale conduit à la capture de Xe par la ligne de vortex pour v_0=15.4 m/s, mais pas pour v_0=23.7 m/s. Nous avons effectué une simulation équivalente en plaçant initialement l'atome Xe à l'intérieur de la gouttelette à 10 Å de la ligne de vortex et en l'envoyant frontalement vers le vortex à une vitesse de 10 m/s. Cette vitesse est de l'ordre de la vitesse thermique d'un atome Xe dans une gouttelette dans des conditions expérimentales, une fois que la gouttelette s'est thermalisée après avoir capturé l'atome Xe (T~0.4 K)[120]. Puisque la position d'équilibre de l'atome Xe est au centre de la gouttelette, il se déplace vers cette région et y reste pendant le reste de la simulation. Dans cette région de la gouttelette, l'atome Xe est également attiré par le vortex, mais il est dévié par l'écoulement superfluide autour de la ligne de vortex et finit par tourner autour de lui. Par conséquent, il est capturé par le vortex sans entrer dans son noyau.

Tableaux de vortex en gouttelettes

L'existence de réseaux de vortex ordonnés à l'intérieur des gouttelettes ^{4}He a été établie par l'apparition de motifs de Bragg dûs à des atomes de Xe piégés à l'intérieur des noyaux de vortex dans des gouttelettes de N=10^8-10^{11} atomes (correspondant à des rayons de 100 à 1000 nm)[104,113]. Nous avons étudié la stabilité d'un ensemble de vortex quantiques comportant jusqu'à n_v=9 vortices à l'intérieur d'une nanogouttelette ^{4}He en utilisant l'approche DFT[114]. Il s'est avéré que la structure favorisée énergiquement pour n_v>6 est un anneau de vortex encerclant un vortex au centre de la gouttelette. Pour n_v=6, la configuration avec un anneau de six vortex se trouve avoir presque la même énergie que l'anneau à cinq avec un vortex au centre. La première structure a été observée expérimentalement[104,113,115], bien que la théorie du vortex classique prédise pour elle un coût d'énergie libre beaucoup plus élevé que pour la seconde[116]. Des structures d'équilibre similaires ont été obtenues par simulations He-DFT pour des nanocylindres d'hélium hébergeant des ensembles de vortex[117].

Nous avons cherché des configurations stationnaires pour un anneau de 6 vortex dans une gouttelette tournante He_{15000} en rotation, en résolvant les équations EL dans le référentiel en corotation avec une vitesse angulaire fixe. Chaque noyau de vortex est rempli avec des atomes d'Ar, et le système est autorisé à relaxer complètement. En fin de simulation, la colonne d'atomes à l'intérieur de chaque noyau de vortex atteint une structure d'équilibre où les atomes Ar sont séparés d'une distance qui est à peu près celle du dimère Ar. Une telle configuration est montrée dans la Figure 7.3. Notez que les noyaux des vortex sont presque des lignes droites, alors que dans un gouttelette non dopée tournant à la même vitesse les lignes de vortex seraient courbées, comme montré par exemple dans la Figure 9.7. Les atomes Ar ne sont pas représentés sur la figure. Les

structures localisées apparaissant dans les noyaux de vortex sont des régions de haute densité, fortement inhomogène, de ^{4}He, et sont dues au potentiel attractif Ar-He.

Les résultats montrent que les atomes Xe et Ar à des vitesses thermiques sont facilement capturés par des gouttelettes d'hélium, avec une section efficace de capture pratiquement égale à la section transversale géométrique de la gouttelette. En ce qui concerne la capture subséquente d'impuretés par des lignes de vortex, la plus grande partie de l'énergie cinétique de l'impureté est perdue dans le processus de capture pendant les premières dizaines de picosecondes. Cela se produit soit par l'éjection d'atomes He promptement émis, soit par la production d'ondes sonores et de grandes déformations dans la gouttelette.

En outre, les simulations montrent également que si la gouttelette héberge un vortex, les impuretés, se déplaçant lentement, sont facilement capturées par la ligne de vortex. Plutôt que d'être piégée à l'intérieur du noyau du vortex, l'impureté se place à une distance proche de celui-ci. Outre la perte d'énergie cruciale lorsque l'impureté frappe la gouttelette, la capture par le vortex est favorisée par un transfert d'énergie supplémentaire de l'impureté à la gouttelette: des déplacements de grande amplitude de la ligne de vortex —comme indiqué dans le ESI[153]— ont lieu, constituant une autre source de la perte d'énergie cinétique dans les dernières étapes de la capture. Une observation connexe est l'apparition de modes Kelvin dans la ligne de vortex, qui n'est pas seulement courbée, mais aussi tordue au cours de la collision.

En conclusion, si les conditions cinématiques de la collision (énergie cinétique et paramètre d'impact) conduisent à la capture de l'impureté par la gouttelette, l'effet de « flipper » provoqué par la surface des gouttelettes peut faciliter la rencontre de l'atome Xe/Ar et de la ligne de vortex —et la capture possible de l'atome par le vortex— puisque les deux ont tendance à rester dans la région interne de la gouttelette. Les résultats le montrent dans le cas de Xe à v_0=200 m/s : Xe est capturé lors de son deuxième passage à travers la gouttelette, alors que cela ne pourrait pas se produire dans l'hélium liquide[152]. Cet effet pourrait expliquer la capture d'impuretés par des lignes de vortex même dans les très grosses gouttelettes utilisées dans l'observation de nanostructures en forme de filaments.

Perspectives d'avenir

Mon travail a porté sur différents aspects de la dynamique en temps réel de la photoexcitation d'un atome de métal alcalin sur la surface d'une nanogouttelette d'hélium. Mener le même type d'études sur d'autres types d'espèces dopantes qui sont solvatées plus profondément à l'intérieur des gouttelettes He (par exemple des métaux alcalino-terreux, ou des métaux de transition) permettrait de mieux comprendre les mécanismes

de désolvatation et d'éjection des atomes d'impuretés excités[154-157].

De plus, une description des couplages induits par l'environnement des gouttelettes He entre les états électroniques et les autres degrés de liberté dans de tels complexes excités serait hautement souhaitable[158,159]. Dans une avancée récente, la relaxation électronique des cations Ba^+ dans les nanogouttelettes He, basée sur une diabatisation des potentiels d'interaction des états électroniques excités de He-Ba^+[160], a été proposée comme un mécanisme pour expliquer l'éjection observée expérimentalement de Ba^+ et Ba^+He_n des gouttelettes d'hélium. Ces mécanismes de relaxation de spin et de relaxation d'état inter-électronique doivent encore être confirmés par des études de dynamique en temps réel.

Enfin, les capacités de l'approche He-DFT pourraient aider à élucider d'autres processus d'intérêt expérimental, comme la capture d'une ou plusieurs impuretés par de grosses gouttelettes hébergeant un réseau de vortex; et comment plusieurs impuretés atomiques, entrant en collision avec une gouttelette en rotation hébergeant des vortex, réagissent en formant de petites grappes, finalement piégés à l'intérieur des noyaux de vortex, comme indiqué par l'apparition de nanostructures en forme de filaments dans des expériences.

Dans toutes ces futures lignes de recherche, ^{4}He-DFT et TDDFT seront des outils essentiels, étant donné leur capacité à décrire avec précision les propriétés d'équilibre et de dynamique des nanogouttelettes d'hélium de taille réaliste, pouvant accueillir des tourbillons, en interaction avec des dopants. Dans ce contexte, il sera extrêmement intéressant de coupler ^{4}He-TDDFT avec la dynamique moléculaire quantique pour aller au-delà de l'approximation du champ moyen de la dynamique du dopant dans l'environnement de l'hélium. Une alternative prometteuse dans l'approche de la fonction de base corrélée (CBF) et son approche multi-composantes récemment développée par Rader *et al.*[161]

Acknowledgements

First of all I would like to thank Anna, who stands by me whatever happens. Without her I would never have had the courage to pursue a PhD. Secondly, I would like to thank my parents, who support me in whatever crazy endeavour I throw myself at. I would also like to thank my thesis supervisor, Nadine Halberstadt, who goes beyond the duties and responsibilities as a supervisor. As well as Manuel Barranco, who's pragmatic no-nonsense approach to research I have come to admire and, together with Nadine Halberstadt, made my time as a PhD student fruitful as well as enjoyable. And lastly I would like to thank my friends and colleagues for making my time inside- as well as outside the lab a very pleasurable time indeed.

This acknowledgment would not be complete without thanking Nicolas Renon and Emmanuel Courcelle of CALMIP who greatly improved the performance of our code and are always available for a helping hand whenever there are bugs to be crushed.

As well as the Université Fédérale Toulouse Midi-Pyrénées for financial support through the "Chaires d'Attractivité 2014" Programme IMDYNHE.

Last but not least I would like to thank Jérôme Cuny, who, as my parraine de thèse, and my goto representative of the Doctoral School, is always available to help make the administrative side of the PhD go as smoothly as possible.

This work has been performed under Grants No. FIS2014-52285-C2-1-P from DGI, Spain, and 2014SGR401 from Generalitat de Catalunya.

The dynamic simulations presented in this work have been carried out thanks to the HPC resources of CALMIP supercomputing center (Grant P1039).

Dr. François M.G.J. Coppens

(30 March 1978)

francois.coppens@irsamc.ups-tlse.fr

31 rue de Figeac, appt. 23
31200 Toulouse

Dutch
+33 7 83 41 77 48

Research interests

Superfluid helium, quantum vortices in superfluids, (time-dependent) density functional theory, Monte Carlo methods, atomic- clusters and cluster collisions, high performance computing, data visualisation

Programming languages, methods, etc.

Fortran

- Parallelisation and optimisation of in-house written code to simulate the quantum dynamics of superfluid ^{4}He using time-dependent He-DFT. Code optimised using Intel's MKL to run on Calmip/EOS, in collaboration with Nicolas Renon and Emmanuel Courcelle from Calmip.
- Publication on Github for public use, with accompanying material explaining the method and how to use the code, with included example calculations:
  - https://github.com/bcntls2016/4hedft
  - https://github.com/bcntls2016/4hedft-vortex
  - https://github.com/bcntls2016/4hetddft-isotropic
  - https://github.com/bcntls2016/4hetddft-anisotropic
- Prepared and taught a 2-day workshop on using He-DFT during the CECAM summer school: https://www.cecam.org/workshop-1381.html

C/C++

Self-written code:

- Ising model (Metropolis and Wolff), study of critical behaviour.
- Nematic liquid crystals (Metropolis), behaviour of topological defects on constrained geometries in the presence/absence of curvature.
- Code profiling and optimisation (using GCC/GProf) for local computer cluster at Lorentz Institute for theoretical physics, Leiden, The Netherlands.

Data analysis and visualisation

- Python, Gnuplot (2D), Matplotlib (2D),
- Paraview (3D)
- UNIX/Linux Bash programming to create automated workflows

Education

2018-current	**Postdoc**: Laboratoire de Physique Théorique (UMR 5152), CNRS NEXT/IRT, France
2015-2018	**PhD in theoretical physics**: Laboratoire Collisions Agrégats Réactivité (UMR 5589), Chaire d'attractivité IMDYNHE 2014 de l'IDEX-UNITI, Université Paul Sabatier, Toulouse, France *Thesis advisor:* dr. N. Halberstadt, prof. dr. M. Barranco *Thesis title:* Ultrafast quantum dynamics of doped super-fluid helium nanodroplets *Defended on:* Friday 15 June 2018.
	Formation: Introduction au Calcul Haute Performance et prise en main du système EOS, Calmip (février 2016)
Professional intermezzo	Groupe OPEN Nederland B.V.; Systems administrator (2014-2015) OGD IT services B.V.; Systems administrator (2013-2014)
2010-2013	**Master in theoretical physics**, Lorentz Institute, Leiden University, the Netherlands *Thesis advisor:* prof. dr. Vincenzo Vitelli *Thesis title:* Monte Carlo simulations of nematic liquid crystals in confined geometries
2005-2010	**Bachelor in physics**, Leiden University, the Netherlands *Thesis advisor:* prof. dr. Martin van Exter *Thesis title:* Near-field correlations in down-converted light with a strongly focused pump
2004-2005	Propedeuse in applied physics, TH Rijswijk, the Netherlands
2003-2004	HAVO (track: Natural sciences & Technology), Roosendaal, the Netherlands *(career reorientation)*
1997-2000	MBO Systems administration, Zoomvliet college, Roosendaal, the Netherlands

Languages

Dutch	Maternal
English	Bilingual (TOEIC score 950 $\sim$ CERF C1)
French	Intermediate: • Alliance Française Toulouse, 4 weeks intensive course (70 hours), CEFR A2 • Alliance Française Toulouse, Evening course (48 hours), CEFR B1
German	working knowledge

Scientific publications

2011 **Type-I spontaneous parametric down-conversion with a strongly focused pump**. H. Di Lorenzo Pires, F. Coppens and M. van Exter. *Phys. Rev. A* **83**(3), pp. 033837(8); doi: 10.1103/PhysRevA.83.033837

2017 **Head-on collisions of Xe atoms against superfluid ^{4}He nanodroplets**. François Coppens, Antonio Leal, Manuel Barranco, Nadine Halberstadt and Martí Pi. *J. Low Temp. Phys.* **187**(5), pp. 439-445; doi: 10.1007/s10909-016-1690-x

2017 **Capture of Xe and Ar atoms by quantized vortices in ^{4}He nanodroplets**. François Coppens, Francesco Ancilotto, Manuel Barranco, Nadine Halberstadt and Martí Pi. *Phys. Chem. Chem. Phys.* **19**(36), pp. 24805-24818; doi: 10.1039/C7CP03307A

2017 **Imaging Excited-State Dynamics of Doped He Nanodroplets in Real-Time**. Johannes von Vangerow, François Coppens, Antonio Leal, Martí Pi, Manuel Barranco, Nadine Halberstadt, Frank Stienkemeier and Marcel Mudrich. *J. Phys. Chem. Lett.* **8**(1), pp. 307-312; doi: 10.1021/acs.jpclett.6b02598

2017 **Density functional theory of doped superfluid liquid helium and nanodroplets**. Francesco Ancilotto, Manuel Barranco, François Coppens, Jussi Eloranta, Nadine Halberstadt, Alberto Hernando, David Mateo and Martí Pi. *Int. Rev. Phys. Chem.* **36**(4), pp. 621-707; doi: 10.1080/0144235X.2017.1351672

2018 **Desorption dynamics of RbHe exciplexes off He nanodroplets induced by spin-relaxation**. François Coppens, Johannes von Vangerow, Manuel Barranco, Nadine Halberstadt, Frank Stienkemeier, Martí Pi and Marcel Mudrich. *Phys. Chem. Chem. Phys.* **20**(14), pp. 9309-9320; doi: 10.1039/C8CP00482J

Talks

2016 **Real-time dynamics in ^{4}He nanodroplets**. *GDR 3575 du CNRS ThéMS*, December; Lille, France

2017 **Xe capture by quantised vortices**. *7e Journées de Dynamique de Sud-Ouest*, June; Montpellier, France

2017 **Dopant Dynamics in Superfluid helium-4 Nanodroplets: from Statics to Time-Dependent He-DFT**. *CECAM School (instructor)*, June; Toulouse, France; url: https://www.cecam.org/workshop-1381.html

2017 **Capture of Xe/Ar by quantised vortices inside He droplets**. *International Symposium Atomic Cluster Collisions*, October; Varadero, Cuba

Poster presentations

2016 **Head-on Collisions of Xe Atoms Against Superfluid ^{4}He Nanodroplets**. *International Conference on Quantum Fluids and Solids*, July; Prague, Czech Republic

2017 **Capture of Xe and Ar atoms by quantised vortices in ^{4}He droplets**. *Conference on Quantum Fluid Clusters*, June; Obergurgl, Austria

2018 **Capture of Xe and Ar atoms by quantised vortices in ^{4}He droplets**. *International Symposium on Quantum Fluids and Solids*, July; Tokyo, Japan

Experience outside of academia

2014-2015 **Groupe OPEN Nederland (full-time)**
Systems administrator

2013-2014 **OGD ICT Services (3 days a week/full-time)**
Customer support and administration of Windows environments

2007-2013 **Various jobs (3 days a week), including**
three years of committee work as secretary, for student association V.S.L. Catena in Leiden. The goal of this committee was to manage its computer network and function as an educational platform for members with an interest in technology and computer science. The network is mixed Windows/Linux environment running on equipment from Cisco, Soekris and VMware.

OGD ICT Services

Leiden Institute of Advanced Computer Science (LIACS)

2004-2007 **Networking4All B.V. (3 days a week)**
Datacentre administrator, Consultant/software developer

(Career reorientation)

2001-2003 **Verburgh B.V., Bergen op Zoom (full-time)**
Netwerk Engineer

2000-2001 **DataByte, Steenbergen (full-time)**
Systems administrator

1998-2000 **Pantra International, Rotterdam (full-time)**
Systems administrator